COMPUTATIONAL MECHANICS FOR SOFT BIOLOGICAL TISSUES

A THESIS SUBMITTED TO
THE GRADUATE SCHOOL OF NATURAL AND APPLIED SCIENCES
OF
MIDDLE EAST TECHNICAL UNIVERSITY

BY

CEM ALTUN

IN PARTIAL FULFILLMENT OF THE REQUIREMENTS
FOR
THE DEGREE OF DOCTOR OF PHILOSOPHY
IN
MECHANICAL ENGINEERING

JANUARY 2023

Approval of the thesis:

COMPUTATIONAL MECHANICS FOR SOFT BIOLOGICAL TISSUES

submitted by **CEM ALTUN** in partial fulfillment of the requirements for the degree of **Doctor of Philosophy in Mechanical Engineering Department, Middle East Technical University** by,

Prof. Dr. Halil Kalıpçılar
Dean, Graduate School of **Natural and Applied Sciences** _____

Prof. Dr. M. A. Sahir Arıkan
Head of Department, **Mechanical Engineering** _____

Assoc. Prof. Dr. Hüsnü Dal
Supervisor, **Mechanical Engineering, METU** _____

Examining Committee Members:

Prof. Dr. F. Suat Kadıoğlu
Mechanical Engineering, METU _____

Assoc. Prof. Dr. Hüsnü Dal
Mechanical Engineering, METU _____

Assoc. Prof. Dr. Ercan Gürses
Aerospace Engineering, METU _____

Prof. Dr. Recep Güneş
Mechanical Engineering, Erciyes University _____

Dr. Mehmet Okan Görtan
Mechanical Engineering, Hacettepe University _____

Date:

I hereby declare that all information in this document has been obtained and presented in accordance with academic rules and ethical conduct. I also declare that, as required by these rules and conduct, I have fully cited and referenced all material and results that are not original to this work.

Name, Surname: Cem Altun

Signature :

ABSTRACT

COMPUTATIONAL MECHANICS FOR SOFT BIOLOGICAL TISSUES

Altun, Cem
Ph.D., Department of Mechanical Engineering
Supervisor: Assoc. Prof. Dr. Hüsnü Dal

January 2023, 202 pages

Computational biomechanics is an active research area, not only to understand the mechanisms behind the behaviours of biological tissues but also to develop medical techniques for surgeries, rehabilitations, and diseases. The thesis mainly composed of two parts namely, growth-induced instabilities and dispersion-type anisotropic viscoelasticity for soft biological tissues.

In the first part of the thesis, planar growth-induced instabilities for a three-dimensional bilayer-type confined tissue is examined. Firstly, a five-field Hu-Washizu type mixed variational formulation for incompressible and inextensible limits is extended for finite growth theory that captures the primary and secondary growth-induced instabilities for anisotropic soft biological tissues. A numerical example is solved by implementing $T2P0F0$ element on the automated differential equation solver, FEniCS. The influence of fiber stiffness on the critical growth parameter, primary and secondary buckling is investigated. The numerical outcomes of this study will help to understand the fiber stiffness effect on the buckling and post-buckling behavior of bilayer-typed anisotropic soft biological tissues.

In the second part of thesis, we proposed five novel formulations for angular-integration-

based dispersion-type anisotropic viscoelastic constitutive models at finite strains where the formulations use bivariate and planar von Mises density distribution functions. Then, a numerical model validation is conducted for the human myocardium. The proposed models use the generalized structure tensor for the baseline hyperelastic mechanical response to reflect the dispersion characteristics along the fiber and sheet directions of the myocardium. A quadratic free-energy function is defined for the viscous response that is mainly composed of logarithmic elastic and micro-viscous strains. The density distribution function is introduced in the constitutive equations by defining two types of formulations, namely, local-based and global-based. In the local-based formulations, we use the density distribution as a part of the micro-viscous free-energy functions. In the global-based formulations, the density distribution function enters the equations during the continuous averaging of the stress and tangent moduli expressions. For the five of proposed models, the overstress response has been identified through either nonlinear or linear evolution laws in each orientation direction by using numerical integration, either over the unit micro-sphere or over the unit planar circle. Then, the fitting performances of the proposed models are examined and compared with the cyclic triaxial shear and triaxial shear relaxation experiments of human passive myocardium from the literature. All models are compared, and their pros and cons are discussed. While local-based formulations suffer from the violation of the normalization condition during the averaging integral stage when the nonlinear evolution is used, the global-based formulations are stable and provide high accuracy for both linear and nonlinear evolutions with a sufficient number of integration points. The proposed formulations provide a histological-based flexible calibration capability for any type of anisotropic soft biological tissue that exhibits either elastic or viscous response.

Keywords: anisotropic viscoelasticity, myocardium, fiber dispersion, growth-induced instability

ÖZ

YUMUŞAK BİYOLOJİK DOKULAR İÇİN HESAPLAMALI MEKANİK

Altun, Cem
Doktora, Makina Mühendisliği Bölümü
Tez Yöneticisi: Doç. Dr. Hüsnü Dal

Ocak 2023 , 202 sayfa

Hesaplamalı biyomekanik, yalnızca biyolojik dokuların davranışlarının arkasındaki mekaniği anlamak için değil, aynı zamanda ameliyatlarda, rehabilitasyonlarda ve hastalıkların tedavisi için gerekli olan tıbbi metotların geliştirilmesi için kullanılan aktif bir araştırma alanıdır. Bu tez, yumuşak biyolojik dokularda büyümeye dayalı düzensizlikler ve dağılım-tipli yöne bağlı viskoelastisite olmak üzere iki ana bölümden oluşmaktadır.

Tezin ilk bölümünde, üç boyutlu çift katmanlı sınırlandırılmış bir dokuda düzlemsel büyümeye bağlı kararsızlıklar incelenmiştir. İlk olarak, sıkıştırılamazlık ve uzatılamazlık sınırlarında kullanabilmek için yöne bağlı davranan yumuşak biyolojik dokularda büyümeye dayalı birincil ve ikincil burkulma davranışını yakalayabilen beş alan değişkenli Hu-Washizu tipi karma bir formülasyon sonlu büyüme teorisi için uyarlanmıştır. $T2P0F0$ eleman formülasyonu otomatik diferansiyel denklem çözücü yazılımı FEniCS'de kodlanarak bir nümerik uygulama çözülmüştür. Lif katılığının kritik büyüme parametresine, birincil ve ikincil düzensizlik moduna olan etkisi araştırılmıştır. Bu çalışmanın sayısal sonuçları, iki katmanlı yapılı yöne bağlı davranış

gösteren biyolojik dokularda burkulma ve burkulma sonrası davranışı üzerindeki lif katılığının etkisinin anlaşılmasına yardımcı olacaktır.

Tezin ikinci bölümünde, formülasyonlarda iki değişkenli ve düzlemsel von Mises yoğunluk dağılım fonksiyonlarının kullanıldığı, dağılım-tipli açısal integrasyona dayalı, yöne bağlı viskoelastik yumuşak biyolojik dokular için beş yeni formülasyon önerilmektedir. Bu modellerin doğrulaması nümerik olarak insan miyokardı davranışı üzerinden gerçekleştirilmiştir. Önerilen modeller, kalp kasının lif ve tabaka yönleri boyunca dağılım özelliklerini yansıtmak için temel hiperelastik mekanik davranışı için genelleştirilmiş yapı tensörü kullanmaktadır. Dokunun viskoz tepkisi için logaritmik elastik ve mikro-viskoz gerinimlerden oluşan ikinci dereceden bir serbest enerji fonksiyonu tanımlanmıştır. Yoğunluk dağılım fonksiyonu, lokal tabanlı ve global tabanlı olmak üzere iki ana formülasyon temelli olarak tanımlanarak malzeme denklemlerine dahil edilmiştir. Lokal tabanlı formülasyonlarda, yoğunluk dağılımı mikro-viskoz serbest enerji fonksiyonlarının bir parçası olarak kullanılmaktadır. Global tabanlı formülasyonlarda, yoğunluk dağılım fonksiyonu, gerilim ve teğet modülünün sürekli ortalaması alınırken denklemlere girmektedir. Önerilen beş model için, gerilim eşleniği olan aşırı gerilim tepkisi, ya birim mikro-küre üzerinde ya da birim düzlemsel daire üzerinde nümerik integrali alınarak her oryantasyon yönünde doğrusal olmayan veya doğrusal evrim yasaları aracılığı ile tanımlanmıştır. Daha sonra, önerilen modellerin performansları incelenmiş ve literatürde insan pasif kalp kası mekanik davranışına yönelik döngüsel üç eksenli kesme ve üç eksenli kesme gevşeme deneyleri ile karşılaştırılmıştır. Lokal tabanlı formülasyonlar, doğrusal olmayan evrim formülasyonları kullanıldığında nümerik integrasyon sırasında normalleşme koşulunu ihlal ederken, global tabanlı formülasyonlar kararlıdır ve yeterli sayıda integral noktası kullanıldığında hem doğrusal hem de doğrusal olmayan evrim formülasyonları için doğruluk sağlamaktadır. Önerilen formülasyonlar, yönden bağımsız veya yöne bağlı bir viskoz tepki sergileyen diğer herhangi bir biyolojik doku için histolojik tabanlı esnek bir kalibrasyon yeteneği sağlamaktadır.

Anahtar Kelimeler: yöne bağlı viskoelastisite, kalp kası, elyaf dağılımı, büyümeye dayalı burkulma

To my wife Kübra and to my sons Kaan & Uras

ACKNOWLEDGMENTS

Research studies presented in this thesis were carried out between 2016-2022. I would like to thank everyone who supported me during this intensive study period. First of all, I would like to thank Assoc. Prof. Dr. Hüsnü Dal for his guidance, encouragement, and patience during all my studies. I would also like to extend a special thank to Prof. Dr. Suha Oral, who supported me, believed in my work, and encouraged me to be included in the Ph.D. program. I would like to thank Assoc. Prof. Dr. Ercan Gürses, who has been on the doctoral thesis monitoring committee from the very beginning and has made valuable contributions and provided guidance.

I also would like to thank Dr. Osman Gültekin for his comments and discussions during the scientific research phases. I would also like to thank Alp Kağan Açan for his contributions and support of teamwork within the scope of the studies.

I would especially like to thank my dear wife, Kübra, who has always been patient with me and spared time for me throughout my intensive doctoral studies, as well as my dear sons, for their understanding and assistance when I devoted myself to my studies.

TABLE OF CONTENTS

ABSTRACT v

ÖZ vii

ACKNOWLEDGMENTS x

TABLE OF CONTENTS xi

LIST OF TABLES xv

LIST OF FIGURES xvii

LIST OF ABBREVIATIONS xxix

CHAPTERS

1 INTRODUCTION 1

1.1 Overview and Backgorund 2

1.2 Growth Phenomena in Biomechanics 6

1.3 Historical Remarks on Structural Features of Myocardium 12

1.4 Proposed Methods and Contribution 16

1.5 The Outline of the Thesis 18

2 BASICS OF CONTINUUM MECHANICS 19

2.1 Kinematics 19

2.2 Stress Measures 25

2.3 Balance Laws of Continuum Thermomechanics 26

2.4 Dissipation Inequality 30

3 GOVERNING EQUATIONS OF THE INCOMPRESSIBLE HYPERELASTIC CONSTITUTIVE MODELING 33

3.1 Isotropic Hyperelasticity 35

3.2 Incompressible Hyperelasticity 38

3.2.1 Lagrangian configuration 39

3.2.2 Eulerian configuration 40

3.2.3 Commonly used isotropic incompressible hyperelastic constitutive models 41

3.3 Anisotropic Hyperelasticity 41

3.4 Two-Field Formulation 44

3.5 Three-Field Formulation 46

3.6 Five-Field Formulation 53

3.6.1 Scalar conjugate pairs for inextensibility (s, λ) 54

3.6.2 Tensorial conjugate pairs for inextensibility $(\boldsymbol{\mathcal{C}}, \boldsymbol{\mathcal{S}})$ 56

3.7 Dual Clamped Patch Test - Comparison of Mixed Element Formulations 57

4 THEORY OF FINITE GROWTH MECHANICS 69

4.1 Kinematic Framework of Finite Growth 70

4.2 Governing Constitutive Equations of Finite Growth 72

4.3 Numerical Examples for Finite Growth 78

4.4 Extended Five-field Formulation for Finite Growth 89

4.5 Planar Growth of Fiber-reinforced Confined 3D Bilayer Stiff film on Compliant Substrate 94

5 DISPERSION-TYPE HYPERELASTIC FORMULATIONS FOR ANISOTROPIC BIOLOGICAL TISSUES 107

5.1 Fiber Dispersion Formulations 110

5.1.1 Generalized structure tensor formulation 110

5.1.2 Generalized structure tensor based bivariate formulation 113

5.1.3 Angular integration dispersion formulation 115

5.2 Examples of Fiber Dispersion Architecture of Biological Tissues . . . 116

6 ANISOTROPIC VISCOELASTIC CONSTITUTIVE MODELLING OF HUMAN MYOCARDIUM 119

6.1 Introduction 119

6.1.1 Hyperelastic constitutive models for passive myocardium . . . 121

6.1.2 Viscoelastic constitutive models for passive myocardium . . . 122

6.2 Governing Equations of Hyperelastic Constitutive Model for Passive Myocardium 124

6.3 Orthotropic Viscoelasticity based on Dispersion-type Hyperelastic Constitutive Model for Passive Myocardium 126

6.3.1 Convolution integral formulation 130

6.3.2 Canonical formulation 131

6.4 Proposed Formulations for Dispersion-type Anisotropic Viscoelasticity 133

6.4.1 Proposed formulations for local-based dispersion-type anisotropic viscoelasticity 136

6.4.1.1 Proposed model-I - local-based bivariate von Mises dispersion formulation 140

6.4.1.2 Proposed model-II - local-based planar and bivariate combined von Mises dispersion formulation 140

6.4.2 Proposed formulations for global-based dispersion-type anisotropic viscoelasticity 143

6.4.2.1 Proposed model-III - global-based bivariate von Mises dispersion formulation 145

6.4.2.2 Proposed model-IV - global-based planar and bivariate combined dispersion formulation 146

6.4.2.3 Proposed model-V - global-based planar von Mises dispersion formulation 147

6.4.3 Numerical sensitivity of the AI-based anisotropic dispersion . 148

6.5 Representative Numerical Examples 151

6.5.1 Numerical results of model-I 155

6.5.2 Numerical results of model-II 158

6.5.3 Numerical results of model-III 161

6.5.4 Numerical results of model-IV 164

6.5.5 Numerical results of model-V 167

7 CONCLUSIONS 175

REFERENCES 179

CURRICULUM VITAE 201

LIST OF TABLES

TABLES

Table 2.1 Mathematical descriptions of physical entities in region $\mathscr{P}$ 28

Table 2.2 Thermodynamic loads 28

Table 2.3 Global forms of the physical balance principles 29

Table 2.4 Strong forms of the physical balance principles 29

Table 4.1 Material parameters used in the analysis of three-dimensional bi-layer structure with free-energy defined in equation 4.48. 98

Table 6.1 Elastic material parameters for the baseline hyperelastic constitutive model [1] where a, a_{f}, a_{s}, a_{fs} are in [kPa], and b, b_{f}, b_{s}, b_{fs} are dimensionless. 154

Table 6.2 Viscous material parameters for the Model-I where μ_f, μ_s are directional shear moduli in [kPa], and η_f, η_s are directional viscosities in [kPa s], $\hat{\beta}$ is the activation parameter, m_f, m_s, a and b are dimensionless. 155

Table 6.3 Viscous material parameters for the Model-II where μ_f, μ_s and μ_n are directional shear moduli in [kPa], and η_f, η_s and η_n are directional viscosities in [kPa s], b is the dimensionless concentration parameter. . . . 158

Table 6.4 Viscous material parameters for the Model-III where μ_f, μ_s are directional shear moduli in [kPa], and η_f, η_s are directional viscosities in [kPa s], $\hat{\beta}$ is the activation parameter, m_f, m_s, a and b are dimensionless. . 162

Table 6.5 Viscous material parameters for the Model-IV where μ_f, μ_s and μ_n are directional shear moduli in [kPa], η_f, η_s and η_n are directional viscosities in [kPa s], $\hat{\beta}$ is the activation parameter, m_f, m_s, m_n are exponents and b is the dimensionless concentration parameter. 165

Table 6.6 Viscous material parameters for the Model-V_1 where μ_f, μ_s, μ_n are directional shear moduli in [kPa], and η_f, η_s, η_n are directional viscosities in [kPa s], $\hat{\beta}$ is the activation parameter, m_f, m_s, a and b are dimensionless. 168

Table 6.7 Viscous material parameters for the Model-V_2 where μ_f, μ_s, μ_n are directional shear moduli in [kPa], and η_f, η_s, η_n are directional viscosities in [kPa s], $\hat{\beta}$ is the activation parameter, m_f, m_s, a and b are dimensionless. 171

LIST OF FIGURES

FIGURES

Figure 1.1 The representation of the nonlinear stiffening of soft tissue is called a J-shape stress-strain curve. At low strains, the wavy-formed fibers do not take on any tension load. Then fibers become aligned in a straight form that takes into account fiber strength in addition to the ground matrix. 3

Figure 1.2 Schematic of anisotropy of tissues (a) Myocardium tissue that consists of distinct collagen fibers, myocardium sheets, and elastin (b) Layered structure of skin tissue. (The skin image was partly generated using Servier Medical Art, provided by Servier, licensed under a Creative Commons Attribution 3.0 unported license) 4

Figure 1.3 Biological examples for growth-induced deformations (a) Growth of the heart for wall thickening (b) Growth of an artery; adopted from [2] 7

Figure 1.4 Examples of growth-induced buckling for biological tissues and electronic device development (a) Flexible complementary metal-oxide semiconductor circuits; adopted from [3] (b) Wrinkling of a flower [4], (c) Instability pattern in bovine esophagus [4], (d) Cortical folding of the human brain 8

Figure 1.5 Illustration of (a)a typical loading-unloading curve of a viscoelastic material (b) typical relaxation curve of a viscoelastic material . 14

Figure 2.1 Nonlinear deformation of an isotropic solid. The underformed configuration $\mathscr{B} \in \mathbb{R}^3$ and the deformed configuration $\mathscr{P} \in \mathbb{R}^3$. $\boldsymbol{\varphi} : \mathscr{B} \times \mathbb{R} \mapsto \mathbb{R}^3$ is the nonlinear field which maps at time $t \in \mathbb{R}_+$ undeformed position $\boldsymbol{X} \in \mathscr{B}$ onto deformed $\boldsymbol{x} = \boldsymbol{\varphi}(\boldsymbol{X}, t) \in \mathscr{P}$. 20

Figure 2.2 Three physically related mapping operations: (a) The deformation gradient $\boldsymbol{F}$, (b) cofactor of the deformation gradient $\mathrm{cof}[\boldsymbol{F}]$, and (c) and the Jacobian $\det[\boldsymbol{F}]$; adopted from [5] 21

Figure 2.3 (a) Definition of right Cauchy Green tensor by pull-back operation of Eulerian metric $\boldsymbol{g}$, (b) Definition of left Cauchy Green tensor by push-forward operation of Lagrangian metric $\boldsymbol{G}$. 22

Figure 2.4 Representation of principal stretches defines the principal invariants of the right Cauchy-Green tensor (I_1, I_2, and I_3), as length, area and volume measures respectively. 24

Figure 2.5 Schematic representation of transversely isotropic solid that composed of two family fibers in the direction of $\boldsymbol{n}_0$ and $\boldsymbol{m}_0$, respectively. . 24

Figure 2.6 Schematic representation of the surface normal and traction vectors in a cut-out region for the deformed and undeformed configurations. 25

Figure 2.7 Schematic diagram of the stress measures that reveals the stress transformations though tangent and cotangent spaces and push-forward and pull-back operations. 27

Figure 3.1 (a) Schematic view of the geometry, boundary conditions and traction load (b) coarse mesh representation with 4 elements per edge c) fine mesh representation with 8 elements per edge. (Units are dimensionless) 48

Figure 3.2 Element types used in numerical Cook's membrane numerical example 49

Figure 3.3 (a) Tip vertical deflection of different element formulations at point "A" (b) Internal pressure result at point "B" of different element formulations. Both plots are provided based on coarse and fine mesh settings 50

Figure 3.4 Normalized elapsed time for different mixed element formulations 50

Figure 3.5 Contours of 4 element per edge and 8 element per edge configurations. (a) Vertical displacement of $T1P0$ element (b) Vertical displacement of $T1P0_{HW}$ element (c) Pressure distribution of $T1P0$ element (d) Pressure distribution of $T1P0_{HW}$ element 51

Figure 3.6 Contours of 4 element per edge and 8 element per edge configurations. (a) Vertical displacement of $T2P0$ element (b) Vertical displacement of $T2P0_{HW}$ element (c) Pressure distribution of $T2P0$ element (d) Pressure distribution of $T2P0_{HW}$ element 52

Figure 3.7 Contours of 4 element per edge and 8 element per edge configurations. (a) Vertical displacement of $T2P1$ element (b) Vertical displacement of $T2CR1$ element (c) Pressure distribution of $T2P1$ element (d) Pressure distribution of $T2CR1$ element 52

Figure 3.8 Finite element design for compressible, extensible, quasi-incompressible and quasi-inextensible hyperelasticity. 58

Figure 3.9 Schematic representation of the geometry and corresponding boundary conditions 59

Figure 3.10 Representation of mesh configurations with different element sizes 60

Figure 3.11 $\nu = 0.3$, Mid-point displacement $u_x(0, 0.5)$ results for (2×2), (4×4), (8×8), (16×16), (32×32) and (64×64) elements per edge in the range of $\mu_f = \{10^2, 10^4, 10^6, 10^8\}$. 61

Figure 3.12 $\nu = 0.3$, the normalized elapsed time for the solution of (32×32) and (64×64) elements per edge where $\mu_f = 10^2$. 62

Figure 3.13 $\nu = 0.49$, Mid-point displacement $u_x(0, 0.5)$ results for (2×2), (4×4), (8×8), (16×16), (32×32) and (64×64) elements per edge in the range of $\mu_f = \{10^2, 10^4, 10^6, 10^8\}$. 63

Figure 3.14 $\nu = 0.49$, Number of total iterations have been performed during Newton-Raphson iterations for (2×2), (4×4), (8×8), (16×16), (32×32) and (64×64) elements per edge in the range of $\mu_f = \{10^2, 10^4, 10^6, 10^8\}$. 64

Figure 3.15 $\nu = 0.49$, the normalized elapsed time for the solution of (32×32) and (64×64) elements per edge at $\mu_f = 10^2$ and $\mu_f = 10^4$. 65

Figure 3.16 Cauchy fiber stress $\boldsymbol{\sigma}_f$ distribution of $T2$, $T2P0$ and $T2P1$ elements for dual clamped patch test where $\nu = 0.49$ and $\mu_f = 10^4$. Stress contours are presented for unit dimensions for (32×32) and (64×64) mesh configurations. 66

Figure 3.17 Cauchy fiber stress $\boldsymbol{\sigma}_f$ distribution of $T2A0$, $T2P0A0$ and $T2P0F0$ elements for dual clamped patch test where $\nu = 0.49$ and $\mu_f = 10^4$. Stress contours are presented for unit dimensions for (32×32), (64×64) mesh configurations for $T2A0$ and for five-field formulations, (128×128) mesh results additionally given. 67

Figure 3.18 Cauchy fiber stress $\boldsymbol{\sigma}_f$ distribution of $T2A1$, $T2P1A1$ and $T2P1F1$ elements for dual clamped patch test where $\nu = 0.49$ and $\mu_f = 10^4$. . . 68

Figure 4.1 Kinematic representation of finite growth. The multiplicative decomposition of the deformation gradient $\boldsymbol{F}$ gives mapping relation based on growth state $\boldsymbol{F}^g$, and the elastic state of the deformation gradient $\boldsymbol{F}^e$. There are defined three configurations at finite growth, the first one is the original stress-free configuration in $\mathscr{B}_0$, the second one is the growth state with stress-free intermediate configuration in $\mathscr{B}_g$ which also leads to incompatibility in general, and the third is the stressed-state in deformed configuration,$\mathscr{B}$. 71

Figure 4.2 Definition of metric and stress tensors for finite growth. *Current metric* in Lagrangian configuration $\boldsymbol{C} = \boldsymbol{F}^T \boldsymbol{g} \boldsymbol{F}$. *Reference metric* in Eulerian configuration $\boldsymbol{c} = \boldsymbol{F}^{-T} \boldsymbol{G} \boldsymbol{F}^{-1}$. The relationship between the Lagrangian-intermediate configuration and intermediate-Eulerian configuration can be defined $\boldsymbol{C}^e = \boldsymbol{F}^{g-T} \boldsymbol{C} \boldsymbol{F}^{g-1}$ and $\boldsymbol{\tau} = \boldsymbol{F}^e \boldsymbol{S}^e \boldsymbol{F}^{eT}$ or directly $\boldsymbol{\tau} = \boldsymbol{F} \boldsymbol{S} \boldsymbol{F}^T$, respectively [6]. 74

Figure 4.3 (a) Geometric unitless dimensions of the 2D plate, (b) finite element setting of the model 79

Figure 4.4 Growth-induced deformation of a 2D plate in different time increments such as $t = 0$, $t = 0.33$, $t = 0.66$ and $t = 1.0$, respectively. The contour provides the variation of J_g. 80

Figure 4.5 The geometrical dimensions (in mm) of a single flower petals and zoomed view of finite element mesh. 80

Figure 4.6 Growth-induced displacement (in mm) contour of flower petal which is subjected to isotropic growth on bottom layer as $\boldsymbol{F}^g = (1 + g)\mathbf{1}$. 81

Figure 4.7 The geometrical unitless dimensions of thin stiff film on compliant soft substrate and zoomed view of finite element mesh. 82

Figure 4.8 The deformation pattern and pressure contours of bilayer structure in different growth g increments in left and right columns, respectively. 83

Figure 4.9 Main ingredients of the brain in terms of volume rendering. (The section view of the brain was partly generated using Servier Medical Art, provided by Servier, licensed under a Creative Commons Attribution 3.0 unported license.) 84

Figure 4.10 Geometric representation of half smooth brain. (a) three-dimensional demonstration (b) two-dimensional sliced piece 86

Figure 4.11 Finite element mesh settings of brain geometry (a) three-dimensional demonstration (b) two-dimensional sliced piece 86

Figure 4.12 Growth-induced deformations and pressure variations of sliced two-dimensional brain with $\mu_{white}/\mu_{gray} = 1/10$ and $\mu_{white}/\mu_{gray} = 1/5$ 87

Figure 4.13 Growth-induced deformations and pressure variations of three-dimensional brain with $\mu_{white}/\mu_{gray} = 1/10$ and $\mu_{white}/\mu_{gray} = 1/5$ ($\times 2$ scaled view) 88

Figure 4.14 Geometrical unitless description of artificial muscle (a) geometric definitions (b) three-dimensional finite element mesh (c) vectorial representation of helical fibers 92

Figure 4.15 Cauchy-type shear stress distribution of artificial muscle geometry at different positive growth values. θ_z represents the angular twist around axial direction. 93

Figure 4.16 Cauchy-type shear stress distribution of artificial muscle geometry at different negative growth values. θ_z represents the angular twist around axial direction. 94

Figure 4.17 Transverse isotropy: stiff fibers embedded in the upper stiff film and stiff fibers embedded in the compliant soft substrate, respectively . . 95

Figure 4.18 Schematic representation of the 3D bilayer structure (stiff film on compliant substrate) with its geometric dimensions. L is the edge length of the square in-plane section, H is the total height including the film and the substrate, $\boldsymbol{n}_0$ is the stiff fiber direction along y axis, L_{cr1} and L_{cr2} are the critical lowest dimensions needed to be taken into account to reflect periodic behaviour of RVE (Representative Volume Element) 96

Figure 4.19 Representation of the long (L=240 unit) and thin (W=1 unit) bilayer structure consist of substrate (red) and stiff film (blue), finite element mesh and zoomed view of FE mesh respectively. 97

Figure 4.20 Representation of the determined wavelengths for different lengths of bilayer structure such as L=15, 30, 60, 120 and 240 units with W=1 units. 99

Figure 4.21 First buckling mode shapes of 2D long and thin bilayer plates with different fiber stiffness reinforcement (scaled by x5). 100

Figure 4.22 Representation of three-dimensional RVE. White lines demonstrate the stiff fibers those are aligned to the y-direction 101

Figure 4.23 Representation of the examples for two randomly generated perturbation boundaries (with red colour) for bilayer stucture. 101

Figure 4.24 Primary instability deformation shape of two randomly generated perturbation boundaries given in Figure 4.23. 102

Figure 4.25 Pressure distribution of the buckling regime of a bilayer plate with monotonically increasing growth, g 103

Figure 4.26 Critical growth parameter variation by fiber stiffness 104

Figure 4.27 Variation of vertical displacements of points A, B, and C; and variation of decoupled forms of energy for the film and substrate, those are subjected to incrementally growth for the following cases; without fiber reinforcement, μ_{fiber}=100 and μ_{fiber}=250, respectively. 105

Figure 4.28 Continuation of Figure 4.27 - Variation of vertical displacements of points A, B, and C; and variation of decoupled forms of energy for the film and substrate, those are subjected to incrementally growth for the following cases; μ_{fiber}=750, μ_{fiber}=1000, μ_{fiber}=2500, respectively. 106

Figure 5.1 (a) The unit micro-sphere and the orientation vector, (b) mean fiber directions of two families of fiber lie on $\boldsymbol{e}_1$-$\boldsymbol{e}_2$ plane. 111

Figure 5.2 (a) Graphical representation of nonlinear relation between the dispersion parameter κ and the concentration parameter b, (b) dispersion characteristics through the density function ρ and the angle of dispersion Θ. The corresponding κ values are $1/3$, $4/15$, $1/5$, $1/11$, $1/20$ and 0 respectively. 112

Figure 5.3 (a) Graphical representation of nonlinear relation between the in-plane dispersion parameter κ_{ip} and the in-plane concentration parameter a, (b) relationship between the out-of-plane dispersion parameter κ_{op} and the out-of-plane concentration parameter b 114

Figure 5.4 The polar plots of the density distribution functions ρ (a) planar von Mises distribution of two families of fibers for a medial layer of human thoracic aorta [7],(b) in-plane von Mises distributions of one family of fibers for intima, media and adventitia layers of healthy abdominal aorta [8] (c) out-of-plane von Mises distributions of one family of fibers for intima, media and adventitia layers of healthy abdominal aorta [8] 117

Figure 5.5 The polar plots of the density distribution functions ρ (a) planar von Mises distribution of one family of fibers for intestine wall layers namely submucosa, longitudinal and circular muscle layers [9],(b) planar von Mises distributions of fiber orientation of rabbit myocardium [10] (c) planar von Mises distributions of sheet orientation of rabbit myocardium [10] 117

Figure 6.1 The schematic view of the section view of the human heart, sliced pieced of the left ventricle and idealized patch of heart wall described within three orthogonal directions, fiber direction, sheet direction and normal direction, respectively. (The realistic images were partly generated using Servier Medical Art, provided by Servier, licensed under a Creative Commons Attribution 3.0 unported license) . . 120

Figure 6.2 Schematically illustration of generalized Maxwell rheological model. Representation of the additively decomposition of isochoric free-energy into equilibrium and non-equilibrium parts. The springs are refers to stored energies and the dashpot represents the energy dissipation through viscous response. 132

Figure 6.3 (a) Demonstration of generalised Maxwell rheological model (b) Idealization of tissue network for non-equilibrium response, the micro-sphere model 134

Figure 6.4 (a) The unit micro-sphere and the orientation vector, (b) mean fiber directions of two families of fiber lie on $\boldsymbol{e}_1$-$\boldsymbol{e}_2$ plane. 135

Figure 6.5 Demonstration of fully symmetric integration points over micro-sphere (a) 21 in half, in total 42 integration points (b) 39 in half, in total 78 integration points 136

Figure 6.6 (a) Demonstration of fully symmetric integration points over planar circle, given for 30 integration points (p_{fs}) in half circle (b) Idealization of tissue network for the non-equilibrium response, the planar circle model (c) Demonstration of fully symmetric integration points over micro-sphere, given for 21 integration points (p_n) in half circle (d) Idealization of tissue network for non-equilibrium response, the micro-sphere model. 141

Figure 6.7 (a) Graphical representation of the relationship between the normalized planar density distribution ρ and the concentration parameter b by numerical integration over micro-sphere for different number of integration points, (b) Graphical representation of the relationship between the normalized bivariate density distribution ρ^{ip} and ρ^{op} and the concentration parameters a and b respectively by the numerical integration over micro-sphere for different number of integration points 149

Figure 6.8 The relationship between the normalized planar density distribution ρ and the concentration parameter b by numerical integration over the unit planar circle for different number of integration points. 150

Figure 6.9 Schmetic demonstration of the experimental steps performed by Sommer et al. [11].(The sliced heart Figure was partly generated using Servier Medical Art, provided by Servier, licensed under a Creative Commons Attribution 3.0 unported license) 152

Figure 6.10 Schematic representation of six triaxial shear modes namely (fs), (sf), (nf), (fn), (sn), (ns), reproduced from [1] 152

Figure 6.11 Elastic triaxial shear test and numerical fits for (fs), (sf), (nf), (fn), (sn), (ns). 153

Figure 6.12 The polar plot of the two families of fibers (f and s) distribution based on density distribution (DD) for the myocardium tissue. 154

Figure 6.13 Model I - The polar plots of the two families of fiber (f) and sheet(s) directions along in-plane distribution and out-of-plane distribution through normal direction (n) for the viscous response of the myocardium. 155

Figure 6.14 Cauchy stress σ vs amount of shear γ of Model-I response with respect to the cyclic triaxial shear test data for six of the shear modes namely (fs), (fn), (sf), (sn), (nf) and (ns). 156

Figure 6.15 Cauchy stress σ vs relaxation time of Model-I response with respect to the triaxial relaxation shear test data for six of the shear modes namely (fs), (fn), (sf), (sn), (nf) and (ns). 157

Figure 6.16 The polar plot of the two families of fibers (f and s) ased on density distributions (DD) for the viscous response of Model II. 159

Figure 6.17 Cauchy stress σ vs amount of shear γ of Model-II response with respect to the cyclic triaxial shear test data for six of the shear modes namely (fs), (fn), (sf), (sn), (nf) and (ns). 160

Figure 6.18 Cauchy stress σ vs relaxation time of Model-II response with respect to the triaxial relaxation shear test data for six of the shear modes namely (fs), (fn), (sf), (sn), (nf) and (ns). 161

Figure 6.19 Model III - The polar plots of the two families of fiber (f) and sheet(s) directions along in-plane distribution and out-of-plane distribution through normal direction (n) for the viscous response of the myocardium. 162

Figure 6.20 Cauchy stress σ vs amount of shear γ of Model-III response with respect to the cyclic triaxial shear test data for six of the shear modes namely (fs), (fn), (sf), (sn), (nf) and (ns). 163

Figure 6.21 Cauchy stress σ vs relaxation time of Model-III response with respect to the triaxial relaxation shear test data for six of the shear modes namely (fs), (fn), (sf), (sn), (nf) and (ns). 164

Figure 6.22 The polar plot of the two families of fibers (f and s) ased on density distributions (DD) for the viscous response of Model IV. 165

Figure 6.23 Cauchy stress σ vs amount of shear γ of Model-IV response with respect to the cyclic triaxial shear test data for six of the shear modes namely (fs), (fn), (sf), (sn), (nf) and (ns). 166

Figure 6.24 Cauchy stress σ vs relaxation time of Model-IV response with respect to the triaxial relaxation shear test data for six of the shear modes namely (fs), (fn), (sf), (sn), (nf) and (ns). 167

Figure 6.25 Model V_1 - The polar plot of the two families of fiber (f) and sheet(s) directions for a planar density distribution 168

Figure 6.26 Cauchy stress σ vs amount of shear γ of Model-V_1 response with respect to the cyclic triaxial shear test data for six of the shear modes namely (fs), (fn), (sf), (sn), (nf) and (ns). 169

Figure 6.27 Cauchy stress σ vs relaxation time of Model-V_1 response with respect to the triaxial relaxation shear test data for six of the shear modes namely (fs), (fn), (sf), (sn), (nf) and (ns). 170

Figure 6.28 Model V_2 - The polar plots of the two families of fiber (f) and sheet(s) directions along in-plane distribution and out-of-plane distribution through normal direction (n) for the viscous response of the myocardium. 171

Figure 6.29 Cauchy stress σ vs amount of shear γ of Model-V_2 response with respect to the cyclic triaxial shear test data for six of the shear modes namely (fs), (fn), (sf), (sn), (nf) and (ns). 172

Figure 6.30 Cauchy stress σ vs relaxation time of Model-V_2 response with respect to the triaxial relaxation shear test data for six of the shear modes namely (fs), (fn), (sf), (sn), (nf) and (ns). 173

LIST OF ABBREVIATIONS

Multi-Word Terms

IGA	Isogeometric analysis
LA	Left atria
RA	Right atria
LV	Left ventricle
RV	Right ventricle
SHG	Second harmonic generation
HW	Hu-Washizu formulation
RVE	Representative volume element
3D	Three-dimensional
2D	Two-dimensional
GST	Generalized structure tensor
AI	Angular integration

Operators and symbols

$\nabla_X(\bullet)$	Gradient operator with respect to undeformed $\boldsymbol{X}$ coordinates
$\nabla_x(\bullet)$	Gradient operator with respect to deformed $\boldsymbol{x}$ coordinates
$cof(\bullet)$	Cofactor operator
$(\bullet)^{-1}$	Inverse operator
$det(\bullet)$	Determinant operator
$tr(\bullet)$	Trace operator
$(\bullet)^T$	Transpose operator
$(\bullet)'$	First derivative
$(\bullet)''$	Second derivative
$D(\bullet)\delta x$	Directional derivative in the direction of x

$sym(\bullet)$	Symmetric part of a tensor
$\Delta(\bullet)$	Increment of a vector/tensor
$\pounds \bullet_{\boldsymbol{v}}$	Lie derivative
$\langle \bullet \rangle$	Continuous integral averaging
$(\dot{\bullet})$	Time derivative
$(\bullet)_{vol}$	Volumetric part
$(\overline{\bullet})$	Isochoric part
$(\bullet)^e$	Elastic part of the vector/tensor
$(\bullet)^g$	Growth part of the vector/tensor
$(\bullet)^*$	Modified quantity based on Generalized Structure Tensor approach
$(\bullet)^v$	Viscous component

Continuum Mechanics

$\mathscr{B}_0$	Reference configuration of the solid body
$\mathscr{B}$	Spatial configuration of the solid body
$\mathscr{B}_g$	Growth state of the solid body
$\partial\mathscr{B}_0$	Reference boundary of the solid body
$\partial\mathscr{B}$	Spatial boundary of the solid body
$\mathscr{P}$	Material points of the body
$\boldsymbol{x}$	Spatial configuration of position vector
$\boldsymbol{X}$	Reference configuration of position vector
$\boldsymbol{u}$	Displacement vector of the material points
$\dot{\boldsymbol{x}}$	Velocity vector of the material points
$\ddot{\boldsymbol{x}}$	Acceleration vector of the material points
$\boldsymbol{F}$	Deformation gradient
J	Jacobian
$d\boldsymbol{X}$	Infinitesimal line element in undeformed configuration

$d\boldsymbol{A}$	Infinitesimal area element in undeformed configuration
dV	Infinitesimal volume element in undeformed configuration
$d\boldsymbol{x}$	Infinitesimal line element in deformed configuration
$d\boldsymbol{a}$	Infinitesimal area element in deformed configuration
dv	Infinitesimal volume element in deformed configuration
$\boldsymbol{G}$	Metric tensor in undeformed configuration
$\boldsymbol{g}$	Metric tensor in deformed configuration
$\boldsymbol{C}$	Right Cauchy-Green tensor
$\boldsymbol{b}$	Left Cauchy-Green tensor
δ_{ij}	Krocnecker delta
$\boldsymbol{E}$	Green-Lagrangian strain tensor
$\boldsymbol{A}$	Almansian strain tensor
$\boldsymbol{R}$	Orthogonal rotation tensor
$\boldsymbol{U}$	Right stretch tensor
$\boldsymbol{V}$	Left stretch tensor
λ_α	Principle stretch
I_α	Invariants
$\boldsymbol{n}_0$	Reference unit vector for the first fiber orientation
$\boldsymbol{m}_0$	Reference unit vector for the second fiber orientation
$\boldsymbol{n}$	Spatial unit vector for the first fiber orientation
$\boldsymbol{m}$	Spatial unit vector for the second fiber orientation
$\boldsymbol{T}$	Lagrangian traction vector
$\boldsymbol{t}$	Eulerian traction vector
$\boldsymbol{\sigma}$	Cauchy stress
$\boldsymbol{P}$	First Piola-Kirchhoff stress
$\boldsymbol{\tau}$	Kirchhoff stress
$\boldsymbol{S}$	Second Piola-Kirchhoff stress

m	Mass
$\mathcal{I}$	Linear momentum
$\mathcal{D}$	Angular momentum
$\mathcal{K}$	Kinetic energy
$\mathcal{E}$	Internal energy
$\mathcal{H}$	Entropy
Γ	Entropy production
$\mathscr{D}$	Dissipation
$\mathscr{D}_{loc}$	Local dissipation
$\mathscr{D}_{con}$	Conductive dissipation
Ψ	Helmholtz free-energy
$\boldsymbol{D}$	Rate of deformation tensor
$\boldsymbol{F}_m$	Mechanical force
$\boldsymbol{M}_m$	Mechanical moment
P	Mechanical power
Q	Thermal power
S	Entropy power
h	Heat flux
r	Heat source for unit mass
θ	Temperature
$\mathcal{K}$	Kinetic energy
P_{int}	Internal stress power
P_{ext}	External work done
e	Internal energy
η_e	Entropy
γ_e	Entropy generation
$\mathbf{1}$	Identity tensor

$\mathbb{A}$	Two-point elasticity moduli tensor
$\mathbb{C}$	Lagrangian elasticity moduli tensor
$\mathbb{c}$	Eulerian elasticity moduli
$\hat{c_\alpha}$	Derivative coefficients for second Piola-Kirchoff stress
$\hat{b_\alpha}$	Derivative coefficients for Kirchhoff stress
μ	Shear modulus
λ	Lame constant
$\mathbb{I}$	Fourth-order identity tensor
$\mathbb{I}_{\boldsymbol{C}^{-1}}$	Fourth-order geometric transformation tensor
p	Internal pressure
k_α	Material coefficients
$\hat{\Pi}$	Potential function
$\hat{\Pi}^{int}$	Internal potential function
$\hat{\Pi}^{ext}$	External potential function
s	Fiber stress
$\boldsymbol{\mathcal{S}}$	Stress-like Lagrangian multiplier
$\boldsymbol{\mathcal{C}}$	Tensorial kinematic variable
g	Scalar growth term
λ_{cr}	Critical wavelength
μ_{film}	Shear modulus of film layer
μ_{subs}	Shear modulus of substrate layer
μ_{fiber}	Fiber stiffness
ρ	Density distribution function
$\boldsymbol{r}$	Unit orientation direction
$\boldsymbol{e}_\alpha$	Unit vectors at Cartesian coordinates
$\boldsymbol{t}$	Stretch vector in spatial configuration
Θ	Elevation angle

Φ	Azimuth angle
b	Concentration parameter
$I_0(\bullet)$	Modified Bessel function of the first kind of order zero
$\boldsymbol{H}$	Generalized structure tensor in Lagrangian configuration
$\boldsymbol{h}$	Generalized structure tensor in Eulerian configuration
κ	Dispersion parameter
E	Strain-like scalar quantity in the direction of mean orientation
ρ_{in}	In-plane density distribution function
ρ_{out}	Out-of-plane density distribution function
a	Concentration parameter of in-plane density distribution function
κ_{in}	Dispersion parameter of in-plane density distribution
κ_{out}	Dispersion parameter of out-of-plane density distribution
ψ^{mic}	Micro-fiber free energy
λ_f	Micro-fiber stretch
w	Weight factor of the set of integration points
$\boldsymbol{f}_0$	Unit vector for the fiber direction
$\boldsymbol{s}_0$	Unit vector for the sheet direction
$\boldsymbol{n}_0$	Unit vector for the sheet direction
$\boldsymbol{\beta}$	Stress-like quantity, internal force
ε	Logarithmic strain
Φ_{disp}	Dissipation potential
$\gamma(\bullet)$	Evolution equation for strain-like internal variables
r	Residual term
$\mathcal{K}$	Local tangent term

CHAPTER 1

INTRODUCTION

This thesis presents two main parts namely, growth-induced instabilities and dispersion-type angular-integration-based anisotropic viscoelasticity for soft biological tissues.

Beginning with hyperelastic constitutive relations, a five-field mixed variational formulation for growth-induced instabilities has been adopted in incompressible and inextensible limits and investigated for the first time in the literature on anisotropic three-dimensional confined tissue, i.e., a thick stiff film on a compliant substrate under planar growth. The numerical example was solved by implementing $T2P0F0$ element on the automated differential equation solver platform, FEniCS [12]. The role of fiber stiffness on primary and secondary instabilities has been demonstrated.

Then, in the second part of the thesis, there are proposed local-based and global-based dispersion-type formulations for anisotropic viscoelasticity to formulate histological-based the directional rate-dependent behaviour of anisotropic soft biological tissues. The novel dispersion-based angular integration-type anisotropic viscoelastic constitutive models have been proposed by using planar and bivariate von Mises density distributions for orthogonal directions. The model has been validated through cyclic triaxial shear and triaxial shear relaxation experiments on human myocardium presented in the literature. The proposed anisotropic viscoelastic constitutive models are in good agreement with the experimental data for the shear characteristics of human myocardium tissue.

1.1 Overview and Backgorund

Mechanical behaviors, strengths, and kinematics of living systems are considered under the biomechanics theory. Biomechanics is an active research subject, not only to understand the mechanism of biological tissues but also the development of treatment methods for injuries and fatal diseases. Although medical operations seem to be unrelated to mechanics; treatments, surgeries, and rehabilitation are directly related to the mechanical response of the tissues from the stress and strain perspective [13]. In the biomechanical area, solid mechanics researches are directly involved in many medical cases such as heart diseases, heart valve prostheses, organ support devices, artificial heart development, replacement of diseased tissues, skin transplantation, stenting on a vein, musculoskeletal diseases, etc. There are also active research topics based on tissue engineering, biomedical materials, and medical device development. Tissue engineering mainly focuses on the recreation of human tissues and the replacement of diseased tissue with a compliant artificial one. It has a key role in understanding pathology, proposing the way for artificial tissue replacement techniques, and developing artificial tissues and organs, prostheses, and medical treatment methods. Biomaterials are considered in two main groups. The first group is the synthetic biomaterials (polymers, composites, metals, ceramics) and the natural biomaterials (cells, tissues, proteins, etc.)[14]. The functional tissue must be biocompatible in terms of strength, stiffness, physiochemical, electro-mechanical, elastic response, and time-dependent response, depending on the application. It should have the capability to mimic the function of the native tissue/organ without disturbing the surrounding anatomy. Therefore, it is significant to have a well-developed mathematical model based on mechanics that describes the material response in an accurate way.

Tissues are classified according to their stiffness properties, such as soft and hard. That definition is a relative measure that takes into account the relationship between force and deformation behaviors. Soft tissues include the central nervous tissue, abdominal organs, brain, lung, muscle, myocardium, and skin, while hard tissues include cartilage, tendon, and bone. For more information on the mechanical properties of human tissues, see the review of Guimaraes et al. [15]. Tissues are composed of cells and extracellular matrix and form organs. The extracellular matrix contains

proteins (collagen, laminin, elastin, etc.) and glycoproteins that form a support-like network for cells, and they have a key role in healing and regeneration. Elastin is a protein that procures long-range elasticity for many of the soft biological tissues [16]. In most soft biological tissues, collagen is the main structural element, and the mechanical behavior of living tissue is determined by the volume density of the collagen and the orientation of the collagen fibers. Soft biological tissue is generally subjected to large strains and undergoes nonlinear deformations. Collagen fibers may be distributed randomly or they can be in a specific orientation. Due to the wavy, disordered form of collagen fibers in the unloaded state, they form a straight line shape, and they are aligned to carry a higher load, especially in tension. They exhibit highly nonlinear exponential increasing stiffness under loading. Therefore, such tissues represent a J-shaped stress-strain response, as shown in Figure 1.1. Tissues can be composed of

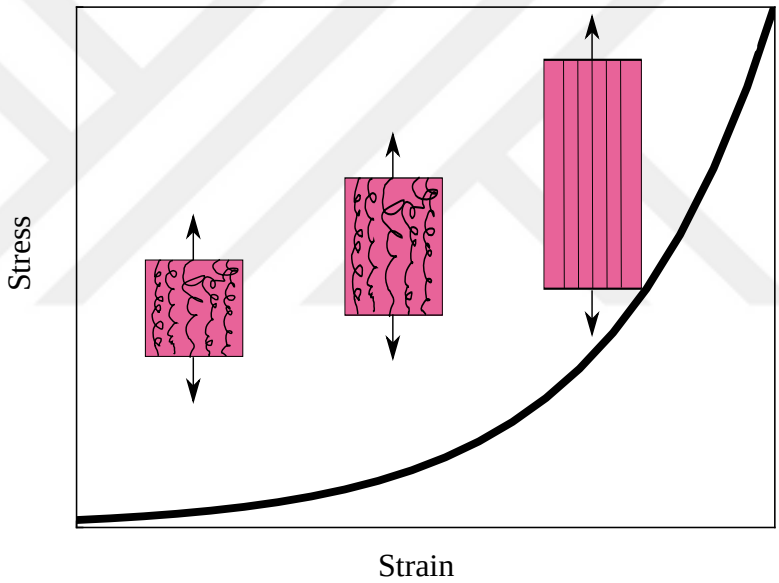

Figure 1.1: The representation of the nonlinear stiffening of soft tissue is called a J-shape stress-strain curve. At low strains, the wavy-formed fibers do not take on any tension load. Then fibers become aligned in a straight form that takes into account fiber strength in addition to the ground matrix.

distinct structural sub-components with distinct properties, which can be combined to form a composite structure with material response direction dependency. This leads to material anisotropy and the capability to sustain high-level loads in specific directions. For example, a myocardium tissue exhibits different mechanical properties

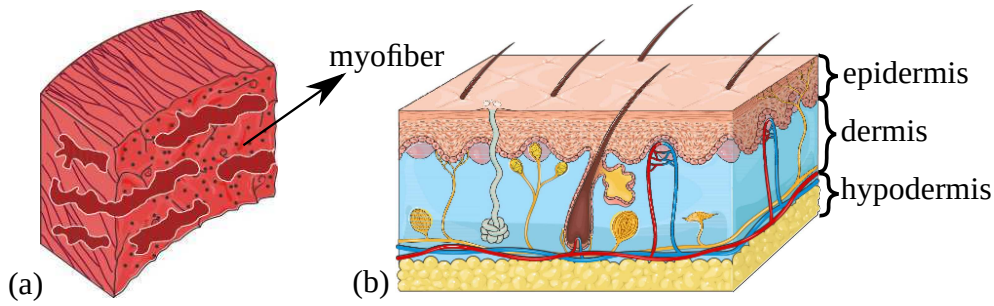

Figure 1.2: Schematic of anisotropy of tissues (a) Myocardium tissue that consists of distinct collagen fibers, myocardium sheets, and elastin (b) Layered structure of skin tissue. (The skin image was partly generated using Servier Medical Art, provided by Servier, licensed under a Creative Commons Attribution 3.0 unported license)

in orthogonal directions due to the fiber bundles and laminated sheet structure. Another anisotropy can be formed by laminated structures such as skin that is made of three different layers of tissues, namely the epidermis, dermis, and hypodermis [15]. The schematic views of anisotropic myocardium and skin tissues are shown in Figure 1.2. Constitutive models are developed to be used analytically and numerically to observe the mechanical response of soft tissues in an accurate way. Due to the large deformation characteristics and nonlinear behaviour of soft biological tissues, their mechanical response cannot be characterized with the basic mechanical constants of linear elasticity [17]. Therefore, a strain energy function based variety of hyperelastic constitutive models were developed to capture mechanical response. Hyperelastic constitutive models are actively used in finite element analysis to get insight into potential risky conditions for the patient, to observe surgical scenarios, and to develop biomaterials that mimic the native tissue for both fibrous and non-fibrous biological tissues. There are also extended advanced constitutive models those are accounts for viscoelasticity [18], electo-mechanical [19], electro-viscoelasticity [20],[21] for the biological tissues [17]. The dynamic behavior of soft biological tissues is characterized by time-dependent responses, such as stress stiffening or stress relaxation. Due to the high water content of the biological tissues, the viscous response is presented under dynamic loading by dissipating energy through unloading. During the cardiac cycle, the viscoelastic response of the surrounding tissues is a good example of the viscous response. High water content of the ground matrix of a tissue does not only

cause the viscous response but also maintain the quasi incompressibility of the material which results a sligth modification in the constitutive level.

There are many experiments conducted on soft biological tissues to examine their directional characteristics. The experiments that are performed on animal tissues provide a good insight into how human tissue can be represented, but they are not fully adaptable for human tissues. Due to the distinct orientation characteristics of the fibrous tissues, there are several types of experiments to obtain the isotropic or anisotropic nature of the samples. These are, uni-axial tension, biaxial tension, pure shear, compression for hyperelastic baseline and cyclic and relaxation tests for time-dependent characteristics, see [17] for more detailed observations.

There are a number of extensive reviews that have been worked on regarding hyperelastic constitutive models of rubber-like materials and biological tissues. Steinmann et al. [22], have compared fourteen of different micro-mechanically based hyperelastic constitute models. Then Dal et al. [5] enlarged the group of 44 hyperleastic constitutive models for rubber-like materials and examined their behaviour under uniaxial, biaxial, and shear deformations. They presented parameter identification procedures for different optimization algorithms. Although these reviews are for rubber-like materials, they provide good insight to understand also the behaviour of soft tissues as well. Then, Chagnon et al. [23] prosed a review to examine the behaviour of the materials based on hyperelastic free energy functions those are mostly used for soft biological tissues. In paralel, [24] examined the rate-independent isotropic and incompressible hyperelastic constitutive models for biological tissues such as the brain, kidney, liver, etc. Similary, Mihai et al. [25] proposed a review that make the comparison of numerical results based on isotropic incompressible hyperleastic constitute models with available experimental data for brain and fat tissues. Then, derivation of the stress and moduli tensors have been carried out for isotropic and anisotropic biological tissues by Cheng et al. [26].

Collagen fibers in fibrous tissues are oriented in distinct directions and are not perfectly aligned but they are dispersed. The effect of the dispersion in tissues, especially in healthy and non-healthy samples, directly affects the mechanical behaviour of the material and is examined in the following reviews. Holzapfel et al. [27], have

presented a critical review of the modeling of fiber dispersion by using angular integration and generalized structure tensor models. They compared their numerical results with the experimental data sets. Lastly, Dal et al. [17] presented the fitting performance of nine hyperelastic constitutive models for soft biological tissues that are based on invariant and dispersion-type modeling. They observed the fitting capability of the models by using optimization techniques on three different human tissues.

1.2 Growth Phenomena in Biomechanics

The formation of a biological tissue is comprised of the following three processes: growth, remodeling, and morphogenesis. Growth mainly accounts for mass or volume change (i.e., cell enlargement, division, or death); remodeling is the change of the material properties (i.e., reorientation of fibers subjected to a driving load); and morphogenesis is related to the shape change (i.e., healing of the biological tissue)[28]. These concepts either can be combined together or they can be an individual process. Since the main research area of the first part of this thesis is growth phenomena, the details of remodeling will be out of scope. The growth phenomenon is responsible for hyperplasia, hypertrophy, and the enlargement of the extracellular matrix. Therefore, the growth mechanism can be either positive (enlargement) or negative (shrinkage), and it can be isotropic, planar, or anisotropic, which may result in residual stresses on the tissue. This may lead to overloading of the material or buckling of the structure. Kuhl [29] states that growth in biological tissues can be categorized in three form called as fiber growth, surface growth and volume growth. Volume growth accounts for identical enlargement or shrinkage in all directions (i.e. tumors, fruit, arteries). Surface growth is a kind of planar growth in a plane without any growth in the normal direction (i.e. , lungs, skin, brain, heart valves, etc.). Lastly, the fiber growth corresponds to the growth only in the longitudinal fiber direction (i.e., plants, muscle, eye, heart etc.). As an example, the volume growth of an artery and the fiber growth of the heart are given in Figure 1.3.

Growth-induced deformations are common phenomena that confront living systems and engineering applications. In a certain level of growth, called critical growth,

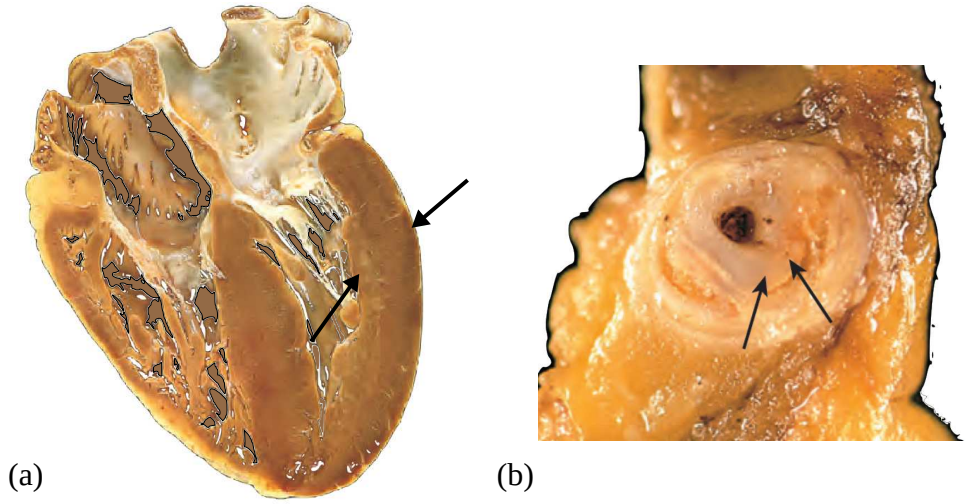

Figure 1.3: Biological examples for growth-induced deformations (a) Growth of the heart for wall thickening (b) Growth of an artery; adopted from [2]

structural instabilities may rise as an indicator of pathological conditions of biological tissues. It also plays a key role in the development of materials for biomedical applications. These materials and tissues are mostly in the form of multi-layer structures, which may have different mechanical properties and fiber reinforcement layouts. The main mechanism of the buckling in a multi-layered structure is the compression type of loading that causes different levels of stresses in the thin stiff film and the compliant substrate; thus, buckling leads to a release of the energy. Fiber stiffness is a critical parameter that designates the critical growth in primary buckling as a wrinkle form. It is significant to understand the mechanism behind the growth-induced instabilities for transversely isotropic materials and to observe the effect of fiber stiffness over primary and secondary instabilities on bilayer systems. Growth-induced deformations may lead to instabilities as they turn into different patterns on advanced engineering materials and soft biological tissues. Mechanism of growth is also used to achieve the desired geometrical form change in biomedical applications. Growth phenomena are widely shown up in nature as in living organisms (plants, tissue, etc.) and in engineering materials such as polymeric gels [30] and stretchable electronics [31]. A wide range of studies have been performed to understand the underlying mechanics of the tissue development subjected to growth and growth-induced instabilities and their biomedical applications such as; folding of the airway [32], cortical folding of the brain [33], cardiac growth [34, 6, 35, 36], wrinkling on spherical geometries

[37, 38], wrinkling on the skin [39, 40], artery growth [28, 41, 42, 43, 44], growing mechanics of muscle [45], instabilities on thin stiff film on a compliant substrate [46, 47, 48, 49], morphogenesis of the plates [50, 51], buckling of swelling hydrogels [30, 52, 53, 54, 55, 56, 57, 58] and torsional actuator modeling [59, 60], to mention but a few. For additional information, we refer to the state-of-the-art reviews on growth, remodeling and morphogenesis of biological tissues [28, 61, 4, 62, 63, 29, 64]. Illustrative example of growth in a soft biological tissue and growth in a biomedical application is presented in Figure 1.4. Most living systems are composed of multi-

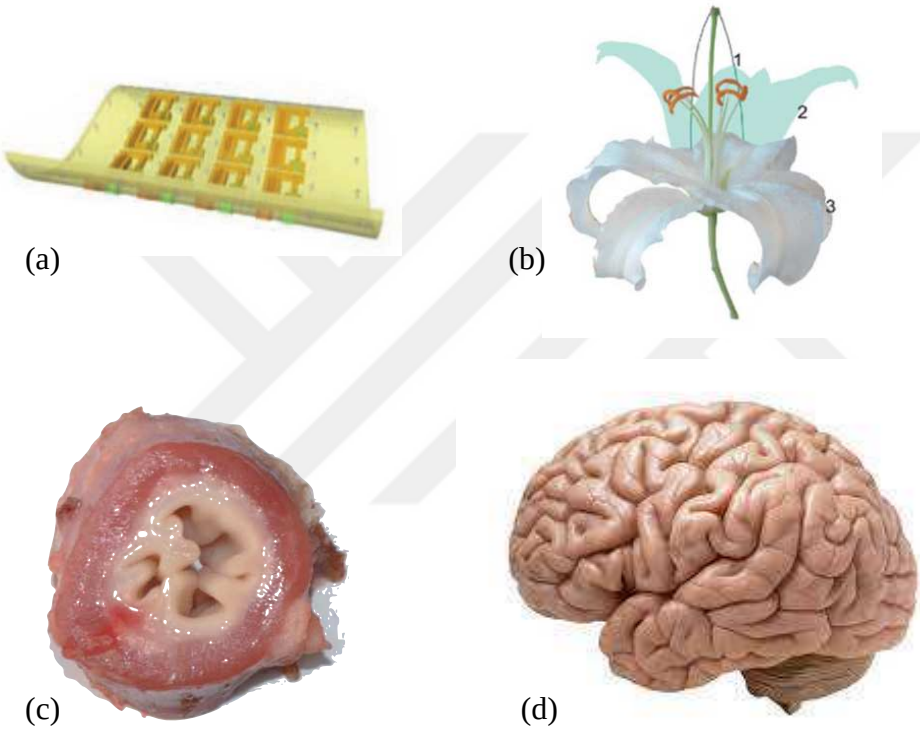

Figure 1.4: Examples of growth-induced buckling for biological tissues and electronic device development (a) Flexible complementary metal-oxide semiconductor circuits; adopted from [3] (b) Wrinkling of a flower [4], (c) Instability pattern in bovine esophagus [4], (d) Cortical folding of the human brain

layered structures possessing different mechanical properties as in biological tissues such as artery, airwall, skin, etc. Such structures are also encountered in flexible electronics [31] and [3]. In nature, most living systems have one or two fiber family reinforcement embedded in different layers of the system for different purposes under

various conditions.

Instabilities of isotropic bilayer plates composed of film and bonded substrate were examined experimentally [31, 47, 65], analytically, and numerically [30, 46, 48, 49, 66, 67, 68]. Khang et al. [31] experimentally observed the mechanical buckling of a micro-scale bilayer system; herewith, they have ended up with thickness, wavelength, strain, and delamination relations. They also highlighted that these instabilities could be used as a measure for elastic moduli of materials. Brau et al. [47] studied the energy requirements of membranes to obtain a new kind of instability initiated as period-doubling both theoretically and numerically. Huang et al. [46] worked on wrinkles in a layered structure experimentally and numerically in two dimensions. They obtained a relationship between the wavelength and the amplitude of wrinkles for substrates with various elastic moduli and thickness; they observed different instability forms such as stripes, labyrinths, and herringbones. In the series works [66, 69, 70], different patterns (stripes, varicose, checkerboard, hexagonal) were analyzed for a bilayer plate under biaxial residual compressive stress in the film. Then the formation of herringbone (zigzag) pattern with increasing residual stress was studied numerically based on a simplified buckling model. Moreover, in the third part of the study, an asymptotic solution was proposed for a plate with an elastic foundation in the limit of large strains. Regarding energy contributions of different instability patterns, Cai et al. [48] focused on a bilayer film/substrate structure subjected to equi-biaxial compressive stress numerically and experimentally, where they observed checkerboard, hexagonal, and herringbone patterns. They ranked the modes in terms of energy, and they ended up with the fact that herringbone mode has the lowest energy, then come the checkerboard with hexagonal and triangular modes. On the other hand, Jia [49] showed that hexagonal patterns minimize the elastic energy, which is the dominant mode. Javili et al. [67] studied growth-induced instabilities based on eigenvalue analysis which does not impose perturbation-dependent definitions. They tested their approach in slender beam and growing film on a soft substrate, and as its outcome, an objective solution was reached. Since this method provides a good initial guess for a nonlinear analysis, it cannot be used for post-buckling behavior. As a follow-up work, Dortdivanlioglu et al. [68] proposed isogeometric analysis (IGA) enhanced with eigenvalue analysis for a thin stiff film on a compliant substrate subjected to

compressive stress. They also compared the isogeometric analysis with finite element analysis, resulting in more accurate predictions with IGA. The relationship between film thickness, film and substrate stiffness ratio, number of wrinkles, and wavelengths were also studied within this study. Additional physical effects were considered by Alawiye et al. [71]. In [71], linear analysis for wrinkling problems with additional considerations of pressure, surface tension, an upper substrate, and fibers were performed. Diffusion-driven time transient swelling on hydrogels was studied in [72, 73]. Considering the numerical efficiency, Kadapa et al. [74] proposed a finite element framework by extending a mixed displacement-pressure formulation using quadratic and linear Bezier elements. They concluded that the model provides good accuracy for exact incompressibility by providing an inf-sup stability condition.

Besides isotropic modeling of bilayer plate, there are also studies on multi-layer structural deformations and instabilities taking into account the fiber reinforcement on layers. These types of structures have mostly been revealed in living systems (bone, muscle, arteries, airway, heart etc.) and biomedical engineering designs such as actuators. As one of the first sets of studies, Rachev et al. [75] studied over remodeling caused by blood pressure of arterial wall. Taber [76] also proposed a growth law for arteries, including orthotropic layers (intima/media and adventitia) reinforced by muscle fibers. Lubarda et al. [45] presented a constitutive theory for stress-dependent evolution equations for isotropic, transversely isotropic, and orthotropic biomaterials. Then, Ciarletta et al. [77] worked on the combined effect of the growth and anisotropy in the epithelial formation using mixed polar coordinates. By the numerical study, they concluded that the result that distribution of residual strains and mechanical properties of fibers embedded in the tissue has a significant effect on instability patterns. Liu et al. [57] proposed a nonlinear finite element procedure for anisotropic swelling that included the chemical potential for anisotropic hydrogel-based bilayers. Although they do not focus on instabilities, they obtained the effects of modulus and fiber orientations in free bending and twisting. Stewart et al. [78] worked on wrinkling instability of bilayer cerebral cortex (grey and white matter) tissue embedded with two family elastic fibers in two dimensions. They showed that wrinkle wavelength is a function of fiber orientation, and the instability can be triggered by increasing the fiber stiffness depending on the fiber angle. There are also studies for macroscopic in-

stabilities taking into account micromechanics based on homogenization [79], Michel et al. [80] extended to microstructural and macroscopic instabilities for plane-strain problems, and then Slesarenkoa et al. [81] focused on macroscopic and microscopic instabilities in three-dimensional periodic fiber-reinforced composites. They found that the volume fraction of fibers determines the first mode of buckling and a high fraction ratio of fibers exceeding a threshold value ends up with long wave instability, whereas a lower fraction of fibers results in microscopic instabilities. Growth-induced nonlinear behavior such as remodeling of fibers [28, 41, 62, 63, 82, 83], free swelling of anisotropic hydrogels [54, 55, 56, 58], anisotropic growth of the heart [35, 36], swelling of tracheal angioedema [84, 85, 86] and growth in fiber-reinforced torsional actuators [59, 60] are extensively studied. For a detailed review accounting for growth-induced nonlinear behavior of fiber-reinfored systems, the interested reader is referred to [28, 62, 63, 29]. *Albeit tremendous amount of work devoted to the aforementioned aspects of growth and remodeling, there is still need for research regarding the the effect of fiber stiffness on growth for primary and secondary instabilities in three-dimensional bilayer fiber-reinforced structures.*

In addition to growth-induced deformations and instabilities those are mentioned above, there is an additional mechanical effect of growth on biological tissues as it may cause pre-stressed state. It has been shown that by opening angle experiments on an artery and on the experiments on left ventricle, there is an evidence of some residual stress appears on the tissue even for unloaded state. Heart is the most complicated organ in the human body and it may be subjected to high pressure load that drives the volumetric growth. There are many difficulties for the numerical modeling of cardiac due to highly non-linear, complex myofiber layout, myofiber dispersion, anisotropic behaviour, viscoelastic response and pre-stressed state due to non-uniform volumetric growth [87]. Experiments are performed for ex vivo or in vitro tissue in the literature but the mechanical behaviour may be different in vivo condition because of the residual stresses. Growth-induced pre-stress effect is an another open research area need to be investigated with accurate mechanical model of the cardiac.

1.3 Historical Remarks on Structural Features of Myocardium

The heart is one of the most complicated organ in mammals. It is an electro-mechanical pump that supplies blood through the vessels to the entire living body. Cardiovascular diseases are prevalent in the population, and they not only have a negative impact on people's lives but can also be fatal. The heart has vital functionality for humans and is subjected to themo-electro-chemo-mechanical conditions. It is important to observe the physiological conditions of the heart, which may have fatal consequences, and to understand the mechanics behind this elite pumping system with its sub-components. Thus, medical treatments, surgery techniques, and rehabilitation methods can be developed. For example, developing an artificial pumping system, ensuring the biocompatibility of transplantation, replacing the heart valve, developing the left ventricular pacemaker device, etc.

The heart is composed of four chambers, called the left and right atria (LA, RA) and the left and right ventricles (LV, RV). While RA is responsible for collecting the deoxygenated blood through the vena cava, LA collects oxygenated blood from the lungs. Atria and ventricles are connected with blood vessels and synchronized via antrioventricular valves. Humphrey [88] describes the ventricle functions as: RV pumps blood through the lungs and LV pumps blood through the aorta. The main pumping function of the heart in the ventricles is governed by the heart wall. The heart wall is composed of three main layers. These are the endocardium (the inner layer), myocardium (the middle layer), and epicardium (the outer layer). Endocardium and epicardium are thin layers that mainly consist of collagen and elastin, and they create an interface region with inner and outer substances. The myocardium is primarily responsible for the heart's pumping function in the wall. It is made up of parallel fibers that are embedded in sheets by extracellular matrix [88]. The orientation of the myofibers makes a smooth transition from the epicardium to the endocardium in a helical form. In the human, myofibers vary from about -70 degrees at the epicardium to nearly +70 degrees at the endocardium. The LV wall thickness is higher than the RV wall thickness due to the fact that the LV is subjected to a higher pressure load to pump the blood to the aorta.

Myocardium is an inhomogeneous, incompressible, pre-stressed, highly nonlinear,

anisotropic, viscoelastic tissue and it is in the form of a composite structure. Myocardium is an oriented and laminated structure [89] that exhibits different mechanical properties in three distinct directions, called fiber direction, sheet direction, and normal direction. Therefore, the myocardium must be considered an ortothropic material. Due to its high water content, it is also considered incompressible. According to experiments performed by Vossoughi et al. [90], they end up with a ratio of the bulk modulus to the shear modulus of nearly 10^5, which also supports the incompressibility assumption. Myocardium also contains patient-specific residual stresses due to the inhomogeneous growth of the heart under different physiological conditions, which may change the mechanical behavior of the tissue. In line with the high water content of the myocardium, it exhibits viscoelastic stress-strain relations under cyclic loading and relaxation tests. Both elastin and collagen are the determinants of the viscous response of the myocardium [89]. The viscoelastic behavior of the material is responsible for energy dissipation when subjected to a time-dependent external load. The resultant stress decreases over time after an instant strain is applied and maintained, a process known as relaxation behavior. If an instant stress is applied to the material and kept constant, it results in further deformation and is called creep behaviour. If there is a cyclic load applied to the material, there will be different stress-stain patterns for the loading and unloading curves. This phenomenon is called hysteresis, and it is a presenter of energy dissipation measures in the system. A typical cycle of loading- unloading, and relaxation curves of a biological tissue is given in Figure 1.5. In this thesis, after presenting growth-induced instabilities in soft biological tissues, we will focus on the viscoelastic passive mechanical response of the LV myocardium under cyclic shear and shear relaxation loads.

It is mandatory to understand the layout structure of the human myocardium in three distinct directions (fiber, sheet, and normal) for accurate numerical modeling. Not only the direction of orthotropic behaviour but also the dispersion characteristics in distinct directions have the key role of mechanical response of the myocardium. The myocardium structure is composed of parallel myocytes those are oriented helical from the inner to outer layer of the heart wall, and these muscle fibers form separated sheet laminates. Rohmer et al. [91] states that fibers (80 μm in length and 5-10 μm in radius) form a group in 3-4 cell of thickness in a laminate oriented in the transverse di-

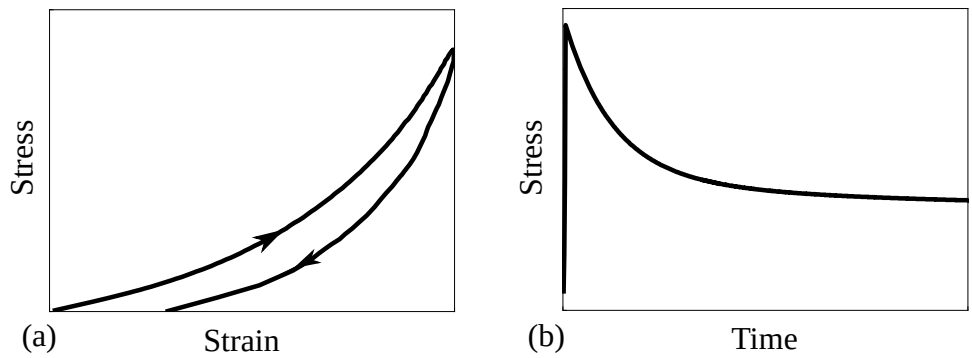

Figure 1.5: Illustration of (a)a typical loading-unloading curve of a viscoelastic material (b) typical relaxation curve of a viscoelastic material

rection in the heart wall. They developed a visualization algorithm, based on diffusion tensor magnetic resonance imaging, to visualize the three-dimensional sub-structures and orientations (fiber, sheet, and normal) of human myocardium. In order to reconstruct the sheet surface and fibers, they used the eigenvectors of the diffusion tensors in a sequence. Then, Sands et al. [92], developed a novel viewing technique to view microstructure that is adaptable to angle variation through transmural depth. They extracted three-dimensional images and obtained the orientation angles of the orthogonal direction for the rat left ventricular wall. Then, the LV remodeling was examined by diffusion tensor imaging for a mouse of myocardial infarction by [93]. They observed the variation in the diffusion tensor, fractional anisotropy, and myofiber distribution as resultant parameters. Sommer et al. [11] obtained the three-dimensional orientation and dispersion of the fibers and sheets for human myocardium, which is novel experimental research. They used second harmonic generation (SHG) microscopy for the detailed examination of myocardial microstructure. As a result, they determined the dispersion and concentration parameter ranges, which are quite important for the mathematical modeling of the constitutive relations. There have been conducted some mechanical tests for myocardium tissue specimens in the literature to obtain the passive mechanical properties. It is not only important to understand the mechanical response of the tissue physically, but it is also significant to perform calibration and determination of parameter sets of numerical constitutive models. Despite the fact that the initial research was done on animal myocardium samples, it provided insight and a vision for understanding human myocardium response. One of

the pioneer experiments has been performed by Pinto et al. [94] by obtaining the viscoelastic response of the rabbit heart muscle by relaxation, creep, and vibration tests. Then Demer et al. [95], applied cyclic load and unloading test in fiber and cross-fiber directions for the canine myocardium. They also performed uniaxial and biaxial loading tests to obtain the non-linear elastic and viscoelastic behaviour of the tissue. They concluded that, the myocardium tissue represents an anisotropic nonlinear elastic response with rate-dependent behaviour (viscoelasticity). Tsaturyan et al. [96], performed experiments to understand the extracellular fluid filtration effect on the viscoelastic behaviour of the myocardium. They showed that a reduction in the porosity of the myocardium tissue slows down the relaxation behaviour. Yin et al. [97], performed biaxial stretching experiments to characterize the three-dimensional mechanical properties of normal and diseased canine myocardium. They also fitted their experimental data with an exponential strain energy function. Then Dokos et al. [98], developed a novel shear testing machine that is able to simple shear deformation in two orthogonal axis and it is able to measure the forces in three axis which is also named triaxial shear testing in literature. They obtained the shear characteristics of rat myocardial tissue as a preliminary study. As a following work, Dokos et al. [99], conducted novel triaxial shear experiments on the myocardium tissues of pigs to characterize the shear mechanical properties of passive myocardium. This work was also referred to by many researchers who work on the development of mathematical constitutive material modeling, so the study can be accepted as pioneering research for the passive shear properties of the myocardium. They sliced a cubic specimen from the LV wall that is aligned with the fiber-sheet orientations, and then they applied sinusoidal simple shear for six shear modes. They concluded that passive myocardium exhibits non-linear viscoelastic shear behaviour, anisotropic shear behaviour in three orthogonal directions, and the shear stiffness of the myocardium is found to be maximum in the fiber direction and minimum in the normal direction. Then, the hyperelastic behaviour of bovine myocardial tissue has been mechanically tested based on uniaxial, biaxial, and equibiaxial loadings by [100]. Sommer et al. [101], proposed a method that makes the measurement of the shear deformations and stresses available for the biaxial extension test, and they demonstrated experimental results based on human myocardial tissue specimens. As a following research, Sommer et al. [11] determined the shear properties of the passive human ventricular myocardium by

performing biaxial extension, triaxial cyclic shear, and shear relaxation experiments. They also revealed the three-dimensional microstructure of cardiac tissue by second harmonic generation microscopy. They obtained the orientations of three principal directions (fiber, sheet, and normal), and they determined the dispersion parameters and concentration parameters for myofibers and sheets. They concluded that, the passive human myocardium is nonlinear, orthotropic, dispersed, and rate-dependent under large deformations. Then Avazmohammadi et al. [102], proposed a methodology that starts with a kinematic analysis to observe the optimum displacement paths and then applies these displacement fields to the cubic myocardium specimen. Lastly, they developed an inverse finite element methodology that simulates the experimental configuration to determine the constitutive model parameter sets. An illuminating research study on the healthy and infarcted myocardial tissue of a rat has been studied by Martonova et al. [103]. They performed uniaxial extension tests for healthy and infarcted tissues and they fitted Holzapfel-Ogden constitutive model parameters with experimental results. Then, they proposed a constitutive model for the infarcted tissue that is based on the combination of myocardium and transversely isotropic scar. They presented that the infarction tissue exhibits a stiffer response than the healthy one.

1.4 Proposed Methods and Contribution

Within the scope of this thesis, we have studied novel formulations for dispersion-type anisotropic viscoelasticity of the human myocardium, both theoretically and numerically. One of the primary goals of the research is to develop viscoelastic constitutive models based on histological data of the tissue's dispersion characteristics. It is not limited to being used for myocardium; these novel formulations can also be used for any other type of isotropic or anisotropic tissue. We start with the decomposition of the free-energy function into equilibrium and non-equilibrium contributions. The baseline hyperelasticity is defined by the generalized structure tensor model. The non-equilibrium response is described by the rheological Maxwell branch with an integrated elastic spring element. It utilizes a quadratic free-energy function in logarithmic space and a quadratic or power-type evolution equation in each orientation direction. The overstress response is obtained through distinct orientation directions

by numerical evaluation of averaging integrals over either the unit micro-sphere or the unit planar circle. Our contributions are as follows:

- development of a novel angular integration-based constitutive model for dispersion-type anisotropic viscoelasticy which is proposed for the first time in the literature to our best knowledge,
- development of global-based and local-based dispersion-type formulations where the density distribution function enters the constitutive equations in different stages,
- development of dispersion-based formulations based on both bivariate von Mises and planar von Mises density distribution functions,
- in addition to the continuous integral over the unit micro-sphere, development of a planar unit circle integral scheme to increase the accuracy of the numerical integrals,
- identifying viscous parameter sets of novel formulations via the triaxial cyclic shear and triaxial shear relaxation experiments conducted in the literature for the human myocardium.

In the other part of the research in this thesis, there has been studied for planar growth-induced instabilities in three-dimensionally confined bilayer tissues/structures, i.e., thick, stiff film on a compliant substrate. Growth-induced instabilities are examined for a different range of fiber stiffness with an extended five-field Hu- Washizu mixed variational formulation in sense of Dal [104]. The quasi-incompressible and quasi-inextensible limits of transversely isotropic materials were considered. A numerical example was solved by implementing the T2P0F0 element on an automated differential equation solver platform, FEniCS. Our contributions are as follows:

- extension of the five-field mixed variational formulation for finite growth problems,
- numerically investigation the role of the fiber stiffness on the critical growth parameter, first instability, and secondary instability modes.

1.5 The Outline of the Thesis

After presenting the introductory sections in Chapter 1, Chapter 2 outlines the basics of continuum mechanics, including kinematics, stress, and strain measures for both isotropic and anisotropic solids with the introduction of balance laws. Chapter 3 presents isotropic and anisotropic incompressible hyperelasticity theory within two-field, three-field, and five-field mixed element formulations provided by numerical comparative examples. Chapter 4 introduces the kinematics of finite growth theory with the derivations of stress and corresponding moduli expressions. Then, numerical examples are provided for different types of growth-induced deformations and instabilities by using FEniCS. Chapter 5 focuses on the theories of fiber dispersion-type formulations for soft biological tissues. It also describes the von Mises type of density distribution functions that are commonly used. In Chapter 6, firstly, the baseline hyperelastic constitutive theory is presented for the human myocardium with the integration of the GST type dispersion formulation. Then, current anisotropic viscoelasticity theories are outlined. Different angular-integration-type dispersion-based formulations are proposed under local-based and global-based classifications. Lastly, the fitting performance of the proposed models are observed numerically with the triaxial cyclic shear and triaxial shear relaxation tests from the literature. Chapter 7 provides a summary of the entire work, outlines the outcomes, and gives recommendations to be taken into account.

CHAPTER 2

BASICS OF CONTINUUM MECHANICS

This chapter presents the fundamental kinematics, strain, and stress measures of general isotropic and anisotropic solids. The chapter layout is as follows: in the first part, fundamental descriptions of the material motion in undeformed and deformed configurations are given. The basic pull-back and push-forward mathematical operations are introduced through metric tensors. Then, strain measures are described in both Lagrangian and Eulerian settings. The fundamental characteristic equation of a second-order tensor is presented to describe the principal invariants. Then, isotropic and anisotropic invariants of the right Cauchy-Green tensor are introduced, which are the significant scalar quantities used to describe the scalar free-energy function in hyperelasticity. Then stress measures are introduced in both undeformed and deformed configurations. Later, the fundamentals of continuum thermodynamic balance laws were summarized. Lastly, Clausis-Duhem inequality has been presented by introducing the Helmholtz free energy function.

2.1 Kinematics

A solid *body* $\mathscr{B}$ is a three-dimensional manifold, that includes material points $\mathscr{P} \in \mathscr{B}$. The movement of the solid can be described by the function of time via bijective mappings

$$\boldsymbol{\chi}(\mathscr{P}, t) = \begin{cases} \mathscr{B} & \rightarrow & \mathscr{B}(\mathscr{P}, t) \in \mathbb{R}^3 \times \mathbb{R}_+ \\ \mathscr{P} & \mapsto & \boldsymbol{x} = \boldsymbol{\chi}_t(\mathscr{P}) = \boldsymbol{\chi}(\mathscr{P}, t). \end{cases} \tag{2.1}$$

The point $\boldsymbol{x} = \boldsymbol{\chi}(\mathscr{P}, t)$ implies the deformed configuration of the particle $\mathscr{P}$ at time $t \in \mathbb{R}_+$. Reference configurations of the points at the reference time (t_0) can

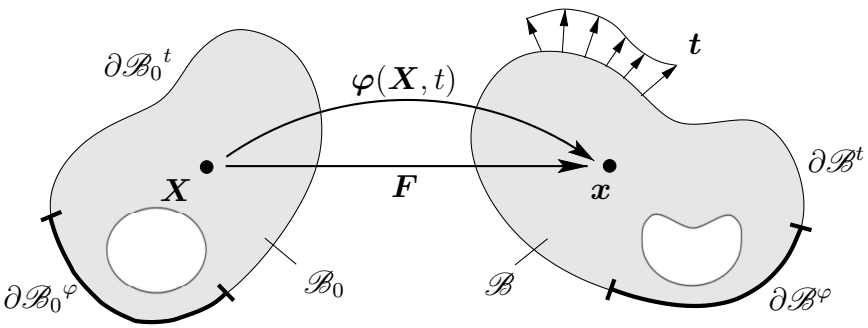

Figure 2.1: Nonlinear deformation of an isotropic solid. The underformed configuration $\mathscr{B} \in \mathbb{R}^3$ and the deformed configuration $\mathscr{P} \in \mathbb{R}^3$. $\boldsymbol{\varphi} : \mathscr{B} \times \mathbb{R} \mapsto \mathbb{R}^3$ is the nonlinear field which maps at time $t \in \mathbb{R}_+$ undeformed position $\boldsymbol{X} \in \mathscr{B}$ onto deformed $\boldsymbol{x} = \boldsymbol{\varphi}(\boldsymbol{X}, t) \in \mathscr{P}$.

be expressed by $\boldsymbol{X} = \boldsymbol{\chi}(\mathscr{P}, t_0) \in \mathbb{R}^3$ and the configuration at a arbitrary time (t) denoted by $\boldsymbol{\chi}_t(\mathscr{P}) = \boldsymbol{\chi}(\mathscr{P}, t)$. The displacement, velocity, and acceleration vectors of the material point at time (t) can be defined by following respectively

$$\begin{aligned} \boldsymbol{u} &:= \boldsymbol{x} - \boldsymbol{X} \\ \dot{\boldsymbol{x}} &:= \frac{\partial \boldsymbol{\chi}(\boldsymbol{X}, t)}{\partial t} \\ \ddot{\boldsymbol{x}} &:= \frac{\partial^2 \boldsymbol{\chi}(\boldsymbol{X}, t)}{\partial t^2} \end{aligned} \tag{2.2}$$

The deformation map can be expressed as $\boldsymbol{\varphi}_t = \boldsymbol{\chi}_t \circ \boldsymbol{\chi}_{t_0}^{-1}(\boldsymbol{X})$ such that

$$\boldsymbol{\varphi}_t(\boldsymbol{X}) = \begin{cases} \mathscr{B}_0 & \rightarrow \quad \mathscr{B} \in \mathbb{R}^3 \\ \boldsymbol{X} & \mapsto \quad \boldsymbol{x} = \boldsymbol{\varphi}(\boldsymbol{X}, t) \end{cases} \tag{2.3}$$

maps the undeformed configuration $\boldsymbol{X} \in \mathscr{B}_0$ of a point onto the deformed configuration $\boldsymbol{x} \in \mathscr{B}$, see Figure 2.1. The deformation gradient is defined as

$$\boldsymbol{F} : T_X\mathscr{B}_0 \rightarrow T_x\mathscr{B}; \quad \boldsymbol{F} := \nabla\boldsymbol{\varphi}_t(\boldsymbol{X}) \tag{2.4}$$

It maps the unit tangent of the undeformed or Lagrangian configuration onto the deformed or Eulerian configuration. The gradient operators $\nabla_X[\bullet]$ and $\nabla_x[\bullet]$ express the spatial derivative with respect to the undeformed $\boldsymbol{X}$ and deformed $\boldsymbol{x}$ coordinates, respectively.

While the deformation gradient $\boldsymbol{F}$ performs the mapping of infinitesimal line element ($d\boldsymbol{X}$) from undeformed state onto deformed state, its cofactor $\mathrm{cof}[\boldsymbol{F}] = \det[\boldsymbol{F}]\boldsymbol{F}^{-T}$

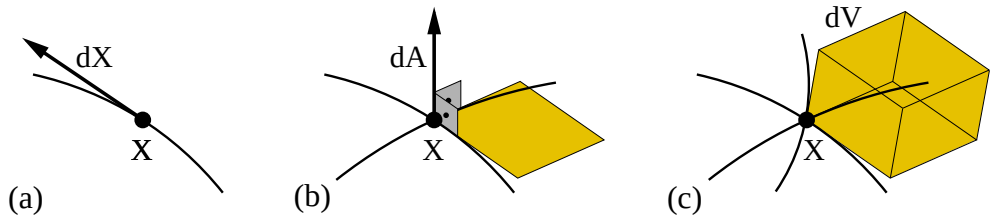

Figure 2.2: Three physically related mapping operations: (a) The deformation gradient $\boldsymbol{F}$, (b) cofactor of the deformation gradient $\mathrm{cof}[\boldsymbol{F}]$, and (c) and the Jacobian $\det[\boldsymbol{F}]$; adopted from [5]

and its determinant (the Jacobian) $J := \det[\boldsymbol{F}] > 0$ characterize the mapping of the infinitesimal area ($d\boldsymbol{A}$) and volume (dV) elements from reference state onto spatial configuration, respectively. These fundamental maps are shown in Figure 2.2.

$$d\boldsymbol{x} = \boldsymbol{F} d\boldsymbol{X} \ , \qquad d\boldsymbol{a} = \mathrm{cof}[\boldsymbol{F}] d\boldsymbol{A} \ , \qquad dv = J dV \ . \tag{2.5}$$

There is an obligation that $J := \det[\boldsymbol{F}] > 0$ which provides the non-negative volume and the condition, is physically necessary. J^{-1} should also exist to perform inverse mapping. There is also need to be defined the metric tensors ($\boldsymbol{G}$ and $\boldsymbol{g}$) to perform mapping between covariant and contravariant points in Lagrangian and Eulerian states, respectively [105]. Here we designate the right Cauchy-Green tensor, and the inverse of the left Cauchy-Green tensor

$$\boldsymbol{C} = \boldsymbol{F}^T \boldsymbol{g} \boldsymbol{F}, \qquad \text{and} \qquad \boldsymbol{c} = \boldsymbol{F}^{-T} \boldsymbol{G} \boldsymbol{F}^{-1} \tag{2.6}$$

It is described as the pull-back operation of the Eulerian metric $\boldsymbol{g}$ and push-forward operation of the Lagrangian metric $\boldsymbol{G}$, respectively and the Finger tensor is defined by $\boldsymbol{b} = \boldsymbol{c}^{-1}$. Here, in the case of Cartesian coordinates, $\boldsymbol{g}$ and $\boldsymbol{G}$ are the same as the identity tensor [6]. In line with that, these metric tensors can also be written in Cartesian coordinates by indicial notation such as; $\boldsymbol{G} = \delta_{AB}$ and $\boldsymbol{g} = \delta_{ab}$. The upper case letters correspond for Lagrangian configuration and the small case letters refer for Eulerian setting. Accordingly, for a tensorial measure, the indicial notation describes whether the quantity is purely or partially (two-point) described in Lagrangian and Eulerian spaces.Then Green-Lagrangian and Almansian strain tensors are defined as

$$\boldsymbol{E} = \frac{1}{2}[\boldsymbol{C} - \boldsymbol{1}] \quad \text{and} \quad \boldsymbol{A} = \frac{1}{2}[\boldsymbol{1} - \boldsymbol{b}^{-1}] \tag{2.7}$$

where $\boldsymbol{E}$ is the strain tensor that measures the change in Lagrangian configuration and $\boldsymbol{A}$ is the strain tensor that measures the change in Eulerian configuration. These quantities can be transformed to each other by covariant pull-back operation as $\boldsymbol{E} = \boldsymbol{F}^T \boldsymbol{A} \boldsymbol{F}$ and by covariant push-forward operation as $\boldsymbol{A} = \boldsymbol{F}^{-T} \boldsymbol{E} \boldsymbol{F}^{-1}$.

Deformation gradient is the two-point tensor which can be described in indicial notation as $F_{aA} = \partial x_a / \partial X_A$. It can be decomposed into pure rotation and pure stretch inducing components as

$$\boldsymbol{F} = \boldsymbol{R}\boldsymbol{U} = \boldsymbol{V}\boldsymbol{R}, \tag{2.8}$$

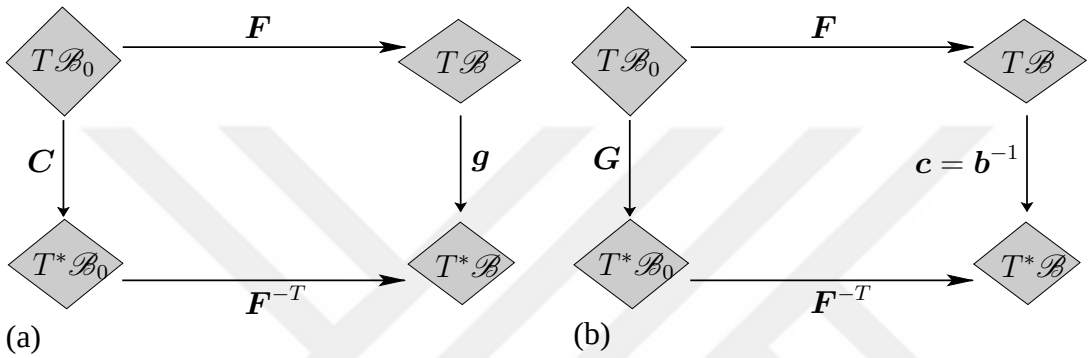

Figure 2.3: (a) Definition of right Cauchy Green tensor by pull-back operation of Eulerian metric $\boldsymbol{g}$, (b) Definition of left Cauchy Green tensor by push-forward operation of Lagrangian metric $\boldsymbol{G}$.

where $\boldsymbol{R}$ is the orthogonal rotation tensor, $\boldsymbol{U}$ is the right stretch tensor, and $\boldsymbol{V}$ is the left stretch tensor. $\boldsymbol{U}$ and $\boldsymbol{V}$ are the symmetric and positive definite tensors. By the equation 2.8, the rotation and stretch can be purely separated. By using relations between equation 2.6 and 2.8, the right Cauchy-Green tensor and left Cauch-Green tensor (defined by $\boldsymbol{b} = \boldsymbol{c}^{-1}$) can be written as $\boldsymbol{C} = \boldsymbol{U}^2$ and $\boldsymbol{b} = \boldsymbol{V}^2$ respectively. Any symmetric tensor can be represented by its eigenvalues λ_i and the corresponding eigenvectors are defined in the orthonormal basis. By the spectral decomposition, the principal stretches can be defined as following

$$\boldsymbol{U} := \textstyle\sum_{i=1}^{3} \lambda_i \boldsymbol{N}_i \otimes \boldsymbol{N}_i \quad \text{and} \quad \boldsymbol{V} := \textstyle\sum_{i=1}^{3} \lambda_i \boldsymbol{n}_i \otimes \boldsymbol{n}_i \tag{2.9}$$

where λ_i is the principal stretch and $\boldsymbol{N}_i$ and $\boldsymbol{n}_i$ are the principal directions in Lagrangian and Eulerian configurations, respectively. The stretch can also be defined by the ratio of infinitesimal length of the $d\boldsymbol{x}$ to undeformed length $d\boldsymbol{X}$ and the length is

defined by the mathematical norms of these vectors as $\lambda = ||d\boldsymbol{x}||/||d\boldsymbol{X}||$.

By using the generalized eigenvalue problems for a second order tensor $\boldsymbol{A}$, the characteristic equation can be obtained as below.

$$\lambda^3 - I_1\lambda^2 + I_2\lambda - I_3 = 0 \tag{2.10}$$

The roots of the equation 2.10 gives the eigenvalues (λ_i) of the tensor $\boldsymbol{A}$. The coefficients of equation 2.10 are called principal invariants of tensor $\boldsymbol{A}$ and described as

$$\begin{aligned} I_1(\boldsymbol{A}) &:= tr(\boldsymbol{A}) \\ I_2(\boldsymbol{A}) &:= \frac{1}{2}\left[[tr(\boldsymbol{A})^2] - tr(\boldsymbol{A}^2)\right] \\ I_3(\boldsymbol{A}) &:= det(\boldsymbol{A}) \end{aligned} \tag{2.11}$$

The principal invariants shown in equation 2.11 can also expressed by the real and positive eigenvalues as

$$\begin{aligned} I_1(\boldsymbol{A}) &:= \lambda_1 + \lambda_2 + \lambda_3 \\ I_2(\boldsymbol{A}) &:= \lambda_1\lambda_2 + \lambda_2\lambda_3 + \lambda_1\lambda_3 \\ I_3(\boldsymbol{A}) &:= \lambda_1\lambda_2\lambda_3 \end{aligned} \tag{2.12}$$

Hyperelastic constitutive laws can be constructed based on a scalar energy function that represents the stored energy in the material. In general, stored free energy for hyperelastic solid is governed by three invariants of the right Cauchy Green tensor. These invariants can be used in combination with any kind of isotropic hyperelastic material model. The isotropic invariants of the right Cauchy-Green tensor can be defined as follows:

$$I_1 := \operatorname{tr}\boldsymbol{C}, \quad I_2 := \frac{1}{2}\left[I_1^2 - \operatorname{tr}(\boldsymbol{C}^2)\right], \quad \text{and} \quad I_3 := \det\boldsymbol{C} = J^2 \tag{2.13}$$

These invariants have physical meanings: (I_1) is the line stretch, (I_2) is the area change, and (I_3) is the volume change of the material. By using equation (2.12), the schematic representations of principal stretches on an infinitesimal element shown in Figure 2.4. If the continuum medium is an anisotropic solid which may be composed of two-family stiff fibers or laminated layered structure in a specific directions, we define Lagrangian unit vectors $\boldsymbol{n}_0$ and $\boldsymbol{m}_0$ as following.

$$\begin{aligned} |\boldsymbol{n}_0|_{\boldsymbol{G}} = 1 \qquad &\text{where} \qquad |\boldsymbol{n}_0|_{\boldsymbol{G}} = (\boldsymbol{n}_0 \cdot \boldsymbol{G}\boldsymbol{n}_0)^{1/2} \ . \\ |\boldsymbol{m}_0|_{\boldsymbol{G}} = 1 \qquad &\text{where} \qquad |\boldsymbol{m}_0|_{\boldsymbol{G}} = (\boldsymbol{m}_0 \cdot \boldsymbol{G}\boldsymbol{m}_0)^{1/2} \ . \end{aligned} \tag{2.14}$$

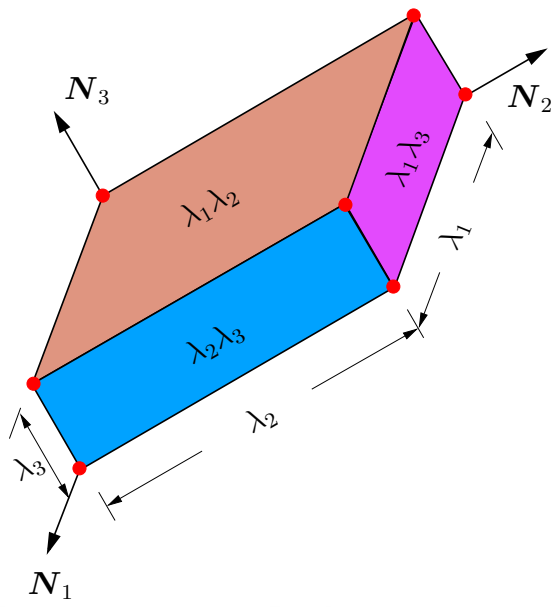

Figure 2.4: Representation of principal stretches defines the principal invariants of the right Cauchy-Green tensor (I_1, I_2, and I_3), as length, area and volume measures respectively.

The generalized schematic of an anisotropic material is shown in Figure 2.5. Then by the tangent map, the deformed configuration of unit vectors can be formed as

$$\begin{aligned} \boldsymbol{n} &= \boldsymbol{F}\boldsymbol{n}_0 \\ \boldsymbol{m} &= \boldsymbol{F}\boldsymbol{m}_0 \end{aligned} \tag{2.15}$$

In addition to the isotropic response, the anisotropic response that is generated by

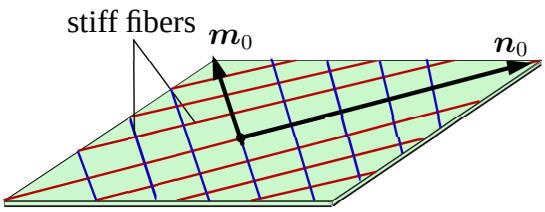

Figure 2.5: Schematic representation of transversely isotropic solid that composed of two family fibers in the direction of $\boldsymbol{n}_0$ and $\boldsymbol{m}_0$, respectively.

two families of fibers, laminates etc. requires additional four invariants I_4, I_5, I_6 and I_7. These additional invariants are introduced in terms of $\boldsymbol{n}_0$ $\boldsymbol{m}_0$ unit vectors of

fibers/laminates in the undeformed configuration

$$\begin{aligned} I_4 &:= \boldsymbol{n}_0 \cdot \boldsymbol{C}\boldsymbol{n}_0 \qquad & I_5 &= \boldsymbol{n}_0 \cdot \boldsymbol{C}^2\boldsymbol{n}_0 \,, \\ I_6 &:= \boldsymbol{m}_0 \cdot \boldsymbol{C}\boldsymbol{m}_0 \qquad & I_7 &= \boldsymbol{m}_0 \cdot \boldsymbol{C}^2\boldsymbol{m}_0 \,, \end{aligned} \tag{2.16}$$

that relates to the energy storage due to fiber/sheet reinforcement in the material. There is also an additional invariant that can be described for the coupling behaviour through two distinct directions:

$$I_8 := \boldsymbol{n}_0 \cdot \boldsymbol{C}\boldsymbol{m}_0 = \boldsymbol{m}_0 \cdot \boldsymbol{C}\boldsymbol{n}_0 \tag{2.17}$$

Invariants I_4 and I_6 represent the square of the stretch in the direction of units vectors. There is not physical corresponding of I_5 and I_7 and those can be dependent on I_1 and I_2, see details in [106].

2.2 Stress Measures

A solid *body* $\mathscr{B}$ is subjected to surface traction $\boldsymbol{t}$ and body forces those generates the stress in the deformed body. While body force acts as a volumetric quantity on $\mathscr{B}$, surface traction is specified in the area in $\partial\mathscr{B}_t$. The schematic representation of the surface normal and traction vectors are shown in undeformed and deformed configuration in Figure 2.6 where the forces acting on the surface are related to each

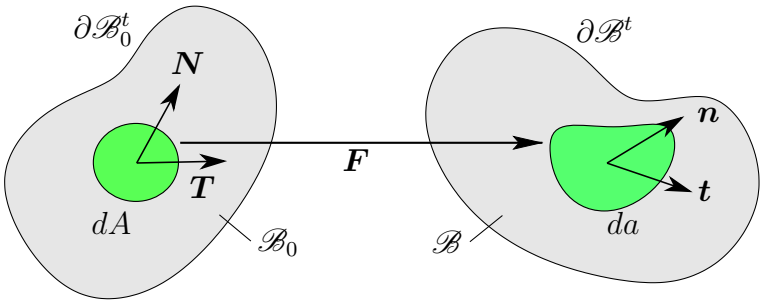

Figure 2.6: Schematic representation of the surface normal and traction vectors in a cut-out region for the deformed and undeformed configurations.

other in the deformed and undeformed setting as

$$\int_{\partial\mathscr{B}_0^t} \boldsymbol{T} dA := \int_{\partial\mathscr{B}^t} \boldsymbol{t} da \tag{2.18}$$

The traction $\boldsymbol{t}$ also known as Cauchy stress vector measures the force per unit deformed area. Then Cauchy's stress theorem defined as

$$\boldsymbol{t}(\boldsymbol{x}, \boldsymbol{n}, t) = \boldsymbol{\sigma} \cdot \boldsymbol{n}, \tag{2.19}$$

The Cauchy stress is also called the true stress, and it is defined in the deformed configuration. Then the first Piola Kirchhoff stress (also known as engineering stress) is defined in reference normal $\boldsymbol{N}$ by using the Piola identity ($\boldsymbol{n}da = J\boldsymbol{F}^{-T}\boldsymbol{N}dA$) as below. The first Piola-Kirchhoff stress tensor is a non-symmetric two point tensor that is defined by the nominal traction vector in the deformed configurations and unit normal in the undeformed configurations.

$$\boldsymbol{P} = J\boldsymbol{\sigma}\boldsymbol{F}^{-T} \tag{2.20}$$

Kirchhoff stress $\boldsymbol{\tau}$ is another measure of stress tensor that is a deformed configuration stress quantity described as below. It is as the weighted stress defined per unit reference volume.

$$\boldsymbol{\tau} = J\boldsymbol{\sigma} \tag{2.21}$$

Then purely Lagrangian stress tensor called second Piola-Kirchhoff tensor $\boldsymbol{S}$ can be defined by the pull back operation of Kirchhoff stress $\boldsymbol{\tau}$ as

$$\boldsymbol{S} = \boldsymbol{F}^{-1}\boldsymbol{\tau}\boldsymbol{F}^{-T} = J\boldsymbol{F}^{-1}\boldsymbol{\sigma}\boldsymbol{F}^{-T} = \boldsymbol{F}^{-1}\boldsymbol{P} \tag{2.22}$$

Although the first Piola-Kirchhoff stress is not a symmetric tensor, the rest of the stress measures for Cauchy ($\boldsymbol{\sigma}$), Kirchhoff ($\boldsymbol{\tau}$) and the second Piola-Kirchhoff ($\boldsymbol{S}$) stress tensors are symmetric. Relations of the all stress tensors are presented schematically over tangent-cotangent space and Lagrangian-Eulerian domains in Figure 2.7.

2.3 Balance Laws of Continuum Thermomechanics

In this section, the balance laws of continuum thermomechanics are summarized as follows: conservation of mass m, conservation of linear momentum ($\mathcal{I}$), conservation of angular momentum ($\mathcal{D}$), conservation of energy ($\mathcal{K}$, $\mathcal{E}$), and conservation of entropy ($\mathcal{H}$), see [107] for further derivations. The physical entities that are the fundamentals of the balance equations are listed in Table 2.1 where the fields ρ_d, $\boldsymbol{u}$, $\boldsymbol{v}$,

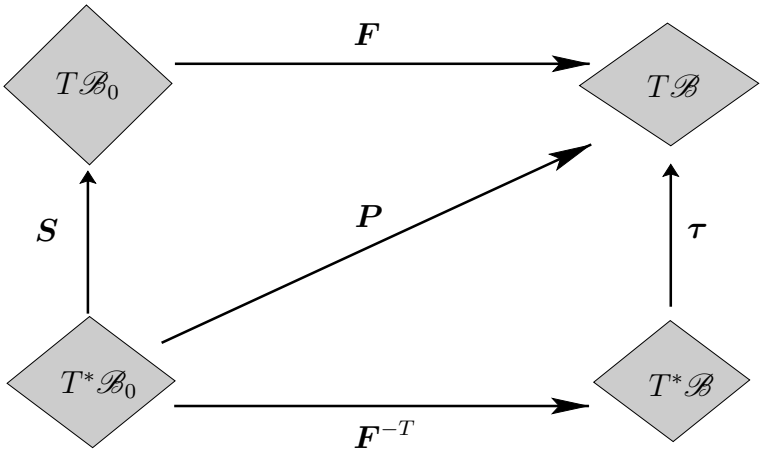

Figure 2.7: Schematic diagram of the stress measures that reveals the stress transformations though tangent and cotangent spaces and push-forward and pull-back operations.

e, η_e and γ_e are the mass density, displacement, velocity, internal energy, entropy, and entropy generation, respectively. The fundamental balance laws of continuum thermomechanics define the relationship based on the physical entities listed in Table 2.1 and global thermodynamic loads as follows: mechanical force ($\boldsymbol{F}_m$), mechanical moment ($\boldsymbol{M}_m$), mechanical power (P), thermal power (Q) and entropy power (S), as listed in Table 2.2. There are three additional variables introduced: heat flux (h), heat source per unit mass (r) and the temperature (θ). Then the conservation of these physical quantities can be defined with respect to time (t) derivatives in Table 2.3. The description of the balance laws can be summarized as follows: conservation of mass states that physical mass in a control volume is fixed quantity and cannot be generated or lost; angular momentum governs the symmetry of Cauchy stress tensor; linear momentum outcomes with Cauchy's equation of motion, balance of energy states that the summation of the rate of change in kinetic energy ($\mathcal{K}$) and the internal stress power (P_{int}) must be equal to the rate of change in external work done (P_{ext}), conservation of entropy governs the second law of thermodynamics which is the inequality rather than an equality as irreversibility condition. After using the relationship between equations listed in Tables 2.3 and 2.2 with mathematical operations such as Gauss divergence integration theorem, integration by parts and localization theorem yields local/strong forms of balance laws shown in Table 2.4.

Table 2.1: Mathematical descriptions of physical entities in region $\mathscr{P}$

Mass	$m = \int_{\mathscr{P}} \rho_d dV$	(2.23)
Linear momentum	$\mathcal{I} = \int_{\mathscr{P}} \rho_d \boldsymbol{v} dV$	(2.24)
Angular momentum	$\mathcal{D} = \int_{\mathscr{P}} \boldsymbol{x} \times \rho_d \boldsymbol{v} dV$	(2.25)
Kinetic energy	$\mathcal{K} = \int_{\mathscr{P}} \frac{1}{2} \rho_d \lvert\boldsymbol{v}\rvert^2 dV$	(2.26)
Internal energy	$\mathcal{E} = \int_{\mathscr{P}} \rho_d e dV$	(2.27)
Entropy	$\mathcal{H} = \int_{\mathscr{P}} \rho_d \eta_e dV$	(2.28)
Entropy production	$\Gamma = \int_{\mathscr{P}} \rho_d \gamma_e dV$	(2.29)

Table 2.2: Thermodynamic loads

Mechanical force	$\boldsymbol{F}_m = \int_{\mathscr{P}} \rho_d \boldsymbol{b} dV + \int_{\partial\mathscr{P}} \boldsymbol{t} dA$	(2.30)
Mechanical couple	$\boldsymbol{M}_m = \int_{\mathscr{P}} \boldsymbol{x} \times \rho_d \boldsymbol{b} dV + \int_{\partial\mathscr{P}} \boldsymbol{x} \times \boldsymbol{t} dA$	(2.31)
Mechanical power	$P = \int_{\mathscr{P}} \rho_d \boldsymbol{b} \cdot \boldsymbol{v} dV + \int_{\partial\mathscr{P}} \boldsymbol{t} \cdot \boldsymbol{v} dA$	(2.32)
Thermal power	$Q = \int_{\mathscr{P}} \rho_d r dV - \int_{\partial\mathscr{P}} h dA$	(2.33)
Entropy power	$\mathcal{S} = \int_{\mathscr{P}} \rho_d \frac{r}{\theta} dV - \int_{\partial\mathscr{P}} \frac{h}{\theta} dA$	(2.34)

Table 2.3: Global forms of the physical balance principles

Conservation of mass	$\frac{d}{dt}m = 0$	(2.35)
Conservation of linear momentum	$\frac{d}{dt}\mathcal{I} = \boldsymbol{F}_m$	(2.36)
Conservation of angular momentum	$\frac{d}{dt}\mathcal{D} = M$	(2.37)
Conservation of energy	$\frac{d}{dt}[\mathcal{K} + \mathcal{E}] = P + Q$	(2.38)
Entropy inequality	$\Gamma = \frac{\mathcal{S}}{dt} - \mathcal{H} \geq 0$	(2.39)

Table 2.4: Strong forms of the physical balance principles

Lagrangian	**Eulerian**	
$\rho_{d0} = \rho_d J$	$\dot{\rho}_d + \rho_d div\boldsymbol{v} = 0$	(2.40)
$Div[\boldsymbol{P}] + \boldsymbol{f}_0 = \rho_{d0}\dot{\boldsymbol{V}}$	$div\boldsymbol{\sigma} + \boldsymbol{f} = \rho_d\dot{\boldsymbol{v}}$	(2.41)
$\boldsymbol{F}^{-1}\boldsymbol{P} = \boldsymbol{P}^T\boldsymbol{F}^{-T}, \boldsymbol{S} = \boldsymbol{S}^T$	$\boldsymbol{\sigma} = \boldsymbol{\sigma}^T$	(2.42)
$\rho_{d0}\dot{e} = \boldsymbol{P} : \boldsymbol{F} + r_0 - Div\boldsymbol{Q}$	$\rho_d\dot{e} = \boldsymbol{\sigma} : \boldsymbol{L} + r - div\boldsymbol{q}$	(2.43)
$\rho_{d0}\gamma_e = \rho_{d0}\dot{\eta}_e - \frac{1}{\theta}(r_0 - Div\boldsymbol{Q})$ $-\frac{1}{\theta^2}\boldsymbol{Q} \cdot \nabla_{\boldsymbol{X}}\theta \geq 0$	$\rho_d\gamma_e = \rho_d\dot{\eta}_e - \frac{1}{\theta}(r - div\boldsymbol{q})$ $-\frac{1}{\theta^2}\boldsymbol{q} \cdot \nabla_{\boldsymbol{x}}\theta \geq 0$	(2.44)

2.4 Dissipation Inequality

The physical equations those are defined in the previous section must obey to the second law of thermodynamic and they must be consistent. Then, the dissipation inequality can be introduced as follows

$$\rho_d \mathscr{D} = \boldsymbol{\sigma} : \boldsymbol{D} + \rho_d \theta \dot{\eta}_e - \rho_d \dot{e} - \frac{1}{\theta} \boldsymbol{q} \cdot \nabla_{\boldsymbol{x}} \theta \geq 0 \tag{2.45}$$

where $\boldsymbol{D}$ is the rate of deformation tensor. The equation 2.45 is also known as Clasius-Duhem Inequality. It can be decomposed into local entropy production $\rho_d \mathscr{D}_{loc}$ and heat conduction induced entropy production $\rho_d \mathscr{D}_{con}$ such as $\rho_d \mathscr{D} = \rho_d \mathscr{D}_{loc} + \rho_d \mathscr{D}_{con} \geq 0$. These dissipation components are called as Clasius-Planck Inequality ($\rho_d \mathscr{D}_{loc}$) and Fourier Inequality ($\rho_d \mathscr{D}_{con}$) and the strong form requires the condition that both of dissipation components are greater or equal to zero. These dissipation components are defined as below

$$\begin{aligned} \rho_d \mathscr{D}_{loc} &= \boldsymbol{\sigma} : \boldsymbol{D} + \rho_d \theta \dot{\eta}_e - \rho_d \dot{e} \geq 0 \\ \rho_d \mathscr{D}_{con} &= -\frac{1}{\theta} \boldsymbol{q} \cdot \nabla_{\boldsymbol{x}} \theta \geq 0 \,, \end{aligned} \tag{2.46}$$

In order to apply the local component ($\mathscr{D}_{loc}$) for solid mechanics processes, we introduce the Helmholtz free energy function (Ψ) through Legendre transformation such that $\Psi = e - \theta \eta_e$. Then, the local component of dissipation yield as follows

$$\rho_d \mathscr{D}_{loc} = \boldsymbol{\sigma} : \boldsymbol{D} - \rho_d \dot{\Psi} - \rho_d \eta_e \dot{\theta} \geq 0 \,, \tag{2.47}$$

and it can be reduced to following form for the isothermal process

$$\rho_d \mathscr{D}_{loc} = \boldsymbol{\sigma} : \boldsymbol{D} - \rho_d \dot{\Psi} \geq 0 \,, \tag{2.48}$$

The first term in equation 2.48 represents the stress power (per unit current volume), and the second term is the stored energy in the material. Equation 2.48 is also referred to the entropy inequality in elasticity, viscoelasticity, damage etc. Additionally, $\rho_d \mathscr{D}_{con}$ is referred to the entropy inequality to heat flow direction. Then, the Helmnholtz free energy and the heat flux can be defined as

$$\Psi = \hat{\Psi}(\boldsymbol{X}, \boldsymbol{F}, \theta, \boldsymbol{\mathcal{I}}, \boldsymbol{g}_\theta) \qquad \text{and} \qquad q = \hat{q}(\boldsymbol{X}, \theta, \boldsymbol{F}, \boldsymbol{g}_\theta) \tag{2.49}$$

where $\boldsymbol{g}_\theta$ is the temperature gradient vector and it should not be confused with metric tensor $\boldsymbol{g}$. The stress power can also be defined in different forms of stress contributions as below

$$\boldsymbol{\sigma} : \dot{\boldsymbol{D}} = J^{-1}\boldsymbol{P} : \dot{\boldsymbol{F}} = J^{-1}\boldsymbol{S} : \dot{\boldsymbol{C}} = J^{-1}\boldsymbol{\tau} : \dot{\boldsymbol{D}} \tag{2.50}$$

By taking the time derivative of Helmholtz free energy (Ψ), it leads

$$\dot{\Psi} = \partial_{\boldsymbol{F}}\Psi : \dot{\boldsymbol{F}} + \partial_\theta\Psi : \dot{\theta} + \partial_{\boldsymbol{\mathcal{I}}}\Psi : \dot{\boldsymbol{\mathcal{I}}} + \partial_{\boldsymbol{g}_\theta}\Psi : \dot{\boldsymbol{g}}_\theta \tag{2.51}$$

Inserting equation 2.51 into 2.47, then local dissipation yields

$$\rho_d\mathscr{D}_{loc} = [J^{-1}\boldsymbol{P} - \rho_d\partial_{\boldsymbol{F}}\Psi] : \dot{\boldsymbol{F}} - \rho_d\partial_{\boldsymbol{\mathcal{I}}}\Psi : \dot{\boldsymbol{\mathcal{I}}} - \rho_d[\eta_e + \partial_\theta\Psi]\dot{\theta} - \rho_d\partial_{\boldsymbol{g}_\theta}\Psi : \dot{\boldsymbol{g}}_\theta \geq 0 \tag{2.52}$$

Equation 2.52 should be thermodynamically consistent by the following form

$$\begin{aligned} &\boldsymbol{P} - \rho_d\partial_{\boldsymbol{F}}\Psi = 0 \\ &\eta_e + \partial_\theta\Psi = 0 \\ &\partial_{\boldsymbol{g}_\theta}\Psi = 0\,, \end{aligned} \tag{2.53}$$

which are the main results of Coleman's method. It concludes that the free energy is a scalar potential for stress and entropy and does not depend on the temperature gradient. This relations are valid for arbitrary $\dot{\boldsymbol{F}}$, $\dot{\theta}$ and $\dot{\boldsymbol{g}}_\theta$. These variables are also called "external variables". Then the equation 2.52 reduces to the following form:

$$\rho_d\mathscr{D}_{loc} = \rho_d\partial_{\boldsymbol{\mathcal{I}}}\Psi : \dot{\boldsymbol{\mathcal{I}}} \geq 0 \tag{2.54}$$

Here, we introduce the $\boldsymbol{\beta} = -\rho_{d0}\partial_{\boldsymbol{\mathcal{I}}}\Psi$ as the thermodynamical force conjugate to the internal variable $\boldsymbol{\mathcal{I}}$ that determine viscoelasticity, plasticity, damage etc. through the flow rule. The internal variables are not coupled to any external force variable. It can be either scalar, vectorial or tensorial depending on its physical representation. For example, it can be a viscous strain in viscoelasticity, a plastic strain in plasticity, or a hardening related quantity, etc. Internal variable evolution is determined by a flow rule that is based on the constitutive evolution function and obeys the second law of thermodynamics.

CHAPTER 3

GOVERNING EQUATIONS OF THE INCOMPRESSIBLE HYPERELASTIC CONSTITUTIVE MODELING

The constitutive equations of the materials are described to reflect the physical response in a mathematical manner. It also defines the relationship between independent and dependent variables such as displacement and stress. Most of the constitutive models are constructed using a phenomenological approach, which takes the macro-behavior of the material into account, and the rest of the models are based on micro-mechanical models that are constructed on the micro-structure of the material by considering statistical mechanics. Materials with a nonlinear reversible response at large stains are covered by hyperelastic models. Mechanical behaviours of the many of critical materials can be captured by isotropic and anisotropic hyperelastic models. For example, soft biological tissues, rubber-like materials, composite materials, etc. Biological tissues are primarily composed of fibers that are remodelled along the loading direction and exhibit mechanical properties that differ from the base tissue matrix. It is significant to examine the mechanical behaviours of tissues to predict the pathological conditions and diseases. Therefore, there have been many mechanical characterization tests and numerical modeling studies for tissues such as the brain, aorta, liver, skin, eye, tongue, muscle, the heart, etc.

Hyperelastic constitutive equations can be determined either by using principal invariants or by using principal stretches in the Helmholtz free energy function. There are also detailed reviews of hyperelastic constitutive models by [108, 109, 22, 110, 111, 5]. Depending on the volumetric resistance of hyperelastic materials, they can be categorized as compressible and incompressible. Because most soft biological tissue is assumed to be incompressible, the main focus of this thesis will be on incompressible

hyperelasticity.

Elastomers, hydrogels, and soft tissues exhibit nearly incompressible hyperelastic mechanical behavior that can be characterized by a free energy density function. Fiber-reinforced soft matrix materials and biological tissues in the inextensibility limit exhibit nearly incompressible and inextensible mechanical responses. Thus, the development of efficient and robust finite element formulations in the quasi-inextensible and quasi-incompressible limits becomes significant. Hyperelastic materials exhibit stiff volumetric response compared to shear response caused by nearly incompressible behavior. Standard displacement-based formulations show poor convergence behavior and inaccurate results for incompressible materials. A similar problem has been revealed in the nearly inextensible limit due to the high stiffness in the fiber directions [112, 113, 104]. Mixed or hybrid element formulations based on variational formulations utilize additional independent variables such as stress or strain as Lagrange multipliers. In this context, we refer to the pioneering works of Pian et al. [114, 115], which were based on the Hellinger-Reissner formulation. These formulations improve the stress approximation of the standard displacement formulation. The mean dilatation formulation with *Q1P0* or *T2P0*-element based on Hu-Washizu type variational principle was introduced by Nagtegaal et al. [116] and extended to large-strain problems by Simo et al. [117]. It was implemented for hyperelastic materials within a nearly incompressible limit by Simo and Taylor [118]. In the element formulation, an additional term was embedded to the potential function as a constraint for the incompressibility [119], adopted in finite element implementation for visco-elastic materials [120], and a novel two-field mixed displacement-pressure formulation was presented by [121] that provides consistent results to three-field formulation. The use of dilatation formulations for fiber-reinforced rubberlike materials and fiber-reinforced soft tissues was presented in [122]. In the scope of this chapter, firstly isotropic hyperelasticity will be covered and some common used hyperelastic free-energy forms will be presented. Then, incompressible formulations will be introduced by volumetric and isochoric splitting. The anisotropic hyperelasticity will be described by one- and two-family fiber reinforcement. After that, a two-field variational formulation will be given to manage incompressibility in the numerical process. Then, a three-field Hu-Washizu formulation will be introduced with numerical

examples that provide comparisons of different finite element formulations. Later, a five-field variational formulation will be presented to cover both incompressibility and inextensibility at the same time. A numerical example of a dual-clamped patch test will be presented at the end of the chapter to compare available mixed elements in the literature.

3.1 Isotropic Hyperelasticity

In this sub-section, constitutive equations of isotropic hyperelasticity will be covered by the determination of stress and moduli from stored free-energy functions. Free-energy functions must be invariant under rigid body motions. Then the following equality must be fullfilled

$$\Psi(\boldsymbol{F}) = \Psi(\boldsymbol{C}) = \Psi(\boldsymbol{E}) \tag{3.1}$$

The free-energy function must be consistent with thermodynamical equilibrium which states that when $\boldsymbol{F} = \mathbf{1}$, the free-energy must be in global minimum which yields the normalization condition to zero energy. Another important aspect is maintaining the stress-free condition at $\boldsymbol{F} = \mathbf{1}$. Recall from equations 2.50, 2.51 and 2.52, stress measures ($\boldsymbol{P}$ and $\boldsymbol{S}$) are conjugate with time derivatives of deformation entities $\dot{\boldsymbol{F}}$ and $\dot{\boldsymbol{C}}$, respectively.

$$\dot{\Psi} = \boldsymbol{P} : \dot{\boldsymbol{F}} = \boldsymbol{S} : \dot{\boldsymbol{E}} \tag{3.2}$$

By using the relation of $\frac{1}{2}\dot{\boldsymbol{C}} = \dot{\boldsymbol{E}}$, the Helmholtz free-energy function and stress relations can be described by following:

$$\begin{aligned} \dot{\Psi} &= \frac{\partial \Psi}{\partial \boldsymbol{C}} : \dot{\boldsymbol{C}} = \frac{\boldsymbol{S}}{2} : \dot{\boldsymbol{C}} \qquad \text{and} \qquad \boldsymbol{S}(\boldsymbol{C}, \boldsymbol{X}) = 2\frac{\partial \Psi}{\partial \boldsymbol{C}} = \frac{\partial \Psi}{\partial \boldsymbol{E}} \\ \dot{\Psi} &= \frac{\partial \Psi}{\partial \boldsymbol{F}} : \dot{\boldsymbol{F}} = \boldsymbol{P} : \dot{\boldsymbol{F}} \qquad \text{and} \qquad \boldsymbol{P}(\boldsymbol{F}, \boldsymbol{X}) = \frac{\partial \Psi}{\partial \boldsymbol{F}} \end{aligned} \tag{3.3}$$

Then the two-point and Lagrangian elasticity moduli can be expressed as respectively,

$$\mathbb{A} = \frac{\partial \boldsymbol{P}}{\partial \boldsymbol{F}} = \frac{\partial^2 \Psi}{\partial \boldsymbol{F} \partial \boldsymbol{F}} \quad \text{and} \quad \mathbb{C} = 2\frac{\partial \boldsymbol{S}}{\partial \boldsymbol{C}} = 4\frac{\partial^2 \Psi}{\partial \boldsymbol{C} \partial \boldsymbol{C}} \tag{3.4}$$

where $\mathbb{A}$ and $\mathbb{C}$ are also called as tangent moduli for two-point and Lagrangian formulations and they are fourth order tensors. Stress and tangent moduli for the Eulerian

configuration can be determined by push-forward operations or alternatively it can be described by the derivative with respect to metric tensor $\boldsymbol{g}$ as following

$$\boldsymbol{\tau} = 2\frac{\partial \Psi}{\partial \boldsymbol{g}} \quad \text{and} \quad \mathbb{c} = 2\frac{\partial \boldsymbol{\tau}}{\partial \boldsymbol{g}} = 4\frac{\partial^2 \Psi}{\partial \boldsymbol{g} \partial \boldsymbol{g}} \tag{3.5}$$

Isotropic hyperelasticity exhibits the material response identical in any direction. Therefore the free-energy (Ψ) can be characterized by invariants of right Cauchy-Green tensor ($\boldsymbol{C}$) which is given in equation 2.13 in previous chapter. Then by using the chain rule the second Piola-Kirchhoff stress stated in equation 3.3 can be described by using invariants as following

$$\boldsymbol{S} = 2\frac{\partial \Psi}{\partial \boldsymbol{C}} = 2\frac{\partial \Psi}{\partial I_1}\frac{\partial I_1}{\partial \boldsymbol{C}} + 2\frac{\partial \Psi}{\partial I_2}\frac{\partial I_2}{\partial \boldsymbol{C}} + 2\frac{\partial \Psi}{\partial I_3}\frac{\partial I_3}{\partial \boldsymbol{C}} \tag{3.6}$$

Corresponding derivatives of invariants with respect to $\boldsymbol{C}$ defined as below

$$\frac{\partial I_1}{\partial \boldsymbol{C}} = \mathbf{1} \quad , \quad \frac{\partial I_2}{\partial \boldsymbol{C}} = I_1\mathbf{1} - \boldsymbol{C} \quad \text{and} \quad \frac{\partial I_3}{\partial \boldsymbol{C}} = I_3\boldsymbol{C}^{-1} = J^2\boldsymbol{C}^{-1} \tag{3.7}$$

By using using eqation 3.7 in 3.6, the definition of $\boldsymbol{S}$ can be written in terms of derivatives coefficients

$$\boldsymbol{S} = \hat{c_1}\mathbf{1} + \hat{c_2}\boldsymbol{C} + \hat{c_3}\boldsymbol{C}^{-1} \tag{3.8}$$

where the coefficients $\hat{c_1}$, $\hat{c_2}$ and $\hat{c_3}$ defined as

$$\hat{c_1} = 2\left(\frac{\partial \Psi}{\partial I_1} + I_1\frac{\partial \Psi}{\partial I_2}\right) \quad , \quad \hat{c_2} = 2\frac{\partial \Psi}{\partial I_2} \quad , \quad \hat{c_3} = 2I_3\frac{\partial \Psi}{\partial I_3} \tag{3.9}$$

Corresponding invariants can also be determined in Eulerian space by using left Cauchy Green tensor ($\boldsymbol{b}$) such as

$$\boldsymbol{\tau} = 2\frac{\partial \Psi}{\partial \boldsymbol{g}} = 2\frac{\partial \Psi}{\partial I_{\boldsymbol{b}1}}\frac{\partial I_{\boldsymbol{b}1}}{\partial \boldsymbol{g}} + 2\frac{\partial \Psi}{\partial I_{\boldsymbol{b}2}}\frac{\partial I_{\boldsymbol{b}2}}{\partial \boldsymbol{g}} + 2\frac{\partial \Psi}{\partial I_{\boldsymbol{b}3}}\frac{\partial I_{\boldsymbol{b}3}}{\partial \boldsymbol{g}} \tag{3.10}$$

Corresponding derivatives of invariants of left Cauchy Green tensor ($I_{\boldsymbol{b}1}$, $I_{\boldsymbol{b}2}$ and $I_{\boldsymbol{b}3}$) with respect to metric tensor $\boldsymbol{g}$ defined as below

$$\frac{\partial I_{\boldsymbol{b}1}}{\partial \boldsymbol{g}} = \boldsymbol{b} \quad , \quad \frac{\partial I_{\boldsymbol{b}2}}{\partial \boldsymbol{g}} = I_{\boldsymbol{b}1}\boldsymbol{b} - \boldsymbol{b}^2 \quad \text{and} \quad \frac{\partial I_{\boldsymbol{b}3}}{\partial \boldsymbol{g}} = J^2\boldsymbol{g}^{-1} \tag{3.11}$$

Then Kirchhoff stress yields to

$$\boldsymbol{\tau} = \hat{b_1}\boldsymbol{b} + \hat{b_2}\boldsymbol{b}^2 + \hat{b_3}\boldsymbol{g}^{-1} \tag{3.12}$$

where the Eulerian coefficients $\hat{b_1}$, $\hat{b_2}$ and $\hat{b_3}$ defined as

$$\hat{b_1} = 2\left(\frac{\partial \Psi}{\partial I_{\boldsymbol{b}1}} + I_{\boldsymbol{b}1}\frac{\partial \Psi}{\partial I_{\boldsymbol{b}2}}\right) \quad , \quad \hat{b_2} = -2\frac{\partial \Psi}{\partial I_{\boldsymbol{b}2}} \quad , \quad \hat{b_3} = 2I_{\boldsymbol{b}3}\frac{\partial \Psi}{\partial I_{\boldsymbol{b}3}} \tag{3.13}$$

One of the general basic example for the isotropic hyperelasticity, which also considers the compressibility, is the compressible Neo-Hookean free-energy function as presented below

$$\Psi = \frac{\mu}{2}(I_1 - 3) - \mu \ln J + \frac{\lambda}{2}(\ln J)^2 \tag{3.14}$$

where μ and λ are the specific material constants such as shear modulus and Lame constant. Notice that, when there is no deformation ($\boldsymbol{C} = \mathbf{1}$) or there is only rigid body motion acts on the solid, the free energy does not store any energy and becomes zero. That result can also be examined by checking the equation 3.14 within ingredients such as $J = \det \boldsymbol{F} = 1$ making $\ln J$ is zero and $I_1 = 3$ which makes the first term is zero. Then the second Piola-Kirchhoff stress can be determined by equation 3.6 as below

$$\boldsymbol{S} = \mu(\mathbf{1} - \boldsymbol{C}^{-1}) + \lambda(\ln J)\boldsymbol{C}^{-1} \tag{3.15}$$

The Kirchhoff stress alternatively can be determined by push-forward of $\boldsymbol{S}$ as following

$$\boldsymbol{\tau} = \boldsymbol{F}\boldsymbol{S}\boldsymbol{F}^T = \mu(\boldsymbol{b} - \boldsymbol{g}^{-1}) + \lambda(\ln J)\boldsymbol{g}^{-1} \tag{3.16}$$

Cauchy stress can be also obtained by $\boldsymbol{\sigma} = \boldsymbol{\tau}/J$. Then Lagrangian tangent moduli can be determined by equation 3.4

$$\mathbb{C} = \lambda \boldsymbol{C}^{-1} \otimes \boldsymbol{C}^{-1} + 2(\mu - \lambda \ln J)\mathbb{I}_{\boldsymbol{C}^{-1}} \tag{3.17}$$

where $\mathbb{I}_{\boldsymbol{C}^{-1}}$ is the fourth-order geometric transformation tensor defined as,

$$\mathbb{I}_{\mathbf{C}^{-1}} := \frac{1}{2}\left(\mathbf{C}^{-1}\overline{\otimes}\mathbf{C}^{-1} + \mathbf{C}^{-1}\underline{\otimes}\mathbf{C}^{-1}\right) . \tag{3.18}$$

where non-standard tensor products can be defined as $[\bullet\overline{\otimes}\circ]_{ijkl} = [\bullet]_{ik}[\circ]_{jl}$ and $[\bullet\underline{\otimes}\circ]_{ijkl} = [\bullet]_{il}[\circ]_{jk}$. By push-forward operation of Lagrangian tangent moduli $\mathbb{C}$, the Eulerian tangent moduli can be found as following

$$\mathbb{c} = \frac{\lambda}{J}\boldsymbol{g}^{-1} \otimes \boldsymbol{g}^{-1} + \frac{2}{J}(\mu - \lambda \ln J)\mathbb{I} \tag{3.19}$$

where $\mathbb{I}$ is the fourth-order identity tensor and defined by indicial notation as below

$$\mathbb{I}_{ijkl} = \frac{1}{2}\left(\delta_{ik}\delta_{jl} + \delta_{il}\delta_{jk}\right) \tag{3.20}$$

3.2 Incompressible Hyperelasticity

Some materials (such as the majority of soft biological tissues) exhibit shape change rather than volume change. The materials that preserve their initial volume during a loading are called incompressible materials. They can be deformed in an isochoric way. In the invariant based free-energy formulations, while I_1 is responsible for isochoric deformations, $I_3 = J^2$ is responsible for volumetric deformations. For the volume preserving materials, the incompressibility constraint is covered by $J = 1$. Due to the fact that, in the next sections of this chapter, the main focus will be on constitutive modeling of the incompressible hyperelasticity.

The incompressibility can be treated as near-incompressible or quasi-incompressible in numerical solutions to avoid numerical difficulties since, when the Poisson's ratio (ν) approach to 0.5, the bulk modulus (κ) of the material goes to infinity. Due to the order of magnitude difference between the shear and bulk responses of the material, it is convenient to split the deformation into volumetric and isochoric parts [123] as follows:

$$\boldsymbol{F} = \boldsymbol{F}_{vol}\bar{\boldsymbol{F}} \quad \text{where} \quad \boldsymbol{F}_{vol} = J^{1/3}\mathbf{1} \quad \text{and} \quad \bar{\boldsymbol{F}} = J^{-1/3}\boldsymbol{F}, \tag{3.21}$$

In the same manner, the volumetric and unimodular part of the right Cauchy Green tensor can be defined as

$$\boldsymbol{C}_{vol} = \boldsymbol{F}_{vol}^T\boldsymbol{F}_{vol} \quad , \quad \bar{\boldsymbol{C}} = \bar{\boldsymbol{F}}^T\bar{\boldsymbol{F}} \quad \text{and} \quad \bar{\boldsymbol{C}} = J^{2/3}\boldsymbol{C}. \tag{3.22}$$

Isotropic hyperelasticity is formulated based on the free energy function, which is defined per unit reference volume through isotropic invariants I_1, I_2, I_3 that are constitutively related to the deformation gradient. For incompressible materials, two of the invariants I_1, I_2 are sufficient to be used in the formulation. The invariant formulation of hyperelasticity is described by the following unimodular isotropic invariants

$$\bar{I}_1 = \operatorname{tr}\bar{\mathbf{C}}\,, \quad \bar{I}_2 = \frac{1}{2}\left[(\operatorname{tr}\bar{\mathbf{C}})^2 - \operatorname{tr}(\bar{\mathbf{C}}^2)\right]\,, \quad \text{and} \quad \bar{I}_3 = \det\bar{\mathbf{C}} = 1\,, \tag{3.23}$$

Then, the free energy function can also be written based on multiplicative decomposition of volumetric and isochoric parts as following

$$\Psi(\boldsymbol{C}) = \Psi_{vol}(\boldsymbol{C}_{vol}) + \Psi_{iso}(\bar{\boldsymbol{C}}) \quad \text{or} \quad \Psi(\boldsymbol{F}) = \Psi_{vol}(\boldsymbol{F}_{vol}) + \Psi_{iso}(\bar{\boldsymbol{F}}), \tag{3.24}$$

In alternative form, the free-energy decomposition is written as

$$\Psi(\boldsymbol{C}) = \Psi_{vol}(J) + \Psi_{iso}(\bar{I}_1,\bar{I}_2) \tag{3.25}$$

Now, Lagrangian and Eulerian configurations of stress and tangent moduli can be obtained based on the volumetric and isochoric split of deformation gradient $\boldsymbol{F}$ in following subsections.

3.2.1 Lagrangian configuration

The second-Piola Kirchhoff stress can be decomposed of

$$\boldsymbol{S} = 2\partial_{\boldsymbol{C}}\Psi = \boldsymbol{S}_{vol} + \boldsymbol{S}_{iso} \tag{3.26}$$

In line with the equation 3.26, the elastic Lagrangian moduli $\mathbb{C}$, can be additively split into volumetric, and isotropic parts respectively.

$$\mathbb{C} = 2\partial_{\boldsymbol{C}}\boldsymbol{S} = 4\partial_{\boldsymbol{C}\boldsymbol{C}}\Psi = \mathbb{C}_{vol} + \mathbb{C}_{iso} \tag{3.27}$$

The volumetric part of the second Piola-Kirchhoff stress $\boldsymbol{S}_{vol}$ reads

$$\boldsymbol{S}_{vol} := 2\partial_{\boldsymbol{C}}\Psi_{vol}(J) = 2\Psi'_{vol}(J)\partial_{\boldsymbol{C}}J \quad \text{where} \quad \partial_{\boldsymbol{C}}J = \frac{1}{2}J\boldsymbol{C}^{-1}, \tag{3.28}$$

Then the volumetric part of the second Piola-Kirchhoff stress can be rewritten as

$$\boldsymbol{S}_{vol} := J\Psi'_{vol}(J)\boldsymbol{C}^{-1} \quad \text{where} \quad p := J\Psi'_{vol}(J) \tag{3.29}$$

where p is the internal pressure term and Ψ'_{vol} is the derivative of volumetric part of the free-energy Ψ_{vol} with respect to J. The Lagrangian moduli expression for the volumetric part is determined as

$$\mathbb{C}_{vol} := 2\partial_{\boldsymbol{C}}\boldsymbol{S}_{vol}(J) = (p + \hat{\kappa}_L)\boldsymbol{C}^{-1} \otimes \boldsymbol{C}^{-1} - 2p\mathbb{I}_{\boldsymbol{C}^{-1}}\,, \tag{3.30}$$

where $\hat{\kappa}_L = J^2\psi''_{vol}(J)$, $\mathbb{I}^{ABCD}_{\boldsymbol{C}^{-1}} = \frac{1}{2}\left[\boldsymbol{C}^{-1}_{AC}\boldsymbol{C}^{-1}_{BD} + \boldsymbol{C}^{-1}_{AD}\boldsymbol{C}^{-1}_{BC}\right]$ and $\psi''_{vol}(J)$ is the second derivative of the volumetric energy function with respect to J. The isochoric part of the second Piola-Kirchhoff stress is obtained as

$$\boldsymbol{S}_{iso} := 2\partial_{\boldsymbol{C}}\psi_{iso}(\bar{\boldsymbol{C}}) = 2\partial_{\bar{\boldsymbol{C}}}\psi_{iso}(\bar{\boldsymbol{C}}) : \partial_{\bar{\boldsymbol{C}}}\bar{\boldsymbol{C}} \tag{3.31}$$

Equation 3.31 can be written explicitly as following

$$\begin{aligned} &\boldsymbol{S}_{iso} := \bar{\boldsymbol{S}} : \mathbb{Q} \quad \text{where} \quad \bar{\boldsymbol{S}} = 2\partial_{\bar{\boldsymbol{C}}}\psi_{iso}(\bar{\boldsymbol{C}}) \\ &\text{and} \quad \mathbb{Q} = \partial_{\bar{\boldsymbol{C}}}\bar{\boldsymbol{C}} = J^{-2/3}\left[\mathbb{I} - \frac{1}{3}\boldsymbol{C}\otimes\boldsymbol{C}^{-1}\right] \end{aligned} \tag{3.32}$$

Then, the Lagrangian moduli for the isotropic response can be expressed as

$$\mathbb{C}_{iso} := 4\partial^2_{\boldsymbol{CC}}\Psi_{iso} = 2\partial_{\boldsymbol{C}}(\bar{\boldsymbol{S}} : \mathbb{Q}) \tag{3.33}$$

The isochoric Lagrangian moduli can be expressed more explicitly such as

$$\begin{aligned} &\mathbb{C}_{iso} := \mathbb{Q}^T : \mathbb{C} : \mathbb{Q} + \bar{\boldsymbol{S}} : \mathbb{H} \quad \text{where} \quad \mathbb{Q} = \frac{\partial\bar{\boldsymbol{C}}}{\partial\boldsymbol{C}} \quad \text{and} \quad \mathbb{H} = 2\frac{\partial\mathbb{Q}}{\partial\boldsymbol{C}} \\ &\text{with} \quad \bar{\boldsymbol{S}} : \mathbb{H} = \frac{2}{3}(\bar{\boldsymbol{S}} : \bar{\boldsymbol{C}})\mathbb{P}_{\boldsymbol{C}^{-1}} - \frac{2}{3}\left[\boldsymbol{S}_{iso}\otimes\boldsymbol{C}^{-1} + \boldsymbol{C}^{-1}\otimes\boldsymbol{S}_{iso}\right] \end{aligned} \tag{3.34}$$

and the fourth-order projection tensor is $\mathbb{P}_{\boldsymbol{C}^{-1}} = \mathbb{I}_{\boldsymbol{C}^{-1}} - (1/3)\boldsymbol{C}^{-1}\otimes\boldsymbol{C}^{-1}$.

3.2.2 Eulerian configuration

The Kirchhoff stress can be decomposed of

$$\boldsymbol{\tau} = 2\partial_{\boldsymbol{g}}\Psi = \boldsymbol{\tau}_{vol} + \boldsymbol{\tau}_{iso} \tag{3.35}$$

The volumetric part of Kirchhoff stress $\boldsymbol{\tau}_{vol}$ can be determined by the push-forward operation such as

$$\boldsymbol{\tau}_{vol} = \boldsymbol{F}\boldsymbol{S}_{vol}\boldsymbol{F}^T = p\boldsymbol{g}^{-1} \tag{3.36}$$

The Eulerian tangent moduli expression for the volumetric part is defined as

$$\mathbb{c}_{vol} := 4\partial^2_{\boldsymbol{gg}}\Psi_{vol} = (p+\hat{\kappa})\boldsymbol{g}^{-1}\otimes\boldsymbol{g}^{-1} - 2p\mathbb{I}\,, \quad \text{with} \quad \hat{\kappa} = J^2\psi''_{vol}(J)\,. \tag{3.37}$$

Then, the isochoric part of the Kirchhoff stress can be defined as

$$\boldsymbol{\tau}_{iso} = \boldsymbol{F}\boldsymbol{S}_{iso}\boldsymbol{F}^T = 2\partial_{\boldsymbol{g}}\Psi_{iso}(\boldsymbol{g};\boldsymbol{F}) = \bar{\boldsymbol{\tau}} : \mathbb{P} \quad \text{where} \quad \bar{\boldsymbol{\tau}} = 2\partial_{\boldsymbol{g}}\Psi_{iso}(\boldsymbol{g};\bar{\boldsymbol{F}}) \tag{3.38}$$

After some mathematical operations, equation 3.38 is simplified to

$$\boldsymbol{\tau}_{iso} = \hat{k}\text{dev}\bar{\boldsymbol{b}} \quad \text{where} \quad \hat{k} = 2\partial_{\bar{I}_1}\Psi_{iso} \tag{3.39}$$

Lastly, by using the equation 3.5 the isochoric part of the Eulerian tangent moduli can be determined as following

$$\mathbb{c}_{iso} = \mathbb{P} : \left[\bar{\mathbb{c}} + \frac{2}{3}(\bar{\boldsymbol{\tau}} : \boldsymbol{g})\mathbb{I} - \frac{2}{3}(\hat{\boldsymbol{\tau}}\otimes\boldsymbol{g}^{-1} + \boldsymbol{g}^{-1}\otimes\bar{\boldsymbol{\tau}})\right] : \mathbb{P}^T \tag{3.40}$$

3.2.3 Commonly used isotropic incompressible hyperelastic constitutive models

There are a variety of types of hyperelastic constitutive models in the literature; those are mostly used for specific kinds of material responses. Not only rubber-like materials, but also biological tissues, are composed of an isotropic response matrix that also creates connections and supports the oriented specific components, such as fibers. In order to reflect the mechanical response of the base matrix material, it is necessary to define an isotropic contribution of free-energy function. The neo-Hookean free-energy function, which is described below, is one of the simplest isotropic hyperleastic constitutive models.

$$\Psi = \frac{1}{2}\mu(I_1 - 3) \tag{3.41}$$

where μ is the shear modulus of the material. It provides a good accuracy in low-medium strain limits. Another common model is Mooney-Rivlin that considers both invariants I_1 and I_2 as following

$$\Psi = \mu_{10}(I_1 - 3) + \mu_{01}(I_2 - 3) \tag{3.42}$$

where μ_{10} and μ_{01} are material constants. It is the extended version of neo-Hookean model. The another important hyperlelastic model is Yeoh model that uses polynomials of the first invariant and expressed as

$$\Psi = C_{10}(I_1 - 3) + C_{20}(I_1 - 3)^2 + C_{30}(I_1 - 3)^3 \tag{3.43}$$

where C_{10}, C_{20} and C_{30} are material constants. Then, Ogden model is defined based on the principal stretches as following

$$\Psi = \sum_{p=1}^{N} \frac{\mu_p}{\alpha_p}(\lambda_1^{\alpha_p} + \lambda_2^{\alpha_p} + \lambda_3^{\alpha_p} - 3) \tag{3.44}$$

where μ_p and α_p are number of material constants depending the value of N.

3.3 Anisotropic Hyperelasticity

Most of the biological tissues and plants are not homogeneous, but they are composed of different kinds of ingredients that exhibit different mechanical properties.

These composite structures can be either layered-type layouts, embedded fibers on a softer ground matrix, or both types. Some of the important examples are; the heart, the artery, the skin, a leaf, etc. These type of composite structures may behave anisotropic, orthotropic and transversely isotropic depending on the mechanical layout. Therefore, it is necessary to define anisotropic mechanical response in the free-energy function. The anisotropy can be in a single direction or it can be in three distinct directions. In order to represent an anisotropic response, there are defined anisotropic invariants in equations 2.16 and 2.17. Then corresponding free-energy function is described by the following form:

$$\Psi(\boldsymbol{g};\boldsymbol{F},\boldsymbol{n}_0,\boldsymbol{m}_0) := \psi_{vol}(J) + \Psi_{iso}(\boldsymbol{g};\boldsymbol{F}) + \Psi_{ani}(\boldsymbol{g};\boldsymbol{F},\boldsymbol{n}_0,\boldsymbol{m}_0) \tag{3.45}$$

where Ψ_{ani} is the energy stored of anisotropic contributions and $\boldsymbol{n}_0$, $\boldsymbol{m}_0$ are the unit vectors for the direction of anisotropy for two-family fibers. For anisotropic materials, there are also anisotropic contributions of stresses and moduli similar to equation 3.45. Stress and tangent moduli relations of volumetric and isochoric parts are already given in the previous section. Therefore, only anisotropic stress and moduli expressions will be summarized here. For two-family fiber contributions, the anisotropic part of the second Piola-Kirchhoff stress and the corresponding anisotropic tangent moduli are defined below

$$\begin{aligned}
\boldsymbol{S}_{ani,4} &= 2\frac{\partial\Psi_{ani}}{\partial\boldsymbol{C}} = 2\frac{\partial\Psi_{ani}}{\partial I_4}\frac{\partial I_4}{\partial\boldsymbol{C}} = 2\Psi'\boldsymbol{n}_0\otimes\boldsymbol{n}_0\\
\boldsymbol{S}_{ani,6} &= 2\frac{\partial\Psi_{ani}}{\partial\boldsymbol{C}} = 2\frac{\partial\Psi_{ani}}{\partial I_6}\frac{\partial I_6}{\partial\boldsymbol{C}} = 2\Psi'\boldsymbol{m}_0\otimes\boldsymbol{m}_0\\
\mathbb{C}_{ani,4} &= 2\frac{\partial\boldsymbol{S}_{ani,4}}{\partial\boldsymbol{C}} = 2\frac{\partial\boldsymbol{S}_{ani,4}}{\partial I_4}\frac{\partial I_4}{\partial\boldsymbol{C}} = 4\Psi''\boldsymbol{n}_0\otimes\boldsymbol{n}_0\otimes\boldsymbol{n}_0\otimes\boldsymbol{n}_0\\
\mathbb{C}_{ani,6} &= 2\frac{\partial\boldsymbol{S}_{ani,4}}{\partial\boldsymbol{C}} = 2\frac{\partial\boldsymbol{S}_{ani,6}}{\partial I_6}\frac{\partial I_6}{\partial\boldsymbol{C}} = 4\Psi''\boldsymbol{m}_0\otimes\boldsymbol{m}_0\otimes\boldsymbol{m}_0\otimes\boldsymbol{m}_0
\end{aligned} \tag{3.46}$$

where the subscripts 4 and 6 represent the two distinct direction of fibers. Similarly, Eulerian stress and moduli expressions are defined as below

$$\begin{aligned}
\boldsymbol{\tau}_{ani,4} &= 2\frac{\partial\Psi_{ani}}{\partial\boldsymbol{g}} = 2\frac{\partial\Psi_{ani}}{\partial I_4}\frac{\partial I_4}{\partial\boldsymbol{g}} = 2\Psi'\boldsymbol{n}\otimes\boldsymbol{n}\\
\boldsymbol{\tau}_{ani,6} &= 2\frac{\partial\Psi_{ani}}{\partial\boldsymbol{g}} = 2\frac{\partial\Psi_{ani}}{\partial I_6}\frac{\partial I_6}{\partial\boldsymbol{g}} = 2\Psi'\boldsymbol{m}\otimes\boldsymbol{m}\\
\mathbb{c}_{ani,4} &= 2\frac{\partial\boldsymbol{S}_{ani,4}}{\partial\boldsymbol{g}} = 2\frac{\partial\boldsymbol{S}_{ani,4}}{\partial I_4}\frac{\partial I_4}{\partial\boldsymbol{g}} = 4\Psi''\boldsymbol{n}\otimes\boldsymbol{n}\otimes\boldsymbol{n}\otimes\boldsymbol{n}\\
\mathbb{c}_{ani,6} &= 2\frac{\partial\boldsymbol{S}_{ani,4}}{\partial\boldsymbol{g}} = 2\frac{\partial\boldsymbol{S}_{ani,6}}{\partial I_6}\frac{\partial I_6}{\partial\boldsymbol{g}} = 4\Psi''\boldsymbol{m}\otimes\boldsymbol{m}\otimes\boldsymbol{m}\otimes\boldsymbol{m}
\end{aligned} \tag{3.47}$$

Since most of the soft biological tissues include fibrous structures that are embedded in the isotropic ground matrix, there should be a defined anisotropic contribution of free-energy in addition to the isotropic response. As it is already stated in equation 3.45, isotropic part of the free-energy (volumetric and isochoric parts) are the same as the free-energies that were introduced in the previous section. In other words, as a isotropic ground matrix material, one of the isotropic free-energy can be preferred according to the physics of the material. Then, the anisotropic contribution is summed up with the isotropic part with a different form of energy function. Some of anisotropic free-energy forms those are common used in biological tissues are summarized below [5]. The one of the developed model by Holzapfel et al. [124] for the artery, which is in exponential form in anisotropic free-energy and only carries load in the tension direction, is as follows:

$$\Psi_{ani}(I_4, I_6) = \frac{k_1}{2k_2} \sum_{i=4,6} \left(\exp[k_2 \langle I_i - 1\rangle^2] - 1\right) \tag{3.48}$$

where k_1 and k_2 are material parameters those need to be determined from experiments. Macaulay brackets $\langle \bullet \rangle$ represents the tension-only behaviour. An extended version of this model proposed by Holzapfel et al. [125]. The extended model includes the first invariant I_1 contribution in the anisotropic part as follows

$$\Psi_{ani}(I_1, I_4) = \text{sgn}\langle I_4 - 1\rangle \frac{k_1}{k_2} \left(\exp(k_2[(1-p_c)(I_1-3)^2 + p_c\langle I_4 - 1\rangle^2]) - 1\right) \tag{3.49}$$

where p_c is a type of transition parameter as $0 \leq p_c \leq 1$ which regulates the anisotropy degree of the free-energy. Another specific anisotropic free-energy form has been developed by Holzapfel et al. [106] to represent the orthotropic response of myocardium tissue. It is in exponential form and also takes the eighth invariant into account which is the coupling effect between two distinct directions as shown below

$$\begin{aligned} \Psi_{ani} &= \frac{a}{2b}\exp[b(I_1-3)] - 1 + \sum_{i=f,s} \frac{a_i}{2b_i}\left(\exp[b_i(I_{4i}-1)^2] - 1\right) \\ &+ \frac{a_{fs}}{2b_{fs}}\left(\exp[b_{fs} I_{8fs}^2] - 1\right), \end{aligned} \tag{3.50}$$

where notations f and s refers to two distinct direction in myocardium tissue called as fiber and sheet directions respectively.

3.4 Two-Field Formulation

It is common in the variational methodology to determine equilibrium equations via a directional derivative and obtain the stationary condition of the energy potential. If it is performed for a single variable as displacement, it yields standard displacement-based finite element formulations, however if it contains more variable such as additional internal pressure degree of freedom leads to mixed variational formulation. It is a common approach to treating numerical difficulties, such as volumetric locking due to incompressibility, by using mixed finite element formulations. Therefore, introducing internal pressure as a penalty parameter is a well-known method to be used in quasi-incompressible problems, and it requires additional discretization and interpolation for the additional variable. If there is one additional variable taken into account, then it yields a two-field finite element formulation.

Soft biological tissues exhibit high resistance to volume change and low resistance to isochoric changes as a result of a high ratio of bulk modulus to shear modulus [107]. It has been shown that incompressible materials deform in an isochoric way. Therefore, it is necessary to apply a numerical treatment to overcome the locking fact by using mixed formulations. In this situation, the volume-preserving constraint should be enforced as $J = 1$ by penalty parameter. The potential functional of hyperelasticity can be defined by the following variational form

$$\hat{\Pi}(\boldsymbol{\phi}, p) := \hat{\Pi}^{int}(\boldsymbol{\phi}) - \hat{\Pi}^{ext}(\boldsymbol{\phi}) + \int_V p(J-1)dV \,, \tag{3.51}$$

where p is the penalty parameter and defined as the internal pressure. Then the internal potential functional is described as

$$\hat{\Pi}^{int}(\boldsymbol{\phi}) := \int_V \Psi(\boldsymbol{g}, \bar{\boldsymbol{F}})\, dV \tag{3.52}$$

and the external potential function is defined by

$$\hat{\Pi}^{ext}(\boldsymbol{\phi}) := \int_V \boldsymbol{\phi} \cdot \rho_0 \bar{\boldsymbol{b}}\, dV + \int_{\partial V} \boldsymbol{\phi} \cdot \bar{\boldsymbol{t}}\, dA \tag{3.53}$$

where $\bar{\boldsymbol{b}}$ is the body force acting to the volume of the body and $\bar{\boldsymbol{t}}$ is the surface traction. By variation of equation (3.51), the stationary conditions can be determined which also yield Euler-Lagrange equations. And then, linearization of these equations yields finite element formulations. As a first step, the stationary condition with respect to

independent variables $\boldsymbol{\phi}$ and p can be obtained by the directional derivatives of the potential functional in the direction of $\delta\boldsymbol{\phi}$ and δp separately. Then the Euler-Lagrange equations are determined as follows:

$$
\begin{aligned}
D\hat{\Pi}(\boldsymbol{\phi},p)[\delta\boldsymbol{\phi}] &= \int_V \left(\left(\boldsymbol{\tau}^{iso} + pJ\boldsymbol{g}^{-1}\right) : \text{sym}(\boldsymbol{g}\nabla_x\delta\boldsymbol{\phi}\right)\, dV - \delta\hat{\Pi}^{ext}(\boldsymbol{\phi}) = 0\,, \\
D\hat{\Pi}(\boldsymbol{\phi},p)[\delta p] &= \int_V \delta p\,(J-1)\,dV = 0\,,
\end{aligned}
\tag{3.54}
$$

where the first term in equation (3.54) contains nonlinearity, and the second term enforce the incompressibility constraint. In a similar way, $(3.54)_1$ can be also written in the Lagrangian configuration as follows

$$
D\hat{\Pi}(\boldsymbol{\phi},p)[\delta\boldsymbol{\phi}] = \int_V \boldsymbol{S}' : D\boldsymbol{E}[\delta\boldsymbol{\phi}]dV + \int_V Jp\text{div}\delta\boldsymbol{\phi}dV - \delta\hat{\Pi}^{ext}(\boldsymbol{\phi}) = 0 \tag{3.55}
$$

The nonlinearity requires a Newton-Raphson solution. Therefore equation (3.54) should be linearized in the direction of increments of $\Delta\boldsymbol{\phi}$ and Δp for both variables $\boldsymbol{\phi}$ and p. The second variation provides the following linearized form

$$
\begin{aligned}
D^2\hat{\Pi}(\boldsymbol{\phi},p)[\delta\boldsymbol{\phi},\delta\boldsymbol{\phi}] &= \int_V \boldsymbol{g}\nabla_x\Delta\boldsymbol{\phi} : \left(\nabla_x\Delta\boldsymbol{\phi}\left(\tau^{iso} + pJ\boldsymbol{g}^{-1}\right)\right) dV \\
&+ \int_V \boldsymbol{g}\nabla_x\delta\boldsymbol{\phi} : \left(pJ\left(\boldsymbol{g}^{-1}\otimes\boldsymbol{g}^{-1} - 2\mathbb{I}_{\boldsymbol{g}^{-1}}\right) + \mathbb{C}^{iso}\right) \\
&: \boldsymbol{g}\nabla_x\Delta\boldsymbol{\phi}dV
\end{aligned}
\tag{3.56}
$$

The consistent linearization of two-field variational formulation stated in equation (3.56) can also be written in the Lagrangian configuration as below

$$
\begin{aligned}
D^2\hat{\Pi}(\boldsymbol{\phi},p)[\delta\boldsymbol{\phi},\Delta\boldsymbol{\phi}] &= \int_V D\boldsymbol{E}\delta\boldsymbol{\phi} : \left(\mathbb{C}^{iso} + pJ\left(\boldsymbol{C}^{-1}\otimes\boldsymbol{C}^{-1} - 2\mathbb{I}\right)\right) \\
&: D\boldsymbol{E}\Delta\boldsymbol{\phi}dV + \int_V \boldsymbol{S} : \left((\nabla_X\Delta\boldsymbol{\phi})^T(\nabla_X\delta\boldsymbol{\phi})\right) dV
\end{aligned}
\tag{3.57}
$$

In general, discontinuous (constant over element) pressure field and continuous (order of 1 or order of 2) polynomial interpolations for the displacement field are used in the mixed formulations.

3.5 Three-Field Formulation

Although there is a treatment for the volumetric locking phenomenon by imposing a two-field mixed formulation, as mentioned in the previous section, a constant pressure definition over the element causes pressure osculations [107]. Therefore, definition of an additional third independent variable, such as volume changing (dilatation) Θ, yields more efficient three-field mixed formulation. This principle is also known as Hu-Washizu variational formulation, and this methodology is widely accepted and commonly used in the literature. Although there is a third independent variable introduced in the Hu-Washizu formulation, the resultant finite element formulations are called $Q1P0$ or $T2P0$. The newly kinematic variable θ is included into the functional as a constraint. In a similar manner to the two-field formulation, the potential functional can be written as

$$\hat{\Pi}(\boldsymbol{\phi}, p) := \hat{\Pi}^{int}(\boldsymbol{\phi}) - \hat{\Pi}^{ext}(\boldsymbol{\phi}) + \int_V p(\theta - J) dV + \int_V \Psi_{vol}(\theta) dV \,, \tag{3.58}$$

where Π^{int} and Π^{ext} are defined in equations (3.52) and (3.53). Then the stationary conditions with respect to $\boldsymbol{\phi}$, J and θ yield to weak forms as following

$$\begin{aligned}
D\hat{\Pi}(\boldsymbol{\phi}, p)[\delta\boldsymbol{\phi}] &= \int_V \left(\left(\boldsymbol{\tau}^{iso} + pJ\boldsymbol{g}^{-1} \right) : \text{sym}(\boldsymbol{g}\nabla_x \delta\boldsymbol{\phi} \right) \, dV - \delta\hat{\Pi}^{ext}(\boldsymbol{\phi}) = 0 \,, \\
D\hat{\Pi}(\boldsymbol{\phi}, p)[\delta p] &= \int_V \delta p \, (J - \theta) \, dV = 0 \,, \\
D\hat{\Pi}(\boldsymbol{\phi}, p)[\delta\theta] &= \int_V \delta\theta (\Psi'_{vol}(\theta) - p) \, dV = 0 \,,
\end{aligned} \tag{3.59}$$

Consistent linearization with respect to $\boldsymbol{\phi}$ leads

$$\begin{aligned}
D^2\hat{\Pi}(\boldsymbol{\phi}, p)[\delta\boldsymbol{\phi}, \Delta\boldsymbol{\phi}] &= \int_V \boldsymbol{g}\nabla_x \delta\boldsymbol{\phi} : \left(\nabla_x \Delta\boldsymbol{\phi} \left(\tau^{iso} + pJ\boldsymbol{g}^{-1} \right) \right) dV \\
&+ \int_V \boldsymbol{g}\nabla_x \delta\boldsymbol{\phi} : \left(pJ \left(\boldsymbol{g}^{-1} \otimes \boldsymbol{g}^{-1} - 2\mathbb{I}_{\boldsymbol{g}^{-1}} \right) + \mathbb{C}^{iso} \right) \\
&: \boldsymbol{g}\nabla_x \Delta\boldsymbol{\phi} dV + \int_V J\boldsymbol{g}\nabla_x \delta\boldsymbol{\phi} : \boldsymbol{g}^{-1} \Delta p dV
\end{aligned} \tag{3.60}$$

The Lagrange multiplier and internal pressure term p and the mean dilatation θ can be defined constant over an element as below

$$\begin{aligned} \bar{\theta} &= \frac{1}{V}\int_B J dV = \frac{V_0}{V}, \\ \bar{p} &= \frac{1}{V}\int_B \Psi'_{vol} dV, \end{aligned} \tag{3.61}$$

Then the incremental forms leads

$$\begin{aligned} \Delta\bar{\theta} &= \frac{1}{V}\int_B J\boldsymbol{g}^{-1} : \boldsymbol{g}\nabla_x \Delta\boldsymbol{\phi} dV, \\ \Delta\bar{p} &= \Psi''_{vol}\Delta\bar{\theta} dV, \end{aligned} \tag{3.62}$$

Pluging of the incremental forms defined in equation 3.62 into 3.60 gives the final form of the linearization. For the interested researcher, see [107] and [126] for the detailed background of the intermediate steps of the derivations.

Cook's Membrane - Two-field and Three-field element comparison

In order to test different mixed element formulations in FEniCS [12], a benchmark problem has been performed. In the numerical applications, Cook's Membrane geometry was preferred which is generally used for patch tests of mixed formulations under both bending and shear [127], [128], [129], [130] and [131]. Finite element mesh of the geometry was created in ANSYS Mechanical and it was transferred to FEniCS by .xml format. It is also possible to create mesh in FEniCS by using simple geometries such as box, sphere etc. However, relatively complex mesh should be imported from another commercial pre-processing platform. Since tetrahedron elements in FEniCS were validated in terms of stability and accuracy, therefore these types of elements are preferred in the analysis. Two distinct finite element models were generated, each with a different mesh size setting per each edges. The goal is to compare alternative mixed element formulations with the same boundary conditions in two different mesh sizes. The membrane was fixed from the blue region in each direction of $\boldsymbol{u}$, and the tangential traction load $\boldsymbol{\sigma n} = (0, 10, 0)^T$ has been applied to the green surface. Corresponding finite element meshes and related boundary conditions are represented visually and graphically in Figure 3.1. Since it is a nonlinear analysis, the load was applied incrementally in 100 steps. In the numerical example, the following isotropic free-energy function has been defined

$$\Psi_{iso} = \frac{\mu}{2}(\bar{I}_1 - 3) \quad \text{and} \quad \Psi_{vol} = \frac{\kappa}{2}(J-1)^2 \tag{3.63}$$

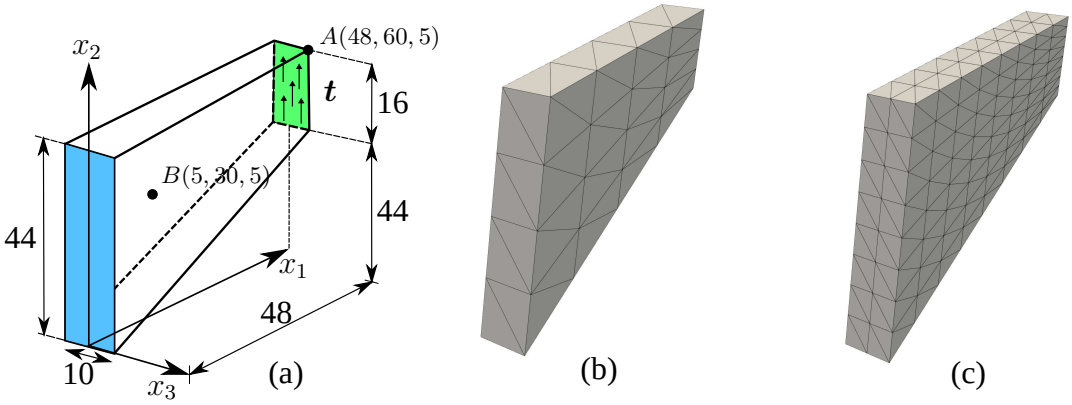

Figure 3.1: (a) Schematic view of the geometry, boundary conditions and traction load (b) coarse mesh representation with 4 elements per edge c) fine mesh representation with 8 elements per edge. (Units are dimensionless)

where μ is the shear modulus and κ is the bulk modulus of the material. The parameters have been defined in the quasi-incompressible limit as $\nu = 0.4999$ and $\mu = 67.11$ units. During the comparison, the tip deflection in x_2 direction is obtained from point A and the pressure is taken from point B. There were different element types with different interpolation orders used to make comparisons in terms of accuracy and solution time. Elements that were used in the analysis are shown in Figure 3.2. The first letter in the notation of the element type describes the geometric shape of the element. Since we use tetrahedron elements in the example, that is referred to as T. The second number following to the first letter is the order of interpolation degree. 1 is used for linear interpolation, 2 is used for quadratic interpolation and 0 is used for pressure degree of freedom stated as P that is formulated as a constant over element. There is also defined a different type of element which uses Crouzeix-Raviart interpolation for the pressure degree of freedom and defined as CRP. While the subscript HW refers for three-field Hu-Washizu element formulation, the remained elements are formed based on two-field mixed formulation. There will be presented resultant contours of independent variables such as displacement, and pressure. As a reference solution, there was solved the same numerical model with 32 elements per edges in ANSYS with Q1P0 element by using the same material properties. The vertical deflection at Point A and internal pressure at point B are given in Figure 3.3 with different mesh settings. There are overlaps of the results of $T1P0_{HW}$-$T1P0$ and $T2P0_{HW}$-$T2P0$

Element Type	Illustration
$T1P0$	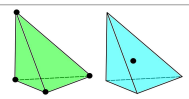
$T2P0$	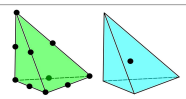
$T2P1$	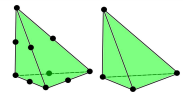
$T1P0_{HW}$	
$T2P0_{HW}$	
$T1CR1$	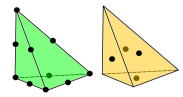

Figure 3.2: Element types used in numerical Cook's membrane numerical example

element formulations. Linear approximation has been performed between the results of 4 and 8 elements per edge configurations. As it is already known that linear interpolation of tetrahedron elements causes shear-locking and exhibit too stiff behaviour. Accordingly, $T1$ element formulations suffer from ill-conditioning and non-accurate results in both displacement and pressure. It also causes the checkerboard pattern for pressure distribution, which is not realistic. The numerical problem can be solved either by using quadratic elements or by replacing tetrahedrons with hexahedrons. The quadratic element formulation for the displacement degree of freedom (i.e. $T2$) elements converges to the reference solution by increasing the mesh count. Some elements converges by increasing trend and some others converges by decreasing manner such as $T2P0_{HW}$ and $T2CR1$. While it seems like the $T2$ interpolations agree with the reference solution, a slight difference appears on pressure plots. By increasing the mesh level, $T2P0_{HW}$ and $T2P0$ provided the most accurate results rather than the other element types. Another important comparison criterion in the FE process is the total elapsed solution time. The normalized solution time for different element formulations is given in Figure 3.4 for the coarse and fine mesh scenarios, respectively. According to computational efficiencies, higher-order interpolations require more computational effort in general. Although, $T2P0$ provides accurate results in

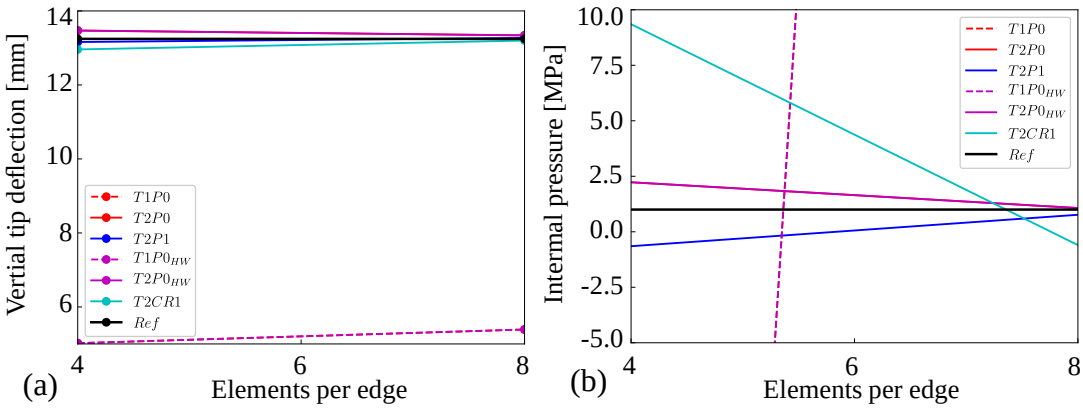

Figure 3.3: (a) Tip vertical deflection of different element formulations at point "A" (b) Internal pressure result at point "B" of different element formulations. Both plots are provided based on coarse and fine mesh settings

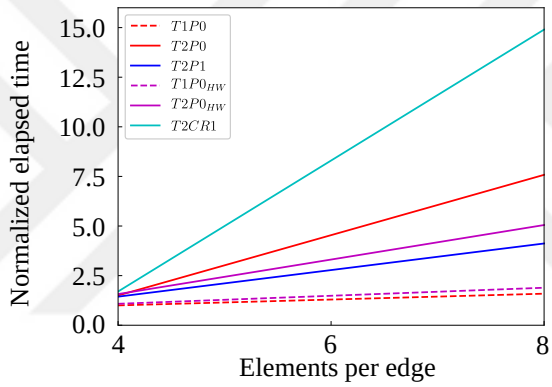

Figure 3.4: Normalized elapsed time for different mixed element formulations

terms of deflection and pressure, it is not the most efficient in terms of computational time, and it requires more iterations in the Newton-Raphson process. By taking into consideration all parameter sets shown in Figures 3.3 and 3.4, $T2P0_{HW}$ three-field Hu-Washizu element formulation provides the best solution. The vertical displacement and pressure contours regarding to $T1P0$ and $T1P0_{HW}$ elements are given for coarse and fine mesh settings in Figure 3.5. It is clearly seen from the results that, linear interpolation of displacement independent variable causes inaccurate stiff bending behavior. Similarly, the pressure contours show an unrealistic checkerboard pattern.

Figure 3.6 presents the displacement and pressure contours of $T2P0$ and $T2P0_{HW}$ elements for coarse and fine meshes. These elements reflect the accurate behaviour

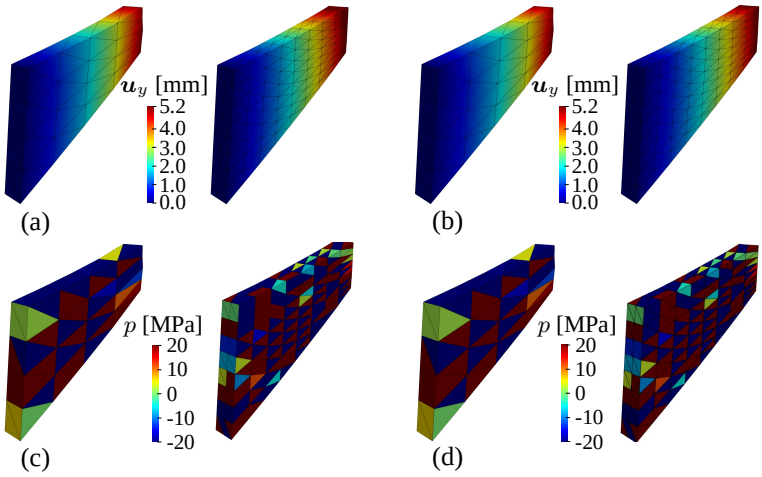

Figure 3.5: Contours of 4 element per edge and 8 element per edge configurations. (a) Vertical displacement of $T1P0$ element (b) Vertical displacement of $T1P0_{HW}$ element (c) Pressure distribution of $T1P0$ element (d) Pressure distribution of $T1P0_{HW}$ element

of both coarse and fine meshes. Since pressure degree of freedom is constant over element, fine mesh setting covers the pressure distribution better. Both two-field and three-field elements exhibit very similar behaviour in terms of displacement and pressure. However, it should be noted from Figure 3.4 that, $T2P0_{HW}$ is not only the most accurate element but also computationally efficient.

Figure 3.7 presents the displacement and pressure contours of $T2P1$ and $T2CR1$ elements for coarse and fine meshes. Using linear interpolation of pressure degree of freedom provides smooth transition of pressure contours, but it is not computationally effective. The pressure distributions of elements $T2P0$ and $T2P1$ are similar in an average sense. Therefore, in literature, the pressure variable is mostly considered as constant over element. There is another element type (Crouzeix-Raviart interpolation) also compared with common elements. CR elements store the pressure constant on each face of the element. The displacement behaviour is similar to other element types. Pressure distribution is also accurate enough, on average. However, there were observed singularities of pressure, especially in boundary condition regions, and causes numerical instabilities. Therefore CR element formulation is accurate enough in overall region but it is not accurate in boundary regions and it is not computationally efficient.

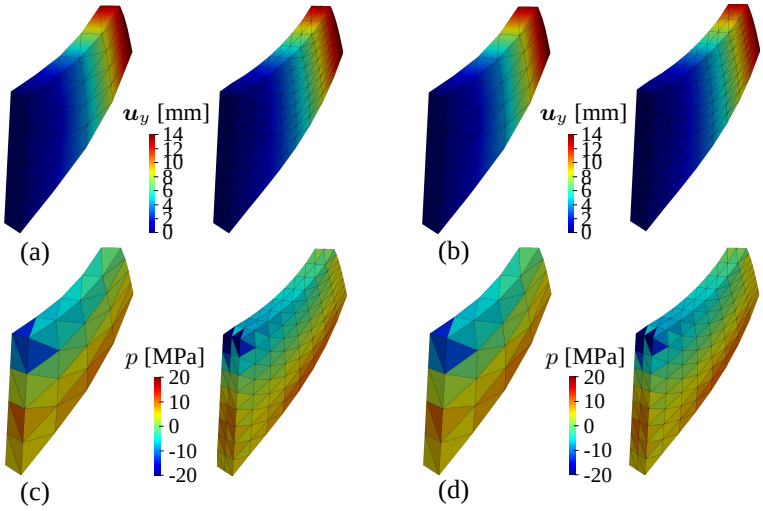

Figure 3.6: Contours of 4 element per edge and 8 element per edge configurations. (a) Vertical displacement of $T2P0$ element (b) Vertical displacement of $T2P0_{HW}$ element (c) Pressure distribution of $T2P0$ element (d) Pressure distribution of $T2P0_{HW}$ element

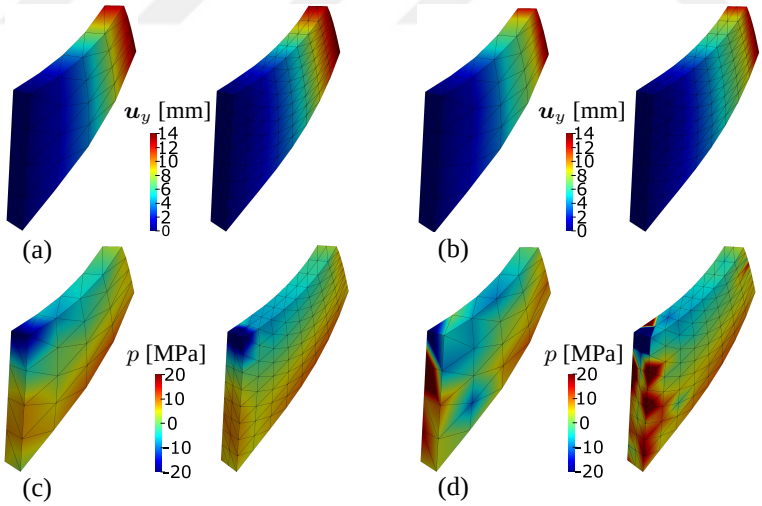

Figure 3.7: Contours of 4 element per edge and 8 element per edge configurations. (a) Vertical displacement of $T2P1$ element (b) Vertical displacement of $T2CR1$ element (c) Pressure distribution of $T2P1$ element (d) Pressure distribution of $T2CR1$ element

3.6 Five-Field Formulation

Fiber-reinforced soft biological tissues may exhibit not only incompressible behavior but can also present an inextensible mechanical response due to the high ground matrix-fiber stiffness ratio. In such numerical situation as we face in the incompressible limit, a similar problem is shown up in the nearly inextensible limit due to the high fiber stiffness. Therefore, it is also necessary to treat the nearly-inextensible problems with a Lagrange multiplier and another kinematic variable.

A mixed variational formulation based on the Hu-Washizu principle for the nearly incompressible and nearly inextensible limits for fiber-reinforced materials was studied in [112, 113, 132, 133, 104] for one family of fibers. Later it was extended to two family fibers for soft biological tissues [134]. The approach of Zdunek et al. [112, 113] is based on the multiplicative decomposition of the deformation gradient into a purely unimodular extensional part, a purely spherical part, and an extension free unimodular part. The mixed element formulation of Dal et al. [104, 134] is based on a five-field Hu-Washizu type variational formulation that has conjugate pairs (p, θ) and (s, λ) for pressure-dilatation and fiber stress-fiber stretch, respectively. The result of the variational formulation is the *Q1P0F0* element which is extended for the inextensibility limit. The formulation is formed based on a vectorial displacement field and two additional scalar conjugate pairs, making five fields in total. On the other hand, Schröder et al. [132] used Hu-Washizu type variational formulation for incompressible part of the formulation and they proposed Simplified Kinematic for anisotropic part. They introduced low-order interpolation (constant over element) for a second-order tensorial Lagrange multiplier conjugate to a tensorial kinematic-like field. They formulated either use of the deformation gradient $\boldsymbol{F}$ or right Cauchy-Green tensor $\boldsymbol{C}$ as the kinematic tensorial function conjugate to stress-like Lagrange multiplier. For a detailed review, we refer to [132, 104, 134] and references therein.

In this section, the five-field formulation proposed by Dal [104] and Schröder et al. [132] will be introduced and compared in detail to observe the accuracy and computational cost of the models.

3.6.1 Scalar conjugate pairs for inextensibility (s, λ)

This model uses scalar conjugate pair (s, λ) for inextensibility constraint in addition to scalar incompressiblity pair (p, θ). The free-energy is decomposed into volumetric, isochoric and anisotropic parts as follows

$$\Psi(\boldsymbol{g}; \boldsymbol{F}, \boldsymbol{n}_0) := \psi_{vol}(J) + \Psi_{iso}(\boldsymbol{g}; \boldsymbol{F}) + \Psi_{ani}(\boldsymbol{g}; \boldsymbol{F}, \boldsymbol{n}_0) \tag{3.64}$$

Note that, since we are working on one-family fiber reinforcement, the anisotropic part is the function of only a single unit vector $\boldsymbol{n}_0$ along the fiber direction. If there are two-family fiber reinforcement, refer equation 3.45 for extended free-energy functional. Corresponding unimodular isotropic and anisotropic invariants are already defined in equations 3.23 and 2.16 respectively. Then similar analogy to free-energy, the Kirchhoff stress can decomposed of as following

$$\boldsymbol{\tau} = 2\partial_{\boldsymbol{g}}\Psi = \boldsymbol{\tau}_{vol} + \boldsymbol{\tau}_{iso} + \boldsymbol{\tau}_{ani} \tag{3.65}$$

where $\boldsymbol{\tau}_{vol}$, $\boldsymbol{\tau}_{iso}$ and $\boldsymbol{\tau}_{ani}$ are already defined in equations 3.36, 3.39 and 3.47. Similarly, the Eulerian tangent moduli can be expressed by volumetric, isochoric and anisotropic parts as below

$$\mathbb{c} = 4\partial^2_{\boldsymbol{gg}}\Psi = \mathbb{c}_{vol} + \mathbb{c}_{iso} + \mathbb{c}_{ani} \tag{3.66}$$

where $\mathbb{c}_{vol}$, $\mathbb{c}_{iso}$ and $\mathbb{c}_{ani}$ are defined in equations 3.37, 3.40 and 3.47. Two Lagrange multiplier are required to be added in the mixed potential to enforce incompressibility and inextensibility behavior. Then the mixed potential can be described as below

$$\begin{aligned}\hat{\Pi}(\boldsymbol{\phi}, p, \theta, s, \lambda) := \hat{\Pi}^{int}(\boldsymbol{\phi}) - \hat{\Pi}^{ext}(\boldsymbol{\phi}) \quad &+ \quad \int_V p(J-\theta)dV + \int_V \Psi_{vol}(\theta)dV \\ &+ \quad \int_V s(I_4 - \lambda)dV + \int_V \Psi_{ani}(\lambda)dV\end{aligned} \tag{3.67}$$

where s is the second Lagrange multiplier as fiber stress and λ is the kinematic entity as fiber stretch. Then additional stationary conditions to equation 3.59 with respect to

s and λ yields additional weak forms as following

$$
\begin{aligned}
D\hat{\Pi}(\boldsymbol{\phi}, p, \theta, s, \lambda)[\delta\boldsymbol{\phi}] &= \int_V \left(\left(\boldsymbol{\tau}^{iso} + pJ\boldsymbol{g}^{-1} + 2s\boldsymbol{n}\otimes\boldsymbol{n}\right) : sym(\boldsymbol{g}\nabla_x\delta\boldsymbol{\phi}\right)\, dV \\
&- \delta\hat{\Pi}^{ext}(\boldsymbol{\phi}) = 0\,, \\
D\hat{\Pi}(\boldsymbol{\phi}, p, \theta, s, \lambda)[\delta p] &= \int_V \delta p\,(J-\theta)\, dV = 0\,, \\
D\hat{\Pi}(\boldsymbol{\phi}, p, \theta, s, \lambda)[\delta\theta] &= \int_V \delta\theta(\Psi'_{vol}(\theta) - p)\, dV = 0, \\
D\hat{\Pi}(\boldsymbol{\phi}, p, \theta, s, \lambda)[\delta s] &= \int_V \delta s\,(I_4 - \lambda)\, dV = 0\,, \\
D\hat{\Pi}(\boldsymbol{\phi}, p, \theta, s, \lambda)[\delta\lambda] &= \int_V \delta\lambda(\Psi'_{ani}(\lambda) - s)\, dV = 0
\end{aligned}
\tag{3.68}
$$

Note that, there appears additional stress term in equation 3.68_1 related with the anisotropic part of the free-energy. Then, similar to equation 3.60, the consistent linearization with respect to $\boldsymbol{\phi}$ leads

$$
\begin{aligned}
D^2\hat{\Pi}(\boldsymbol{\phi}, p, \theta, s, \lambda)[\delta\boldsymbol{\phi}, \Delta\boldsymbol{\phi}] &= \int_V \boldsymbol{g}\nabla_x\delta\boldsymbol{\phi} : \left(\nabla_x\Delta\boldsymbol{\phi}\left(\tau^{iso} + pJ\boldsymbol{g}^{-1} + 2s\boldsymbol{n}\otimes\boldsymbol{n}\right)\right) dV \\
&+ \int_V \boldsymbol{g}\nabla_x\delta\boldsymbol{\phi} : \left(pJ\left(\boldsymbol{g}^{-1}\otimes\boldsymbol{g}^{-1} - 2\mathbb{I}_{\boldsymbol{g}^{-1}}\right) + \mathbb{C}^{iso}\right) \\
&: \boldsymbol{g}\nabla_x\Delta\boldsymbol{\phi} dV \\
&+ \int_V J\boldsymbol{g}\nabla_x\delta\boldsymbol{\phi} : \boldsymbol{g}^{-1}\Delta p dV \\
&+ \int_V \boldsymbol{g}\nabla_x\delta\boldsymbol{\phi} : 2\Delta s\boldsymbol{n}\otimes\boldsymbol{n} dV
\end{aligned}
\tag{3.69}
$$

The similar methodology, that were applied for p and θ in equations 3.61 and 3.62, the second Lagrange multiplier and the fiber stress term s and fiber stretch λ can be defined constant over an element as below

$$
\bar{\lambda} = \frac{1}{V}\int_B I_4 dV = \frac{V_0}{V}, \quad \text{and} \quad \bar{s} = \frac{1}{V}\int_B \Psi'_{ani} dV, \tag{3.70}
$$

Then the incremental forms leads

$$
\Delta\bar{\lambda} = \frac{1}{V}\int_B 2\boldsymbol{n}\otimes\boldsymbol{n} : \boldsymbol{g}\nabla_x\Delta\boldsymbol{\phi} dV, \quad \text{and} \quad \Delta\bar{s} = \Psi''_{ani}\Delta\bar{\lambda} dV, \tag{3.71}
$$

Pluging of the incremental forms defined in equation 3.71 into 3.69 gives the final form of the linearization, see [104] for further details. The mixed variational formulation leads to $Q1P0F0$ or $T2P0F0$ five-field finite element formulation.

3.6.2 Tensorial conjugate pairs for inextensibility $(\boldsymbol{\mathcal{C}}, \boldsymbol{\mathcal{S}})$

This model uses second-order tensorial conjugate pair $(\boldsymbol{\mathcal{S}}, \boldsymbol{\mathcal{C}})$ for inextensibility constraint in addition to scalar incompressiblity pair (p, θ). The model is very similar to the previous one as it decomposes the free-energy, stress and moduli expressions in same manner with equations 3.64, 3.65 and 3.66. The difference between the two of the five-field models comes out in the second Lagrange multiplier and the kinematic entity. Schröder et al. [132] described the second Lagrange multiplier and its conjugate as a second-order tensors. While the proposed model by [104] is formulated based on the constraint over fiber stretch I_4, the tensorial model enforce the inextensibility constraint based on right Cauchy-Green tensor $\boldsymbol{C}$. Then the mixed potential can be described as below

$$\begin{aligned}\hat{\Pi}(\boldsymbol{C}, p, \theta, \boldsymbol{\mathcal{S}}, \boldsymbol{\mathcal{C}}) := \hat{\Pi}^{int}(\boldsymbol{\phi}) - \hat{\Pi}^{ext}(\boldsymbol{\phi}) \quad &+ \quad \int_V p(J-\theta)dV + \int_V \Psi_{vol}(\theta)dV \\ &+ \quad \int_V \boldsymbol{\mathcal{S}} : (\boldsymbol{C} - \boldsymbol{\mathcal{C}})dV + \int_V \Psi_{ani}(\boldsymbol{\mathcal{C}})dV\end{aligned} \tag{3.72}$$

where $\boldsymbol{\mathcal{S}}$ is the second-order tensor for the second Lagrange multiplier as anisotropic stress tensor and $\boldsymbol{\mathcal{C}}$ is the second-order tensor for the kinematic entity. Stationary conditions with respect to $\boldsymbol{\phi}$, p, θ , $\boldsymbol{\mathcal{S}}$ and $\boldsymbol{\mathcal{C}}$ yields to the following weak forms

$$\begin{aligned}
D\hat{\Pi}(\boldsymbol{C}, p, \theta, \boldsymbol{\mathcal{S}}, \boldsymbol{\mathcal{C}})[\delta\boldsymbol{\phi}] &= \int_V \frac{1}{2}\delta\boldsymbol{C} : \left(2\partial_{\boldsymbol{C}}\Psi + pJC^{-1} + \boldsymbol{\mathcal{S}}\right) dV \\
&- \delta\hat{\Pi}^{ext}(\boldsymbol{\phi}) = 0\,, \\
D\hat{\Pi}(\boldsymbol{C}, p, \theta, \boldsymbol{\mathcal{S}}, \boldsymbol{\mathcal{C}})[\delta p] &= \int_V \delta p\,(J-\theta)\,dV = 0\,, \\
D\hat{\Pi}(\boldsymbol{C}, p, \theta, \boldsymbol{\mathcal{S}}, \boldsymbol{\mathcal{C}})[\delta\theta] &= \int_V \delta\theta(\Psi'_{vol}(\theta) - p)\,dV = 0, \\
D\hat{\Pi}(\boldsymbol{C}, p, \theta, \boldsymbol{\mathcal{S}}, \boldsymbol{\mathcal{C}})[\delta\boldsymbol{\mathcal{C}}] &= \int_V \delta\boldsymbol{\mathcal{C}} : (\partial_{\boldsymbol{\mathcal{C}}}\Psi_{ani} - \frac{1}{2}\boldsymbol{\mathcal{S}})\,dV = 0\,, \\
D\hat{\Pi}(\boldsymbol{C}, p, \theta, \boldsymbol{\mathcal{S}}, \boldsymbol{\mathcal{C}})[\delta\boldsymbol{\mathcal{S}}] &= \int_V \delta\boldsymbol{\mathcal{S}} : (\boldsymbol{C} - \boldsymbol{\mathcal{C}})\,dV = 0
\end{aligned} \tag{3.73}$$

Discretization of the four additional fields θ, p, $\boldsymbol{\mathcal{S}}$ and $\boldsymbol{\mathcal{C}}$ are defined as constant over the element similar to the equations 3.70 and 3.71, see [132] for further details. The mixed variational formulation lead to $Q1P0A0$ or $T2P0A0$ five-field finite element formulation.

3.7 Dual Clamped Patch Test - Comparison of Mixed Element Formulations

In this numerical example, it is aimed to focus on the accuracy and efficiency of different types of finite element formulations shown in Figure 3.8, in different physical conditions such as compressible, extensible, nearly incompressible, and nearly inextensible cases. The descriptions of the elements as following: $T2$ refers for standard displacement element with quadratic interpolation, $T2P0$ and $T2P1$ are the three-field Hu-Washizu mean dilatation formulations with different pressure-dilatation interpolations, $T2A0$ and $T2A1$ are the three-field that uses tensorial formulations for newly added independent variables for inextensibility constraint, $T2P0A0$ and $T2P1A1$ are the five-field formulation that includes scalar pair for incompressibility constraint and tensorial pair of additional independent variables for inextensibility limits and lastly $T2P0F0$ and $T2P1F1$ are the five-field mixed formulations composed of scalar pairs for additional independent variables for the both incompressibility and inextensibility limits. In the solution of this numerical problem, FeniCS [12] has been used for the finite element analysis software. The linear elements constructed by 3 nodes, the quadratic elements formed by 6 nodes, and constant interpolation over an element are also generated for the different types of element formulations. The square shaped (1x1 dimensions) 2D geometry is defined in line with [132] and it is clamped at the upper and lower edge boundaries as a fixed support. A uniform traction is applied as $\boldsymbol{q} = 30$ and it is incrementally applied at the left vertical edge of the square geometry. Since the model is in 2D space, nodes are fixed in the normal $\boldsymbol{x}_3$-direction. The corresponding geometry and boundary conditions are presented in Figure 3.9.

The following free-energy function that is proposed by [132], has been used in the numerical example.

$$\Psi = \frac{\lambda}{4}(I_3 - 1) - \left(\frac{\lambda}{2} + \mu\right) \ln(\sqrt{I_3}) + \frac{\mu}{2}(I_1 - 3) + \mu_f \langle I_4 - 1 \rangle^2 \tag{3.74}$$

Element Type	Illustration
$T2$	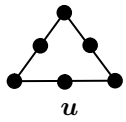
$T2P0$	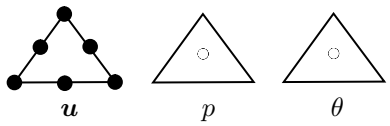
$T2P1$	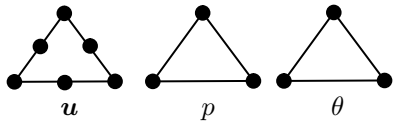
$T2A0$	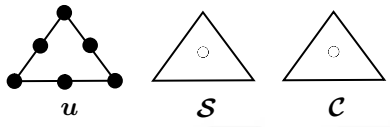
$T2A1$	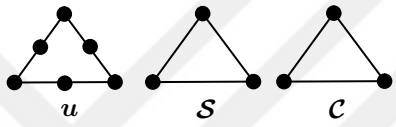
$T2P0F0$	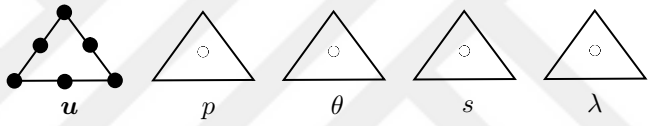
$T2P1F1$	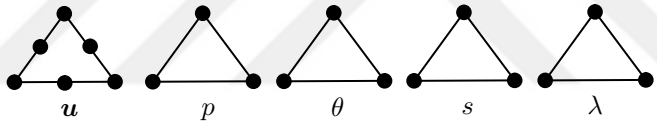
$T2P0A0$	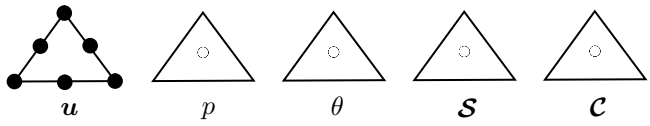
$T2P1A1$	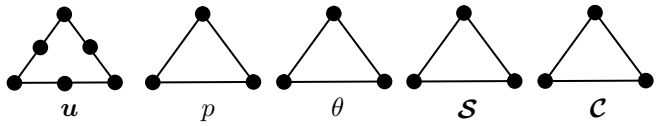

Figure 3.8: Finite element design for compressible, extensible, quasi-incompressible and quasi-inextensible hyperelasticity.

where the first three terms in equation 3.74 is the isotropic contribution of the free-energy function and the last term is the anisotropic part due to the one family fiber reinforcement. The anisotropic part of the free energy is defined by Macaulay brackets $\langle \bullet \rangle$ that represent the tension-only behavior. λ is the Lamé constant, μ is the shear modulus of the base ground matrix and μ_f is the fiber stiffness. The fol-

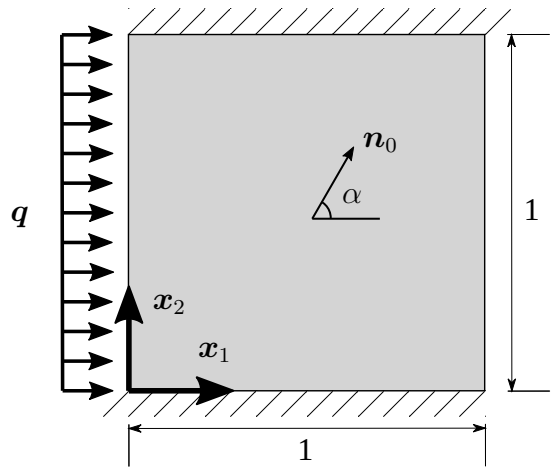

Figure 3.9: Schematic representation of the geometry and corresponding boundary conditions

lowing relations can be used to calculate other mechanical constants such as $\lambda = \nu E/\left((1+\nu)(1-2\nu)\right)$ and $\mu = E/\left(2(1+\nu)\right)$ where E is the Young's modulus of the material and ν is the Poisson's ratio.

The ground matrix material is reinforced by one family of fibers with $\alpha = 60^0$ angle with the horizontal plane. The fiber's unit normal is described by $\boldsymbol{n}_0 = (0.5, \sqrt{3}/2)^T$. The fiber stiffness μ_f is defined as a parameter set such as $\mu_f = \{10^2, 10^4, 10^6, 10^8\}$ to observe the robustness of the elements especially in inextensible limits. Similarly, Poisson's ratio is also defined in two sets $\nu = \{0.3, 0.49\}$ to examine the element formulations in compressible and near-incompressible limits. The elastic modulus is defined as a constant $E = 200$.

For all of the cases, the initial time step increment is taken as $\Delta t = 1$. During the Newton-Ralphson iteration process, the maximum iteration steps for each time increment were defined as 20. If the solution does not converge in this range, the simulation is restarted and the time step increment is divided by $1/2^n$ where n is the power factor that is increased by 1 whether the solution faces any divergence issues. The process continues until the time step reaches to $1/2^7$. There are defined coarse to fine sets of finite element meshes: 2, 4, 8, 16, 32 and 64 elements per edge, and they are generated with triangular elements. The mesh layout is set to symmetric with respect to the two major axis $\boldsymbol{x}_1$ and $\boldsymbol{x}_2$ to decrease the effect of the mesh layout

dependencies in the results. The mesh configurations are shown in Figure 3.10.

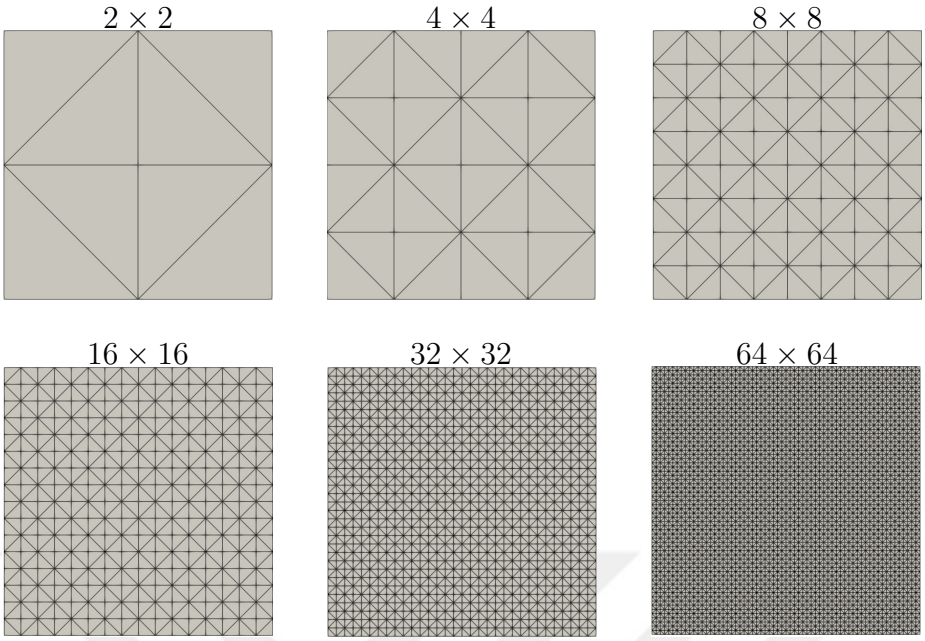

Figure 3.10: Representation of mesh configurations with different element sizes

In the first set of solution for $\nu = 0.3$, the additional field variables in three-field and five-field formulations are taken as constant over element. Hence, $T2$, $T2P0$, $T2A0$, $T2P0A0$ and $T2P0F0$ elements are compared in terms of deformation and elapsed solution time. The mid-point deflection $u_x(0.0, 0.5)$ of the left edge has been tracked for all of the mesh configurations and for obtained for the wide range of μ_f fiber stiffness values. Accordingly, the mid-point deflection (along $\boldsymbol{x}_2$ direction) results are presented in Figure 3.11. These graphs reveal the compressible material response of the different element formulations for variety of fiber stiffness range. All of the elements converges to same mid-point displacement value for the $\mu = \{10^2, 10^4\}$ however they approaches the final value of displacement in a different convergence trend. For the case of $\mu = \{10^6\}$, $T2$ is divergent and $T2P0$ exhibit a convergence behaviour. In the high level of near-inextensibility limit such as $\mu = \{10^8\}$, only the elements those treats the inextensibility constraint by additional field variables as $T2A0$, $T2P0A0$ and $T2P0F0$ exhibit convergence trend by identical results. The solution efficiency is an another critical resultant parameter that is demonstrated in Figure 3.12 for $\mu_f = 10^2$ with (32×32) and (64×64) element configurations. Due to having a relatively low number of degrees of freedom for $T2$ and $T2P0$ elements,

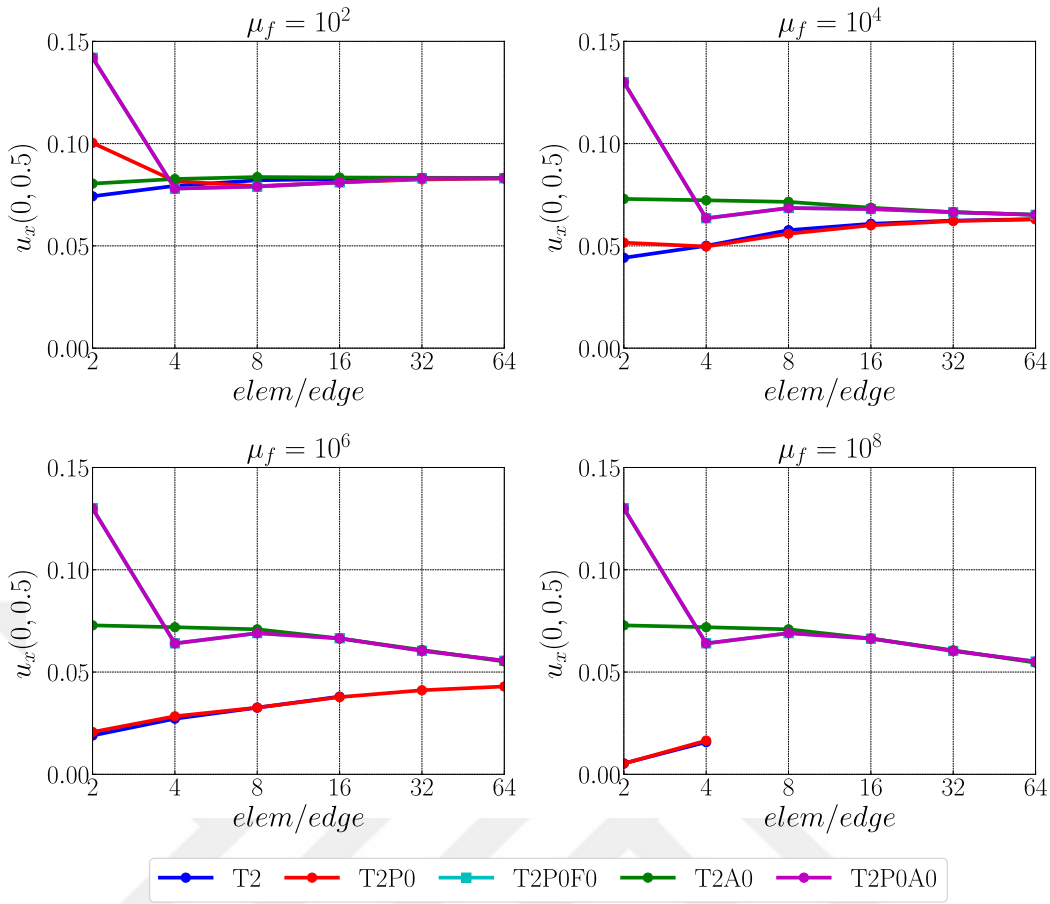

Figure 3.11: $\nu = 0.3$, Mid-point displacement $u_x(0, 0.5)$ results for (2×2), (4×4), (8×8), (16×16), (32×32) and (64×64) elements per edge in the range of $\mu_f = \{10^2, 10^4, 10^6, 10^8\}$.

these are the most cost-effective in terms of solution time. However, these elements are not convergent in high fiber stiffness materials, then the best option appears to be the $T2P0F0$ which can be used in both incompressible limits and inextensible limits. $T2P0F0$ is competitive with standard types of elements, and it does not slow the simulation as expected. Although, $T2A0$ and $T2P0A0$ are also good candidates for accuracy and convergence, they fall behind in terms of computational effectiveness. In the second set of the solution for $\nu = 0.49$, all of the element formulations shown in Figure 3.8 have been tested in the near-incompressible case. In the cases where $\mu_f = 10^2$ and $\mu_f = 10^4$, all element types have been tested in the numerical model. However, due to the difficulties of the convergence level for more stiff cases such as $\mu_f = 10^6$ and $\mu_f = 10^8$, only the element which have low-order interpolation

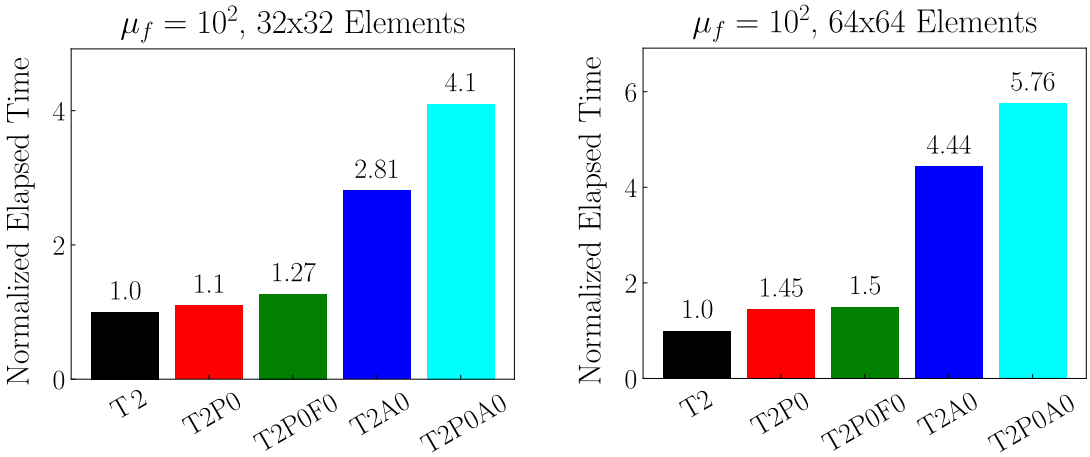

Figure 3.12: $\nu = 0.3$, the normalized elapsed time for the solution of (32×32) and (64×64) elements per edge where $\mu_f = 10^2$.

formulations have been preferred to be used.

In the second set of the solutions, elements listed in Figure 3.8 are compared in terms of mid-point deflection behaviour, iteration trends with respect to different fiber stiffness value, normalized elapsed solution time, and Cauchy-type fiber stress contours. Figure 3.13 shows the mid-point $u_x(0, 0.5)$ deflection characteristics for different element formulations where $\nu = 0.49$. For the relatively moderate fiber stiffness configuration ($\mu_f = 10^2 - 10^4$), all the elements are convergent to the same value. However, there are observed locking phenomena for almost all element formulations when using coarse mesh settings such as (2×2). $T2$ and $T2P0$ exhibit divergence behaviour at $\mu_f = 10^6$ and $\mu_f = 10^8$. However, $T2A0$, $T2P0A0$ and $T2P0F0$ present excellent and robust deflection behaviour. Especially $T2A0$ element even shows accurate results for the coarse meshes. Besides, $T2P0F0$ and $T2P0A0$ are identical, and their lines are overlapping each other.

The total number of iterations that have been performed during the solution is an important indicator of the robustness of the different element formulations, as shown in Figure 3.14. It can be clearly seen that, for the relatively low fiber stiffness such as $\mu = 10^2$, all of the elements exhibit a good convergence. However, when the fiber stiffness increased to $\mu = 10^4$, Hu-Washizu-type mixed pressure-dilatation elements suffers while converging, especially for high resolution mesh configurations. For $\mu = 10^6$ and $\mu = 10^8$, standard displacement element $T2$ and $T2P0$ are divergent

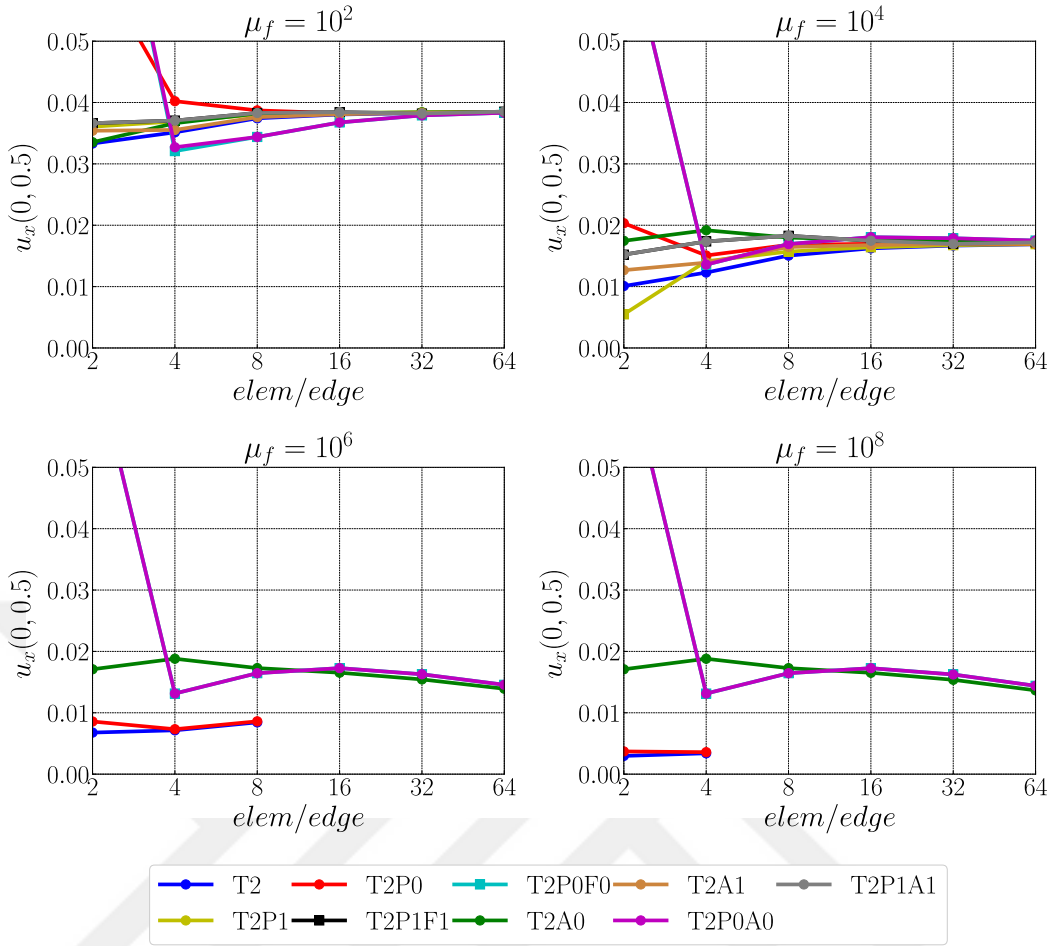

Figure 3.13: $\nu = 0.49$, Mid-point displacement $u_x(0, 0.5)$ results for (2×2), (4×4), (8×8), (16×16), (32×32) and (64×64) elements per edge in the range of $\mu_f = \{10^2, 10^4, 10^6, 10^8\}$.

even for the low resolution meshes. However $T2A0$, $T2P0A0$ and $T2P0F0$ elements shows excellent agreement with each other and reach the solution in a very robust way with similar iteration numbers for all of mesh resolutions.

The computational cost of the elements have been demonstrated for $\mu_f = 10^2$ and $\mu_f = 10^4$ where all the elements exhibit convergence behaviours for all of mesh resolutions, see Figure 3.15. Since it is more proper to observe the computational effectiveness of high-resolution meshes, results are given for (32×32) and (64×64) mesh settings. As expected, low-order elements, which have fewer independent variables in their formulations, spend the least computational time during the solution, i.e. $T2$ and $T2P0$. However, these elements suffer from locking in higher fiber stiff-

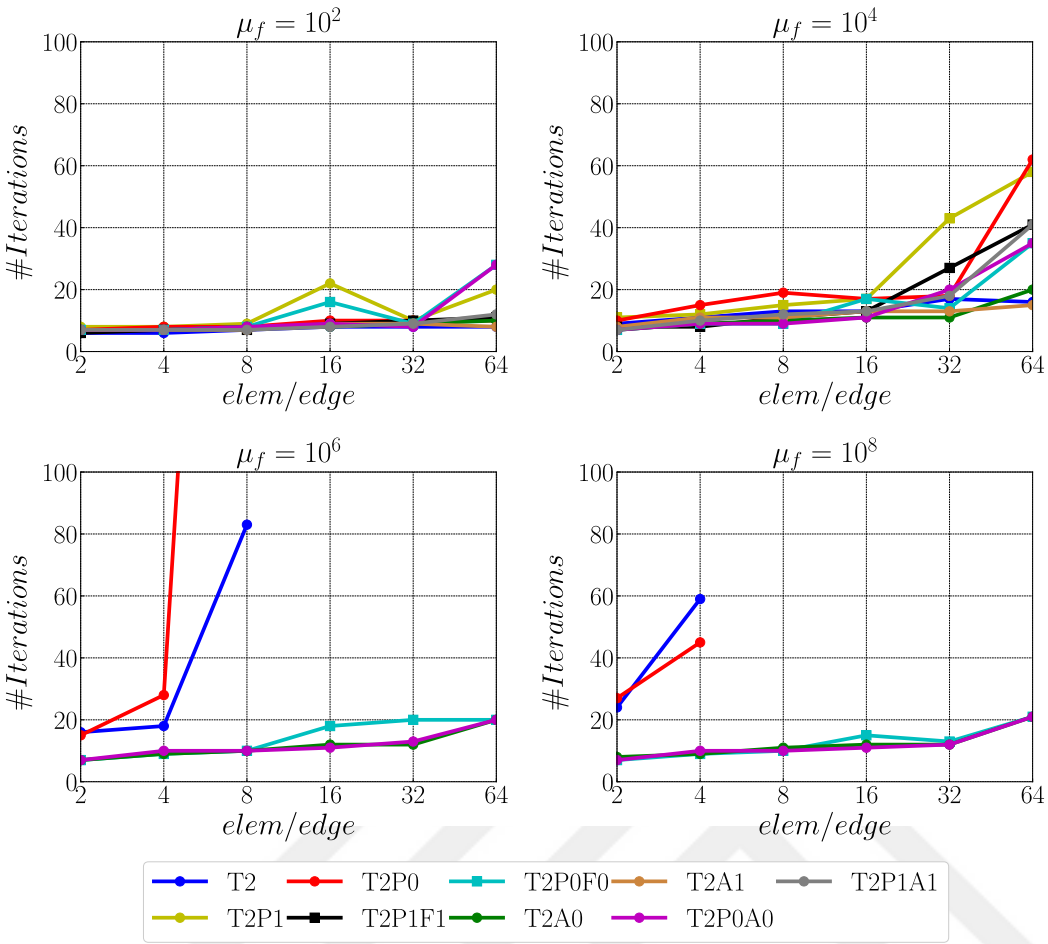

Figure 3.14: $\nu = 0.49$, Number of total iterations have been performed during Newton-Raphson iterations for (2×2), (4×4), (8×8), (16×16), (32×32) and (64×64) elements per edge in the range of $\mu_f = \{10^2, 10^4, 10^6, 10^8\}$.

ness materials as it is already shown in Figure 3.14. There are very high computational costs revealed due to the linear interpolations of $T2A1$ and $T2P1A1$ elements, which makes the analysis too slow and inefficient. It should be noted that, although $T2P1F1$ has also the high-order interpolations for additional independent variables, it has a similar computational times with $T2A0$ and $T2P0A0$. $T2P0F0$ element is the most cost effective in terms of computational robustness and nearly 4 times faster than $T2P0A0$ element formulation. Since these elements represent identical solutions, due to the difference between the scalar and tensorial formulations, the additional tensorial calculations slow down the solution process of $T2P0A0$ formulation. Figures 3.16, 3.17 and 3.18 demonstrate the Cauchy-type fiber stress distributions for

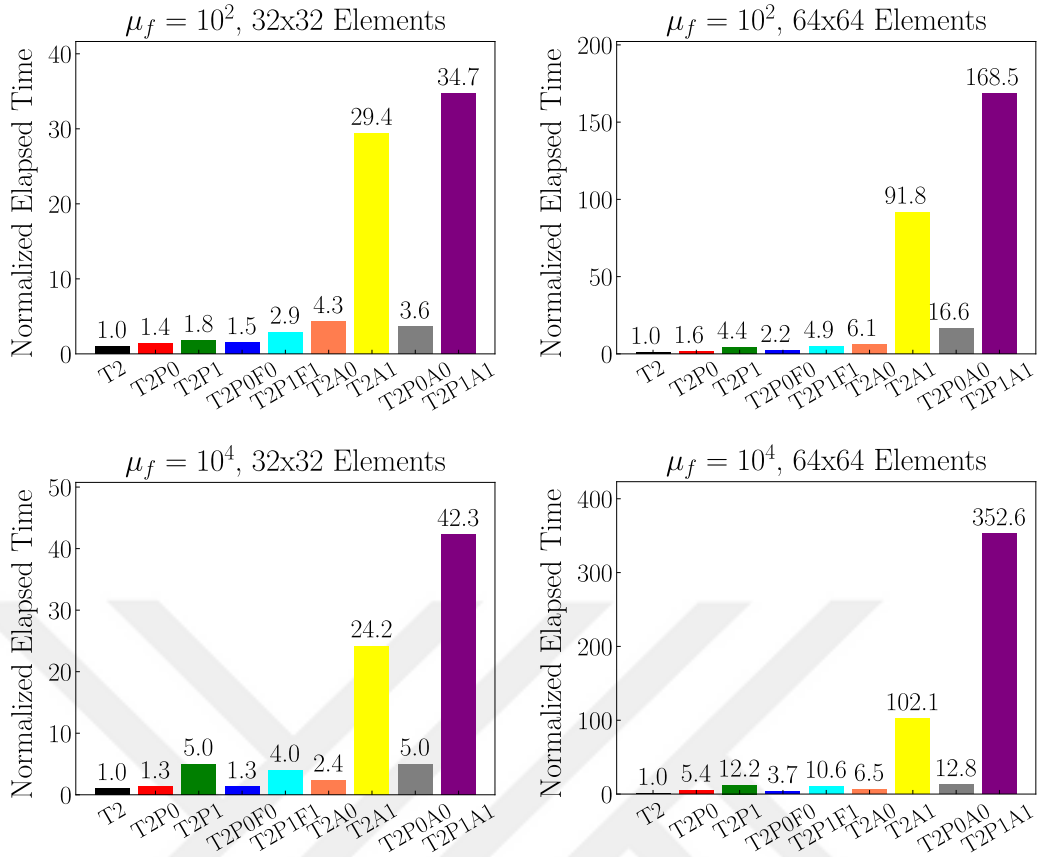

Figure 3.15: $\nu = 0.49$, the normalized elapsed time for the solution of (32×32) and (64×64) elements per edge at $\mu_f = 10^2$ and $\mu_f = 10^4$.

all element types where $\mu_f = 10^4$. Standard displacement element $T2$ and three-field Hu-Washizu elements $T2P0/T2P1$ represent a localized stress region. However, the stress distribution exhibits quick jumps between elements as spikes and oscillations are observed. Increasing the mesh resolution to (64×64), also increases the stress localization but does not treat the discontinuous stress variation between elements, which causes poor accuracy. On the other hand, $T2A0$, $T2P0A0$ and $T2P0F0$ elements demonstrate very smooth stress distribution, and there are not any examined spike-type discontinuities. In order to observe the mesh-dependency in a better way, there are also additional (128×128) mesh resolution presented in Figure 3.17. It shows that, for the low resolution meshes, smooth stress distribution is sufficient on average; however, increasing the mesh resolution reveals the smooth stress localization due to the fiber reinforcement. This outcome is related to the interpolation capability of triangular elements, and this issue can be fixed by using high resolution

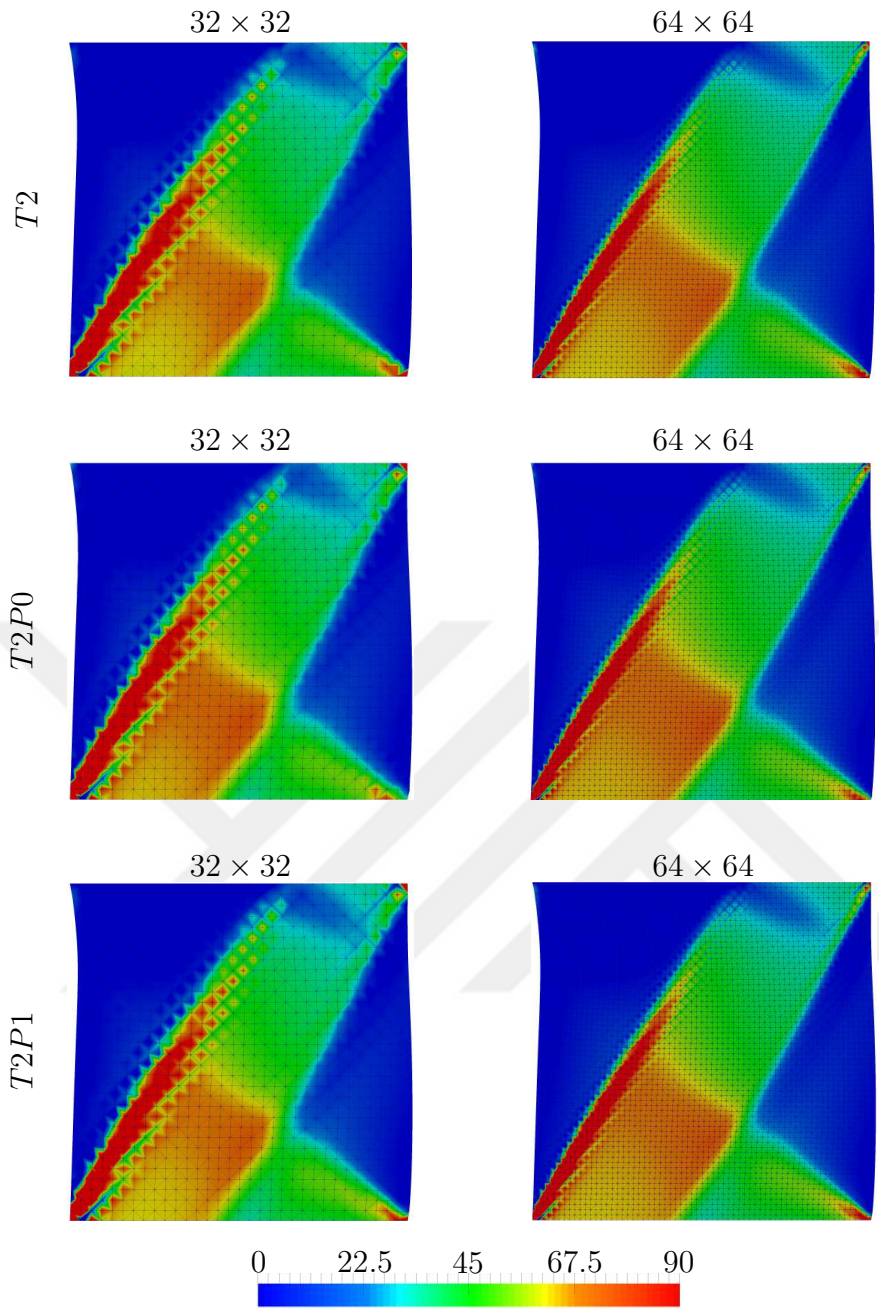

Figure 3.16: Cauchy fiber stress $\boldsymbol{\sigma}_f$ distribution of $T2$, $T2P0$ and $T2P1$ elements for dual clamped patch test where $\nu = 0.49$ and $\mu_f = 10^4$. Stress contours are presented for unit dimensions for (32×32) and (64×64) mesh configurations.

meshes. Figure 3.18 presents the stress contours of higher order elements such as $T2A1$, $T2P1A1$ and $T2P1F1$. These elements exhibit very similar characteristics between each other and the localized stresses have also been observed. Similarly, stress contours are smooth and similar to high resolution mesh trends of low-order

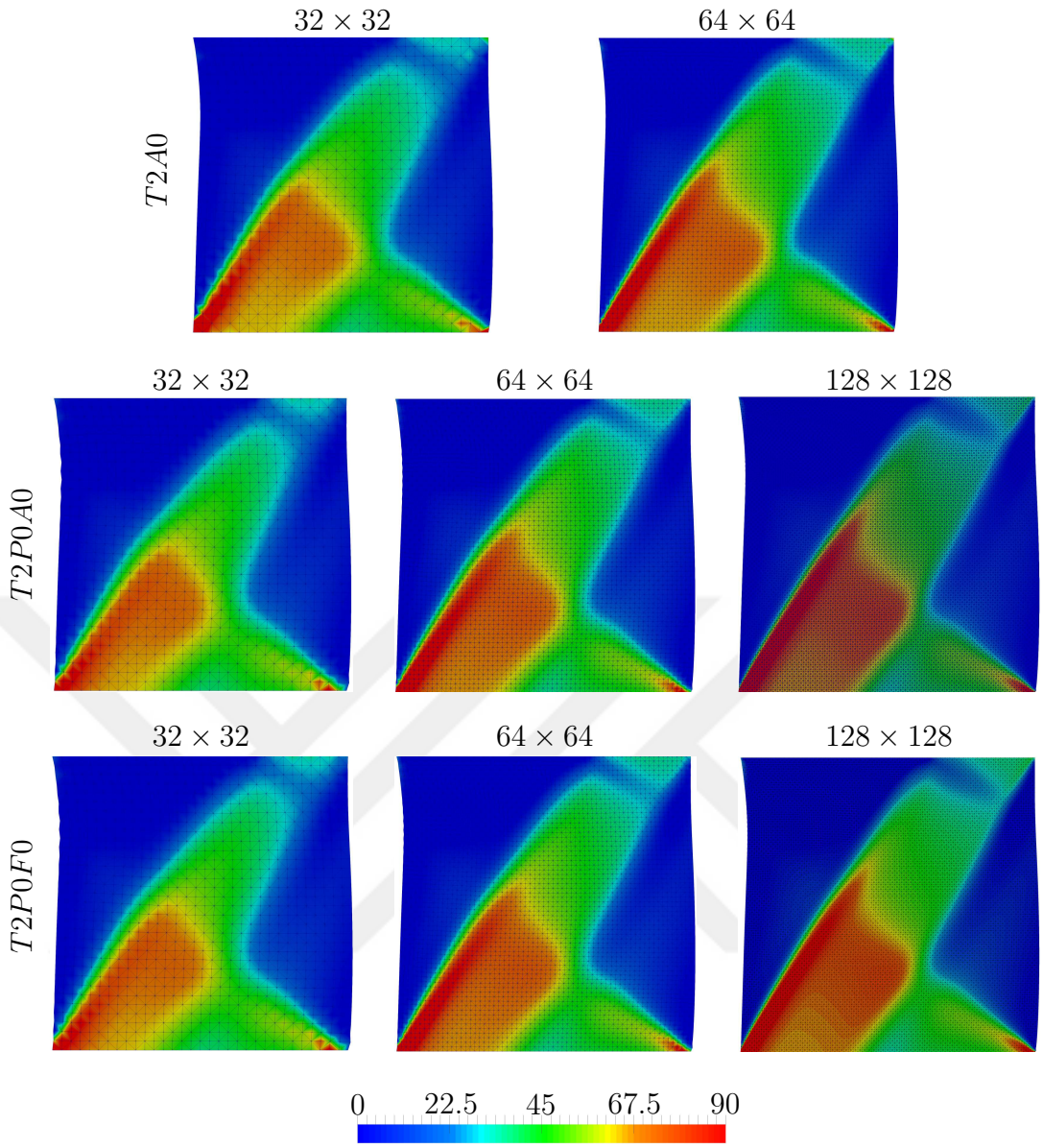

Figure 3.17: Cauchy fiber stress $\boldsymbol{\sigma}_f$ distribution of $T2A0$, $T2P0A0$ and $T2P0F0$ elements for dual clamped patch test where $\nu = 0.49$ and $\mu_f = 10^4$. Stress contours are presented for unit dimensions for (32×32), (64×64) mesh configurations for $T2A0$ and for five-field formulations, (128×128) mesh results additionally given.

elements shown in Figure 3.18. Since the computational cost is quite high for high-order elements, low-order elements are a good candidate to solve near-incompressible and near-inextensible material response.

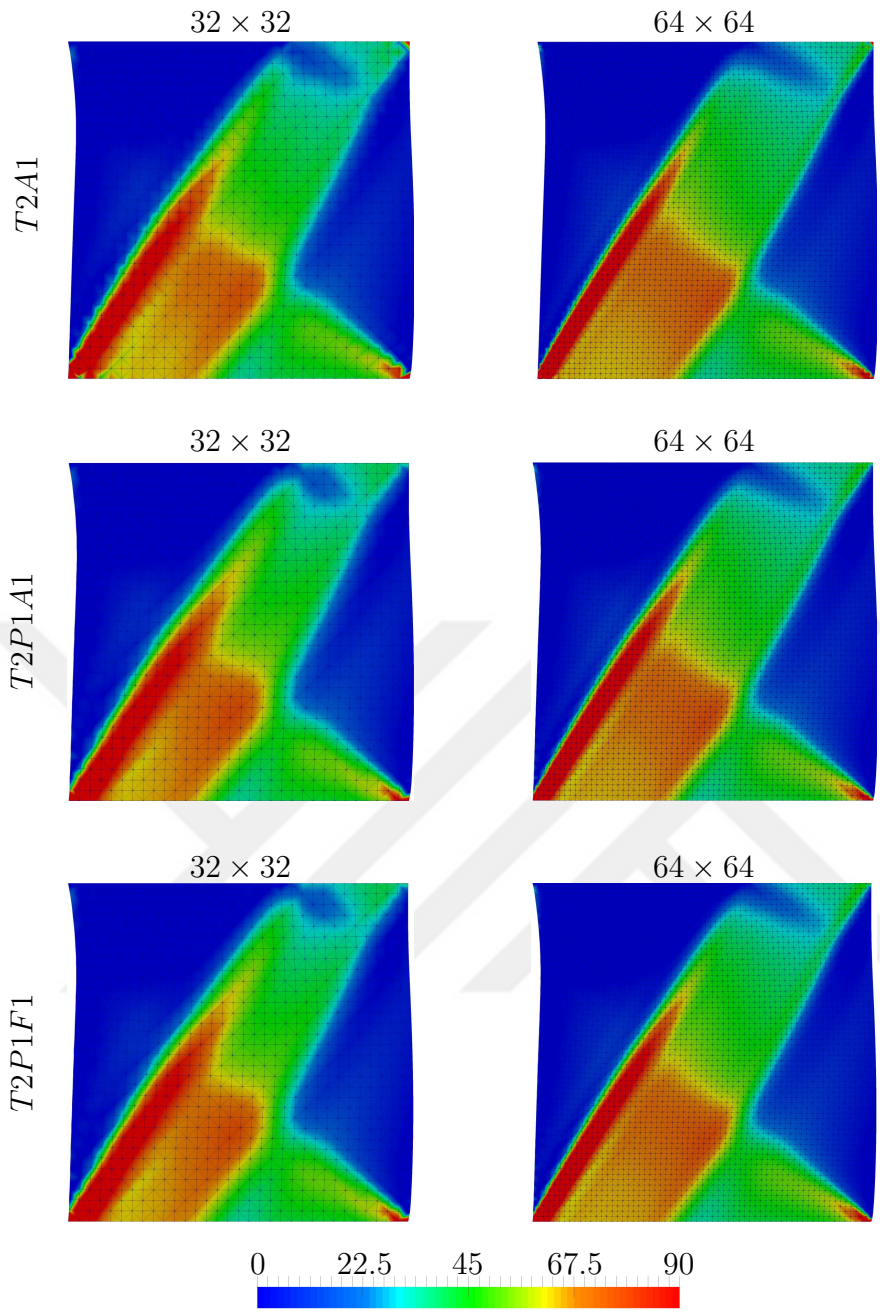

Figure 3.18: Cauchy fiber stress $\boldsymbol{\sigma}_f$ distribution of $T2A1$, $T2P1A1$ and $T2P1F1$ elements for dual clamped patch test where $\nu = 0.49$ and $\mu_f = 10^4$.

CHAPTER 4

THEORY OF FINITE GROWTH MECHANICS

Growth-induced deformations show up in living systems (tissue, plants, etc.) and the development of engineering devices. It is the mechanism that can be driven by different physics, such as chemical or mechanically induced, in biological tissues. The detailed introduction to the growth-induced deformations and instabilities is given in Chapter 1. Growth beyond the physiological limit causes pathological conditions in biological tissues. Due to the growth, tissues can be subjected to remodelling, residual stress, and instabilities; these can be indicators of pathological diseases. The growth-induced deformations are mostly found in arteries, muscles, tumors, the heart, etc. For example, the growth can be the reason of the eccentric and concentric hypertrophy in the heart. The physics behind the eccentric growth is chronic volume overload. On the other hand, chronic pressure overload causes the concentric hypertrophy and ventricular wall thickening [6]. The growth-induced instabilities can also be revealed mostly in the airways, brain, skin, etc. While brain folding is a consequence of the cell-division and formation of the brain, instabilities of the regular shape of biological organs such as the airways are a result of pathological conditions. The mechanics of growth-induced deformations and instabilities need to be understood to estimate the post-behaviour and development treatment methodologies such as tumor invasion, stent restenosis, tissue expansion etc. [29]. Since most of the tissues are composed of a multi-layer isotropic or anisotropic layout, compression type of loading causes different levels of stress in the thin stiff film and the compliant substrate; thus, buckling leads to a release of energy. The stiffness variation of the layers, the fiber contribution, fiber stiffness, and growth isotropy or anisotropy are the critical factors that trigger instabilities.

The finite growth can be modeled as a scalar parameter or as a second order tensor. Based on the application, it can be either defined as an internal variable and obtained through a driving mechanism or it can be directly defined within a confined domain by a scalar known quantity, which can be the direct input of the model. The growth mechanism can be isotropic or anisotropic which are categorized into volume growth, area growth and fiber growth. More detailed background information and details can be found in [29].

In this chapter, firstly the kinematic framework of finite growth will be presented based on elastic and growth decomposition of deformation gradient. Then constitutive equations will be given in the context of stress and corresponding moduli. In the following section, types of finite growth tensors will be presented. Then, numerical examples consisting of growth-induced deformations and instabilities will be provided on the Python-based automated finite element software FEniCS [12]. Afterwards, the five-field Hu-Washizu type mixed variational formulation was applied for the finite growth problems using $T2P0F0$ element formulation. The planar growth-induced primary and secondary instabilities on three-dimensional bilayer type tissue will be presented numerically.

4.1 Kinematic Framework of Finite Growth

This section presents the kinematics of growth phenomena in a general framework and can be used for isotropic, transversely isotropic, orthotropic, and anisotropic hyperelastic solids. The kinematics is based on the multiplicative decomposition of the deformation gradient into elastic and growth tensors in the sense of Rodriguez [135] are introduced. A hyperelastic response in the intermediate state is considered. The descriptions of the motion of the body based on the reference and spatial configurations are already given in Chapter 2. Therefore same steps will not be repeated in this section. In the finite growth formulation, the key kinematic definition is the multiplicative decomposition of the deformation gradient $\boldsymbol{F}$ into a reversible elastic part $\boldsymbol{F}^e$, and an irreversible growth part $\boldsymbol{F}^g$ [135] as follows:

$$\boldsymbol{F} := \nabla_X \boldsymbol{\varphi}_t(\boldsymbol{X}) = \boldsymbol{F}^e \boldsymbol{F}^g \tag{4.1}$$

The growth configuration is also stated as incompatible whether the elastic configuration satisfies the compatibility, see Figure 4.1. In line with that, the growth term affects the constitutive equations, and the baseline elastic response is described in the intermediate configuration.

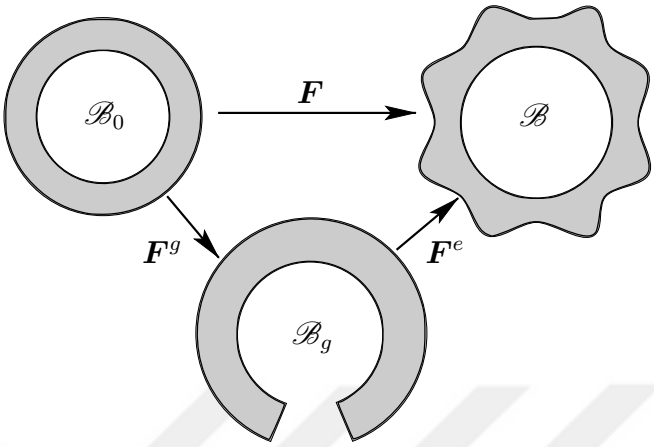

Figure 4.1: Kinematic representation of finite growth. The multiplicative decomposition of the deformation gradient $\boldsymbol{F}$ gives mapping relation based on growth state $\boldsymbol{F}^g$, and the elastic state of the deformation gradient $\boldsymbol{F}^e$. There are defined three configurations at finite growth, the first one is the original stress-free configuration in $\mathscr{B}_0$, the second one is the growth state with stress-free intermediate configuration in $\mathscr{B}_g$ which also leads to incompatibility in general, and the third is the stressed-state in deformed configuration,$\mathscr{B}$.

In the same way as split of the deformation gradient $\boldsymbol{F}$, the Jacobian J is also multiplicatively decomposed into reversible elastic volume change $J^e = \det[\boldsymbol{F}^e]$ and an irreversible grown volume change $J^g = \det[\boldsymbol{F}^g]$[136].

$$J := \det[\boldsymbol{F}] = J^e J^g \tag{4.2}$$

The condition $J := \det[\boldsymbol{F}] > 0$, $J^e := \det[\boldsymbol{F}^e] > 0$ and $J^g := \det[\boldsymbol{F}^g] > 0$ provides the non-penetrable deformations. Furthermore, the reference $\mathscr{B}_0$ and the spatial $\mathscr{B}$ manifolds are locally furnished with the covariant reference $\boldsymbol{G}$ and current $\boldsymbol{g}$ metric tensors in the neighbourhoods $\mathcal{N}_X$ of $\boldsymbol{X}$ and $\mathcal{N}_x$ of $\boldsymbol{x}$, respectively. For the mapping between the co- and contravariant objects in Lagrangian and Eulerian states, these metric tensors are needed [105]. In addition, these metric tensors also show forth the

map between the reference $\mathscr{B}_0$ and the intermediate configuration $\mathscr{B}_g$ and between the intermediate configuration $\mathscr{B}_g$ and the spatial state $\mathscr{B}$.

By the Nanson's formula, the total area change can also be decomposed into elastic and growth area change as following

$$J\boldsymbol{F}^{-T}\boldsymbol{n}_0 dA = \boldsymbol{n}da \quad \text{where} \quad J\boldsymbol{F}^{-T} = (J^g\boldsymbol{F}^{g-T})(J^e\boldsymbol{F}^{e-T}) \tag{4.3}$$

where $\boldsymbol{N}$ is the unit normal in the undeformed configuration. Similarly, the stretch λ can also be decomposed into elastic λ^e and growth component λ^g as below

$$\lambda = ||\boldsymbol{F}\cdot\boldsymbol{n}_0|| = \lambda^e\lambda^g \quad \text{where} \quad \lambda^g = ||\boldsymbol{F}^g\cdot\boldsymbol{n}_0|| \tag{4.4}$$

Then, we designate the right Cauchy Green tensor, the inverse of the left Cauchy Green tensor, and the elastic right Cauchy Green tensor,

$$\boldsymbol{C} = \boldsymbol{F}^T\boldsymbol{g}\boldsymbol{F}, \qquad \boldsymbol{c} = \boldsymbol{F}^{-T}\boldsymbol{G}\boldsymbol{F}^{-1} \qquad \text{and} \qquad \boldsymbol{C}^e = \boldsymbol{F}^{eT}\boldsymbol{g}\boldsymbol{F}^e, \tag{4.5}$$

as the covariant pull back of the spatial metric $\boldsymbol{g}$ and push forward of the Lagrangian metric $\boldsymbol{G}$, respectively. Here, in the case of Cartesian coordinates, $\boldsymbol{g}$ and $\boldsymbol{G}$ are the same as the identity tensor [6]. In order to keep the kinematics in a wide coverage, we suppose to consider for the case of anisotropy such as one-family fiber reinforcement. Then, we define the Lagrangian unit vector $\boldsymbol{n}_0$ standing for the fiber direction in continuum as

$$|\boldsymbol{n}_0|_{\boldsymbol{G}} = 1 \qquad \text{where} \qquad |\boldsymbol{n}_0|_{\boldsymbol{G}} = (\boldsymbol{n}_0\cdot\boldsymbol{G}\boldsymbol{n}_0)^{1/2} \ . \tag{4.6}$$

Then through the tangent map deformed configuration can be formed as

$$\boldsymbol{n} = \boldsymbol{F}^e\boldsymbol{F}^g\boldsymbol{n}_0 \ . \tag{4.7}$$

The boundaries of the domain can be split into Dirichlet and Neumann type as $\partial\mathscr{B} = \partial\mathscr{B}^\varphi \cup \partial\mathscr{B}^t$ and $\partial\mathscr{B}^\varphi \cap \partial\mathscr{B}^t = \emptyset$.

4.2 Governing Constitutive Equations of Finite Growth

The second law of thermodynamics states a positive dissipation by stress power and the objective rate of free energy. The dissipation inequality can be applied to form

thermodynamically consistent stress relations as

$$\mathscr{D} = \boldsymbol{S} : \frac{1}{2}\dot{\boldsymbol{C}} - \dot{\psi} = \hat{\boldsymbol{P}} : \dot{\boldsymbol{F}} - \dot{\psi} = \boldsymbol{\tau} : \frac{1}{2}\boldsymbol{\pounds}_{\boldsymbol{v}}\boldsymbol{g} - \dot{\psi} \geq 0 \tag{4.8}$$

It is significant to notice that $\hat{\boldsymbol{P}}$ implies the mixed-variant Piola tensor, which is represented by $\hat{\boldsymbol{P}} := \boldsymbol{g}\boldsymbol{P}$ [6]. The Lie derivative of the spatial metric, $\boldsymbol{\pounds}_{\boldsymbol{v}}\boldsymbol{g} = (\boldsymbol{g}\boldsymbol{l} + \boldsymbol{l}^T\boldsymbol{g})$, is equivalent to the symmetric rate of deformation tensor. $\boldsymbol{l} = \dot{\boldsymbol{F}}\boldsymbol{F}^{-1}$ is the spatial velocity gradient. By the evaluation of the dissipation inequality, stress derivations can be performed. In finite growth, hyperelasticity constitutive equations are assumed to be held on the elastic state, and growth represents an intermediate stress-free state. Depending on the microstructure of the material or the tissue, the form of the growth tensor $\boldsymbol{F}^g$ can be either isotropic or anisotropic. Stress arises in the solid domain due to the elastic part of the deformation gradient $\boldsymbol{F}^e$. The growth does not have any energy contribution to the free energy function, meaning that purely growth tensor does not cause any stress in the body. The growth tensor can directly either be dependent on a scalar strain-type variable or strain or stress driven microstructure leads the growth evolution. It can be defined by evolution equations based on an internal variable. This type of growth depends on the growth criteria as it seen in the flow rule in plasticity formulation, and growth initiates when the mechanical driving force exceeds the threshold level. For the sake of convenience, in this study, it is assumed that every continuum point exceeds the threshold level in the solid body; hence growth tensor $\boldsymbol{F}^g$ can be driven by independent certain scalar variables.

In general, fiber-reinforced rubber polymers, fibrous soft biological tissues, and reinforced composite elastomers exhibit nearly incompressible responses and, in the reinforcement direction, nearly inextensible behavior. Depending on the physical conditions, these solids can be subjected to growth or shrinkage, resulting in compression or tension in the matrix and fibers, respectively. In a general framework, in line with the macro-level continuum approach, we introduce the elastic Helmholtz free energy function for one fiber family elastomers or soft tissues that is additively split into volumetric, isotropic, and anisotropic parts.

$$\psi(\boldsymbol{g}; \boldsymbol{F}^e, \boldsymbol{n}_0) := \psi_{vol}(J^e) + \psi_{iso}(\boldsymbol{g}; \boldsymbol{F}^e) + \psi_{ani}(\boldsymbol{g}; \boldsymbol{F}^e, \boldsymbol{n}_0) \tag{4.9}$$

In general, stored free energy for hyperelastic solid is governed by three invariants of the right Cauchy Green tensor as it is given in Chapter 2. In growth-induced

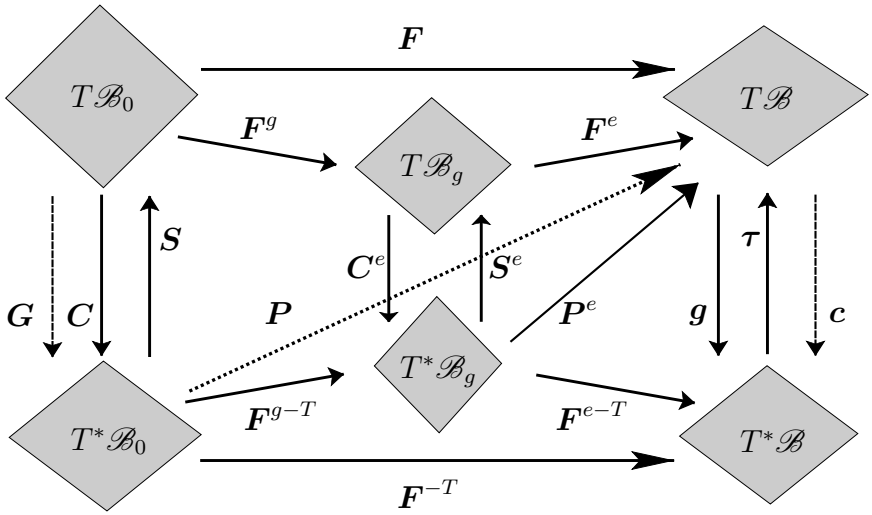

Figure 4.2: Definition of metric and stress tensors for finite growth. *Current metric* in Lagrangian configuration $\boldsymbol{C} = \boldsymbol{F}^T \boldsymbol{g} \boldsymbol{F}$. *Reference metric* in Eulerian configuration $\boldsymbol{c} = \boldsymbol{F}^{-T} \boldsymbol{G} \boldsymbol{F}^{-1}$. The relationship between the Lagrangian-intermediate configuration and intermediate-Eulerian configuration can be defined $\boldsymbol{C}^e = \boldsymbol{F}^{g-T} \boldsymbol{C} \boldsymbol{F}^{g-1}$ and $\boldsymbol{\tau} = \boldsymbol{F}^e \boldsymbol{S}^e \boldsymbol{F}^{eT}$ or directly $\boldsymbol{\tau} = \boldsymbol{F} \boldsymbol{S} \boldsymbol{F}^T$, respectively [6].

hyperelasticity free energy formulation, elastic invariants are determined as

$$I_1^e := \operatorname{tr} \boldsymbol{C}^e, \quad I_2^e := \frac{1}{2}\left[I_1^{e2} - \operatorname{tr}(\boldsymbol{C}^{e2})\right], \quad \text{and} \quad I_3^e := \det \boldsymbol{C}^e = J^{e2} \tag{4.10}$$

The elastic right Cauchy Green tensor $\boldsymbol{C}^e = \boldsymbol{F}^{g-T} \boldsymbol{C} \boldsymbol{F}^{g-1}$ is defined in the intermediate configuration. In addition to the isotropic response, the elastic anisotropic response that is generated by fibers should be defined. These additional invariants are introduced in terms of $\boldsymbol{n}_0$ unit vector of fibers in the undeformed configuration

$$I_4^e := \boldsymbol{n}_0 \cdot \boldsymbol{C}^e \boldsymbol{n}_0 \qquad I_5^e = \boldsymbol{n}_0 \cdot \boldsymbol{C}^{e2} \boldsymbol{n}_0 \tag{4.11}$$

that relates the energy storage due to fiber reinforcement in the material. By evaluating the dissipation inequality (4.8), the second Piola-Kirchhoff stress $\boldsymbol{S}$, the Piola stress $\boldsymbol{P}$ and the Kirchhoff stress $\boldsymbol{\tau}$, can be obtained thermodynamically conjugate to the right Cauchy Green deformation tensor $\boldsymbol{C}$, and deformation gradient $\boldsymbol{F}$, and the current metric $\boldsymbol{g}$, respectively [6, 67]. Then Kirchhoff stress $\boldsymbol{\tau}$ can be determined by the push forward of the second Piola-Kirchhoff stress $\boldsymbol{S}$ as below. The mapping

schematic of tensorial quantities are given in Figure 4.2.

$$\begin{aligned}
\boldsymbol{S} &= 2\partial_{\boldsymbol{C}}\psi = 2\partial_{\boldsymbol{C}^e}\psi : \partial_{\boldsymbol{C}}\boldsymbol{C}^e = \boldsymbol{F}^{g-1}\cdot\boldsymbol{S}^e\cdot\boldsymbol{F}^{g-T}\,, \\
\boldsymbol{P} &= \partial_{\boldsymbol{F}}\psi = \partial_{\boldsymbol{F}^e}\psi : \partial_{\boldsymbol{F}}\boldsymbol{F}^e = \boldsymbol{P}^e\cdot\boldsymbol{F}^{g-T}\,, \\
\boldsymbol{\tau} &= 2\partial_{\boldsymbol{g}}\psi = \boldsymbol{F}^e\cdot\boldsymbol{S}^e\cdot\boldsymbol{F}^{eT}
\end{aligned} \tag{4.12}$$

Corresponding tangent moduli $\mathbb{C}$, $\mathbb{A}$, and $\mathbb{c}$ can be derived by push forward and pull back operations from elastic moduli $\mathbb{C}^e$, $\mathbb{A}^e$, and $\mathbb{c}^e$, which can be determined by taking the second derivative with respect to conjugate tensors $\boldsymbol{C}$, $\boldsymbol{F}$ and $\boldsymbol{g}$, respectively [6, 67].

$$\begin{aligned}
\mathbb{C} &= 2\partial_{\boldsymbol{C}}\boldsymbol{S} = 2\partial_{\boldsymbol{C}}(\boldsymbol{F}^{g-1}\cdot\boldsymbol{S}^e\cdot\boldsymbol{F}^{g-T}) = \left[\boldsymbol{F}^{g-1}\bar{\otimes}\boldsymbol{F}^{g-1}\right] : \mathbb{C}^e : \left[\boldsymbol{F}^{g-T}\bar{\otimes}\boldsymbol{F}^{g-T}\right]\,, \\
\mathbb{A} &= \partial_{\boldsymbol{F}}\boldsymbol{P} = \partial_{\boldsymbol{F}}(\boldsymbol{P}^e\cdot\boldsymbol{F}^{g-T}) = \left[\boldsymbol{1}\bar{\otimes}\boldsymbol{F}^{g-T}\right] : \mathbb{A}^e : \left[\boldsymbol{1}\bar{\otimes}\boldsymbol{F}^{g-T}\right]\,, \\
\mathbb{c} &= 2\partial_{\boldsymbol{g}}\boldsymbol{\tau} = [\boldsymbol{F}\bar{\otimes}\boldsymbol{F}] : \mathbb{C} : \left[\boldsymbol{F}^T\bar{\otimes}\boldsymbol{F}^T\right]
\end{aligned} \tag{4.13}$$

where $\bar{\otimes}$ implies non-standard tensor product and can be defined as $[\bullet\bar{\otimes}\circ]_{ijkl} = [\bullet]_{ik}\,[\circ]_{jl}$. After defining Lagrangian, Eulerian, and two-point stress relations with elastic components in equation (4.12), it is required to derive corresponding the elastic second Piola-Kirchhoff stress $\boldsymbol{S}^e$ and the Kirchhoff stress $\boldsymbol{\tau}$. It should be noted that, Kirchhoff stress can be determined by the push forward of the second Piola-Kirchhoff stress. Although, as the outcome of the Eulerian configuration is more compact, we prefer to give both deformed and undeformed configurations in this study.

Depending on the nature of the material or the tissue, the growth tensor $\boldsymbol{F}^g$ can be isotropic, transversely isotropic, orthotropic or anisotropic [29]. The simplest approach is to express the growth tensor as isotropic; with this approach, the growth amount is equal in all directions. It can be a function of one scalar growth parameter, g, and then the isotropic growth tensor is defined as:

$$\boldsymbol{F}^g = [1+g]\,\boldsymbol{1} \tag{4.14}$$

where $\boldsymbol{1}$ is the identity tensor. It is also categorized as the volumetric growth. For example, tumors, arteries, and fruits may be subjected to volume growth. Note that, g is the scalar growth parameter here and should not be confused by metric tensor $\boldsymbol{g}$.

In some notations, the growth multiplier is denoted by ν^g. Then it can be specified by the evolution equations for different types of growth tensors. If the growth parameter g is zero, the growth tensor becomes equal to identity ($\boldsymbol{F}^g = \mathbf{1}$) which means there is no growth. Parameter g can be positive or negative, corresponding to growth or shrinkage in the solid, respectively. A special case of growth, namely transversely isotropic, planar growth, isotropic in-plane growth, or area growth. For example, airway walls, skin, brain, heart, and heart valve leaflets may be subjected to the area growth [29]. It exhibits uneven growth along different orthogonal axes. In this way, the growth tensor $\boldsymbol{F}^g$ is defined as

$$\boldsymbol{F}^g = [1+g]\,\mathbf{1} - g\,[\boldsymbol{m}_0 \otimes \boldsymbol{m}_0] \tag{4.15}$$

where $\boldsymbol{m}_0$ is the unit normal of membrane in the reference configuration. Equation (4.15) describes an in plane growth within membrane and there is no growth along $\boldsymbol{m}_0$ direction. For the transversely isotropic growth, the inverse of the growth tensor $\boldsymbol{F}^{g-1}$ can be defined as below [136]

$$\boldsymbol{F}^{g-1} = \left[\frac{1}{1+g}\right]\mathbf{1} - \frac{1}{g}\,[\boldsymbol{m}_0 \otimes \boldsymbol{m}_0] \tag{4.16}$$

Another type of growth can be categorized into fiber growth. It is the growth type only accounts along the fiber direction $\boldsymbol{m}_0$ and there is not any growth in other directions. It can be defined as following

$$\boldsymbol{F}^g = \mathbf{1} + [g+1]\,\boldsymbol{m}_0 \otimes \boldsymbol{m}_0 \tag{4.17}$$

Fiber growth causes the fiber lengthening such as the change of λ_g. Growth of the plant stems, eye, heart, skeletal muscle and hair can be given as example of fiber growth in a specific direction. By considering the orthotopic behaviour of the most biological tissues (i.e. myocardium tissue), the growth tensor can be introduced by the following form

$$\boldsymbol{F}^g = g^f \boldsymbol{f}_0 \otimes \boldsymbol{f}_0 + g^s \boldsymbol{s}_0 \otimes \boldsymbol{s}_0 + g^n \boldsymbol{n}_0 \otimes \boldsymbol{n}_0 \tag{4.18}$$

where $\boldsymbol{f}_0$, $\boldsymbol{s}_0$ and $\boldsymbol{n}_0$ are the unit vectors of three distinct orthogonal directions in the reference configuration. For mechanical driven growth flow rule, see [6]. In case of defining the growth tensor through the evolution law, then the general form of the Lagrangian moduli $\mathbb{C}$ is defined in the following form:

$$\mathbb{C} = 2\frac{d\boldsymbol{S}}{d\boldsymbol{C}} = 2\frac{\partial \boldsymbol{S}}{\partial \boldsymbol{C}} + 2\left[\frac{\partial \boldsymbol{S}}{\partial \boldsymbol{F}^g} : \frac{\partial \boldsymbol{F}^g}{\partial \boldsymbol{g}^g}\right] \otimes \frac{\partial \boldsymbol{g}^g}{\partial \boldsymbol{C}} \tag{4.19}$$

where $\boldsymbol{g}^g$ is the tensor that composed of growth multipliers. The first term in equation 4.19 is nothing but the moduli term that is defined in equation 4.13_1. In the absence of the evolution rule, or in other words, if the growth multipliers are scalar independent constants, then the equation 4.19 reduces to the first term. Otherwise the second term of equation 4.19 yields to

$$\begin{aligned}\frac{\partial \boldsymbol{S}}{\partial \boldsymbol{F}^g} = \frac{\partial(\boldsymbol{F}^{g-1}\boldsymbol{S}^e\boldsymbol{F}^{g-T})}{\partial \boldsymbol{F}^g} &= -\left[\boldsymbol{F}^{g-1}\bar{\otimes}\boldsymbol{S} + \boldsymbol{S}\underline{\otimes}\boldsymbol{F}^{g-1}\right] - \left[\boldsymbol{F}^{g-1}\bar{\otimes}\boldsymbol{F}^{g-1}\right] \\ &: \frac{1}{2}\mathbb{C}^e : \left[\boldsymbol{F}^{g-T}\underline{\otimes}\boldsymbol{C}^e + \boldsymbol{C}^e\bar{\otimes}\boldsymbol{F}^{g-T}\right]\end{aligned} \tag{4.20}$$

The third and the last term in equation 4.19 is related with the definition of the growth tensor $\boldsymbol{F}^g$ and the evolution law of growth terms $\boldsymbol{g}^g$.

Since we consider the tissue behaviour as an incompressible, one-family fiber reinforced (transversely isotropic) that exhibits hyperelastic reponse, similar to the free energy decomposition in (4.9), the elastic second Piola-Kirchhoff stress $\boldsymbol{S}^e$ is defined as additively decoupled terms, namely volumetric, isotropic, and anisotropic such as

$$\boldsymbol{S}^e = 2\partial_{\boldsymbol{C}^e}\psi^e = \boldsymbol{S}^e_{vol} + \boldsymbol{S}^e_{iso} + \boldsymbol{S}^e_{ani} \tag{4.21}$$

In line with the (4.21), the elastic Lagrangian moduli $\mathbb{C}^e$, can be additively split into volumetric, isotropic, and anisotropic parts respectively.

$$\mathbb{C}^e = 2\partial_{\boldsymbol{C}^e}\boldsymbol{S}^e = 4\partial_{\boldsymbol{C}^e\boldsymbol{C}^e}\psi^e = \mathbb{C}^e_{vol} + \mathbb{C}^e_{iso} + \mathbb{C}^e_{ani} \tag{4.22}$$

The volumetric part of the elastic second Piola-Kirchhoff stress $\boldsymbol{S}^e_{vol}$ reads

$$\boldsymbol{S}^e_{vol} := 2\partial_{\boldsymbol{C}^e}\psi^e_{vol}(J^e) = p^e\boldsymbol{C}^{e-1} \tag{4.23}$$

The Lagrangian moduli expression for the volumetric part is determined as

$$\begin{aligned}&\mathbb{C}^e_{vol} := 2\partial_{\boldsymbol{C}^e_{vol}}\boldsymbol{S}^e_{vol}(J^e) = (p^e + \hat{\kappa}_L)\boldsymbol{C}^{e-1}\otimes\boldsymbol{C}^{e-1} - 2p^e\mathbb{I}_{\boldsymbol{C}^{e-1}}\,, \\ &\text{with} \quad \hat{\kappa}_L = J^{e\,2}\psi''^e_{vol}(J^e)\end{aligned} \tag{4.24}$$

where $\mathbb{I}^{ABCD}_{\boldsymbol{C}^{e-1}} = \frac{1}{2}\left[\boldsymbol{C}^{e-1}_{AC}\boldsymbol{C}^{e-1}_{BD} + \boldsymbol{C}^{e-1}_{AD}\boldsymbol{C}^{e-1}_{BC}\right]$. The isotropic elastic second Piola-Kirchhoff stress is obtained as

$$\boldsymbol{S}^e_{iso} := 2\partial_{\boldsymbol{C}^e}\psi^e_{iso}(\boldsymbol{C}^e) = 2\partial_{\boldsymbol{I}^e_1}\Psi_{iso}\mathbf{1} \tag{4.25}$$

Then, the Lagrangian elastic moduli for the isotropic response can be derived as

$$\mathbb{C}^e_{iso} := 2\partial_{\boldsymbol{C}^e}\boldsymbol{S}^e_{iso}(\boldsymbol{C}^e) = 4\partial_{\boldsymbol{I}^e_1\boldsymbol{I}^e_1}\Psi^e_{iso}\mathbf{1}\otimes\mathbf{1} \tag{4.26}$$

The last term of the elastic second Piola-Kirchhoff stress is the anisotropic response due to fiber reinforcement that can be derived as

$$\boldsymbol{S}^e_{ani} := 2\partial_{\boldsymbol{C}^e}\psi^e_{ani}(I_4) = 2\partial_{\boldsymbol{I}^e_4}\Psi_{ani}\boldsymbol{n}_0\otimes\boldsymbol{n}_0 \tag{4.27}$$

Finally, the corresponding anisotropic elastic Lagrangian moduli read

$$\mathbb{C}^e_{ani} := 2\partial_{\boldsymbol{C}^e}\boldsymbol{S}^e_{ani}(I_4) = 4\partial_{\boldsymbol{I}^e_4\boldsymbol{I}^e_4}\Psi^e_{ani}\boldsymbol{n}_0\otimes\boldsymbol{n}_0\otimes\boldsymbol{n}_0\otimes\boldsymbol{n}_0 \tag{4.28}$$

By applying pull-back mathematical operation to elastic second Piola-Kirchhoff stress $\boldsymbol{S}^e$ such as $\boldsymbol{S} = \boldsymbol{F}^{g-1}\boldsymbol{S}^e\boldsymbol{F}^{g-T}$, we determine the second Piola-Kirchhoff stress $\boldsymbol{S}$ in reference configuration as following

$$\boldsymbol{S} = 2\frac{\partial\Psi}{\partial\boldsymbol{C}} = p\boldsymbol{C}^{-1} + 2\partial_{\boldsymbol{I}^e_1}\Psi_{iso}\boldsymbol{C}^{g-1} + 2\partial_{\boldsymbol{I}^e_4}\Psi_{ani}c^2\boldsymbol{n}_0\otimes\boldsymbol{n}_0 \tag{4.29}$$

where c is the scaling factor that is resultant of $\boldsymbol{F}^{g-1}\cdot\boldsymbol{n}_0 = c\boldsymbol{n}_0$ where it depends on the choice of growth tensor $\boldsymbol{F}_g$ and it is formed by growth multiplier g. Then by applying push forward mathematical operation to second Piola-Kirchhoff stress $\boldsymbol{S}$ such as $\boldsymbol{\tau} = \boldsymbol{F}\boldsymbol{S}\boldsymbol{F}^T$, we determine the Kirchhoff stress $\boldsymbol{\tau}$ in spatial configuration as following

$$\boldsymbol{\tau} = 2\partial_{\boldsymbol{g}}\Psi = p\boldsymbol{g}^{-}1 + 2\partial_{\boldsymbol{I}^e_1}\Psi_{iso}\boldsymbol{b} + 2\partial_{\boldsymbol{I}^e_4}\Psi_{ani}c^2\boldsymbol{n}\otimes\boldsymbol{n} \tag{4.30}$$

Then corresponding moduli in reference and spatial configurations can be found by using equations 4.19 and 4.13.

4.3 Numerical Examples for Finite Growth

In this section, variety of numerical examples regarding growth-induced deformations, such as the inhomogeneous growth of a two-dimensional plate, isotropic growth of a bilayer formed of a flower petal, and numerical examples focused on instabilities such as post-buckling of a two-dimensional bilayer structure and cortical folding of the brain in two and three-dimensional cases, will be given.

Inhomogeneous growth of a plate

This example is demonstrated to reveal the effect of the growth in a simple geometry. In line with [74] and [137], plain strain assumption has been applied to 2D rectangular plate geometry. Geometrical dimensions and finite element setting have been given in Figure 4.3. The geometry has been constraint along the edge $X = 0$ and the origin

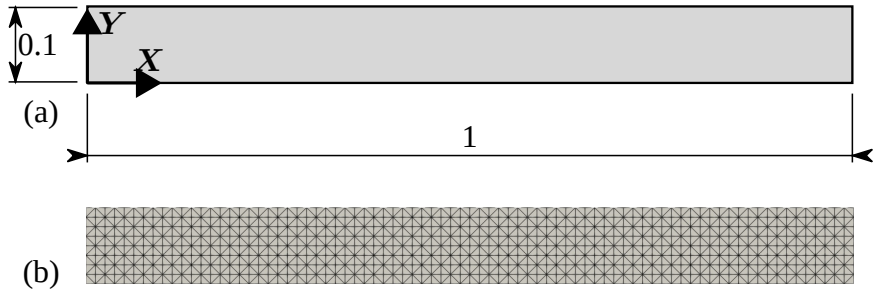

Figure 4.3: (a) Geometric unitless dimensions of the 2D plate, (b) finite element setting of the model

corner node at $X = 0$ and $Y = 0$ are fixed to prevent displacement in any directions. In the hyperelastic model, $T2P0$ element formulation has been used based on the following free-energy function:

$$\Psi = \frac{\mu}{2}(\bar{I}_1 - 3) + \frac{\kappa}{2}(J^e - 1)^2 \tag{4.31}$$

where $\mu = 10^3$ and $\kappa = 10^3\mu$ that leads to nearly incompressible limit. The growth tensor is defined inhomogeneous though the height as following

$$\boldsymbol{F}^g = \begin{bmatrix} 1 + \pi Y & 0 & 0 \\ 0 & 1 & 0 \\ 0 & 0 & 1 \end{bmatrix} \tag{4.32}$$

The growth tensor was applied incrementally in 50 steps. The distribution of growth component of Jacobian J^g is given in Figure 4.4. Due to the inhomogeneous growth definition along $\boldsymbol{Y}$ axis as in equation 4.32, it creates growth gradient in vertical direction and bends the plate. Note that, since there is no constraint to prevent its free-motion, it results in zero volumetric stress, such as $p = 0$ in the entire domain.

3D growth of a bilayer flower petal

Different growth fractions of each layer of bilayered structures may lead to a variety of shapes because of their geometries or surrender constraints. This mechanism

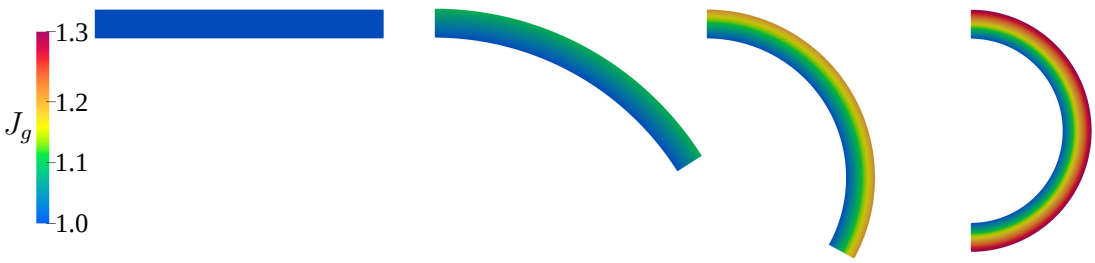

Figure 4.4: Growth-induced deformation of a 2D plate in different time increments such as $t = 0$, $t = 0.33$, $t = 0.66$ and $t = 1.0$, respectively. The contour provides the variation of J_g.

is very common for plants and even for actuators that mimic nature, such as a gripper. The flower petal is considered a two-layered structure with different mechanical properties, as proposed by Wang et al. [138] and used by [74]. The top layer which is not subjected to growth, has a $t_t = 0.03$ unit thickness with $\mu_t = 1000$ unit shear modulus. The bottom layer that presents the isotropic growth, has has a $t_b = 0.02$ unit thickness with $\mu_b = 10\mu_t$ unit shear modulus. The geometric representation of the single flower petal with its dimensions and finite element mesh configuration is given in Figure 4.5. The petal is fixed in three directions to prevent movement from the bottom face of the triangular root region. Isotropic type of growth tensor $\boldsymbol{F}^g = (1+g)\mathbf{1}$

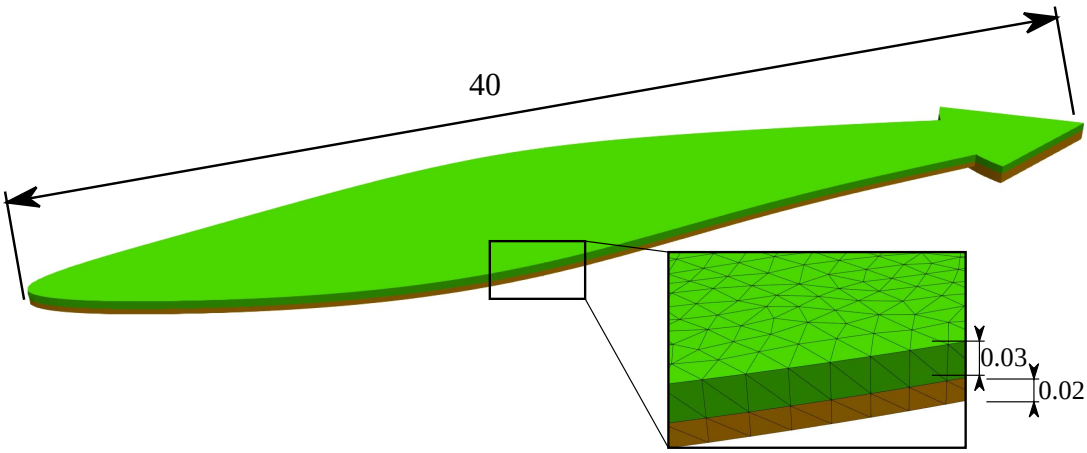

Figure 4.5: The geometrical dimensions (in mm) of a single flower petals and zoomed view of finite element mesh.

has been introduced for the bottom layer of the petal where $g = 0.05$ and applied incrementally. The hyperelastic free-energy function is defined the same as in equa-

tion 4.31. The bulk modulus of the top and bottom layers are defined as $\kappa_t = 10^3\mu_t$ and $\kappa_b = 10^3\mu_b$ respectively. The isotropic growth-induced deformations are given in Figure 4.6 for different value of growth multiplier g.

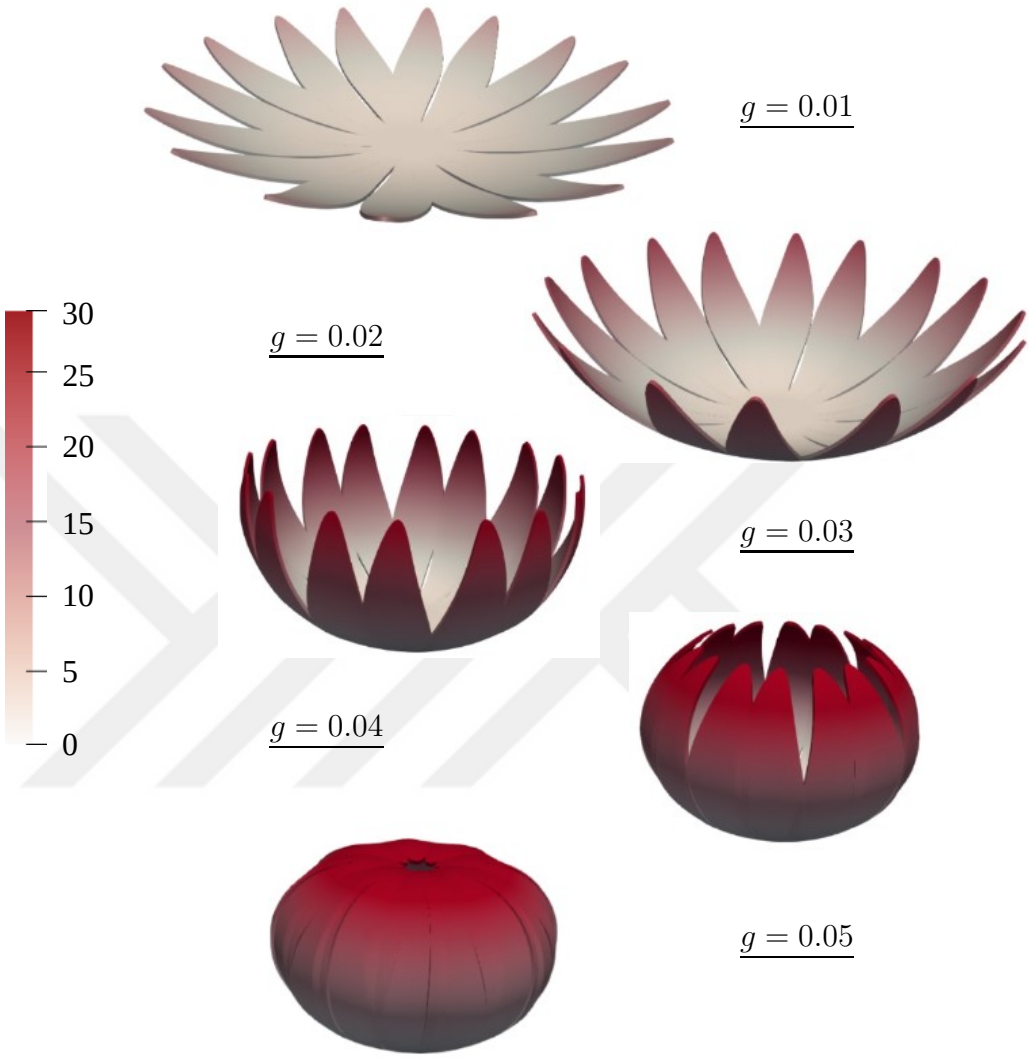

Figure 4.6: Growth-induced displacement (in mm) contour of flower petal which is subjected to isotropic growth on bottom layer as $\boldsymbol{F}^g = (1+g)\mathbf{1}$.

Two-dimensional growth-induced instabilities of bilayer structure

Since most of the biological tissues are made of layered structures that have different mechanical properties. Due to the variation of growth initiation between layers, there may be compressive stress and resulting instabilities such as wrinkling or more

complex post-buckling behaviours. This phenomenon is well captured during the development of the tissue, observation of pathological issues, or the development of treatment methods. For example, wrinkling of the skin and folding of the airways are common observances in terms of growth-induced instabilities. In this example, two-dimensional growth-induced instabilities will be analyzed for a thin stiff film on a compliant soft substrate [68]. The geometrical description and a portion of the finite element mesh are presented in Figure 4.7. The length of the geometry is defined as

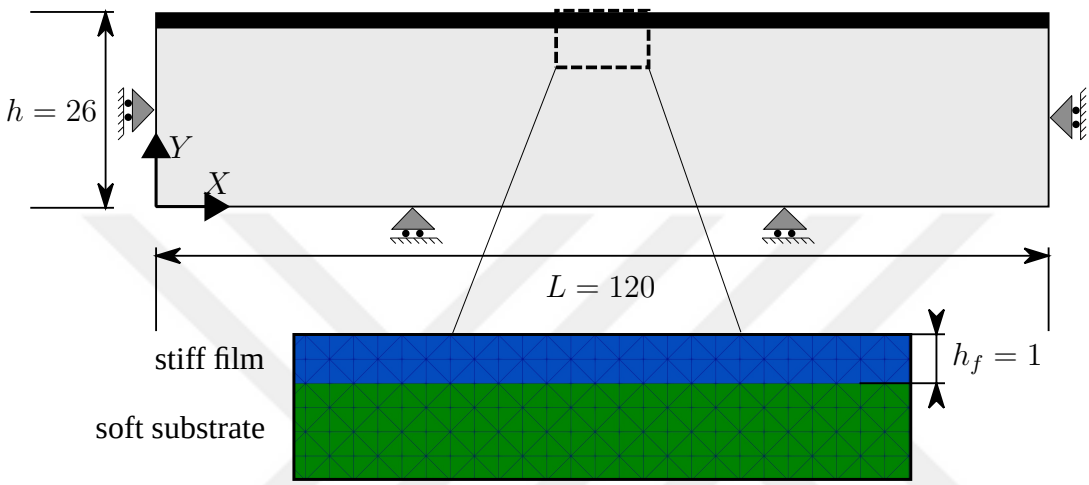

Figure 4.7: The geometrical unitless dimensions of thin stiff film on compliant soft substrate and zoomed view of finite element mesh.

$L = 120$, the height of the substrate is $h_s = 25$ and the height of the stiff film is $h_f = 1$. The left ($X = 0$) and right ($X = 120$) walls are fixed along Y axis and the movement in X is set to free. Additionally, the bottom edge of the substrate where $Y = 0$ is fixed along Y axis to prevent motion and kept free in X axis. $24,960\ T2P0$ elements have been used in two-dimensional plain-strain problem.

The hyperelastic free-energy function is defined the same as in equation 4.31. The shear modulus of the substrate is taken as $\mu_s = 1$ and the shear modulus of the film layer is $\mu_f = 100\mu_s$. In addition, the bulk modulus of the substrate and the stiff film layers are defined as $\kappa_s = 10^3\mu_s$ and $\kappa_f = 10^3\mu_f$ respectively which sets the Poisson's ratio as $\nu = 0.4999$.

Two of the layers are subjected to isotropic growth in two-dimensional domain such as $\boldsymbol{F}^g = (1 + g)\mathbf{1}$. There are defined variable incremental sub-steps to catch and

observe the post behaviours of instabilities such as between $\Delta_t = 10^{-3} - 10^{-4}$. Since the rectangular domain in Figure 4.7 is numerically perfectly generated and it does not reflect material disorders. Therefore, in such problems, to initiate the instabilities, there should be defined perturbations that will have no effect on the results. To account that, eccentric traction force (around 10^{-4} order of magnitude) has been defined in the two nodes at the top of stiff film layer along vertical axis. The displacement response and corresponding pressure contours at different growth increments are given in Figure 4.8. For the predefined mechanical properties, due

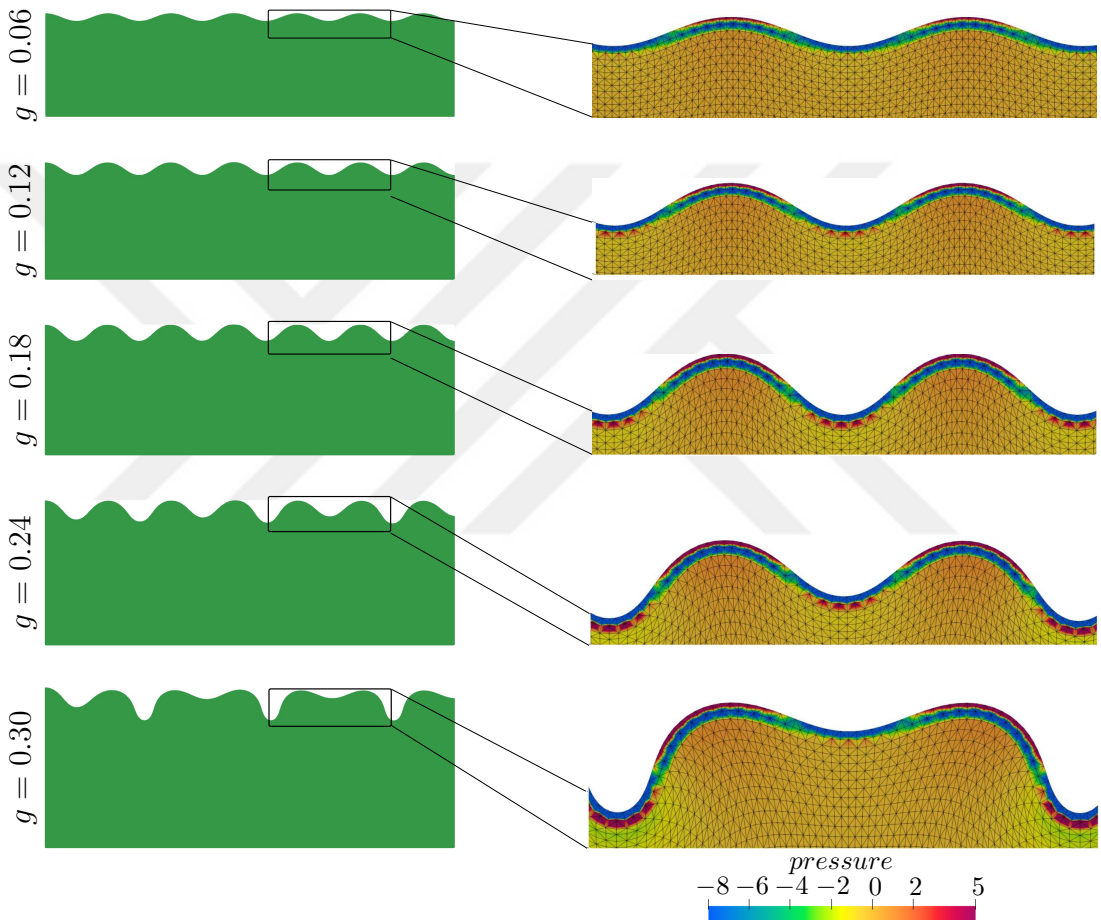

Figure 4.8: The deformation pattern and pressure contours of bilayer structure in different growth g increments in left and right columns, respectively.

to the stiffness ratio between the stiff film and soft substrate, compression stress is revealed, causing instabilities by releasing the energy. The first buckling appears at $g = 0.024$ as a sinusoidal wrinkling form and the secondary buckling is observed at $g = 0.2346$ as periodic-doubling form.

Growth-induced cortical folding of the brain

In this sub-section, growth-induced cortical folding of the human brain with different stiffness ratios between the gray and white matter will be analyzed in two and three dimensions. The brain is mainly composed of white matter as sub-cortex and gray matter as cortex. In this study, it is assumed that the brain, which is composed of these tissues and other inner sub-organs, is neglected. The brain is multi-layer layout and is subjected to compression between layers, resulting in folding and wrinkling patterns. The sliced schematic view of the brain is given in Figure 4.9. The brain is

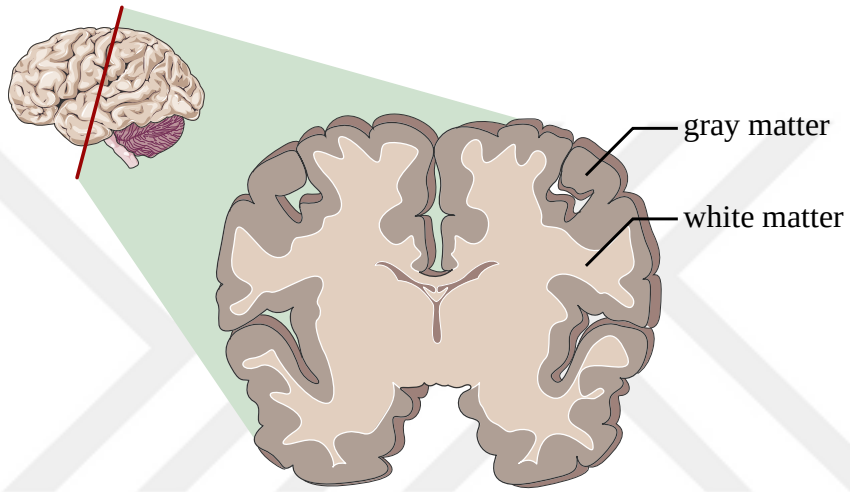

Figure 4.9: Main ingredients of the brain in terms of volume rendering. (The section view of the brain was partly generated using Servier Medical Art, provided by Servier, licensed under a Creative Commons Attribution 3.0 unported license.)

grown as a complex folded structure, and there have been significant research efforts to understand the brain's morphology [33, 139, 140, 25, 141, 142, 143, 144]. The brain complexity in the outer surface of human brain increases with ageing [140]. Budday et al. [139] mentioned that larger mammals have larger brain and that also relates the folding complexity. However, cortical thickness can be different in different species regardless of the size. There is a stiffness contrast between the brain layers (gray and white matter), which is about order of one. There is also difference between the growth development of the layers. In this study, it is assumed that only gray matter is subjected to isotropic growth but white matter is on the rest. Budday et al. [140] suggested the growth ratio between brain layers is about 100, therefore,

we neglect the growth in the substrate in this example. The following Neo-Hooken free-energy functional has been defined

$$\Psi(\boldsymbol{C}^e) = \frac{\mu}{2}\left(I_1^e - 3 - 2\ln(J^e)\right) + \frac{\lambda}{2}\ln^2(J^e) \tag{4.33}$$

where λ and μ are Lame constant and shear modulus respectively. In line with [140] we take shear modulus of gray matter as $\mu_{gray} = 3.3 \times 10^{-3}$ MPa and the shear modulus of white matter is defined to examine as a result of two different stiffness ratio as $1/10$ and $1/5$. Bulk modulus of two layers are taken as $\kappa_{gray} = 10^3\mu_{gray}$ and $\kappa_{white} = 10^3\mu_{white}$ that results with near-incompressibility condition.

Although the white matter is anisotropic in nature because of the axonal fibers, in the literature the brain is mostly modelled as two layered isotropic material as we follow same here. Axons are not only contributing to the anisotropy but their layout is too complex in the brain, see Louis et al. [142]. In order to make a realistic simulation, three-dimensional CAD geometry of a human brain was taken from [145] by permission who created the solid geometry of a real human brain by using magnetic resonance imaging. Since the MRI belongs to mature human, it is already folded in complex pattern. Our aim is to initiate the instabilities from the unfolded brain geometry, the STL geometry file is shrink to observe the nearly unfolded configuration. Since the brain is partially folded on birth, the example that we follow here covers the brain grown for a fetus. See, Huang et al. [146] who has examined the characterization of human fetal brain in different time stages. Then after shrinking the brain geometry to get smooth surface, it is neccessary to define the thickness of gray matter layer for the human brain. Fischl et al. [147] and Narr et al. [148] mentioned that the cortex has a thickness and varies between 1 to 4.5 mm and has 2.5 mm an overall average thickness. The thickness variation is common in different regions of the brain. In the view of such information, we created a final geometry for the unfolded human brain that has average thickness of 2.5 mm for the layer of gray matter. Since we perform both two-dimensional and three-dimensional growth analysis of the brain, two geometrical configurations are given in Figure 4.10. In order to take computational efficiency into the account, three-dimensional analysis has been performed by using half of the entire brain. In two-dimensional configuration, the sliced geometry of the brain was constrained at the bottom edge and prevented movement in the vertical axis, see Figure 4.10. In three-dimensional configuration, there is defined

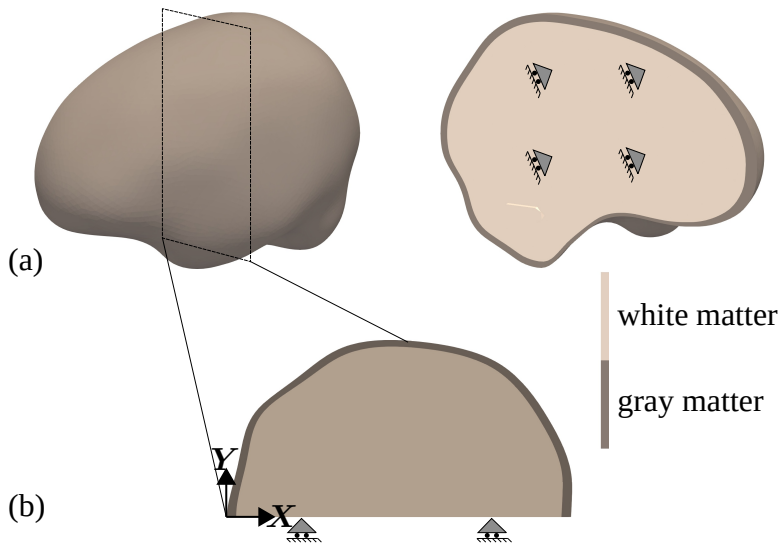

Figure 4.10: Geometric representation of half smooth brain. (a) three-dimensional demonstration (b) two-dimensional sliced piece

symmetry boundary condition in the half sliced surface of the brain geometry and displacements are fixed normal to the surface and other degree of freedoms are set to free. The finite element setting of two of the model are given in Figure 4.11. $T2P0$

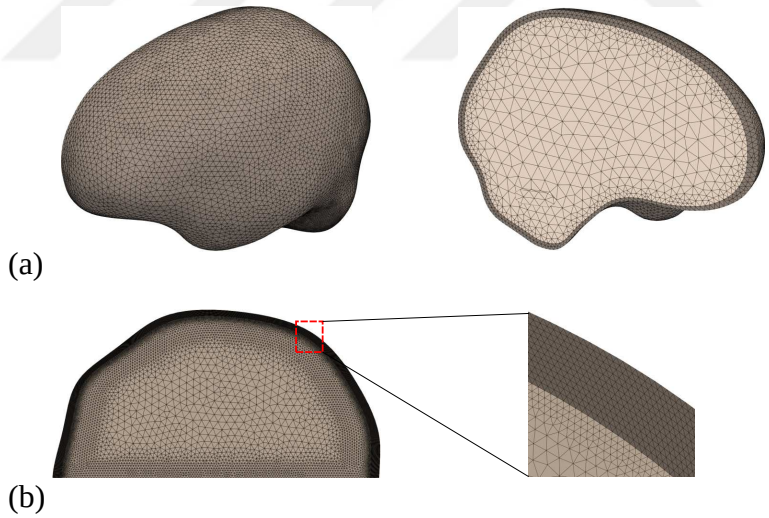

Figure 4.11: Finite element mesh settings of brain geometry (a) three-dimensional demonstration (b) two-dimensional sliced piece

element formulation has been used for the both model. The growth has been defined isotropically such as $\boldsymbol{F}^g = (1+g)\mathbf{1}$ and applied incrementally. Since those two-dimensional and three-dimensional geometries are realistic in terms of their shape,

they have smooth curvatures. Therefore there is no need to define an perturbation as a traction or displacement. The growth-induced deformation plots are given based on pressure contours for two-dimensional model with different gray matter/white matter shear modulus ratios such as $\mu_{white}/\mu_{gray} = 1/10$ and $\mu_{white}/\mu_{gray} = 1/5$ in Figure 4.12. The plots are given for different incremental growth state. The instabilities reveals by increasing the growth multiplier g due to the energy release of the grown stiff and thin layer of gray matter. It is also concluded that, the higher shear modulus ratio causes the instability initiation in a smaller g value. The growth-induced deformation

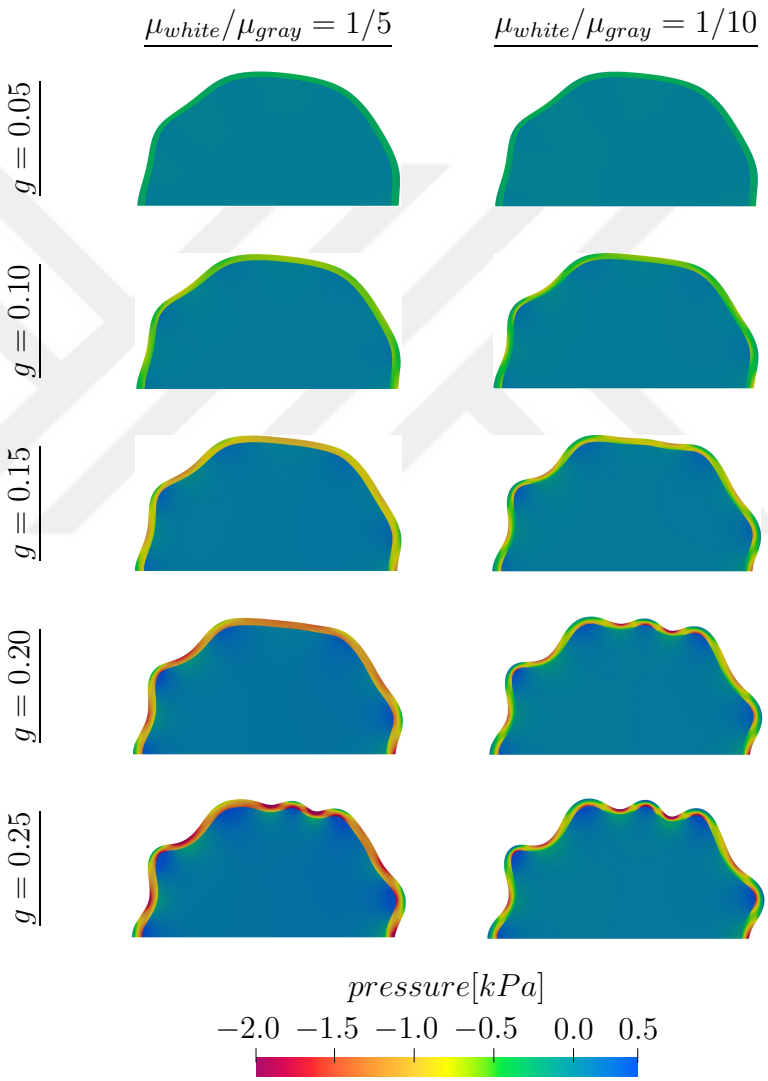

Figure 4.12: Growth-induced deformations and pressure variations of sliced two-dimensional brain with $\mu_{white}/\mu_{gray} = 1/10$ and $\mu_{white}/\mu_{gray} = 1/5$

plots are given based on pressure contours for three-dimensional model with differ-

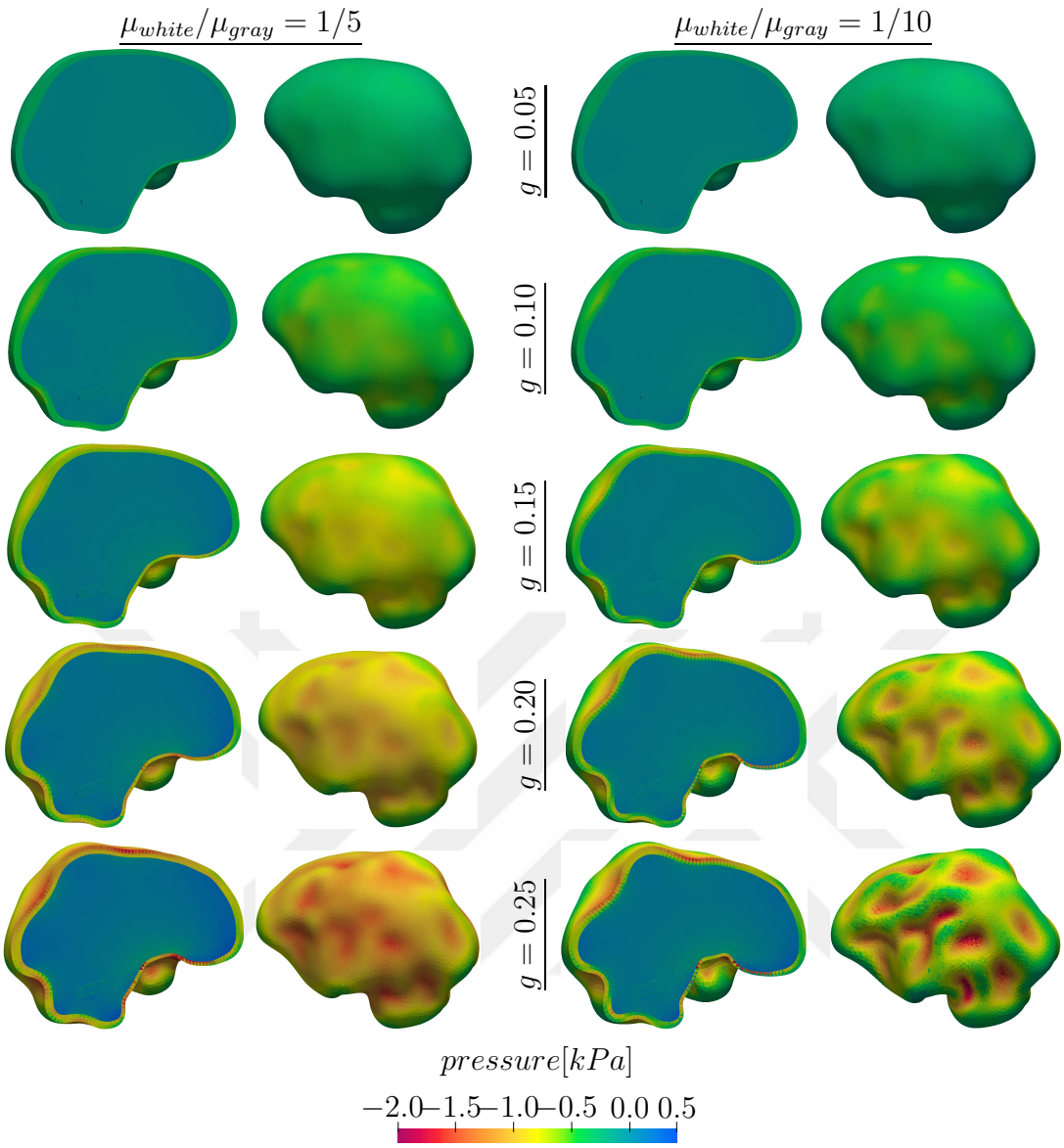

Figure 4.13: Growth-induced deformations and pressure variations of three-dimensional brain with $\mu_{white}/\mu_{gray} = 1/10$ and $\mu_{white}/\mu_{gray} = 1/5$ ($\times 2$ scaled view)

ent gray matter/white matter shear modulus ratios such as $\mu_{white}/\mu_{gray} = 1/10$ and $\mu_{white}/\mu_{gray} = 1/5$ in Figure 4.13. For each growth incremental image, two views are given, such as the inner and outer views of the brain model, to better observe growth-induced instabilities. Similarly to the two-dimensional case, when the stiffness ratio between film and substrate increases, the instability is triggered at an earlier stage. Therefore, it results in wrinkles that have a higher amplitude level. Growth-induced folding patterns of the brain are very clearly seen at $g = 0.10$ growth level. It can be

noted from Figure 4.13 that during the buckling and post-buckling stages, while concave patterns have positive pressure contours, convex regions have negative pressure distributions.

4.4 Extended Five-field Formulation for Finite Growth

In this section, the scalar conjugate pair type of five-field mixed variational formulation in the sense of [104] is extended for growth-induced deformations. In general, fibrous soft biological tissues exhibit nearly incompressible responses and, in the reinforcement direction, nearly inextensible behavior. It is essential to capture and understand the mechanics behind growth-induced deformations and critical instability conditions in three dimensions for fiber-reinforced tissues and bilayer structures. In section 4.1, field equations and corresponding state variables for fiber-reinforced transversely isotropic hyperelastic solid is already presented for growth-induced problems. Corresponding stress and moduli expressions are also derived for both Lagrangian and Eulerian configurations. In this section, the mixed variational formulation, which leads to the quasi-incompressible and quasi-inextensible element formulation, will be introduced. Finally, a five-field mixed variational formulation and respective Euler-Lagrange equations are demonstrated. Since we decomposed the deformation gradient into irreversible growth and reversible elastic part $\boldsymbol{F} = \boldsymbol{F}^e \boldsymbol{F}^g$, the elastic part responsible for mapping of incompatible intermediate configuration to the compatible deformed configuration. Therefore the free-energy is only the function of elastic part of the deformation gradient $\boldsymbol{F}^e$ and the growth component $\boldsymbol{F}^g$ does not have any contribution to stress evolution. We will extend the five-field variational formulation for finite growth based on the additively split of the free-energy function into volumetric, isotropic and anisotropic parts as stated in equation 4.9. The potential functional can be defined as below for the *finite elasticity*

$$\hat{\Pi}(\boldsymbol{\phi}) := \hat{\Pi}^{int}(\boldsymbol{\phi}) - \hat{\Pi}^{ext}(\boldsymbol{\phi}) \,, \tag{4.34}$$

where

$$\hat{\Pi}^{int}(\boldsymbol{\phi}) := \int_V \Psi^e(\boldsymbol{g}, \boldsymbol{F}^e)\, dV \quad \text{and} \quad \hat{\Pi}^{ext}(\boldsymbol{\phi}) := \int_V \boldsymbol{\phi} \cdot \rho_0 \bar{\boldsymbol{b}}\, dV + \int_{\partial V} \boldsymbol{\phi} \cdot \bar{\boldsymbol{t}}\, dA \,. \tag{4.35}$$

For the elastic loading, the stored energy in the body can be defined by $\hat{\Pi}^{int}(\boldsymbol{\phi})$, and $\hat{\Pi}^{ext}(\boldsymbol{\phi})$ refers to the work done by external forces. In equation (4.34), ρ_0, $\bar{\boldsymbol{b}}$, and $\bar{\boldsymbol{t}}$ are the density, body force, and the surface traction, respectively. $\Psi^e(\boldsymbol{g}, \boldsymbol{F}^e)$ is the volume-specific elastic Helmholtz free energy. The boundary value problem can be determined from the elastic potential by the principle of minimum potential energy in the variational form

$$\boldsymbol{\phi}_t = \mathrm{Arg}\{\inf_{\boldsymbol{\phi}_t \in \mathscr{W}} \hat{\Pi}(\boldsymbol{\varphi}, t)\} \tag{4.36}$$

subject to Dirichlet-type boundary condition

$$\mathscr{W} = \{\boldsymbol{\phi}_t \mid \boldsymbol{\phi}_t \in \mathscr{B} \quad \wedge \quad \boldsymbol{\phi}_t = \bar{\boldsymbol{\phi}} \quad \text{on} \quad \partial\mathscr{B}_u\}\,. \tag{4.37}$$

Due to the stationary condition of the elastic potential $\hat{\Pi}(\boldsymbol{\phi})$, the variation of (4.36) along with localization theorem yields the Euler-Lagrange equation

$$J\,\mathrm{div}[J^{-1}\boldsymbol{\tau}] + \rho_0\bar{\boldsymbol{b}} = 0 \tag{4.38}$$

yielding to the balance of linear momentum for static problems in the domain $\mathscr{B}$ along with Neumann-type boundary condition

$$\boldsymbol{P}\cdot\boldsymbol{N} = \boldsymbol{\tau}\cdot\boldsymbol{n} = \bar{\boldsymbol{T}} \qquad \text{on} \qquad \partial\mathscr{B}_t \tag{4.39}$$

where we have used the identity of *Nanson's formula* as $J\boldsymbol{F}^{-T}\boldsymbol{N}\;dA = \boldsymbol{n}\;da$.

The quasi-incompressible and quasi-inextensible behavior can be sustained by two additional penalty terms in the decomposed representation (3.64) of the free energy functional as

$$\hat{\Pi}(\boldsymbol{\phi}, p^e, \theta, s^e, \lambda) := \int_V \pi^*(\boldsymbol{\phi}, p^e, \theta, s^e, \lambda)\;dV - \hat{\Pi}^{ext}(\boldsymbol{\varphi})\,. \tag{4.40}$$

The mixed potential density π^* in equation (4.40) is defined as

$$\pi^*_{int}(\boldsymbol{\varphi}, p^e, \theta, s^e, \lambda) = \Psi_{iso}(\boldsymbol{g}, \boldsymbol{F}^e) + p^e(J^e - \theta) + \psi_{vol}(\theta) + s^e(I^e_4 - \lambda) + \psi_{ani}(\lambda)\,. \tag{4.41}$$

Here, p^e, s^e are penalty parameters in intermediate state pair to the kinematic quantities θ, λ. The deformation of a solid body enforced by incompressibility and inextensibility constraints is sustained by the mixed saddle point principle as follows

$$\{\boldsymbol{\phi}, \theta, p^e, \lambda, s^e\} = \mathrm{Arg}\{\inf_{\boldsymbol{\phi}\in\mathscr{W}} \inf_{\theta} \inf_{\lambda} \sup_{p^e} \sup_{s^e} \hat{\Pi}(\boldsymbol{\phi})\}\,. \tag{4.42}$$

Taking the first variation of (4.40) with respect to $\boldsymbol{\phi}$, p^e, θ, s^e and λ provides the weak form

$$
\begin{aligned}
D\hat{\Pi}(\boldsymbol{\phi}, p^e, \theta, s^e, \lambda)[\delta\boldsymbol{\phi}] &= \int_V \{\big(\boldsymbol{\tau}_{iso} + p^e J^e \boldsymbol{g}^{-1} + 2s^e \boldsymbol{n} \otimes \boldsymbol{n}\big) \\
&: \tfrac{1}{2}\boldsymbol{\pounds}_{\delta\boldsymbol{\phi}}\boldsymbol{g}\}\, dV - \delta\hat{\Pi}^{ext}(\boldsymbol{\phi}) = 0\,, \\
D\hat{\Pi}(\boldsymbol{\phi}, p^e, \theta, s^e, \lambda)[\delta p^e] &= \int_V \delta p^e\, (J^e - \theta)\, dV = 0\,, \\
D\hat{\Pi}(\boldsymbol{\phi}, p^e, \theta, s^e, \lambda)[\delta\theta] &= \int_V \delta\theta\, (\Psi'^e_{vol}(\theta) - p^e)\, dV = 0\,, \\
D\hat{\Pi}(\boldsymbol{\phi}, p^e, \theta, s^e, \lambda)[\delta s^e] &= \int_V \delta s^e\, (I^e_4 - \lambda)\, dV = 0\,, \\
D\hat{\Pi}(\boldsymbol{\phi}, p^e, \theta, s^e, \lambda)[\delta\lambda] &= \int_V \delta\lambda\, (\Psi'^e_{ani}(\lambda) - s^e)\, dV = 0\,,
\end{aligned}
\tag{4.43}
$$

The mixed finite element formulation can be determined based on equation 4.43. Taking the first variation of 4.41, Euler-Lagrange equations can be determined as

$$
\begin{aligned}
&1. \quad J\,\mathrm{div}[J^{-1}\boldsymbol{\tau}] + \rho_0\bar{\boldsymbol{b}} = 0 \\
&2. \quad J^e - \theta = 0 \\
&3. \quad \Psi'^e_{vol}(\theta) - p^e = 0 \\
&4. \quad I^e_4 - \lambda = 0 \\
&5. \quad \Psi'^e_{ani}(\lambda) - s^e = 0
\end{aligned}
\tag{4.44}
$$

in the Neumann-type boundary conditions $\mathscr{W}_t = \{\boldsymbol{\sigma}\cdot\boldsymbol{n} = \boldsymbol{t} \quad \text{on} \quad \partial\mathscr{B}_t\}$. The consistent linearization of the mixed potential is the same as defined in equation 3.69 in the reference state. It has been implemented and discretized in Python-based open-source finite element platform *FEniCS* [12]. The linear Newton iterations are solved through MUltifrontal Massively Parallel sparse direct Solver (MUMPS)[149] in numerical examples.

<u>Growth-induced torsional artificial muscle</u>

Skeletal muscles exhibit tensile stretch activation and perform angular rotation with the skeleton [150]. To be used in soft robotics and wearable devices, artificial muscles studies have been well-attracted by researchers to develop artificial muscles those mimic the biological skeleton muscle [151, 152, 150]. There are different type of

studies on actuators those can be categorized based on; shape memory alloys, piezoelectric materials, multilayer structures, electroactive polymers, pneumatic or fluidic, fiber-reinforced and nano-reinforced structures. Using a fiber-reinforced type of structure provides the advantage of tuning the stiffness and the direction of the extension/ contraction, or torsion amount. It can also provide large strain deformations with reversible twist and untwist behaviour. In order to simulate the torsional artificial muscle, a numerical example has been performed with embedded one-family stiff fibers on a soft base matrix. The base matrix is incompressible, and fibers can be considered inextensible. Therefore, it is very suitable to use $T2P0F0$ five-field element formulation. Helical fiber layout in a cylindrical base matrix material is able to generate angular rotation by volume change. The helical angle determines the movement direction and behaviour and it is also adjustable by changing the fiber stiffness. The definition of the artificial muscle geometry and its mesh layout are presented in Figure 4.14. The radius of the cylinder is 10 unit, the length is 150 unit. The base soft

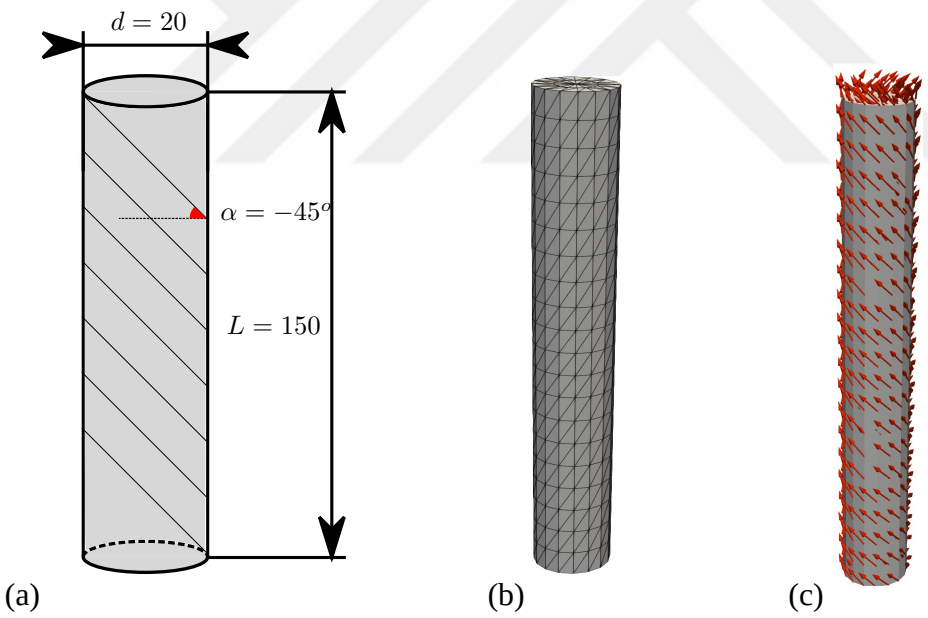

Figure 4.14: Geometrical unitless description of artificial muscle (a) geometric definitions (b) three-dimensional finite element mesh (c) vectorial representation of helical fibers

material is reinforced by one-family stiff fibers with $\alpha = -45^o$ helical angle. The

free-energy function is considered as Yeoh model by the following form:

$$\begin{aligned}\Psi^e(\bar{\boldsymbol{F}}^e) &= c_1(\bar{I}_1^e - 3) + c_2(\bar{I}_1^e - 3)^2 + c_3(\bar{I}_1^e - 3)^3 \\ &+ \frac{\kappa}{4}\left(J^{e2} - 2\ln J^e - 1\right) + \mu_f\langle I_4^e - 1\rangle^2\end{aligned} \tag{4.45}$$

where $c_1 = 0.25$ MPa, $c_2 = 0.2$ MPa and $c_3 = -0.006$ MPa are material constants taken from [104] , $\kappa = 100$ MPa is the bulk modulus and $\mu_f = 100$ MPa is the fiber stiffness, respectively. The cylinder is fixed from the bottom circular face in all directions to prevent any movement. The growth is defined only in the direction of fibers that also states the fiber growth condition as given in equation 4.17. For a positive number of growth multiplier g corresponds the volume growth in fiber directions and for the negative g, the reflects the shrinkage in the fiber direction. Both case causes a reverse torsion to each other. In the numerical example of artificial muscle, both case has been analysed. The fiber growth-induced deformations for the positive and negative growth multiplier g are given in Figure 4.15 Figure 4.16 respectively, with Cauchy-type shear stress contours. While growth in the fiber direction causes pos-

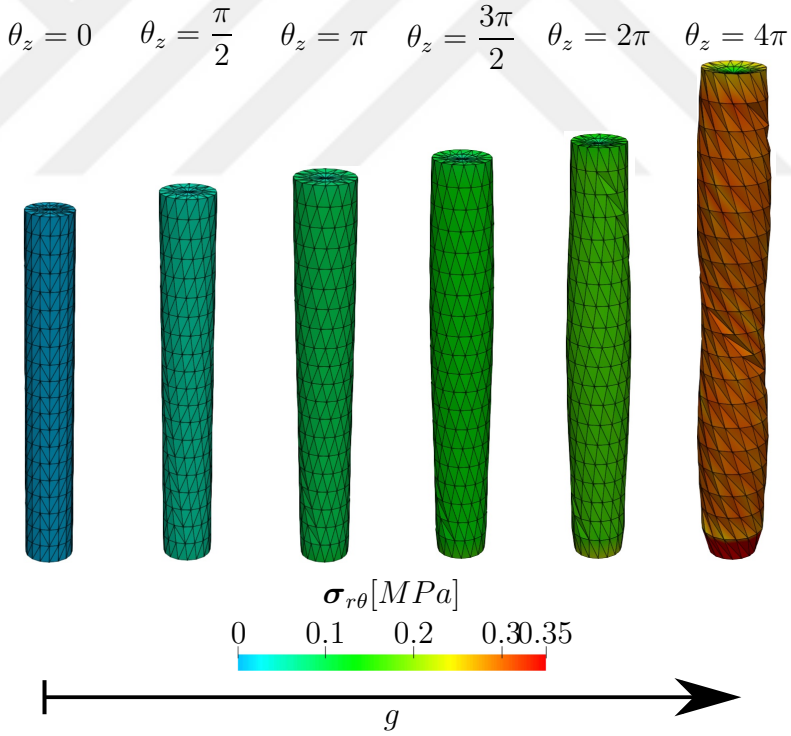

Figure 4.15: Cauchy-type shear stress distribution of artificial muscle geometry at different positive growth values. θ_z represents the angular twist around axial direction.

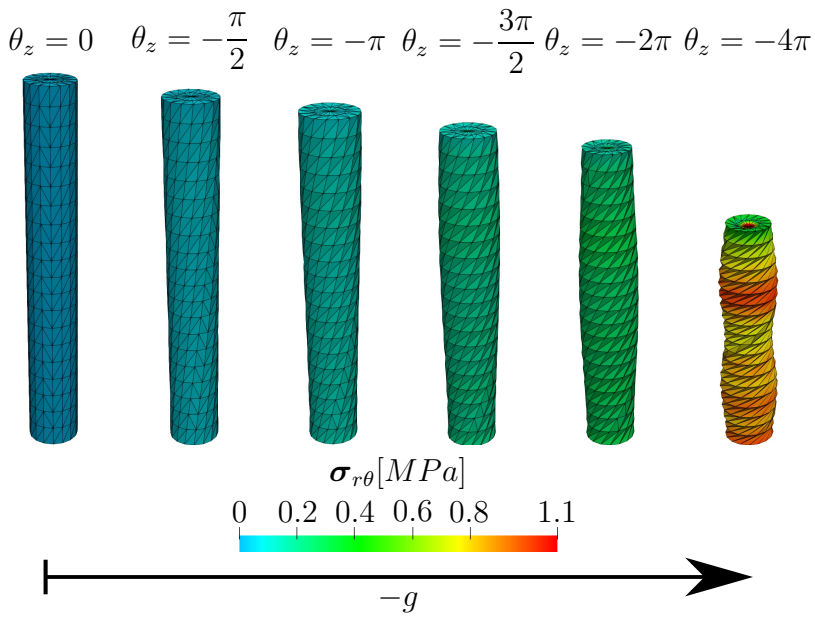

Figure 4.16: Cauchy-type shear stress distribution of artificial muscle geometry at different negative growth values. θ_z represents the angular twist around axial direction.

itive torsion with axial expansion, shrinkage in the fiber direction results in negative torsion with axial contraction. In both cases, localized regions are shown up due to high twist, which also causes element distortion at high levels. By adjusting the fiber angle and stiffness, the angular twist/axial expansion/contraction ratio can be varied depending on the requirements.

4.5 Planar Growth of Fiber-reinforced Confined 3D Bilayer Stiff film on Compliant Substrate

In this section, we present the growth-induced instabilities of fiber-reinforced bilayer confined tissue by performing on the finite element analysis program FEniCS [12] based on extended five-field element formulation. Since the effect of fiber stiffness on the instabilities for three-dimensional problems are missing in the literature, we outlined a procedure starting from two-dimensional case and set of the three-dimensional boundaries accordingly, then we examined the growth-induced instabilities for three-dimensional bilayer structure in a different range of fiber stiffness in both extensible and inextensible limits. The effect of fiber stiffness on bifurcation points of primary

and secondary instabilities have been examined in terms of growth parameter g, wavelength, displacement amplitudes and energies. Numerical outcomes of this study will help to understand the fiber stiffness effect on the buckling and post-buckling behaviour of bilayer tissues.

In general, fiber-reinforced rubber polymers, fibrous soft biological tissues, and reinforced composite elastomers exhibit nearly incompressible responses and, in the reinforcement direction, nearly inextensible behavior. It is common to observe that the growth of multi-layered materials (stiff bilayer film, hydrogels, etc.) or tissues (skin, artery, plant, etc.) can cause instabilities in the form of wrinkles, stripes, and secondary buckling shapes under residual stresses. The multi-layered materials can be composed of layers of different isotropic materials with different stiffnesses (e.g., stiff film on a compliant soft substrate). They can be formed by combinations of isotropic and fiber-reinforced anisotropic materials that we usually observe in nature, see Figure 4.17. Depending on the physical conditions, these solids can be subjected to growth or shrinkage, resulting in compression or tension in the matrix and fibers, respectively. A numerical example is demonstrated in this section through a bound-

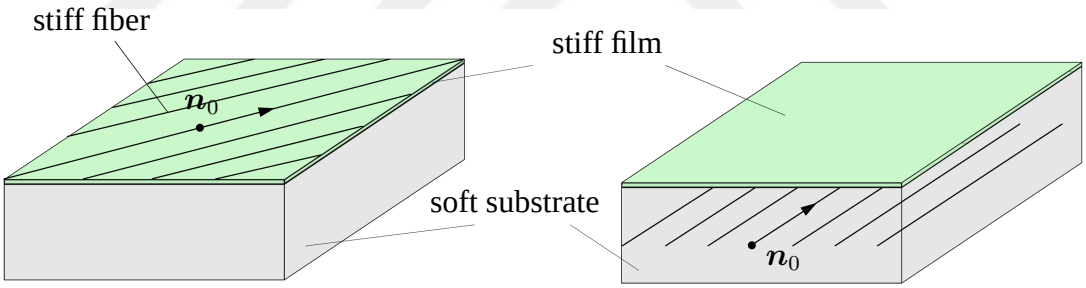

Figure 4.17: Transverse isotropy: stiff fibers embedded in the upper stiff film and stiff fibers embedded in the compliant soft substrate, respectively

ary value problem. As a mathematical representative case, the effect of the stiffness of the fibers, which exist in the stiff film, on the critical growth parameter of instability state under the planar growth are studied using *T2P0F0* element in the open-source automated finite element program *FEniCS* for a 3D stiff film on a compliant substrate. Since the domain being analyzed is a confined part/patch of the tissue, like a representative volume element, it is necessary to define boundary conditions properly to represent the overall behaviour accurately. The schematic illustration of the

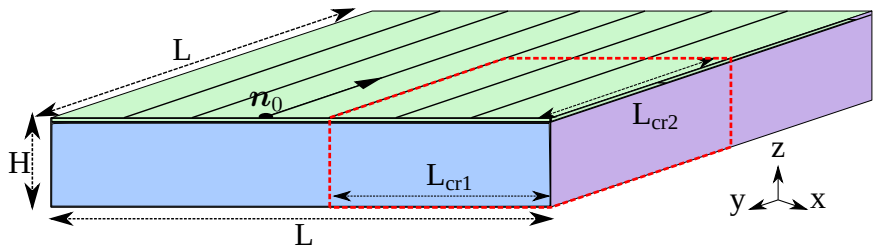

Figure 4.18: Schematic representation of the 3D bilayer structure (stiff film on compliant substrate) with its geometric dimensions. L is the edge length of the square in-plane section, H is the total height including the film and the substrate, $\boldsymbol{n}_0$ is the stiff fiber direction along y axis, L_{cr1} and L_{cr2} are the critical lowest dimensions needed to be taken into account to reflect periodic behaviour of RVE (Representative Volume Element)

3D bilayer structure is shown in Figure 4.18. In order to reflect the infinitely long plate analogy along x and y-axes, we assume that buckling behaviour of the structure repeats itself periodically with a critical wavelength (λ_{cr}). Thus, we define periodic boundary conditions on side walls (blue and purple faces and opposite faces in 4.18). In order to define periodic boundary conditions, we constrained these face pairs by displacement relations on the left face at $x = 0$ and on the right face at $x = L_{cr1}$ as shown below:

$$\begin{aligned} &x^L - x^R = L_{cr1} \\ &y^L = y^R \qquad \text{and} \qquad u^L - u^R = 0 \\ &z^L = z^R \end{aligned} \tag{4.46}$$

Similary, we define periodic boundary relations on the front face at $y = 0$ and on the rear face at $y = L_{cr2}$ as show below:

$$\begin{aligned} &x^F = x^B \\ &y^F - y^B = L_{cr2} \qquad \text{and} \qquad u^F - u^B = 0 \\ &z^F = \boldsymbol{z}^B \end{aligned} \tag{4.47}$$

where the superscripts R, L, F, and B refer to the left, right, front, and back sides, respectively. Since an infinitely long and wide structure is modeled as a finite-sized computational domain with periodic boundary conditions, the fiber direction is no

longer significant for the one family fiber configuration. In other words, for single-family fiber models with periodic boundary conditions, the same buckling modes are obtained for different angles. Therefore, the initial fiber angle $\boldsymbol{n}_0$ is aligned to the y-direction as $\boldsymbol{n}_0 = [0 \quad 1 \quad 0]^T$. In addition to periodic boundary conditions on the sides, the bottom face of the substrate is fixed in all directions.

In the definition of a periodic boundary condition, it is essential to determine the critical (characteristic) geometric dimensions; it can also be introduced as the minimum size of RVE, which reflects the actual periodic behavior without enforcing any constraint on the overall structural stiffness. The minimum critical lengths along the x and y-axes are shown in Figure 4.18 as L_{cr1} and L_{cr2}. If the RVE size is not properly chosen, the computations could miss or artificially enforce buckling mode. In order to capture the minimum required RVE size, three-dimensional long but thin bilayer structure models are defined along the fiber direction such that $L = 240$ unit, $H = 4$ unit, and $W = 1$ unit dimensions, see Figure 4.19. The total height $H = 4$ units, where 3.5 units correspond to the substrate and 0.5 units to the stiff film. The aim of the three-dimensional long but thin bilayer structure model is to identify characteristic wavelength (λ_{cr}) in a long regime by decreasing the effect of wall boundary conditions. Since single-family fiber reinforcement is studied in this study, fibers are defined along the y-axis. Then periodic boundary conditions for left-right and front-back face couples are defined as 4.46 and 4.47. In this study, the ratio of the shear modulus of the film layer (μ_f) to the substrate (μ_s) is 100, which also provides a larger wavelength [68]. Since this study aims to observe the effect of in-plane aligned fibers

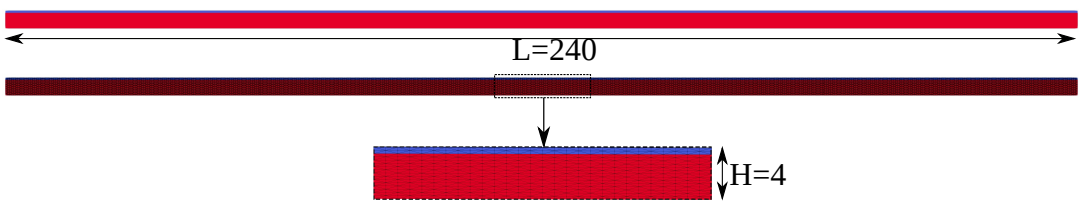

Figure 4.19: Representation of the long (L=240 unit) and thin (W=1 unit) bilayer structure consist of substrate (red) and stiff film (blue), finite element mesh and zoomed view of FE mesh respectively.

on bilayer three-dimensional structure buckling, fiber stiffness is the key parameter to

be tested for a wide range. Accordingly, fiber stiffness values are taken as μ_{fiber}=100, 250, 750, 1000, 2500. The three-dimensional bilayer structure is subjected to planar growth on both layers, and the growth parameter g monotonically increases with time step. It is important to capture buckling modes of the bilayer structure with the proper time step increment Δt. The initial time step is defined as 1×10^{-4}, and it is divided by two when a convergence problem is encountered. After the first buckling initiation, the time step is also initialized to 1×10^{-4} and it is kept constant until it reaches the secondary buckling stage. This process continues until the Newton-Raphson algorithm does not converge within 20 steps, even at the fifth loop of the time step division process. In order to trigger buckling at the critical growth value, a perturbation needs to be applied. In this study, the perturbation is defined as a minimal eccentric distributed load along x and y-directions. The free-energy function is considered as the following form in equation 4.48 and the corresponding material parameters used in the three-dimensional bilayer structure are given in Table 4.1.

$$\Psi^e(\boldsymbol{F}^e) = \frac{\lambda}{2}(J^e - 1)^2 + \frac{\mu}{2}(I_1^e - 2ln(J^e) - 3) + \mu_f\langle I_4^e - 1\rangle^2 \tag{4.48}$$

Table 4.1: Material parameters used in the analysis of three-dimensional bilayer structure with free-energy defined in equation 4.48.

Parameter	Value	Unit	Parameter	Value	Unit
μ_{film}	10^2	[–]	μ_{subs}	1.0	[–]
κ_{film}	10^5	[–]	κ_{subs}	10^3	[–]
μ_{fiber}	$100, 250, 750, 1000, 2500$	[–]	$\boldsymbol{n}_0$	$[0, 1, 0]$	[–]

In order to determine the critical buckling wavelength (λ_{cr}) and related RVE dimensions, three-dimensional long but thin bilayer structural geometry (see Figure 4.19) was analyzed for each fiber stiffness (μ_{fiber}) values listed in Table 4.1. It is aimed to observe the periodicity of the buckling behavior for all of the fiber stiffnesses and identifying the critical/characteristic lengths for the RVE that are needed for post-buckling analysis.

Periodic boundary condition enforces the same displacement vectors on boundary regions. Therefore, for a sinusoidal periodicity such as wrinkling instability, the wave-

length of the wrinkling is an essential parameter. However, due to the periodic boundary conditions, the structure is enforced to have an integer amount of sinusoidal wave pattern. In order to relax this constraint, we have performed analyses for different lengths (L) of two-dimensional bilayer structure. Although, Figure 4.19 described the structure length that defined in analysis $L = 240$ unit, we have also examined the wavelength characteristics of different lengths, starting from $L = 15$, 30, 60, 120 and finally after revealing the convergence trend for each fiber stiffness we stopped at $L = 240$. The wavelength characteristics for different plate lengths have been shown in Figure 4.20. In Figure 4.20, some of the lines overlaps to each other, however it

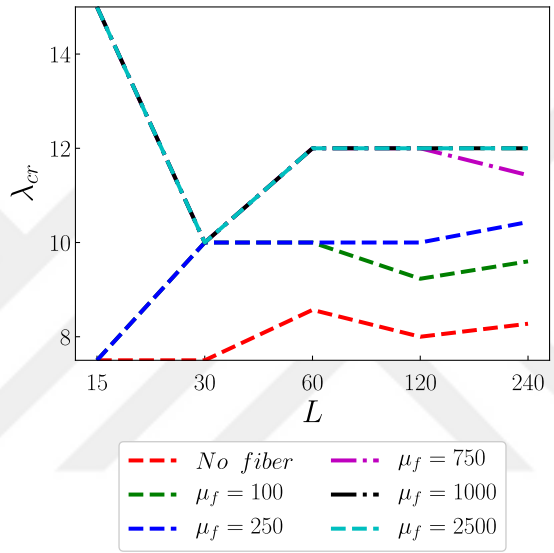

Figure 4.20: Representation of the determined wavelengths for different lengths of bilayer structure such as L=15, 30, 60, 120 and 240 units with W=1 units.

is clear to identify from the final wavelength results. It is obtained that small size of length outcomes with erroneous wavelength dimensions. Based on the stiffness characteristics of the fibers, the wavelength round-up round-down the integer value of sine wave pattern. It is possible to increase length-size further but the exact wavelength can be found at infinity. Since small amounth of change in wavelength does not effect the research interest of this study, $L = 240$ provides sufficient results in terms of determining of the critical wavelengths for each fiber stiffness. Then, the first buckling mode of bilayer structure without and with fibers has been observed and shown in Figure 4.21. Due to the contribution of fiber stiffness to the directional stiffness of the film, each model in Figure 4.21 leads to a different critical growth value g and

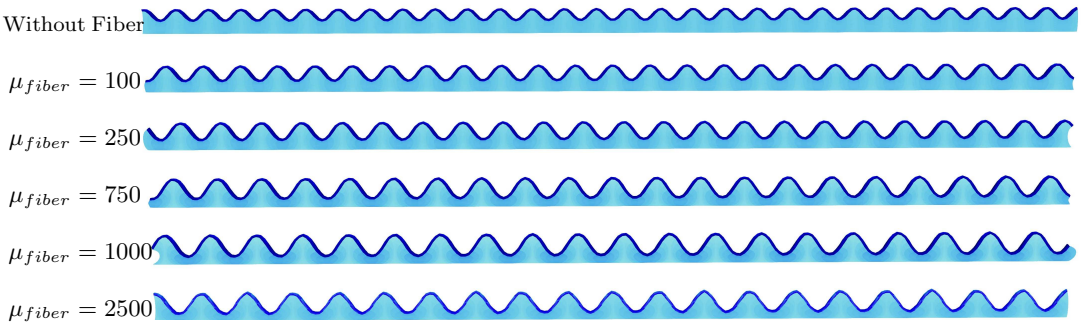

Figure 4.21: First buckling mode shapes of 2D long and thin bilayer plates with different fiber stiffness reinforcement (scaled by x5).

a different wavelength. The wavelength information acquired from Figure 4.21 will be used for the three-dimensional rectangular in-plane section of the bilayer structure as shown in Figure 4.18 to examine the first buckling mode and post-buckling behavior. As shown in Figure 4.21, the number of wrinkles decreases by increasing the fiber stiffness μ_{fiber}. It also means that the characteristic/critical wavelength increases with the fiber stiffness μ_{fiber}. In order to reflect infinite plate behavior with periodic boundary conditions and capture at least a single wrinkle in the three-dimensional RVE, the minimum critical length L_{cr2} should be at least (λ_{cr}) unit. It can also be concluded that harmonics of (λ_{cr}) will also capture the exact buckling shape. Since the buckling behavior in the x-direction (perpendicular to fibers) is likely to be decoupled from fibers and represent a behavior similar to the no fiber case, it requires a smaller wavelength to capture post-buckling mode in the x-direction. Therefore, for the bilayer model shown in Figure 4.18, L_{cr1} is taken as the same as L_{cr2} making the bilayer plate have a square in-plane section. To enlarge the coverage of the buckling more precisely within two wrinkles, L_{cr} is set to $2\lambda_{cr}$, which makes the geometrical dimensions $2\lambda_{cr} \times 2\lambda_{cr} \times H$ as shown in Figure 4.22.

In the light of these geometrical characteristic information, the effects of fiber stiffness over the primary buckling and the post-buckling regime was examined for the model shown in Figure 4.22. Before deciding the application method of the perturbation as eccentric distributed load along x and y-directions, we examined the sample instabilities with random perturbation definitions. We have divided the top of the stiff film layer into square small regions. The square small regions have the same width with the element sizes. Then, we selected randomly ten of small regions to

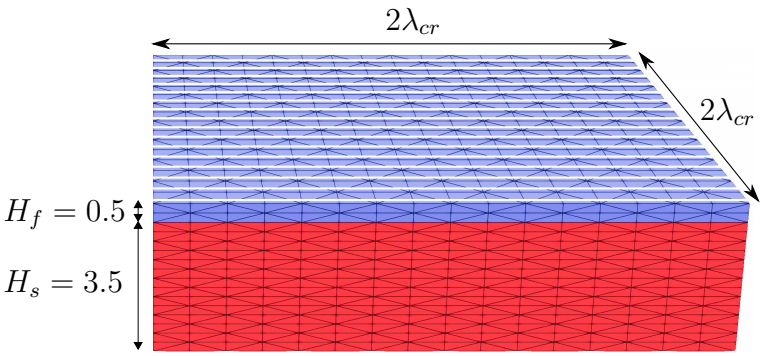

Figure 4.22: Representation of three-dimensional RVE. White lines demonstrate the stiff fibers those are aligned to the y-direction

apply traction perturbations. The perturbation magnitude is also defined randomly and it can take a negative or positive amount of load. Two of the examples of random boundaries that have been created for the randomness effects are shown in Figure 4.23. The first instability results of the two different perturbation definitions given

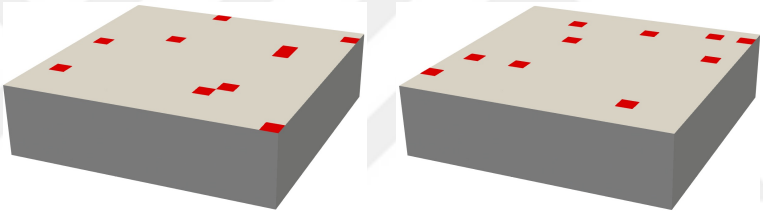

Figure 4.23: Representation of the examples for two randomly generated perturbation boundaries (with red colour) for bilayer stucture.

in Figure 4.23, are presented in Figure 4.24. It is concluded that the location of perturbation does not change the critical growth that initiates the instability, however, the magnitude and location of the perturbation causes phase change of the sine form of the wrinkle. Since we define periodic boundary condition to the side-walls, that phase shift does not affect the results.

Figure 4.25 shows pressure contours in a growth time-line where the structure is subjected to planar growth. The resultant units should be determined accordingly to the selection of consistent unit system in the modeling. Figure 4.25 gives the results for isotropic bilayer plate and fiber-reinforced bilayer structure that have μ_{fiber}=100, 250, 750, 1000 and 2500. It can be seen that in the isotropic case without fiber contribution, the first buckling triggered simultaneously in x and y-directions at the same

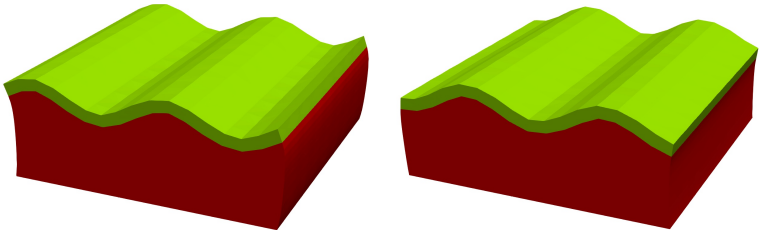

Figure 4.24: Primary instability deformation shape of two randomly generated perturbation boundaries given in Figure 4.23.

time due to isotropic nature. The isotropic case yields to a labyrinth shape by increasing the growth parameter further, as reported in [46]. For the primary buckling patterns of fiber-reinforced plates, it is clearly observed that buckling behaviors are similar, but the critical growth value that causes instability differs from each other. Furthermore, in the first buckling shape, sinusoidal wrinkles are initiated along the fiber direction, which causes energy relaxation of fibers in the critical growth parameter. Post-buckling behavior results as a secondary wrinkle with a different form and amplitude in the transverse direction perpendicular to fibers. Moreover, it is also obtained that the form of wrinkles that are observed in the first buckling mode shifts from sinusoidal to triangular shape by increasing fiber stiffness. It can be noted from Figure 4.25 that during the buckling and post-buckling stage, while concave patterns have positive pressure contours, convex regions have negative pressure.

Figure 4.26 presents the effect of fiber stiffness on the critical growth parameter that initiates buckling. While the vertical axis represents the fiber stiffness, the horizontal axis shows the planar growth parameter. Each deformed bilayer plate image corresponds to a state having a critical growth parameter that initiates either the first or the second buckling for each fiber stiffness. It is observed that the critical growth parameter decreases with the fiber stiffness for the first buckling. However, the secondary buckling modes are triggered within a small range of growth parameters close to each other. Since fibers are aligned to the y-axis, the fiber stiffness directly affects the critical growth in this direction. On the other hand, in the x-direction, which is perpendicular to fibers, the fibers do not affect material behavior. Nevertheless, they still are not fully decoupled from each other. The geometric form of the first buckling mode have also an effect on the secondary buckling at the post-buckling stage by shifting it to higher critical growth compared to isotropic (without fiber) case.

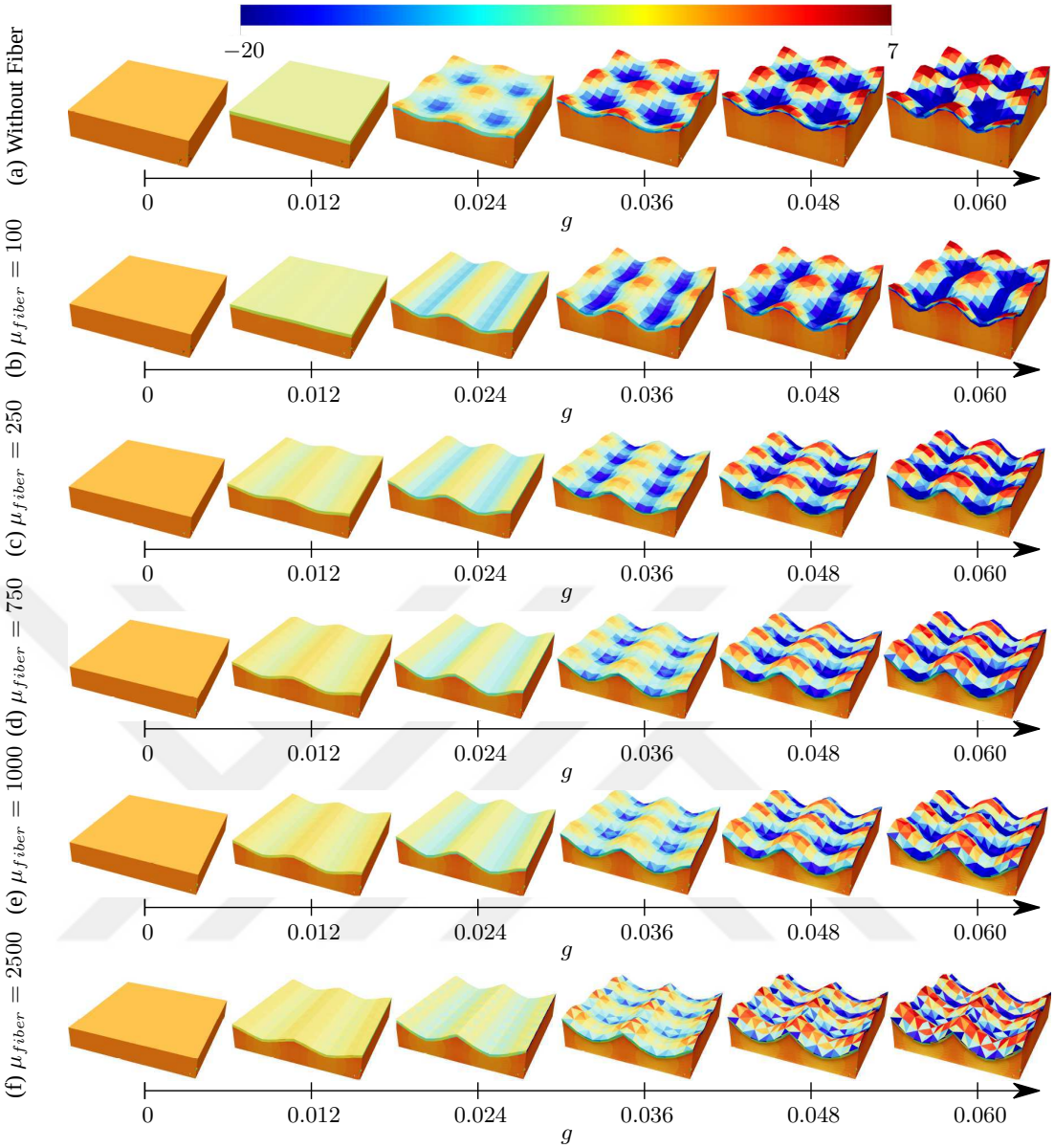

Figure 4.25: Pressure distribution of the buckling regime of a bilayer plate with monotonically increasing growth, g

Out-of-plane displacement and stored energy variations during the growth are also significant indicators to determine the critical growth parameter. The right column in Figures 4.27 and 4.28 shows the isotropic, volumetric, and anisotropic energy variation of the film and substrate separately. The left column represents vertical displacement change during growth at points A, B, and C. These specific points are located at the maximum and minimum displacement points on concave and convex regions of deformed shape. For each case in Figures 4.27 and 4.28, it is clearly seen that vertical

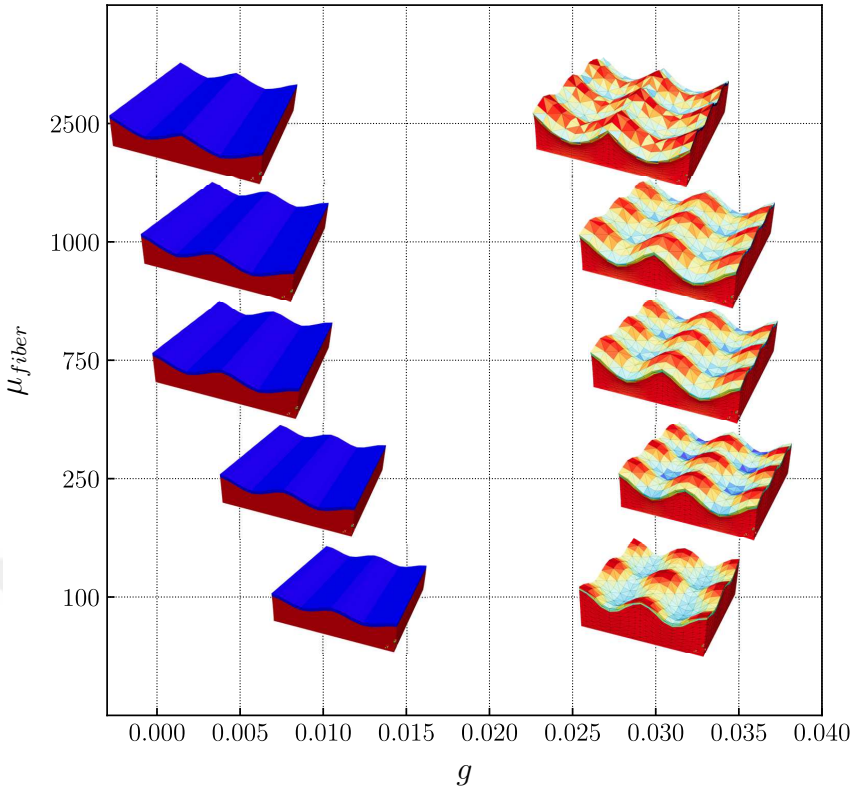

Figure 4.26: Critical growth parameter variation by fiber stiffness

displacements of three points are the same until it reaches the bifurcation point where buckling initiates. In the isotropic bilayer plate, the vertical displacement patterns of the three points seem different from anisotropic ones. The reason is due to the isotropic nature of the bilayer plate, where the first buckling is simultaneously triggered both in x and y-directions at the same time. Later, the buckling shape starts to evolve to the labyrinth form at the second bifurcation point. Fiber-reinforced stiff film models show two different bifurcation points until 0.04 g level. These bifurcations correspond to the first buckling initiation along the fiber direction, and the second buckling initiates perpendicular to the fiber direction. In alignment with Figure 4.26, it is observed that by increasing the fiber stiffness, the critical growth parameter decreases. For example, the first buckling initiates at $g = 0.0116$ for $\mu_{fiber} = 100$, while it initiates at $g = 0.0026$ for $\mu_{fiber} = 2500$. For the intermediate values of fiber stiffness, the critical growth parameter is revealed between this range. The second buckling initiation is observed in a small range of $g = 0.028 - 0.032$ levels. The

second buckling is affected by the geometrical shape of the first buckling mode. Dif-

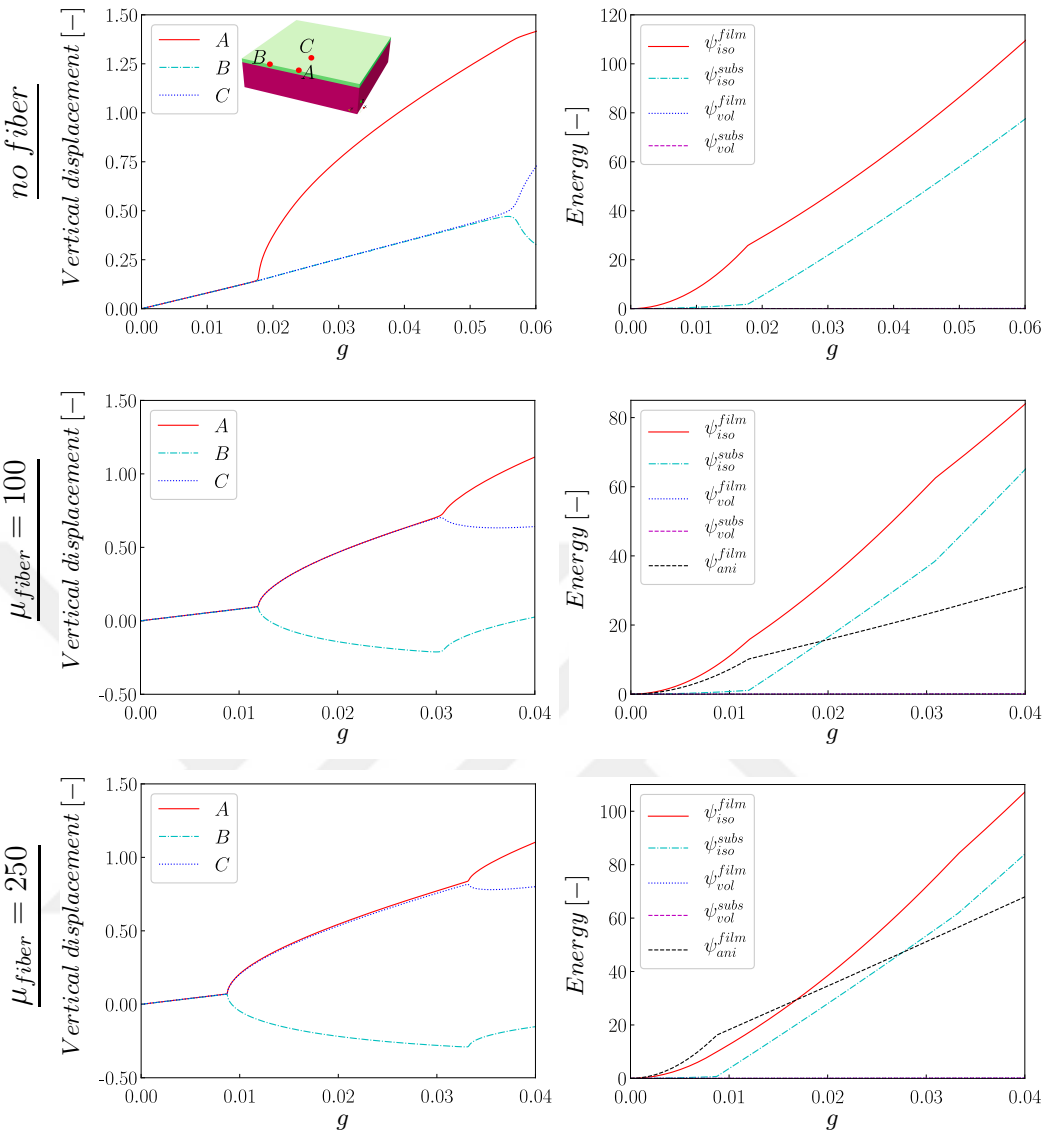

Figure 4.27: Variation of vertical displacements of points A, B, and C; and variation of decoupled forms of energy for the film and substrate, those are subjected to incrementally growth for the following cases; without fiber reinforcement, μ_{fiber}=100 and μ_{fiber}=250, respectively.

ferent parts of the stored energies in the film and the substrate are shown in the right column in Figures 4.27 and 4.28. Due to the sudden energy release, abrupt changes and kinks in energy plots are observed. Tracking energy is a better indicator than the displacement variations to identify the bifurcation as energy is scalar quantity and location independent. While the slope of the isotropic energy of the film shows a

decrease at the first buckling for lower fiber stiffnesses, it increases for higher fiber stiffnesses. It is concluded that the first buckling is the combination of energy release of stiff film and stiff fibers. When the fiber stiffness increases, the energy contribution of fibers to the first instability increases as well. Furthermore, the isotropic energy of the film and substrate layer has a key role in the initiation of the secondary buckling.

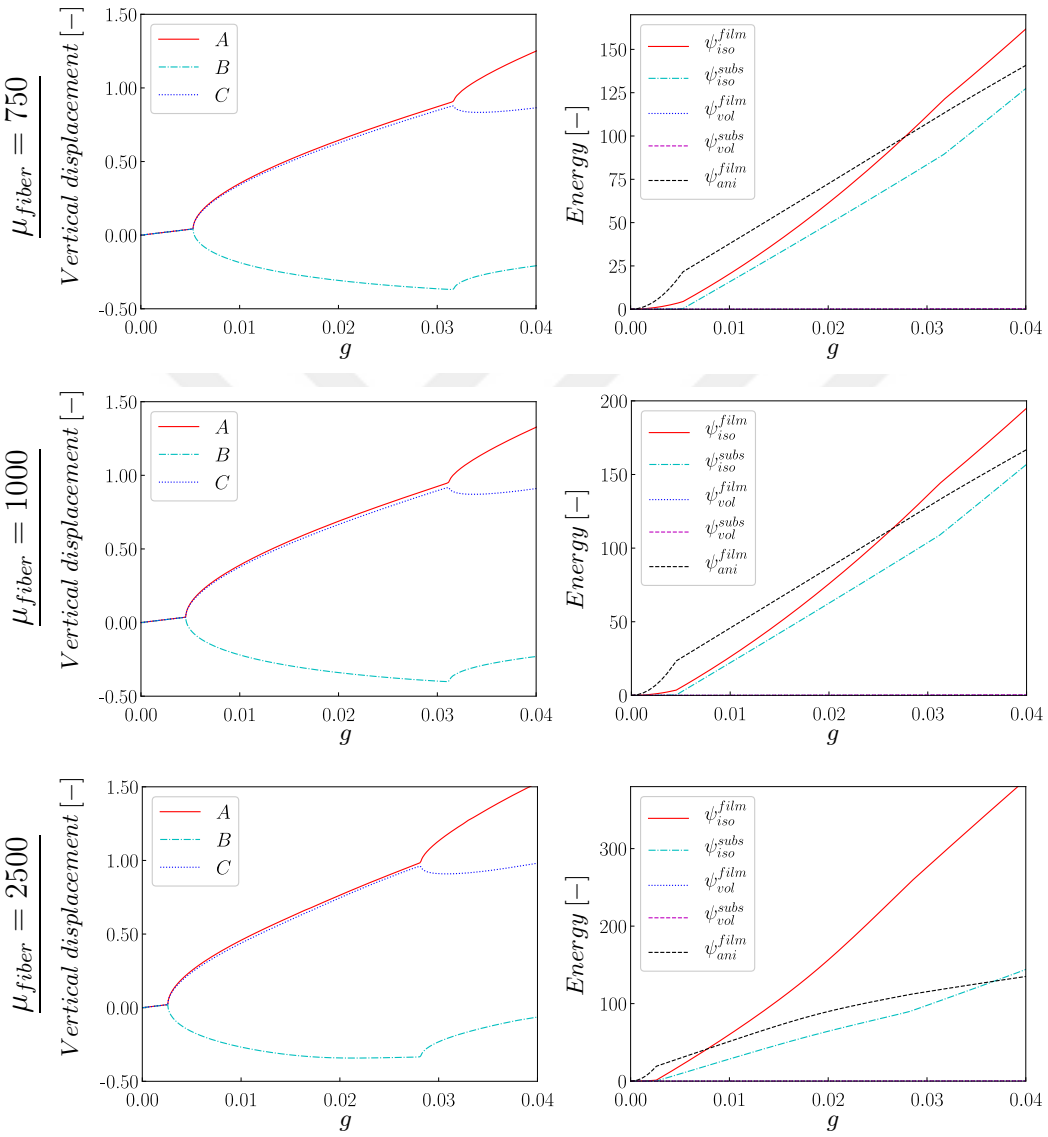

Figure 4.28: Continuation of Figure 4.27 - Variation of vertical displacements of points A, B, and C; and variation of decoupled forms of energy for the film and substrate, those are subjected to incrementally growth for the following cases; μ_{fiber}=750, μ_{fiber}=1000, μ_{fiber}=2500, respectively.

CHAPTER 5

DISPERSION-TYPE HYPERELASTIC FORMULATIONS FOR ANISOTROPIC BIOLOGICAL TISSUES

Both soft and hard biological tissues mostly contain fiber reinforcements those are integrated to base isotropic tissue matrix. Volume fraction, stiffness characteristics and orientation of the fibers are the main determining factors of the mechanical behaviour of anisotropic tissue. In previous chapters, the anisotropic contribution of fibers have been considered as they perfectly aligned in the orientation direction. Most of the hyperleastic constitutive models are constructed in a phenomenological way by fitting the material constants with experimental data. Many experiments and imaging results showed that anisotropic tissues contained dispersed fibers around a mean orientation. The dispersion characteristics of fibers can be reflected in constitutive models through histological data. One of the pioneering research has been proposed by Lanir [153]. They proposed a constitutive model that took the nonuniformity of the fiber layouts into account based on the fibers' angular distributions. The total free-energy is constructed using the angular integral over the fiber orientation directions, which is also called the angular integration. Based on the proposed work of Lanir, Sacks [154] constructed a constitutive model for bovine pericardium that contains fiber orientations though beta distribution function via angular integral. Holzapfel et al. [125] proposed a constitutive model that contains a scalar parameter that is responsible for the transition between isotropic and anisotropic conditions. Then, Gasser et al. [155] proposed an approach for fiber dispersion called the Generalized Structure Tensor (GST), which is one of the milestones for the next proposed models of research. The proposed constitutive model reflects the in-plane dispersion-type anisotropy of the adventitial and intimal layers of arterial tissue. The model uses a new defined scalar parameter in anisotropic part of the free-energy which is derived though von

Mises density distribution to characterize the fiber dispersion behaviour. The second key dispersion-type anisotropic modeling is proposed by Alastrué et al. [156]. The model is also called an Angular Integration (AI) approach that uses von Mises density distribution by using different orientation directions of micro-fibres through the unit micro-sphere. Then the integral averaging is covered through several cubarutes for micro-sphere those contains variety numbers of integration points over the unit sphere. Schriefl et al. [157], observed the fiber dispersion characteristics of healthy and diseased abdominal aortic tissues. They highlighted that, the out-of-plane dispersion characteristics increased for the diseased tissue. Therefore it is also essential to consider out-of-plane dispersion distribution at the constitutive level. Holzapfel et al. [158] pointed out that, since the in-plane dispersion is much more important than the out-of-plane dispersion, rotationally symmetric dispersion models are not suitable for human arterial layers. As an extension of [155], they introduced a non-symmetric dispersion constitutive model by defining a new type of structure tensor based on the von Mises distribution. Then they derived a bivariate von Mises distribution that is able to reflect the fiber dispersion distribution at the out-of-planes for arteries. They also presented an overview of the proposed or studied dispersion models based on AI and GST formulations that use Beta, Gaussian, von Mises, ellipsoidal, and Bingham density distributions. Melnik et al. [159] made the comparison of two family fibers depends on different dispersion characteristics with AI and GST formulations. The study contains not only the generalized GST and AI formulations but also the formulations that exclude the fibers in compression. They concluded that there appears a difference between these approaches in the high dispersion occurrence. On the contrary, Holzapfel et al. [160] showed that the results of two of the formulations, AI and GST are identical in both small and large deformations. They fit each model to uniaxial data in different directions for the adventitia of the aorta. Volokh [161], proposed a dispersion-type constitutive model for the arterial wall that is based on structure tensors and allows the exclusion of fibers in compression. They studied the auxetic effect based on fiber dispersion. Similarly, Holzapfel et al. [162] proposed a method for the exclusion of fibers in compression for the GST approach. They performed simple extension and shear to present the effect of exclusion of fibers and they claimed that both AI and GST formulations result in equivalent results. Then, Anssari-Benam et al. [163], presented a transversely isotropic, rate-dependent consti-

tutive formulation based on planar fiber dispersion by using Lorentzian distribution for aortic valve subjected to biaxial deformations under different stretch rates. A new kind of fiber density function is proposed based on fiber kinematics. They showed that the proposed model well-captures the experimental results, shear thinning behaviour and viscous response of the tissue. Li et al. [7] proposed dispersion-type of formulation that uses triangular integration over unit sphere. This approach is kind of the representation of separate fiber direction over each triangular area based on elementary density of the fibers. The summation of each anisotropic fiber contributions over unit sphere determined the overall free-energy. Then continuum damage and softening behaviour is implemented on the model by numerical examples. Their proposed model is able to well-capture the fiber dispersion characteristics, damage and softening together. Horvat et al. [8] enlarged the application of fiber dispersion formulations to growth and remodeling of arterial walls. They used GST approach with mixture of growth and remodeling and defined a fiber pre-stretched tensorial definition that is able to work with dispersion model. They performed numerical examples for proposed model to observe the dispersion effect and mean orientation on growth and stresses in the wall. They also present that, there is an high level effect of the dispersion characteristics and layout on the growth-induced stress evolution. For further details regarding to fiber dispersion formulations studied in literature, there are state-of-the-art reviews presented by [27] and [17]. Holzapfel et al. [27] provides the critical review of AI and GST models by demonstrating the numerical examples and fitting capability of the models with experimental data of abdominal aortic aneurysm. Dal et al. [17], presented the detailed review for invariant and fiber dispersion-type of formulations for soft biological tissues and observed the fitting performance of the constitutive models to three different experimental data of human tissues.

In this chapter, two main fiber dispersion-type formulations namely, Angular Integration (AI) and Generalized Structure Tensor (GST), for anisotropic hyperelastic soft tissues will be presented. The models will be given in three-dimensional and planar for GST approach and three-dimensional for AI model where both of the models are based on the von Mises density distributions. Then, in order to demonstrate the characteristics of density distribution functions those are used for the fiber dispersion, there will be given polar plots for different kinds of biological soft tissues.

5.1 Fiber Dispersion Formulations

It has been studied in the literature that not only the fiber mean direction but their dispersion characteristics have significant effect on the mechanical response of the tissue. Taking into account of the dispersion in the constitutive level helps to understand the histological relation between experimental and numerical results. It has also shown that dispersion architecture of healthy and diseased or healthy and injured tissue exhibit different fiber distribution those were mentioned by [164] and [165] respectively. To reflect the dispersion formulation into the constitutive models there have been proposed different kind of dispersion-type formulations those defines the stress-strain behaviour. Those models are based on a density probability distribution function that fits with the histological data of the tissue [17]. There are two different main dispersion-type formulation outlined in the literature those are generelized structure tensor (GST) forumulation and angular integration (AI) formulation. These approaches will be introduced in this section.

5.1.1 Generalized structure tensor formulation

The generalized structure tensor formulation is proposed by [155], where the fiber density distribution is notated as $\rho(\boldsymbol{r})$ that characterize the distribution of fibers in arbitrary unit vector $\boldsymbol{r}$. In the origin of the study, the orientation direction is also stated as $\boldsymbol{M}$ but we will use $\boldsymbol{r}$ notation here. The unit vector $\boldsymbol{r}$ is defined in Eulerian angles such that defined in the range of $\theta \in [0, \pi]$ and $\phi \in [0, 2\pi]$, demonstrated in Figure 5.1. Let Lagrangian unit fiber orientation $\boldsymbol{r}$ on an unit sphere and the fiber density function in the direction of $\boldsymbol{r}$ is $\rho(\boldsymbol{r})$. The unit fiber orientation $\boldsymbol{r}$ is described with spherical coordinates as

$$\boldsymbol{r} = \sin\Theta\cos\Phi\boldsymbol{e}_1 + \sin\Theta\sin\Phi\boldsymbol{e}_2 + \cos\Theta\boldsymbol{e}_3, \tag{5.1}$$

where $\boldsymbol{e}_1$, $\boldsymbol{e}_2$ and $\boldsymbol{e}_3$ represents the unit vectors at Cartesian coordinates. The deformed state of $\boldsymbol{r}$ is expressed with stretch vector $\boldsymbol{t} = \boldsymbol{F}\boldsymbol{r}$. Then, the density distribution function $\rho(\boldsymbol{r})$ is defined to present the fiber orientations around the mean

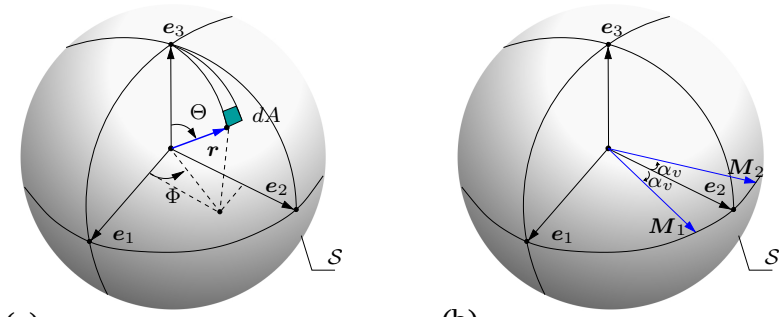

(a) (b)

Figure 5.1: (a) The unit micro-sphere and the orientation vector, (b) mean fiber directions of two families of fiber lie on $\boldsymbol{e}_1$-$\boldsymbol{e}_2$ plane.

direction and it is normalized over the unit sphere as following:

$$\frac{1}{4\pi}\int_{\omega}\rho(\boldsymbol{r})d\omega = 1 \tag{5.2}$$

where $\omega = \sin\Theta d\Theta d\Phi$. Then the symmetric generalized structure tensor is defined as

$$\frac{1}{|\mathcal{S}|}\int_{\mathcal{S}}\rho(\boldsymbol{r}(\Theta,\Phi))\boldsymbol{r}\otimes\boldsymbol{r}dA \tag{5.3}$$

where $|\mathcal{S}| = 4\pi$ is the area of the unit sphere. Gasser et al. [155] formulated π-periodic von Mises distribution as a fiber density distribution around $\boldsymbol{M}$ for a planar condition. The von Mises distribution function is a scalar quantity which is used for probability distribution that represents normal distribution projected over sphere. It is a function of Θ which is centered around 0 and concentration parameter b which is the determinator of the anisotropy level of the distribution. The standard von Mises distribution function is

$$\bar{\rho}(\Theta) = \frac{\exp[b(\cos(2\Theta)]}{2\pi I_0(b)} \quad \text{where} \quad I_0(b) = \frac{1}{\pi}\int_0^{\pi}\exp(b\cos\Theta)d\Theta\,, \tag{5.4}$$

where $I_0(b)$ represents the notation of modified Bessel function of the first kind of order zero. By integrating equation 5.4 according to 5.2 gives the following relation

$$I \equiv \int_0^{\pi}\bar{\rho}(\Theta)\sin\Theta d\Theta \equiv \frac{\exp(-b)}{2\sqrt{2\pi b}}\frac{\text{erfi}(\sqrt{2b})}{I_0(b)} \tag{5.5}$$

where $\text{erfi}(x) = -\text{i}\,\text{erf}(x)$ is the imaginary error function. Then the normalized von Mises distribution can be determined by $\rho(\Theta) = \bar{\rho}(\Theta)/I$ as following:

$$\rho(\Theta) = 4\sqrt{\frac{b}{2\pi}}\frac{\exp[b(\cos(2\Theta)+1)]}{\text{erfi}\sqrt{2b}}\,. \tag{5.6}$$

By inserting equation 5.6 into the equation 5.3 , the generalized structure tensor can be written as

$$\boldsymbol{H} = \kappa \mathbf{1} + (1 - 3\kappa)\boldsymbol{M} \otimes \boldsymbol{M} \quad \text{with} \quad \kappa = \frac{1}{4}\int_0^{\pi} \rho(\Theta)\sin^3\Theta d\Theta \tag{5.7}$$

κ and b parameters are nonlinearly related to each other by equations 5.6 and 5.7 and κ can be determined by numerical integration of 5.7_2. The dispersion parameter κ has the upper and lower limits due to physical aspects of the material behaviour as it can be defined in the range of $\kappa \in [0, 1/3]$. It directly integrated to the constitutive model with generalized structure tensor as a scalar multiplier represented in equation 5.7_1. The lower limit $\kappa = 0$ recovers the distinct anisotropy by yielding of concentration parameter b to infinity and the upper limit $\kappa = 1/3$ leads to an isotropic constitutive response which also brings the concentration parameter $b = 0$. The relationship between $\rho - \Theta$ and $\kappa - b$ are presented graphically in Figure 5.2. Then, the second

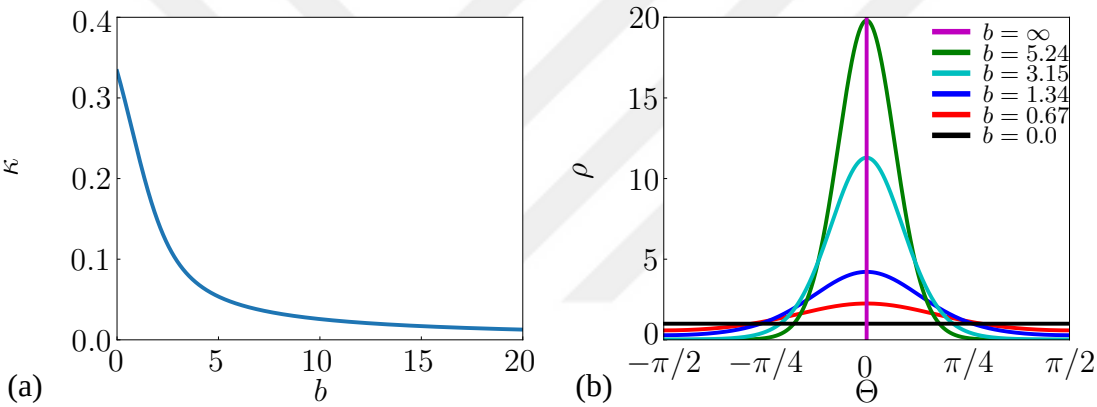

Figure 5.2: (a) Graphical representation of nonlinear relation between the dispersion parameter κ and the concentration parameter b, (b) dispersion characteristics through the density function ρ and the angle of dispersion Θ. The corresponding κ values are $1/3$, $4/15$, $1/5$, $1/11$, $1/20$ and 0 respectively.

Piola Kirchhoff stress and the Kirchoff stress can be defined in the following form:

$$\begin{aligned} \boldsymbol{S} &= 2\partial_{\boldsymbol{C}}\Psi = 2\left[\frac{\partial U}{\partial J}\frac{\partial J}{\partial \boldsymbol{C}} + \frac{\partial \Psi_{iso}}{\partial I_1}\frac{\partial I_1}{\partial \boldsymbol{C}} + \frac{\partial \Psi_{ani}}{\partial E}\frac{\partial E}{\partial \boldsymbol{C}}\right] \\ \boldsymbol{\tau} &= 2\partial_{\boldsymbol{g}}\Psi = 2\left[\frac{\partial U}{\partial J}\frac{\partial J}{\partial \boldsymbol{g}} + \frac{\partial \Psi_{iso}}{\partial I_1}\frac{\partial I_1}{\partial \boldsymbol{g}} + \frac{\partial \Psi_{ani}}{\partial E}\frac{\partial E}{\partial \boldsymbol{g}}\right] \end{aligned} \tag{5.8}$$

where E is construct the strain like scalar quantity in the direction of mean orientation and it is defined in Lagrangian and Eulerian configurations as following

$$E = \boldsymbol{H} : \boldsymbol{C} - 1 \quad \text{and} \quad E = \boldsymbol{h} : \boldsymbol{g} - 1 \tag{5.9}$$

5.1.2 Generalized structure tensor based bivariate formulation

Holzapfel et al. [158], extended the GST approach, which provides rotational symmetric distribution based on planar distribution, to GST based bivariate formulation. The formulation not only takes the dispersion characteristics into account in-plane but also adds the out-of-plane contribution to the formulation. By experimental histological observations, they obtained the fiber distributions not only effective in planar plane but also there is minor effect on the out-of-plane for arteries. They concluded that the in-plane and out-of-plane fiber distributions are uncoupled from each other. Then the fiber density probability function is multiplicatively decomposed into in-plane $\rho_{ip}(\Phi)$ and out of plane $\rho_{op}(\Theta)$ contributions as follows:

$$\rho(\boldsymbol{r}) = \rho_{ip}(\Phi)\rho_{op}(\Theta). \tag{5.10}$$

where the angles Φ and Θ demonstrated over micro-sphere schematically in Figure 5.1_1. The probability density function is defined for the in-plane by a basic von Mises distribution as follows

$$\rho_{ip}(\Phi) = \frac{\exp[a(\cos(2\Theta)]}{I_0(a)} \quad \text{where} \quad I_0(a) = \frac{1}{\pi}\int_0^{\pi} \exp(a\cos\alpha)d\alpha \tag{5.11}$$

where a is the concentration parameter and $I_0(a)$ is the modified Bessel function of the first kind of order zero. If the in-plane $\rho_{ip}(\Phi)$ density function divided by 2π, the normalized version can be found. The out of plane probability density distribution is defined as

$$\rho_{op}(\Theta) = 2\sqrt{\frac{2b}{\pi}}\frac{\exp[b(\cos(2\Theta)-1)]}{\text{erf}(\sqrt{2b})} \ . \tag{5.12}$$

where b is the concentration parameter for out-of-plane distribution. By using the similar normalized relation defined by equation 5.2 with $\omega = \cos\Theta d\Theta d\Phi$, the normalization equations yields

$$\frac{1}{4\pi}\int_0^{2\pi} \rho_{ip}(\Phi)d\Phi \int_{-\pi/2}^{\pi/2} \rho_{op}(\Theta)\cos\Theta d\Theta = 1 \tag{5.13}$$

By defining the in-plane normalization as follows

$$\frac{1}{2\pi}\int_0^{2\pi} \rho_{ip}(\Phi)d\Phi = 1 \tag{5.14}$$

then equation 5.13 reduces to out-of-plane normalization as below

$$\int_{-\pi/2}^{\pi/2} \rho_{op}(\Theta)\cos\Theta d\Theta = 2 \tag{5.15}$$

Then, the scalar quantities of dispersion for in-plane (κ_{ip}) and out-of-plane (κ_{op}) are defined

$$\kappa_{ip} = \frac{1}{\pi}\int_0^{\pi} \rho_{ip}(\Phi)\sin^2\Phi d\Phi \quad \text{with} \quad \kappa_{op} = \frac{1}{4}\int_{-\pi/2}^{\pi/2} \rho_{op}(\Theta)\cos^3\Theta d\Theta \tag{5.16}$$

The generalized structure tensor can be obtained as

$$\boldsymbol{H} = \frac{1}{4\pi}\int_{\Phi=-\pi}^{\pi}\int_{\Theta=-\pi/2}^{\pi/2} \rho_{ip}(\Phi)\rho_{op}(\Theta)\boldsymbol{N}\otimes\boldsymbol{N}\cos\Theta d\Theta d\Phi \tag{5.17}$$

By using the relationship of equations 5.17 and 5.16, the structure tensor yields the following form

$$\boldsymbol{H} = 2\kappa_{ip}\kappa_{op}\mathbf{1} + 2\kappa_{op}(1-2\kappa_{ip})\boldsymbol{M}_f\otimes\boldsymbol{M}_f + (1-2\kappa_{op}(1+\kappa_{ip}))\boldsymbol{M}_n\otimes\boldsymbol{M}_n \tag{5.18}$$

where $\boldsymbol{M}_f$ and $\boldsymbol{M}_n$ are the mean fiber orientation direction and normal direction perpendicular to the main plane, respectively. $\kappa_{ip} \in [0,1]$ and $\kappa_{op} \in [0,1/2]$ where these parameters are determined by using the histology and imaging data of the tissue. The relationship between the scalar density distribution quantity κ and concentration parameters are given for both in-plane and out-of-plane distributions in Figure 5.3. Note that κ_{ip} and κ_{op} defined in larger range of interval than the given range in Figure

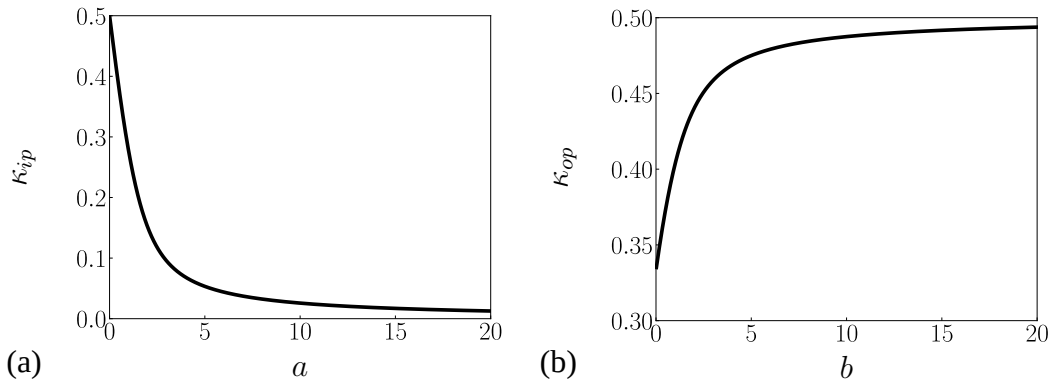

Figure 5.3: (a) Graphical representation of nonlinear relation between the in-plane dispersion parameter κ_{ip} and the in-plane concentration parameter a, (b) relationship between the out-of-plane dispersion parameter κ_{op} and the out-of-plane concentration parameter b

5.3. However, the negative values of concentration factors represents non-physical behaviour and therefore omitted from plots.

5.1.3 Angular integration dispersion formulation

Micro-sphere based angular integration formulation for the anisotropic finite elasticity proposed by Alastrué et al. [156]. The anisotropic contribution of the tissue is defined by using von Mises distribution functions through orientation directions. The micro-fiber directions are considered in the concept of chain-based structure. Then homogenization has been performed by numerical integral over the unit sphere. For the numerical integration step there have been defined several cubatures by Heo et al. [166] for the micro-sphere. The anisotropic free-energy is defined as the angular-integration of micro-fiber free energies over the micro-sphere that contributes in discrete orientation sets based on von Mises probability function $\rho(\boldsymbol{r})$

$$\Psi_{ani} = \frac{1}{|\mathcal{S}|}\int_{\mathcal{S}} \rho(\boldsymbol{r}, \boldsymbol{M})\Psi^{\text{mic}}(\lambda_f)\, dA, \quad \text{where} \quad |\mathcal{S}| = 4\pi, \tag{5.19}$$

where $|\mathcal{S}|$ is the total surface area of the unit sphere and $dA = \sin(\Theta)d\Theta d\Phi$. The notation λ_f represents the micro-fiber stretch in the direction of $\boldsymbol{r}$ and it can be introduced by using stretch vector $\boldsymbol{t} = \boldsymbol{F}\boldsymbol{r}$.

$$\lambda_f = \sqrt{\boldsymbol{t} \cdot \boldsymbol{g}\boldsymbol{t}} \tag{5.20}$$

The contributions of each chains in the orientations directions can also be stated as following

$$\Psi_{ani} = \sum_{k=1}^{p} \Psi^{mic}(\lambda_f), \tag{5.21}$$

Each of the orientation direction can also be stated as the averaging of the total number of p contributions of micro-fiber energies as introduced in equation 5.19. The contribution of each set of orientations to the macroscopic level can be defined as a continuous average over micro-sphere as follows

$$\langle \bullet \rangle = \frac{1}{|\mathcal{S}|}\int_{\mathcal{S}} (\bullet)\, dA \approx \sum_{k=1}^{p} w^k\, (\bullet)^k \quad \text{and} \quad \Psi_{ani}(\boldsymbol{F}, \boldsymbol{r}) = \langle \rho(\boldsymbol{r})\Psi^{mic} \rangle \tag{5.22}$$

where ${w^k}_{k=1:p}$ are the weight factors of the set integration points related with discrete orientation directions ${\boldsymbol{r}^k}_{k=1:p}$ and p is the total number of integration points. Then the Kirchhoff stress can be written as

$$\boldsymbol{\tau} = 2\partial_{\boldsymbol{g}}\Psi = 2\left[\frac{\partial U}{\partial J}\frac{\partial J}{\partial \boldsymbol{g}} + \frac{\partial \Psi_{iso}}{\partial I_1}\frac{\partial I_1}{\partial \boldsymbol{g}} + \frac{\partial \Psi_{ani}}{\partial \lambda_f}\frac{\partial \lambda_f}{\partial \boldsymbol{g}}\right] \tag{5.23}$$

and the more explicit form of the Kirchhoff stress reads

$$\boldsymbol{\tau} = \int_{\mathcal{S}} \rho(\boldsymbol{r}) \Psi'^{mic} \lambda_f^{-1} \boldsymbol{t} \otimes \boldsymbol{t} dA - p\boldsymbol{g}^{-1} + 2c_1 \boldsymbol{b} \tag{5.24}$$

where c_1 is the constant that is determined by the derivative of Ψ_{iso} with respect to I_1. The π-periodic rotational symmetric von Mises distribution described as

$$\rho(\Theta) = 4\sqrt{\frac{b}{2\pi}} \frac{\exp[b(\cos(2\Theta) + 1)]}{\text{erfi}\sqrt{2b}} \tag{5.25}$$

5.2 Examples of Fiber Dispersion Architecture of Biological Tissues

In this section, there will be presented polar plots for both planar and bivariate von Mises density distributions those are published in the literature based on histological data. There have been reported many of fiber dispersion data [156, 27, 158, 164, 7, 8, 167, 168, 169, 170], based on von Mises density distributions for artery. Since it is composed of anisotropic layered-type structure and layers have different fiber orientations and distributions, the dispersion characteristics of fibers reflects high influence on mechanical response of the constitutive models. The density distributions of the intima, media and adventitia layers based on von Mises distribution are given in polar plots in Figure 5.4. Liu et al. [9] proposed dispersion based formulation for the intestine walls including submucosa, longitudinal and circular muscle layers. Eriksson et al. [10], presented a formulation for the dispersion characteristics of fiber and sheet orientations of rabbit myocardium and they fit the planar von Mises distributions parameters to experimentally measured histological data. The corresponding planar von Mises distribution architecture of the intestine wall layers and fiber-sheet orientations of a rabbit myocardium are shown by polar plots in Figure 5.5. Longitidunal and circular muscle layers of intestinal walls are nearly isotropic with scalar dispersion parameters $\kappa_{long} = 0.30$ and $\kappa_{circ} = 0.32$. However, submucosa exhibit slightly anisotropic fiber dispersion with $\kappa_{sub} = 0.25$. The orientation angles are $\Theta = 65^o, 40^o, 30^o$, respectively. On the other hand, the rabbit myocardium tissue is highly anisotropic in both fiber and sheet orientations. It is assumed that the fiber and sheet directions are orthogonal to each other. The scalar dispersion parameter for the fiber is $\kappa_f = 0.00765$ which corresponds to $b_f = 32.517$ and the scalar dispersion parameter for the sheet direction is $\kappa_s = 0.0249$ that corresponds to $b_s = 10.28$.

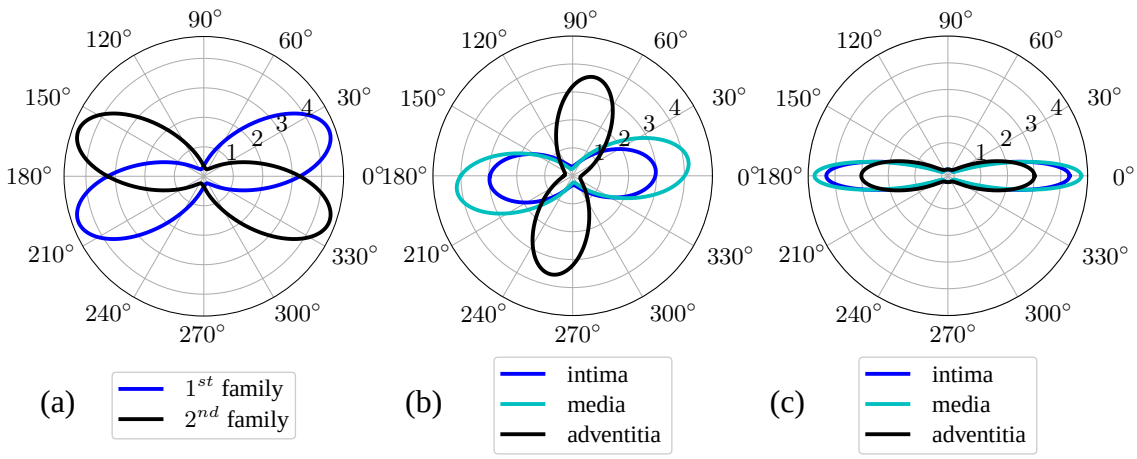

Figure 5.4: The polar plots of the density distribution functions ρ (a) planar von Mises distribution of two families of fibers for a medial layer of human thoracic aorta [7],(b) in-plane von Mises distributions of one family of fibers for intima, media and adventitia layers of healthy abdominal aorta [8] (c) out-of-plane von Mises distributions of one family of fibers for intima, media and adventitia layers of healthy abdominal aorta [8]

Since their density localization differ to each other in terms of amplitude, their plots are given separately to clear view.

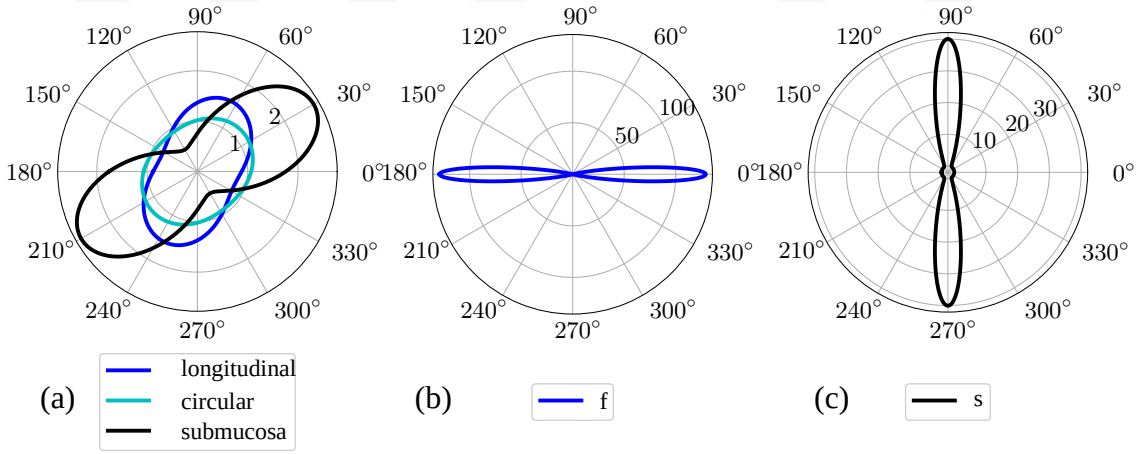

Figure 5.5: The polar plots of the density distribution functions ρ (a) planar von Mises distribution of one family of fibers for intestine wall layers namely submucosa, longitudinal and circular muscle layers [9],(b) planar von Mises distributions of fiber orientation of rabbit myocardium [10] (c) planar von Mises distributions of sheet orientation of rabbit myocardium [10]

CHAPTER 6

ANISOTROPIC VISCOELASTIC CONSTITUTIVE MODELLING OF HUMAN MYOCARDIUM

6.1 Introduction

The heart is the primary component of the cardiovascular system, and pathological conditions related to the heart may have a vital impact on human life. Historically, cardiovascular diseases (CVDs) are not only a disease related to the diet of modern people, but also the most deadly medical conditions that have always been encountered since ancient times [171]. According to the World Health Organization, CVDs are the leading cause of death, taking the lives of around 17.9 million people each year. In general, clinical therapies for CVDs are more a rule-of-thumb, than a systematic therapy design based on scientific criteria. The heart is an electromechanical pump that supplies blood through the vessels to the entire living body, and it is subjected to thermo-electro-chemo-mechanical conditions. Hence, understanding the biomechanics of the heart may lead to the development of more accurate treatment techniques (medical treatments, surgery techniques, rehabilitation methods, etc.) alongside understanding the pathology itself. For example, developing an artificial pumping system, developing transplantation techniques, replacing the heart valve, developing the left ventricular pacemaker device, etc. To this respect, the interest in computational cardiovascular mechanics has increased tremendously in the last few decades. However, understanding the mechanics of the heart is a challenging task due to its sophisticated structure. In this chapter, we aim to develop a novel constitutive model that describes the mechanical behavior of the passive myocardium.

The heart wall is made of three main layers. These are the endocardium, myocardium,

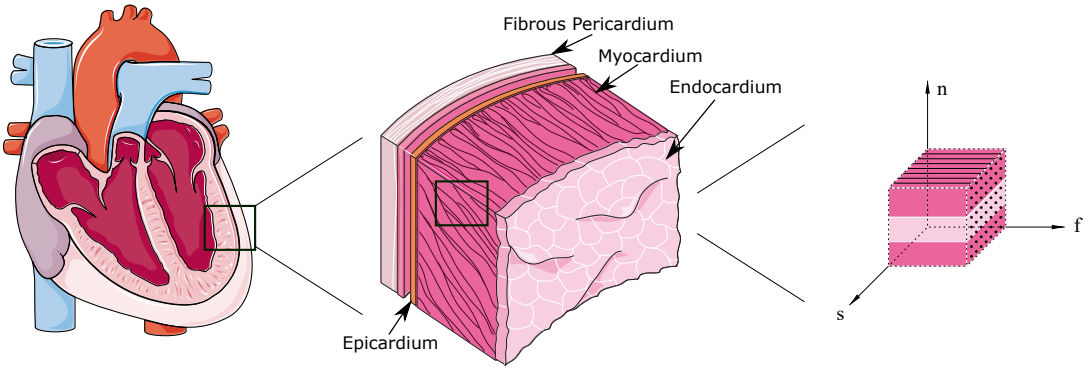

Figure 6.1: The schematic view of the section view of the human heart, sliced pieced of the left ventricle and idealized patch of heart wall described within three orthogonal directions, fiber direction, sheet direction and normal direction, respectively. (The realistic images were partly generated using Servier Medical Art, provided by Servier, licensed under a Creative Commons Attribution 3.0 unported license)

and epicardium. Endocardium and epicardium are thin layers that mainly consist of collagen and elastin, and they create an interface region with inner and outer substances. The myocardium is primarily responsible for the heart's pumping function in the wall. It is made up of parallel fibers that are embedded in sheets by extracellular matrix [88]. The orientation of the myofibers makes a smooth transition from the epicardium to the endocardium in a helical form. In the human, myofibers vary from about -70 degrees at the epicardium to nearly +70 degrees at the endocardium. The LV wall thickness is higher than the RV wall thickness due to the fact that the LV is subjected to a higher pressure load to pump the blood to the aorta. The schematic view of the section view of the human heart, sliced pieces of the left ventricle, and the schematic continuum approach of the myocardium tissue are given, respectively, in Figure 6.1. The historical remarks on the structural features of the myocardium have already been mentioned in detail in section 1.3. As an highlight to Chapter 1, the mechanical behavior of the tissues is highly influenced by the structural arrangement of fibers. Therefore, morphological studies are essential to identify the mechanical response of the tissues. In a recent study, Sommer et al. [11] quantitatively measured in-plane and out-of-plane dispersion of fibers from mean fiber direction and sheet direction for samples extracted from human myocardium. They also performed monotonic biaxial and triaxial shear experiments along with cyclic experiments and

observed that myocardial tissue exhibits non-linear orthotropic material behavior. Before, Sommer et al. [11], similar observations were outlined by Dokos et al. [99] for pig heart.

6.1.1 Hyperelastic constitutive models for passive myocardium

Several hyperelastic constitutive models for myocardial tissue have been proposed in over years, beginning with the isotropic models [172], continuing with transversely isotropic models based on invariants [173] and on Green-Lagrange strain tensor [174]. Unequivocally, these models were not able to describe orthotropic anisotropic mechanical behaviour of the myocardium. Later on, orthotropic models were proposed by Nash & Hunter [175], and Schmid et al. [176]. One of the most successful model proposed by Holzapfel & Ogden [106] which is based on invariants. Göktepe et al. [177] implemented this constitutive model in a general purpose finite element program [178] and also showed the fitting performance of the model based on experiments of Dokos et al. [99]. Nevertheless, the aforementioned models lack describing dispersed nature of collagen fibers. In fact, the first model to incorporate the dispersed structure of collagen fibers was proposed by Lanir [153] for epidermal tissue. They utilized a density distribution function to describe the dispersion of fibers in microstructural level and used angular integration to obtain the macroscopic mechanical behaviour of the tissue. Following the work of Lanir, several dispersion-based anisotropic hyperelastic models have been developed for various types of soft tissues, e.g., Driessen et al. [179] for aortic valve and arterial wall, Alastrué et al. [156, 180] for blood vessels, Gasser et al. [155] and Holzapfel et al. [158] for arterial wall. For the case of myocardium, Eriksson et al. [10] modified the model of Holzapfel & Ogden [106] to take into account of dispersion along the fiber and sheet directions using the generalized structure tensor approach proposed by Gasser et al. [155]. The numerical performance of this model was adressed among other by, e.g., Cansiz et al. [18] and Gültekin et al. [1].

6.1.2 Viscoelastic constitutive models for passive myocardium

The above-mentioned models treat the myocardium as an hyperelastic material. However, according to the observations of Dokos et al. [99] on pig heart, myocardial tissue shows stress relaxation and hysteresis response in all shear modes for the cyclic triaxial shear test. Furthermore, Sommer et al. [11] obtained similar observations for the human myocardium when conducting stress relaxation tests along with cyclic triaxial shear and cyclic biaxial tests. In addition, aforementioned studies addressed the directional dependence of the tissue for different test modes.

One of the earliest attempt to model the viscoelastic behavior of the myocardium was made by Loeffler & Sagawa [181]. They developed a one-dimensional viscoelastic model for both passive and active reponse of cat myocardium. The passive response was developed by a rheological model consisting of a spring connected to two Maxwell elements in parallel. Later on, Yang & Taber [182] proposed a biphasic (consists of fluid and solid phases) viscoelastic model that takes into account the contribution of extracellular fluid flow to the viscoelastic behavior of passive cardiac muscle. Following this work, Huyghe et al. [183] developed a transversely isotropic biphasic model that also incorporates viscoelasticity due to shear deformation in an isotropic manner. However, these models were not able to capable of describing anisotropic viscoelastic behavior of the myocardial tissue entirely. More comprehensive models were proposed by Kaliske [184] and Holzapfel & Gasser [185] in finite linear viscoelastic settings where stress update is derived with convolution integral in analogy to a small strain setting. More general orthotropic viscoelastic formulation were developed by Cansiz et al. [18] and Gültekin et al. [1]. The equilibrium response of the both models are identical and based on the dispersion-based hyperelastic formulation proposed by Eriksson et al. [10]. On the other hand, the viscous response of the myocardial tissue in the sense of Cansiz et al. [18] delivered by a canonical representation in terms of strain-like internal variables conjugate to driving viscous stresses, while Gültekin et al. [1] pursues a convolution representation of the viscous overstresses. The interested readers may refer to Gültekin & Dal [186] for the comparison of these two models [18, 1] based on human myocardium dataset [11].

Furthermore, the recent fractional derivative based orthotropic viscoelastic model on passive myocardium, as documented in Nordsletten et al. [187], demonstrates good fitting performance on the human myocardium dataset.
From the view of modelling overall function of heart, the importance of viscoelasticity in cardiac cycle was revealed by Cansiz et al. [20, 21] and Tikenoğulları et al. [188]. Cansiz et al. [20] presented an unified theory for orthotropic electro-viscoelastic response of myocardium by extending the formulation of Cansiz et al. [18] and Göktepe et al. [189]. Later on, Cansiz et al. [21] extended their work to reveal the mechanisms of the defibrillation phenomenon by elaborating on the bidomain setting as described by Dal et al. [19]. Recently, Tikenoğulları et al. [188] succesfully embedded the viscous formulation of Gültekin et al. [1]. The common observation of these works is adressing the importance of the viscous effects in overall function of hearth.

In this chapter, firstly, a proper hyperelastic constitutive model proposed by [106] will be presented by deriving the stress and consistent tangent moduli expressions. The deformation gradient is multiplicatively decomposed into spherical and unimodular parts; accordingly, the free energy function is additively decomposed into volumetric and isochoric parts. Then, we adopt the formulation of [10] and hyperelastic formulation will be revised by integration of dispersion kinematics. Further, we also additively decompose the free energy function into equilibrium and non-equilibrium parts with the assumption that non-equilibrium part is related to the volume-preserving deformations. Rheological Maxwell model and convolution integral formulations have been introduced for non-equilibrium response of myocardium. Then, we proposed five novel formulations for the angular integration type dispersion-based anisotropic viscoelastic constitutive model for myocardium. Non-equilibrium response of the myocardium is modeled by a rheological device consisting of a spring with a Maxwell element in parallel. The viscoelasticity is modelled through one dimensional Maxwell branch with a quadratic free energy function in logarithmic strain space and a quadratic and power type dissipation potential in each orientation direction. The overstress response is then obtained by the numerical integration over the unit micro-shpere and over the planar circle for the orthogonal directions of myocardium.

6.2 Governing Equations of Hyperelastic Constitutive Model for Passive Myocardium

In this section, hyperelastic constitutive model of myocardium will be presented based on the formulation proposed by Holzapfel et al. [106]. We start with the multiplicative decomposition of the deformation gradient $\boldsymbol{F} = \boldsymbol{F}_{vol}\bar{\boldsymbol{F}}$ into volumetric $\boldsymbol{F}_{vol}$ and unimodular $\bar{\boldsymbol{F}}$ in order to impose incompressibility nature of the tissue. The related kinematic relations are already given in equation 3.21. Due to the high water content of myocardium similar to the most of the biological tissues, it is assumed to reflect an incompressible behaviour [101]. Then Jacobian leads to $J = \boldsymbol{F}_{vol} = 1$ for incompressibility condition. The identity tensor is defined by $\mathbf{1}$. Isotropic hyperelasticity is formulated based on the free energy function, which is defined per unit reference volume through isotropic invariants I_1, I_2, I_3 those are constitutively related to the deformation gradient. For incompressible materials, two of the invariants I_1, I_2 are sufficient to be used in the formulation. The invariant formulation of hyperelasticity is described by equation 3.23.

For orthotropic tissues, additional unimodular invariants $I_{4f,s,n}, I_{5f,s,n}$, relates the material response through distinct unit vectors for fiber $\boldsymbol{f}_0$, sheet $\boldsymbol{s}_0$, and normal $\boldsymbol{n}_0$. Isochoric counterparts of unit vectors in Eulerian configuration are defined as $\boldsymbol{f} = \bar{\boldsymbol{F}}\boldsymbol{f}_0$, $\boldsymbol{s} = \bar{\boldsymbol{F}}\boldsymbol{s}_0$, and $\boldsymbol{n} = \bar{\boldsymbol{F}}\boldsymbol{n}_0$. Coupled orthotropic behaviour along unit vectors is described by I_8. Unimodular description of orthotropic invariants are defined as

$$
\begin{aligned}
\bar{I}_{4f} &= \boldsymbol{f}_0 \cdot \bar{\boldsymbol{C}}\boldsymbol{f}_0\,, & \bar{I}_{4s} &= \boldsymbol{s}_0 \cdot \bar{\boldsymbol{C}}\boldsymbol{s}_0\,, & \bar{I}_{4n} &= \boldsymbol{n}_0 \cdot \bar{\boldsymbol{C}}\boldsymbol{n}_0\,, \\
\bar{I}_{5f} &= \boldsymbol{f}_0 \cdot \bar{\boldsymbol{C}}^2\boldsymbol{f}_0\,, & \bar{I}_{5s} &= \boldsymbol{s}_0 \cdot \bar{\boldsymbol{C}}^2\boldsymbol{s}_0\,, & \bar{I}_{5n} &= \boldsymbol{n}_0 \cdot \bar{\boldsymbol{C}}^2\boldsymbol{n}_0\,, \\
\bar{I}_{8fs} &= \boldsymbol{f}_0 \cdot \bar{\boldsymbol{C}}\boldsymbol{s}_0\,, & \bar{I}_{8fn} &= \boldsymbol{f}_0 \cdot \bar{\boldsymbol{C}}\boldsymbol{n}_0\,, & \bar{I}_{8sn} &= \boldsymbol{s}_0 \cdot \bar{\boldsymbol{C}}\boldsymbol{n}_0\,.
\end{aligned}
\tag{6.1}
$$

$\bar{I}_{4f}$, $\bar{I}_{4f}$ and $\bar{I}_{4n}$ define the material behaviour along distinct fiber ($\boldsymbol{f}_0$), sheet ($\boldsymbol{s}_0$) normal ($\boldsymbol{n}_0$) directions. It should be noted that $\bar{I}_{5f}$, $\bar{I}_{5f}$ and $\bar{I}_{5n}$ are related with $\bar{I}_1$ and $\bar{I}_2$ [106]. Therefore fourth invariants are enough to use the behaviour in orthotropic directions. Then, the orientation related structure tensors can be described as dyadic

product of orientation vectors as shown below.

$$\begin{aligned} \boldsymbol{H}_f &= \boldsymbol{f}_0 \otimes \boldsymbol{f}_0\,, & \boldsymbol{H}_s &= \boldsymbol{s}_0 \otimes \boldsymbol{s}_0\,, & \boldsymbol{H}_n &= \boldsymbol{n}_0 \otimes \boldsymbol{n}_0\,, \\ \boldsymbol{H}_{fs} &= \mathrm{sym}(\boldsymbol{f}_0 \otimes \boldsymbol{s}_0)\,, & \boldsymbol{H}_{fn} &= \mathrm{sym}(\boldsymbol{f}_0 \otimes \boldsymbol{n}_0)\,, & \boldsymbol{H}_{sn} &= \mathrm{sym}(\boldsymbol{s}_0 \otimes \boldsymbol{n}_0)\,, \end{aligned} \tag{6.2}$$

Göktepe et al. [177] mentioned that the $\boldsymbol{f}_0$ orientation refers to coiled perimysial fibers oriented along the long axis of the myocytes, and lying in the sheet. The orientation $\boldsymbol{s}_0$ is normal to the sheet plane and refers to sparse direction of perimysial collagens that connect myocardial sheets. The orientation $\boldsymbol{n}_0$ is orthogonal to $\boldsymbol{f}_0$ and $\boldsymbol{n}_0$, it represents the tightly bound endomysial collagen in the sheet and layouts perpendicular to cardiomyocyte axis. The specific form of the isochoric free-energy function for the passive myocardium is defined as below in line with Holzapfel et al. [106, 177]

$$\begin{aligned} \bar{\Psi}^e(\bar{\boldsymbol{C}}) &= \frac{a}{2b}\left\{\exp[b(\bar{I}_1 - 3)] - 1\right\} + \sum_{i=f,s} \frac{a_i}{2b_i}\left\{\exp[b_i(\bar{I}_{4i} - 1)^2] - 1\right\} \\ &+ \frac{a_{fs}}{2b_{fs}}\left\{\exp[b_{fs}\bar{I}_{8fs}^2] - 1\right\}, \end{aligned} \tag{6.3}$$

where the first term in equation (6.3) accounts for isotropic matrix response , the second term contributes for additional stiffness due to anisotropic response in the fiber and sheet directions and the last term is coupled behaviour (relative shear) of fiber-sheet interaction. a, a_{f}, a_{s}, a_{fs}, b, b_{f}, b_{s}, b_{fs} are material constants, which should be non-negative numbers to satisfy the necessary condition for stability. $\bar{I}_{4n}$ is omitted from the free-energy equation above. Since its behaviour is obtained by the combination of $\bar{I}_1$, $\bar{I}_{4f}$ and $\bar{I}_{4s}$; $\bar{I}_{4n}$ is dependent to others [106]. Next, the unimodular elastic part of the stress $\bar{\mathbf{S}}^e$ in can be defined by

$$\bar{\boldsymbol{S}}^e = \bar{\Psi}_1^{e'}\mathbf{1} + \bar{\Psi}_{4f}^{e'}\boldsymbol{H}_f + \bar{\Psi}_{4s}^{e'}\boldsymbol{H}_s + \bar{\Psi}_{8fs}^{e'}\boldsymbol{H}_{fs}, \tag{6.4}$$

where $\bar{\Psi}_1^{e'}$, $\bar{\Psi}_{4f}^{e'}$, $\bar{\Psi}_{4s}^{e'}$ and $\bar{\Psi}_{8fs}^{e'}$ are the scalar values those are resultant terms of the derivation with respect to corresponding invariants and derived as below. The volu-

metric part of the stress can also be determined by $\boldsymbol{S}^{vol} = p\boldsymbol{C}^{-1}$.

$$
\begin{aligned}
\bar{\Psi}_1^{e'} &:= 2\partial_{\bar{I}_1}\bar{\Psi}^e = a\exp[b(\bar{I}_1 - 3)]\,, \\
\bar{\Psi}_{4f}^{e'} &:= 2\partial_{\bar{I}_{4f}}\bar{\Psi}^e = 2a_f(\bar{I}_{4f} - 1)\,\exp[b_f(\bar{I}_{4f} - 1)^2]\,, \\
\bar{\Psi}_{4s}^{e'} &:= 2\partial_{\bar{I}_{4s}}\bar{\Psi}^e = 2a_s(\bar{I}_{4s} - 1)\,\exp[b_s(\bar{I}_{4s} - 1)^2]\,, \\
\bar{\Psi}_{8fs}^{e'} &:= 2\partial_{\bar{I}_{8fs}}\bar{\Psi}^e = 2a_{fs}\bar{I}_{8fs}\,\exp(b_{fs}\bar{I}_{8fs}^2)\,.
\end{aligned}
\tag{6.5}
$$

Then, corresponding elastic unimodular part of Lagrangian moduli reads,

$$
\bar{\mathbb{C}}^e = \bar{\Psi}_1^{e''}\,\mathbf{1}\otimes\mathbf{1} + \bar{\Psi}_{4f}^{e''}\,\boldsymbol{H}_f\otimes\boldsymbol{H}_f + \bar{\Psi}_{4s}^{e''}\,\boldsymbol{H}_s\otimes\boldsymbol{H}_s + \bar{\Psi}_{8fs}^{e''}\,\boldsymbol{H}_{fs}\otimes\boldsymbol{H}_{fs}\,. \tag{6.6}
$$

where $\bar{\Psi}_1^{e''}$, $\bar{\Psi}_{4f}^{e''}$, $\bar{\Psi}_{4s}^{e''}$ and $\bar{\Psi}_{8fs}^{e''}$ are the scalar coefficients for unimodular elastic moduli those are resultant terms of the second derivation with respect to corresponding invariants and they obtained by

$$
\begin{aligned}
\bar{\Psi}_1^{e''} &:= 4\partial^2_{\bar{I}_1\bar{I}_1}\bar{\Psi}^e = 2ab\,\exp[b(\bar{I}_1 - 3)]\,, \\
\bar{\Psi}_{4f}^{e''} &:= 4\partial^2_{\bar{I}_{4f}\bar{I}_{4f}}\bar{\Psi}^e = 4a_f[1 + 2b_f(\bar{I}_{4f} - 1)^2]\,\exp[b_f(\bar{I}_{4f} - 1)^2]\,, \\
\bar{\Psi}_{4s}^{e''} &:= 4\partial^2_{\bar{I}_{4s}\bar{I}_{4s}}\bar{\Psi}^e = 4a_s[1 + 2b_s(\bar{I}_{4s} - 1)^2]\,\exp[b_s(\bar{I}_{4s} - 1)^2]\,, \\
\bar{\Psi}_{8fs}^{e''} &:= 4\partial^2_{\bar{I}_{8fs}\bar{I}_{8fs}}\bar{\Psi}^e = 4a_{fs}(1 + 2b_{fs}\bar{I}_{8fs}^2)\,\exp(b_{fs}\bar{I}_{8fs}^2)\,.
\end{aligned}
\tag{6.7}
$$

6.3 Orthotropic Viscoelasticity based on Dispersion-type Hyperelastic Constitutive Model for Passive Myocardium

In this section, kinematic equations will be modified based on the GST dispersion formulation. Then the general constitutive framework of orthotropic viscoelasticity will be presented by the decomposition of the free-energy into equilibrium and non-equilibrium response. The orthotropic viscoelastic formulation will be given two separate formulations, namely, convolution integral representation and conanical representation, in the sense of Gültekin et al. [1] and Cansiz et al. [18], respectively.

In line with section 5.1.1, κ_f and κ_s are defined for the two scalar structural parameters reflecting the fiber and sheet distributions, respectively in sense of [10]. The modified unimodular fourth invariants in the direction of fiber and sheet are defined

as

$$\bar{I}^*_{4f} = \kappa_f \bar{I}_1 + (1 - 3\kappa_f)\bar{I}_{4f} \quad \text{and} \quad \bar{I}^*_{4s} = \kappa_s \bar{I}_1 + (1 - 3\kappa_s)\bar{I}_{4s}\,, \tag{6.8}$$

In [155], Gasser et al. defined the collagen fiber distribution rotationally symmetric around a mean fiber direction $\boldsymbol{M}$. They formulated π-periodic von Mises distribution as a fiber density distribution around $\boldsymbol{M}$ for a planar condition. The von Mises distribution function is a one-dimensional probability distribution that represents the normal distribution projected over the unit sphere. The theoretical details are given in Chapter 5. Then, the modified structure tensors that reflect the fiber dispersion along orthogonal directions $\boldsymbol{f}$ and $\boldsymbol{s}$ are defined as

$$\boldsymbol{H}^*_f = \kappa_f \mathbf{1} + (1 - 3\kappa_f)\boldsymbol{f}_0 \otimes \boldsymbol{f}_0 \quad \text{and} \quad \boldsymbol{H}^*_s = \kappa_s \mathbf{1} + (1 - 3\kappa_s)\boldsymbol{s}_0 \otimes \boldsymbol{s}_0\,. \tag{6.9}$$

Double-contracted of structure tensors in equation (6.9) with unimodular part of the Cauchy-Green tensor $\bar{\boldsymbol{C}}$ gives the modified fourth invariants in orthogonal directions ($\bar{I}^*_{4f,s} = \bar{\boldsymbol{C}} : \mathbf{H}^*_{f,s}$).

The constitutive material formulation is presented in Lagrangian configuration which is based on additive decomposition of the free energy function composed of isotropic and anisotropic parts. The free energy further split into volumetric and isochoric part as a function of Jacobian J, and unimodular part of the left Cauchy-Green tensor $\bar{\boldsymbol{C}}$, respectively. The free energy function is described as

$$\hat{\Psi} := \Psi(\boldsymbol{C}, \boldsymbol{H}; \boldsymbol{\mathcal{I}}) = \Psi_{vol}(J) + \bar{\Psi}_{iso}(\bar{\boldsymbol{C}}, \boldsymbol{H}; \boldsymbol{\mathcal{I}}) + \bar{\Psi}_{ani}(\bar{\boldsymbol{C}}; \boldsymbol{\mathcal{I}}) \tag{6.10}$$

where $\boldsymbol{\mathcal{I}}$ denotes the set of internal variables those reveals viscoelastic behaviour of the material. With the use of Clasius-Planck inequality refer [107], the second Piola-Kirchhoff stress tensor ($\boldsymbol{S}$) and a stress-like quantity also known as internal force ($\boldsymbol{\beta}$) reads

$$\boldsymbol{S} = 2\partial_{\boldsymbol{C}}\Psi(\boldsymbol{C}, \boldsymbol{H}; \boldsymbol{\mathcal{I}}) \quad \text{and} \quad \boldsymbol{\beta} = -\partial_{\boldsymbol{\mathcal{I}}}\Psi(\boldsymbol{C}, \mathbf{H}; \boldsymbol{\mathcal{I}})\,, \tag{6.11}$$

The second Piola-Kirchhoff stress tensor in equation (6.11) decomposed of volumetric and isochoric parts as,

$$\boldsymbol{S} = \boldsymbol{S}_{vol} + \mathbf{S}_{iso}\,, \quad \text{where} \quad \boldsymbol{S}_{vol} := 2\partial_{\boldsymbol{C}}\Psi_{vol}(J) \quad \text{and} \quad \boldsymbol{S}_{iso} := 2\partial_{\boldsymbol{C}}\bar{\Psi}(\bar{\boldsymbol{C}}, \boldsymbol{H}; \boldsymbol{\mathcal{I}})\,. \tag{6.12}$$

The volumetric part of the second Piola-Kirchhoff stress tensor reads

$$\boldsymbol{S}_{vol} = \Psi'_{vol}(J) J \boldsymbol{C}^{-1}\,, \quad \text{where} \quad \hat{\Psi}'_{vol}(J) = \partial_J \Psi_{vol}(J) \quad \text{and} \quad p = J \partial_J \Psi_{vol}(J) \tag{6.13}$$

where p is the internal pressure term. The isochoric part of the second Piola-Kirchhoff stress tensor defined as

$$\boldsymbol{S}_{iso} = \bar{\boldsymbol{S}} : \mathbb{Q} \quad \text{with} \quad \bar{\boldsymbol{S}} := 2\,\partial_{\bar{\boldsymbol{C}}} \bar{\Psi}(\bar{\boldsymbol{C}}, \boldsymbol{H}, \boldsymbol{\mathcal{I}}) \quad \text{and} \quad \mathbb{Q} := \partial_{\boldsymbol{C}} \bar{\boldsymbol{C}} \tag{6.14}$$

where $\mathbb{Q}$ and $\mathbb{I}$ are the fourth order deviatoric projection and identity tensors, respectively. They are defined as following

$$\mathbb{Q} = J^{-2/3} \left[\mathbb{I} - \frac{1}{3} \boldsymbol{C} \otimes \boldsymbol{C}^{-1} \right]\,, \qquad \text{where} \quad \mathbb{I} := \frac{1}{2} \left(\mathbf{1} \overline{\otimes} \mathbf{1} + \mathbf{1} \underline{\otimes} \mathbf{1} \right) \tag{6.15}$$

The free-energy function in equation (6.10) can split into according to elastic and viscous response of the material, i.e.

$$\bar{\Psi}(\bar{\boldsymbol{C}}, \boldsymbol{H}; \boldsymbol{\mathcal{I}}) = \bar{\Psi}^e(\bar{\boldsymbol{C}}, \boldsymbol{H}) + \bar{\Psi}^v(\bar{\boldsymbol{C}}; \boldsymbol{\mathcal{I}}) \tag{6.16}$$

Similarly, the unimodular part of second Piola-Kirchhoff stress ($\bar{\boldsymbol{S}}$) is also decomposed into the elastic ($\bar{\boldsymbol{S}}^e$) and viscous ($\bar{\boldsymbol{S}}^v$)components as;

$$\bar{\boldsymbol{S}} = \bar{\boldsymbol{S}}^e + \bar{\boldsymbol{S}}^v \tag{6.17}$$

The elastic and viscous parts of unimoduar second Piola-Kirchoff stress are defined as a conjugate of unimodular part of right Cauchy-Green tensor ($\bar{\boldsymbol{C}}$)

$$\bar{\boldsymbol{S}}^e := 2 \partial_{\bar{\boldsymbol{C}}} \bar{\Psi}^e(\bar{\boldsymbol{C}}, \boldsymbol{H}) \quad \text{and} \quad \bar{\boldsymbol{S}}^v := 2 \partial_{\bar{\boldsymbol{C}}} \bar{\Psi}^v(\bar{\mathrm{C}}; \boldsymbol{\mathcal{I}}) \tag{6.18}$$

In order to get the solution of a nonlinear problem, it is required to solve it with incremental steps through Newton iterations. In this point, algorithmic tangent is introduced as the decomposition of volumetric and isochoric parts as

$$\Delta \boldsymbol{S} := \mathbb{C}^{algo} : \frac{1}{2} \Delta \boldsymbol{C}\,, \qquad \text{where} \quad \mathbb{C}^{algo} = \mathbb{C}_{vol} + \mathbb{C}^{algo}_{iso} \tag{6.19}$$

The volumetric part of the Lagrangian moduli can be derived directly from the free-energy as a closed-form expression

$$\mathbb{C}_{vol} := 4\,\partial^2_{\boldsymbol{C}\boldsymbol{C}} \Psi_{vol}(J) = \left[J^2 \Psi''_{vol}(J) + J \Psi'_{vol}(J) \right] \boldsymbol{C}^{-1} \otimes \boldsymbol{C}^{-1} - 2J \mathbb{I}_{\boldsymbol{C}^{-1}} \tag{6.20}$$

where superscript "$\prime$ " and " $\prime\prime$" represent the first and the second derivative with respect to the dependent variable (J). The isochoric part of the algorithmic Lagrangian moduli is expressed as

$$\mathbb{C}_{iso}^{algo} = \mathbb{Q}^T : \bar{\mathbb{C}}^{algo} : \mathbb{Q} + \frac{2}{3}\left(\bar{\boldsymbol{S}} : \bar{\boldsymbol{C}}\right)\mathbb{P}_{\boldsymbol{C}^{-1}} - \frac{2}{3}\left(\boldsymbol{S}_{iso} \otimes \boldsymbol{C}^{-1} + \boldsymbol{C}^{-1} \otimes \boldsymbol{S}_{iso}\right) \quad (6.21)$$

The unimodular part of algorithmic Lagrangian moduli is decomposed into elastic and viscous parts

$$\bar{\mathbb{C}}^{algo} = \bar{\mathbb{C}}_e + \bar{\mathbb{C}}_v^{algo} \quad (6.22)$$

The equlibrium part of the unimodular algorithmic Lagrangian moduli can be derived from the free-energy function and the non-equlibrium part can be derived in incremental form with time discretization,respectively.

$$\bar{\mathbb{C}}_e = 4\,\partial^2_{\bar{\boldsymbol{C}}\bar{\boldsymbol{C}}}\bar{\Psi}^e(\bar{\boldsymbol{C}}, \boldsymbol{H}) \quad (6.23)$$

Then, by inserting the dispersion-type modified invariants described in equation 6.8 into the the free-energy function defined in equation 6.3, the modified GST based dispersion-type free-energy function for the equilibrium response can be written as below in line with [10] and [1]

$$\begin{aligned} \bar{\Psi}^e(\bar{\boldsymbol{C}}) &= \frac{a}{2b}\left\{\exp[b(\bar{I}_1 - 3)] - 1\right\} + \sum_{i=f,s}\frac{a_i}{2b_i}\left\{\exp[b_i(\bar{I}^*_{4i} - 1)^2] - 1\right\} \\ &+ \frac{a_{fs}}{2b_{fs}}\left\{\exp[b_{fs}\bar{I}^2_{8fs}] - 1\right\}, \end{aligned} \quad (6.24)$$

As the additively decomposition of the free-energy function is introduced in equation 6.10, the volumetric part of the free-energy which satisfy zero stress state in unloaded condition, is defined as

$$\Psi_{vol}(J) = \kappa(J - \ln J - 1) \quad (6.25)$$

where κ is the bulk modulus, which should not be confused with the dispersion-related parameter described in equation 6.9. The first and the second derivatives of the volumetric free-energy with respect to Jacobian (J) are defined to be used in equations 6.13 and 6.20 for the corresponding stress and moduli derivations. Then, unimodular part of the elastic stress $\boldsymbol{S}^e$ which is defined in equation 6.4 can be modified through dispersion-type generalized structure tensors as below

$$\bar{\boldsymbol{S}}^e = \bar{\Psi}_1^{e'}\mathbf{1} + \bar{\Psi}_{4f}^{e'}\boldsymbol{H}_f^* + \bar{\Psi}_{4s}^{e'}\boldsymbol{H}_s^* + \bar{\Psi}_{8fs}^{e'}\boldsymbol{H}_{fs} \quad (6.26)$$

where the modified scalar derivative coefficients are introduced as follows

$$\begin{aligned}
\bar{\Psi}_1^{e'} &:= 2\partial_{\bar{I}_1}\bar{\Psi}^e = a\exp[b(\bar{I}_1-3)]\,,\\
\bar{\Psi}_{4f}^{e'} &:= 2\partial_{\bar{I}_{4f}^*}\bar{\Psi}^e = 2a_f(\bar{I}_{4f}^*-1)\,\exp[b_f(\bar{I}_{4f}^*-1)^2]\,,\\
\bar{\Psi}_{4s}^{e'} &:= 2\partial_{\bar{I}_{4s}^*}\bar{\Psi}^e = 2a_s(\bar{I}_{4s}^*-1)\,\exp[b_s(\bar{I}_{4s}^*-1)^2]\,,\\
\bar{\Psi}_{8fs}^{e'} &:= 2\partial_{\bar{I}_{8fs}}\bar{\Psi}^e = 2a_{fs}\bar{I}_{8fs}\,\exp(b_{fs}\bar{I}_{8fs}^2)
\end{aligned} \tag{6.27}$$

Then, corresponding modified elastic unimodular part of Lagrangian moduli yields,

$$\bar{\mathbb{C}}_e = \bar{\Psi}_1^{e''}\,\mathbf{1}\otimes\mathbf{1} + \bar{\Psi}_{4f}^{e''}\,\boldsymbol{H}_f^*\otimes\boldsymbol{H}_f^* + \bar{\Psi}_{4s}^{e''}\,\boldsymbol{H}_s^*\otimes\boldsymbol{H}_s^* + \bar{\Psi}_{8fs}^{e''}\,\boldsymbol{H}_{fs}\otimes\boldsymbol{H}_{fs} \tag{6.28}$$

Then the scalar second derivative coefficient are revised as follows

$$\begin{aligned}
\bar{\Psi}_1^{e''} &:= 4\partial^2_{\bar{I}_1\bar{I}_1}\bar{\Psi}^e = 2ab\,\exp[b(\bar{I}_1-3)]\,,\\
\bar{\Psi}_{4f}^{e''} &:= 4\partial^2_{\bar{I}_{4f}^*\bar{I}_{4f}^*}\bar{\Psi}^e = 4a_f[1+2b_f(\bar{I}_{4f}^*-1)^2]\,\exp[b_f(\bar{I}_{4f}^*-1)^2]\,,\\
\bar{\Psi}_{4s}^{e''} &:= 4\partial^2_{\bar{I}_{4s}^*\bar{I}_{4s}^*}\bar{\Psi}^e = 4a_s[1+2b_s(\bar{I}_{4s}^*-1)^2]\,\exp[b_s(\bar{I}_{4s}^*-1)^2]\,,\\
\bar{\Psi}_{8fs}^{e''} &:= 4\partial^2_{\bar{I}_{8fs}\bar{I}_{8fs}}\bar{\Psi}^e = 4a_{fs}(1+2b_{fs}\bar{I}_{8fs}^2)\,\exp(b_{fs}\bar{I}_{8fs}^2)
\end{aligned} \tag{6.29}$$

6.3.1 Convolution integral formulation

We will follow the convolution integral representation in sense of Gültekin et al. [1]. By considering one-dimensional rheological generalized Maxwell model, the first order linear differential equation for the evolution of viscous stresses is defined for the linear viscoelasticity. The exact integration of the linear evolution equation can be defined as follows

$$\dot{\bar{\boldsymbol{S}}}_i^v + \frac{\bar{\boldsymbol{S}}_i^v}{\tau_i} = \epsilon_i\dot{\bar{\boldsymbol{S}}}_i^e\,, \quad \bar{\mathbf{S}}_i^v(t=0) = \mathbf{0} \tag{6.30}$$

where the subscript "i" is used for f, s, n, fs as separate stress components. The differential equation satisfies the zero stress state though initial conditions and it can also be used to determine viscous strain as an variable. τ_i is the relaxation time in seconds. It can be defined as $\tau_i = \eta/\mu$, where η is the viscosity and μ is the shear modulus of the material through orthogonal directions. ϵ_i is the positive dimensionless parameter that work with isochoric stress component. The closed form of solution of equation 6.30 comes out with the convolution integral form as below

$$\bar{\boldsymbol{S}}_i^v = \int_0^t \exp\left(-\frac{t-s}{\tau_i}\right)\epsilon_i\dot{\bar{\boldsymbol{S}}}_i^e ds. \tag{6.31}$$

The approximation of integral 6.31 can be written in the time interval $[t_n, t_{n+1}]$ as

$$\bar{\boldsymbol{S}}^v_{i,n+1} = \int_0^{t+1} \exp\left(-\frac{t_{n+1}-s}{\tau_i}\right) \epsilon_i \dot{\bar{\boldsymbol{S}}}^e_i ds. \tag{6.32}$$

where $t_{n+1} = t_n + \Delta t$ then the integral 6.32 can be split into time intervals as $[0, t_n]$ and $[t_n, t+1]$ as below

$$\begin{aligned} \bar{\boldsymbol{S}}^v_{i,n+1} &= \int_0^{t_n} \exp\left(-\frac{\Delta t}{\tau_i}\right) \exp\left(-\frac{t_n - s}{\tau_i}\right) \epsilon_i \dot{\bar{\boldsymbol{S}}}^e_i ds \\ &+ \int_{t_n}^{t+1} \exp\left(-\frac{t_{n+1}-s}{\tau_i}\right) \epsilon_i \dot{\bar{\boldsymbol{S}}}^e_i ds. \end{aligned} \tag{6.33}$$

In order to approximate the integral 6.33, we consider the mid-point rule,

$$\int_{t_n}^{t+1} \exp\left(-\frac{t_{n+1}-s}{\tau_i}\right) \epsilon_i \dot{\bar{\boldsymbol{S}}}^e_i ds = \Delta t \left[\exp\left(-\frac{t_{n+1}+s}{\tau_i}\right) \dot{\bar{\boldsymbol{S}}}^e_i\right] \tag{6.34}$$

where $s = (t_n + t_{n+1})/2$. Then the viscous stress yield to the final form as

$$\bar{\boldsymbol{S}}^v_{i,\,n+1} = \exp\left(-\frac{\Delta t}{2\tau_i}\right) \left[\exp\left(-\frac{\Delta t}{2\tau_i}\right) \bar{\boldsymbol{S}}^v_{i,\,n} - \epsilon_i \bar{\boldsymbol{S}}^e_{i,\,n}\right] + \exp\left(-\frac{\Delta t}{2\tau_i}\right) \epsilon_i \bar{\boldsymbol{S}}^e_{i,\,n+1}\,, \tag{6.35}$$

The first term in equation 6.35, represents the t_n and the second term represents the t_{n+1} contributions, respectively. Then, viscous unimodular part of the tangent moduli $\bar{\mathbb{C}}^{algo}_v$ can be determined as

$$\bar{\mathbb{C}}^{n+1}_{v,i} = \exp\left(-\frac{\Delta t}{2\tau_i}\right) \epsilon_i \bar{\mathbb{C}}^{n+1}_{iso,i} \tag{6.36}$$

This algorithm is a second order accurate one-step algorithm for linear viscoelasticity.

6.3.2 Canonical formulation

Canonical representation for viscoelasticity is a common approach for both the linear and nonlinear evolution of the overstress response of the material. In this approach, internal variable set $\mathcal{I}$ can be either defined in tensorial or scalar strain-like variables conjugate to overstress. In sense of Miehe et al. [190], Dal et al. [120] and Cansiz et al. [18], the viscous response of the tissue are defined as logarithmic strain in each orientation directions f, s and n as following

$$\varepsilon_f := \frac{1}{2}\ln(\sqrt{\bar{I}_{4f}})\,, \qquad \varepsilon_s := \frac{1}{2}\ln(\sqrt{\bar{I}_{4s}})\,, \qquad \varepsilon_n := \frac{1}{2}\ln(\sqrt{\bar{I}_{4n}})\,, \tag{6.37}$$

The relationship between the storage $\bar{\Psi}^v$ and the dissipation potential Φ_{disp} is described by Biot [191] as

$$\partial_{\varepsilon_i^v}\bar{\Psi}_i^v(\varepsilon_i, \varepsilon_i^v) + \partial_{\dot{\varepsilon}_i^v}\Phi_{disp,i}(\dot{\varepsilon}_i^v) = 0 \quad \text{and} \quad \varepsilon_i^v(0) = \varepsilon_i^{v0}\,, \tag{6.38}$$

where $i = f, s, n$. For the non-equilibrium response, one-dimensional Maxwell rheological model in the logarithmic strain space is introduced in each distinct orthogonal direction and illustrated schematically in Figure 6.2. The specific form of the vicous

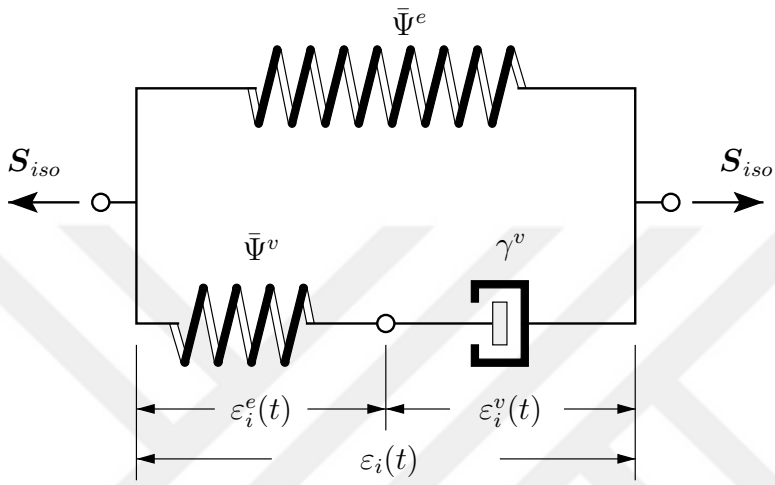

Figure 6.2: Schematically illustration of generalized Maxwell rheological model. Representation of the additively decomposition of isochoric free-energy into equilibrium and non-equilibrium parts. The springs are refers to stored energies and the dashpot represents the energy dissipation through viscous response.

part of the free-energy is described as a quadratic function as below

$$\bar{\Psi}^v(\varepsilon_i; \varepsilon_i^v) = \frac{1}{2}\sum_{i=f,s,n} \mu_i^v(\varepsilon_i - \varepsilon_i^v)^2\,, \tag{6.39}$$

where μ^v is the viscous shear modulus in orthogonal directions along fiber, sheet and normal. ε_i^v is the strain-like internal variables and in total the internal variable set $\boldsymbol{\mathcal{I}}$ contains three of scalar quantity in this formulation. The logarithmic stresses and the thermodynamical forces conjugate to the internal variables are described as follows

$$\sigma_i^v := \partial_{\varepsilon_i}\bar{\Psi}^v(\varepsilon_i, \varepsilon_i^v) \quad \text{and} \quad \beta_i := -\partial_{\varepsilon_i^v}\bar{\Psi}^v(\varepsilon_i, \varepsilon_i^v)\,, \tag{6.40}$$

For the specific choice of the viscous free energy function($\bar{\Psi}^v$), $\sigma_i^v = \beta_i$ equality can be maintained. The proper choose of the dissipation potential and algorithmic

process of the non-equilibrium response will be presented in the context of proposed dispersion-type anisotropic viscoelasticity formulation in the next section.

6.4 Proposed Formulations for Dispersion-type Anisotropic Viscoelasticity

As outlined in the above sections, dispersion-based anisotropic formulations are not considered in the literature for the rate-dependent behavior of tissues. Biological tissues are mostly considered as they include reinforced fibers embedded in an isotropic ground tissue matrix. From many of experimental studies, it was revealed that fiber distribution is not perfectly aligned in the specific orientation but it is dispersed around a mean fiber direction [192], [193], [93], [11]. Current state-of-the art dispersion-based anisotropic models account for the mechanical response of the myocardium using hyperelasticity theory. In this section, we propose an angular integration type dispersion-based anisotropic viscoelastic constitutive models. The deformation gradient is multiplicatively decomposed into spherical and unimodular parts; accordingly, the free energy function is additively decomposed into volumetric and isochoric parts, as introduced in section 6.2. Further, we also additively decompose the free energy function into equilibrium and non-equilibrium parts with the assumption that non-equilibrium part is related to the volume-preserving deformations. For equilibrium response, we adopt the formulation of Eriksson et al. [10] and details are given in section 6.3. Non-equilibrium response of myocardium is modelled through one dimensional rheological device consists of a spring with a Maxwell element in parallel with a quadratic free energy function in logarithmic strain space including density distribution function ρ. The viscous free-energy function introduced as the additively decomposition of micro-viscous free-energy functions in each orientation directions based on the affine approach. Then, quadratic and power-type dissipation potentials for each orientation direction have been presented for the different proposed models. The overstress response is then obtained by the numerical integration over the unit sphere for the fiber, sheet and normal directions. We quantitatively investigate the performance of the proposed framework with respect to available experimental data of Sommer et al. [11] in this chapter.

Firstly, we outline the general framework for a dispersion-type anisotropic viscoelas-

tic constitutive model for passive myocardium at finite strain in Lagrangian configuration. Then, by using these relations we will identify the differences of proposed formulations one-by-one.

By using equation 6.10, we decompose the free-energy function into volumetric, isochoric and anisotropic parts. The illustration of Maxwell rheological model and idealized network over unit sphere of the tissue are presented in Figure 6.3. $\bar{\Psi}^e$ and $\bar{\Psi}^v$ are isochoric parts of elastic and viscoleastic free-energies respectively and γ^v is the energy dissipation due to viscous effects. $\varepsilon_k(t)$ is the total logarithmic strain quantity decomposed of elastic $\varepsilon^e(t)$ and viscous $\varepsilon^v(t)$ parts which are related to each other through orientation directions on micro-sphere where k is the total number of micro orientation directions over the unit sphere. Let Lagrangian unit fiber orientation $\boldsymbol{r}$ on

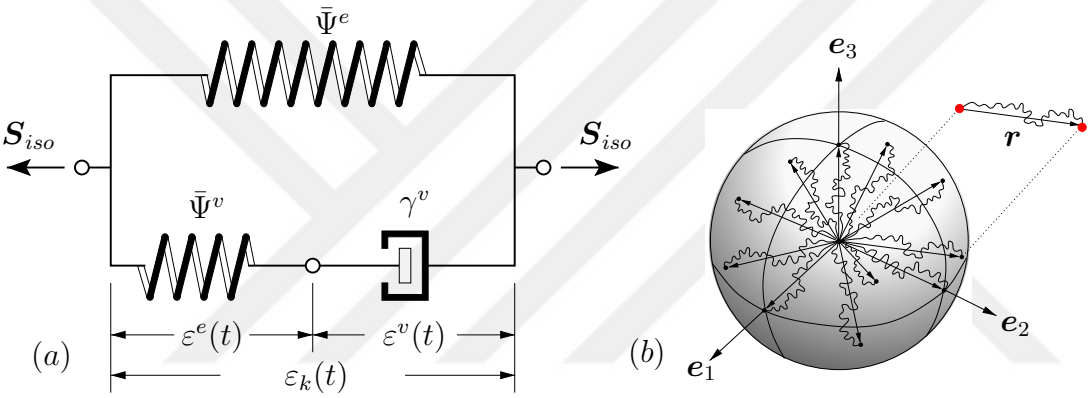

Figure 6.3: (a) Demonstration of generalised Maxwell rheological model (b) Idealization of tissue network for non-equilibrium response, the micro-sphere model

an unit sphere and the fiber density function in the direction of $\boldsymbol{r}$ is $\rho(\boldsymbol{r})$. The unit fiber orientation $\boldsymbol{r}$ is described with spherical coordinates as

$$\boldsymbol{r} = \sin\theta\cos\phi\boldsymbol{e}_1 + \sin\theta\sin\phi\boldsymbol{e}_2 + \cos\theta\boldsymbol{e}_3, \tag{6.41}$$

defined in Eulerian angles $\theta \in [0, \pi]$ and $\phi \in [0, 2\pi]$, see Figure 6.4. The deformed state of $\boldsymbol{r}$ is expressed with isochoric stretch vector $\boldsymbol{t} = \bar{\boldsymbol{F}}\boldsymbol{r}$. The non-equilibrium part of the model is constructed based on a quadratic free energy function in the logarithmic strain space. Quadratic-type or a power-type of dissipation potential are introduced those leads to the linear or nonlinear evolution equations in orientation directions, respectively. The overstress response will be determined by the numerical integration over the unit sphere with, i.e. 21 and 39 quadrature points. The numerical

integration over the sphere provides a numerical evaluation of averaging integrals by a discrete set of orientations. It provides sufficient accuracy and computationally inexpensive algebraic expressions [194]. The schematic representation of integration points are shown in Figure 6.5. The micro affine-stretch of a line element in the $\boldsymbol{r}$ orientation and corresponding logarithmic strain are defined as follows

$$\lambda_k = \sqrt{I_{4,k}} \quad \varepsilon_k = \frac{1}{2}\ln(\lambda_k), \quad \text{where} \quad I_{4,k} = t_{k,1}^2 + t_{k,2}^2 + t_{k,3}^2, \tag{6.42}$$

where subscript k is the set of discrete orientations in the micro-sphere.

We proposed two main approaches for formulations of dispersion effects through density distribution $\rho(\boldsymbol{r})$. In the first approach, namely local-based dispersion, we impose the density distribution over the mechanical viscous properties of the tissue, such as μ or η, viscous shear modulus and viscosity, respectively. In the second approach, we define the density distribution in a global manner that acts as a multiplier for the micro-viscous free energies. Both methods reach the overall stress and moduli expressions by integral averaging over the unit micro-sphere. In the following sub-sections, we will introduce these two approaches with a sub-proposed formulation for dispersion-type viscoelasticity.

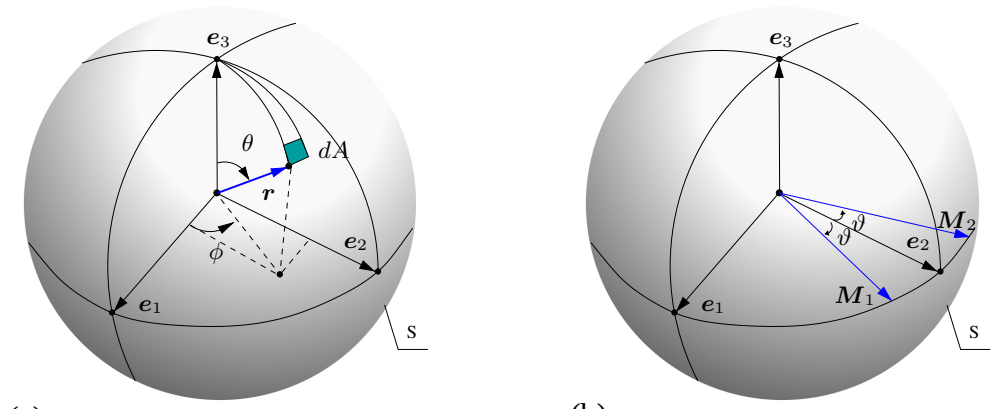

(a) (b)

Figure 6.4: (a) The unit micro-sphere and the orientation vector, (b) mean fiber directions of two families of fiber lie on $\boldsymbol{e}_1$-$\boldsymbol{e}_2$ plane.

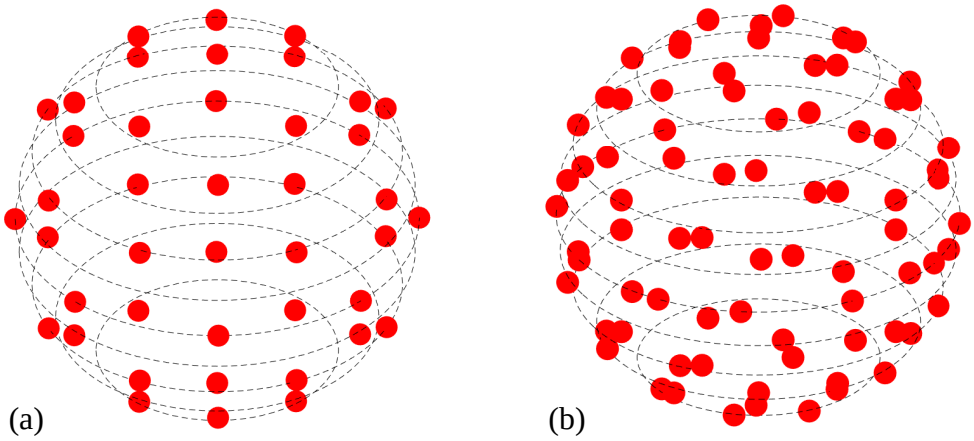

Figure 6.5: Demonstration of fully symmetric integration points over micro-sphere (a) 21 in half, in total 42 integration points (b) 39 in half, in total 78 integration points

6.4.1 Proposed formulations for local-based dispersion-type anisotropic viscoelasticity

In the local-based dispersion formulations, we introduce density distribution function $\rho(\boldsymbol{r})$ into the micro-viscous free-energy as an mechanical property multiplier. Accordingly, the non-equilibrium part of the macroscopic free energy is defined as the angular-integration of micro-viscous free energies over the unit micro-sphere that contributes in discrete orientation sets based on von Mises probability function $\rho(\boldsymbol{r})$

$$\bar{\Psi}^{v}(\bar{\boldsymbol{C}}, \boldsymbol{F}; \boldsymbol{\mathcal{I}}) = \bar{\Psi}^{v}(\boldsymbol{\varepsilon}; \boldsymbol{\mathcal{I}}) = \frac{1}{|\mathcal{S}|} \int_{\mathcal{S}} \bar{\Psi}^{micv}(\boldsymbol{F}, \boldsymbol{r})\, dA, \tag{6.43}$$

where $|\mathcal{S}| = 4\pi$ is the total area of the unit sphere. The contribution of each set of orientations to the macroscopic level can be defined as a continuous average over micro-sphere as follows

$$\langle \bullet \rangle = \frac{1}{|\mathcal{S}|} \int_{\mathcal{S}} (\bullet)\, dA \approx \sum_{k=1}^{p} w^{k} \left(\bullet\right)^{k} \quad \text{and} \quad \bar{\Psi}^{v}(\bar{\boldsymbol{C}}, \boldsymbol{F}; \boldsymbol{\mathcal{I}}) = \langle \psi^{micv}(\varepsilon, \varepsilon^{v}) \rangle, \tag{6.44}$$

where ${w^{k}}_{k=1:p}$ are the weight factors of the set integration points related with discrete orientation directions ${\boldsymbol{r}^{k}}_{k=1:p}$ and p is the total number of integration points. The corresponding orientation directions ($\boldsymbol{r}$) and weight factors (w) are described in [195], [196] and [166] with different numbers of integration points over the unit sphere. In these studies, Heo et al. [166] have also worked on the methodology of

cubature formulation for the sphere. Differently from the GST based dispersion of the elastic part of the material defined in equation 5.4; for the viscous part, there is defined bivariate von Mises distribution. In line with [158], the total probability distribution $\rho(\boldsymbol{r})$ is defined in the uncoupled form of multiplicatively decomposition of two distinct probability densities related with in-plane $\rho_{ip}(\Phi)$ and out of plane $\rho_{op}(\Theta)$ as stated in equation 5.10. Then, the logarithmic stresses and the thermodynamical forces conjugate to the internal variables are described as follows:

$$\sigma_k^v := \partial_{\varepsilon_k} \bar{\Psi}_k^{micv}(\varepsilon_k, \varepsilon_k^v) \quad \text{and} \quad \beta_k := -\partial_{\varepsilon_k^v} \hat{\bar{\Psi}}_k^{micv}(\varepsilon_k, \varepsilon_k^v)\,, \tag{6.45}$$

For the specific choice of the micro-viscous free energy function($\bar{\Psi}^{micv}$), $\sigma_k^v = \beta_k$ equality can be maintained. Accordingly the viscous free energy is defined in the quadratic form as follows

$$\bar{\Psi}_k^{micv}(\varepsilon_k, \varepsilon_v) = \frac{1}{2}\rho_k(\boldsymbol{r})\mu^v(\varepsilon_k - \varepsilon_k^v)^2, \tag{6.46}$$

Then, by using the relation between equations 6.45 and 6.46, the logarithmic stress and thermodynamical stress-like thermodynamical force are obtained as following in the orientation directions

$$\sigma_k^v := \rho_k(\boldsymbol{r})\mu^v(\varepsilon_k - \varepsilon_k^v) \quad \text{and} \quad \beta_k := \sigma_k^v \tag{6.47}$$

The dissipated energy in the dashpot of the Maxwell element shown in Figure 6.3_1 can be defined by power-type of generic dissipation potential on discrete set of orientation as

$$\Phi_{disp}(\dot{\boldsymbol{\mathcal{I}}}) = \sum_{k=1:p} \Phi_{disp,k}(\dot{\varepsilon}_k^v) \quad \text{where} \quad \Phi_{disp,k}(\dot{\varepsilon}_k^v) = \frac{\hat{\beta}^2}{\eta}\frac{(1+m)}{(2+m)}\left(\frac{\eta}{\hat{\beta}}|\dot{\varepsilon}_k^v|\right)^{\frac{2+m}{1+m}} \tag{6.48}$$

where $\hat{\beta}$ is the stress like parameter taken as 1.0 for unit consistency, η is the viscosity parameter in the orientation direction, and m is the parameter that identifies the transition between linear and nonlinear viscoelastic evolution laws. Equation 6.48 will lead to a linear form of evolution equation if $m = 0$ which will end up in a closed form expression for the internal variable ε_k^v. On the other hand if $m > 0$, the evolution equation become the nonlinear function of overstress β and it will require local Newton iterations in time discretization. Both linear and nonlinear solution of the evolution equation will be provided below. The relationship between the storage

and the dissipation potential is described by

$$\partial_{\varepsilon_k^v}\bar{\Psi}_k^v(\varepsilon_k,\varepsilon_k^v)+\partial_{\dot{\varepsilon}_k^v}\Phi_{disp,k}(\dot{\varepsilon}_k^v)=0 \quad \text{and} \quad \varepsilon_k^v(0)=\varepsilon_k^{v0}\,, \tag{6.49}$$

Linear Evolution Equation

After some mathematical manipulations defined by Biot [191], by using 6.48 and 6.45 , the linear evolution equations for the interval variables can be obtained in the orientation directions as

$$\dot{\varepsilon}_k^v=\dot{\gamma}_k^v(\beta_k)\,, \quad \text{where} \quad \dot{\gamma}_k^v(\beta_k)=\frac{\beta_k}{\eta} \tag{6.50}$$

To compute the internal variable at current time-step $n+1$, we describe equation 6.50_1 by backward Euler integration scheme which leads as follows

$$\varepsilon_{k,\,n+1}^v=\varepsilon_{k,\,n}^v+\Delta t\gamma_k^v(\beta_{k,\,n+1})\,, \tag{6.51}$$

By using equations 6.50 and (6.51) the internal variable can be determined as a closed form expression as follows

$$\varepsilon_{k,\,n+1}^v=\frac{(\Delta t/\eta)\rho(\boldsymbol{r})\mu\varepsilon_{k,\,n+1}+\varepsilon_{k,\,n}^v}{(1+\Delta t\rho(\boldsymbol{r})\mu/\eta)}\,, \tag{6.52}$$

Then, the unimodular part of the second Piola-Kirchoff stress of the viscous response can be written as a continuous average though orientations directions

$$\bar{\boldsymbol{S}}^v=\sum_{k=1:p}4\bar{\Psi}_{4k}^{v\prime}\boldsymbol{r}_k\otimes\boldsymbol{r}_k w_k\,, \tag{6.53}$$

where $\bar{\Psi}_{4k}^{v\prime}$ is the derivative resultant of the micro-viscous free-energy with respect to the orientation invariants which is related with the stretch as shown in equation 6.42_1 and defined explicity as follows

$$\bar{\Psi}_{4k}^{v\prime}:=2\partial_{\bar{I}_{4k}}\bar{\Psi}^v(\boldsymbol{\varepsilon};\boldsymbol{\mathcal{I}})=\frac{\sigma_k}{\bar{I}_{4k}}\,, \tag{6.54}$$

Then, the unimodular part of the algoritmic viscous tangent moduli can be expressed in the compact form as

$$\bar{\mathbb{C}}_v^{algo}=\sum_{k=1:p}2\bar{\Psi}_{4k}^{v\prime\prime}\boldsymbol{r}_k\otimes\boldsymbol{r}_k\otimes\boldsymbol{r}_k\otimes\boldsymbol{r}_k w_k\,. \tag{6.55}$$

where $\bar{\Psi}^{v''}_{4k}$ is the second derivative of the micro-viscous free-energy with respect to the orientation invariants and defined as

$$\bar{\Psi}^{v'}_{4_k} := \frac{(c_k - 2\sigma_k)}{I^2_{4k}} \quad \text{where} \quad c_k = \frac{\partial_{\sigma_k}}{\partial_{\varepsilon_k}} = \frac{\partial_{\sigma_k}}{\partial_{\varepsilon^e_k}} \left(1 - \frac{\partial_{\varepsilon^v_k}}{\partial_{\varepsilon_k}}\right) = \frac{\rho(\boldsymbol{r})\mu\eta}{\eta + \Delta t \rho(\boldsymbol{r})\mu} \,. \tag{6.56}$$

Non-linear Evolution Equation

In equation 6.48$_2$, $m > 0$ makes to evolution equation in nonlinear form of overstress and it is need to be solved by local Newton iterations. By using the relations of equations 6.48 and 6.49,the following evolution equation for strain-like internal variables obtained

$$\dot{\varepsilon}^v_k = \gamma^v_k(\beta_k) \text{ , where } \quad \gamma^v_k(\beta_k) = \frac{1}{\eta} \left| \frac{\beta_k}{\hat{\beta}} \right|^m \beta_k \tag{6.57}$$

The evaluation of the internal variable $\varepsilon^v_{k,n+1}$ at the current step is obtained by unconditionally stable backward-Euler integration scheme as it is already introduced in equation 6.51. The residual expression r_k is defined as a function of internal variable ε^v_k

$$r_k(\varepsilon^v_{k,\,n+1}) := \varepsilon^v_{k,\,n+1} - \varepsilon^v_{k,\,n} - \Delta t\, \gamma^v_k(\beta_{k,\,n+1}) = 0 \tag{6.58}$$

which requires local Newton iteration step $i + 1$

$$\varepsilon^{v,\,i+1}_{k,\,n+1} = \varepsilon^{v,\,i}_{k,\,n+1} - r^i_k \,/\, \mathcal{K}^i_k \tag{6.59}$$

where the local tangent term $\mathcal{K}^i_k$ is defined as follows

$$\mathcal{K}^i_k := \partial_{\varepsilon^v_{k,\,n+1}} r_k \Big|_{\varepsilon^{v,\,i}_{k,\,n+1}} = 1 - \Delta t \frac{(m+1)}{\eta} \left| \frac{\beta^i_{k,\,n+1}}{\hat{\beta}} \right|^m \partial_{\varepsilon^v_{k,\,n+1}} \beta^i_{k,n+1} \tag{6.60}$$

The unimodular part of the second Piola-Kirchoff stress and corresponding tangent moduli of the viscous response can be written identical form that is stated in equations 6.53 and 6.55. Then the c_k term in equation 6.56 can be obtained as follows

$$c_k = \frac{\partial \sigma_k}{\partial \varepsilon_k} = \frac{\partial \sigma_k}{\partial \varepsilon^e_k} \left(1 - \frac{\partial \varepsilon^v_k}{\partial \varepsilon_k}\right) = \frac{\partial \sigma_k}{\partial \varepsilon^e_k} \frac{1}{\mathcal{K}_k} \,. \tag{6.61}$$

Note that, the last derivative term in equation 6.60 and the derivative term in equation 6.61 are directly depend on the choice of the free-energy form. By using the relations of equations 6.46 and 6.47 for the specific choice of the free-energy, both derivatives gives the same result as $\rho(\boldsymbol{r})\mu$.

6.4.1.1 Proposed model-I - local-based bivariate von Mises dispersion formulation

In proposed model I, there is used single bivariate von Mises density distribution $\rho(\boldsymbol{r})$ for the sheet and fiber orientations. However, fiber and sheet directions formulated based on their own shear modulus such as $\mu_{v,f}$ and $\mu_{v,s}$ respectively. Since there are defined different shear moduli for the fiber and sheet directions, it requires the integral averaging over unit micro-sphere for each of the direction. Then the micro-viscous free energy functions along fiber and sheet directions are defined as follows:

$$\begin{aligned} \bar{\Psi}^{\mathrm{micv,f}}_{k=1:p}(\varepsilon_k, \varepsilon^{v,f}_k) &= \tfrac{1}{2}\rho(\boldsymbol{r}_k)\mu^{\mathrm{v,f}}(\varepsilon_k - \varepsilon^{v,f}_k)^2 \\ \bar{\Psi}^{\mathrm{micv,s}}_{k=p+1:2p}(\varepsilon_k, \varepsilon^{v,s}_k) &= \tfrac{1}{2}\rho(\boldsymbol{r}_k)\mu^{\mathrm{v,s}}(\varepsilon_k - \varepsilon^{v,s}_k)^2 \end{aligned} \tag{6.62}$$

where p is the total number of integration points over micro-sphere. There is defined two separate free-energy function and it requires twice of internal variables than the used integration points. For example, if there is used 21 integration points such as $p = 21$, then the number of total interval variables will be 42 that includes 21 internal variable for the fiber direction and 21 for the sheet directions. In the same logic, the local tangent terms $\mathcal{K}^i_k$ reads

$$\begin{aligned} \mathcal{K}^f_{k=1:p} &:= 1 - \Delta t \tfrac{(m+1)}{\eta^f} \left| \tfrac{\beta^f_{k,\,n+1}}{\hat{\beta}} \right|^m \rho(\boldsymbol{r}_k)\mu^{\mathrm{v,f}} \\ \mathcal{K}^s_{k=p+1:2p} &:= 1 - \Delta t \tfrac{(m+1)}{\eta^s} \left| \tfrac{\beta^s_{k,\,n+1}}{\hat{\beta}} \right|^m \rho(\boldsymbol{r}_k)\mu^{\mathrm{v,s}} \end{aligned} \tag{6.63}$$

6.4.1.2 Proposed model-II - local-based planar and bivariate combined von Mises dispersion formulation

In proposed model II, we formulate an angular-integration type anisotropic viscoelastic constitutive model at finite strains that uses planar and bivariate von Mises distribution functions for different orthogonal directions to capture fiber dispersion for soft biological tissues. It utilizes a quadratic free-energy function in the logarithmic space and a linear evolution equation in each orientation direction. The overstress response is obtained through distinct orientation directions by numerical evaluation of averaging integrals over the unit micro-sphere by making use of p_n number of quadrature

points for the normal contribution and over the unit planar circle by using p_{fs} number of quadrature points for the fiber-sheet plane.

Since we present the unit fiber direction $\boldsymbol{r}$ in a planar circle for $\boldsymbol{f} - \boldsymbol{s}$ plane, then θ in equation 6.41 drops out and $\boldsymbol{r}$ reduces in two dimensional vector in $\boldsymbol{e}_1 - \boldsymbol{e}_2$ plane. The main reason of the requirement of the planar circle integration in the in-plane, is covering even for the nearly anisotropic dispersion behaviours such as the cases where the concentration parameter $b > 100$. Otherwise less number of quadrature points over micro-sphere cannot sustain the normalization of overall density function ρ which can cause inaccurate results, see Figure 6.7. The numerical integration over the circle and sphere provides a numerical evaluation of averaging integrals for a discrete set of orientations. The schematic representation of integration points and stretch vectors over a planar circle and the micro-sphere is shown in Figure 6.6. The

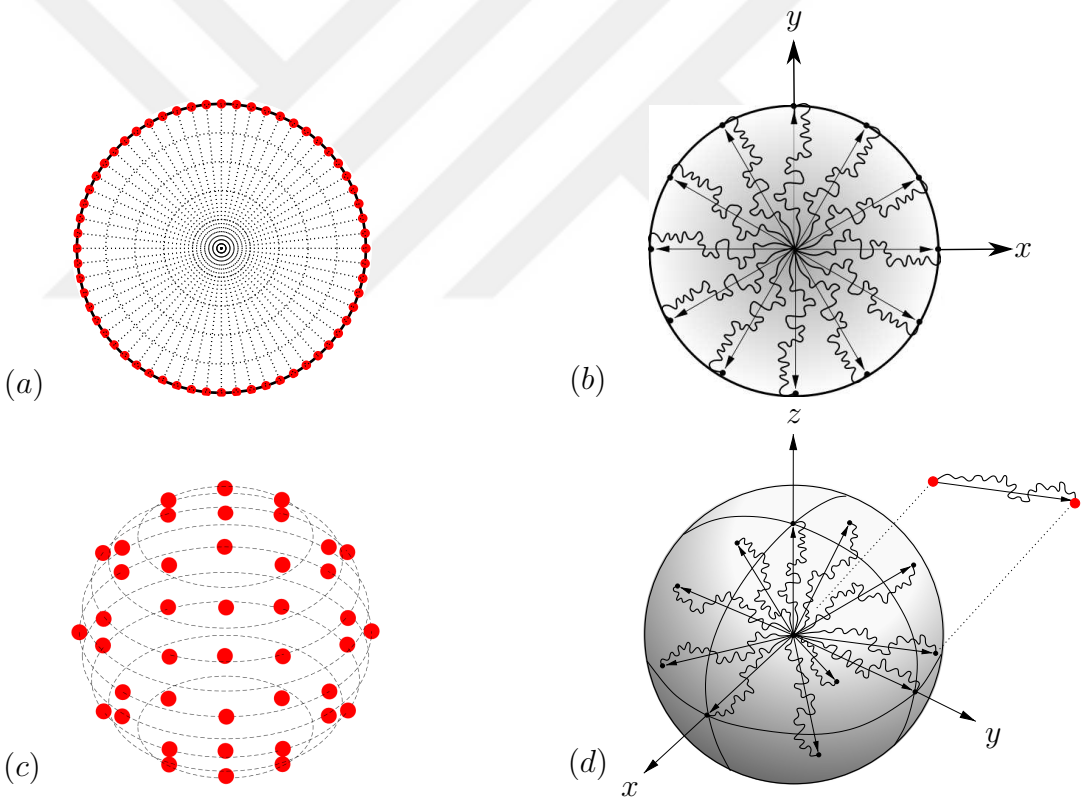

Figure 6.6: (a) Demonstration of fully symmetric integration points over planar circle, given for 30 integration points (p_{fs}) in half circle (b) Idealization of tissue network for the non-equilibrium response, the planar circle model (c) Demonstration of fully symmetric integration points over micro-sphere, given for 21 integration points (p_n) in half circle (d) Idealization of tissue network for non-equilibrium response, the micro-sphere model.

micro affine-stretch of a line element in the $\boldsymbol{r}$ orientation and corresponding logarithmic strain are defined similarly as in equation 6.42. Note that, since the location of integration points are different in a circle and a sphere, the orientation directions are also different from each other, see Figure 6.6. The non-equilibrium part of the macroscopic free energy is defined as the angular-integration of micro-viscous free energies over the planar circle and micro-sphere in discrete orientation sets based on von Mises probability function which is defined equation 6.43. However, that relation is valid for unit micro-sphere approach. Note that, when the integration to be performed over planar circle, $|\mathcal{S}|$ will describe the total circumference of the unit circle which corresponds for 2π and the integrand dA should be replaced with $d\phi$. By the proposed model II, it is aimed to sustain the normality of dispersion of fibers and sheets in-plane by taking the circular planar integration and the normal direction contributes isotropic way by the integral averaging over the micro-sphere. The model uses $2p_{fs} + p_n$ internal variables in total. It is because the planar integration points may be different from the unit-sphere integration points. In addition to that, there have been defined distinct mechanical properties for orthogonal directions in fiber, sheet, and normal, such as shear moduli (μ_f, μ_s and μ_n) and viscosity (η_f, η_s and η_n). Then the resultant micro-viscous free energy forms are given below where ρ_f and ρ_s are the same density distributions along the orthogonal directions, and ρ_n is the density distribution to describe the behaviour for normal orientation. It is mainly contributes to isotropic behaviour of the viscous stress if ρ_n is taken as 1.

$$\begin{aligned}
\bar{\Psi}^{\mathrm{micv,f}}_{k=1:p_{fs}}(\varepsilon_k, \varepsilon_k^{v,f}) &= \tfrac{1}{2}\rho_f(\boldsymbol{r}_k)\mu^{\mathrm{v,f}}(\varepsilon_k - \varepsilon_k^{v,f})^2 \\
\bar{\Psi}^{\mathrm{micv,s}}_{k=p_{fs}+1:2p_{fs}}(\varepsilon_k, \varepsilon_k^{v,s}) &= \tfrac{1}{2}\rho_s(\boldsymbol{r}_k)\mu^{\mathrm{v,s}}(\varepsilon_k - \varepsilon_k^{v,s})^2 \\
\bar{\Psi}^{\mathrm{micv,n}}_{k=1:p_n}(\varepsilon_k, \varepsilon_k^{v,n}) &= \tfrac{1}{2}\rho_n(\boldsymbol{r}_k)\mu^{\mathrm{v,n}}(\varepsilon_k - \varepsilon_k^{v,n})^2
\end{aligned} \tag{6.64}$$

The second Piola-Kirchhoff stress of the viscous response reads to continuous averaging through orientation directions as follows

$$\begin{aligned}
\bar{\boldsymbol{S}}^v &= \textstyle\sum_{k=1:p_{fs}} 4\bar{\Psi}^{v'}_{f,4k}\boldsymbol{r}_k \otimes \boldsymbol{r}_k w_k \\
&+ \textstyle\sum_{k=p_{fs}+1:2p_{fs}} 4\bar{\Psi}^{v'}_{s,4k}\boldsymbol{r}_k \otimes \boldsymbol{r}_k w_k \\
&+ \textstyle\sum_{k=1:p_n} 4\bar{\Psi}^{v'}_{n,4k}\boldsymbol{r}_k \otimes \boldsymbol{r}_k w_k
\end{aligned} \tag{6.65}$$

Then corresponding algorithmic viscous tangent moduli can be written as

$$\begin{aligned}\bar{\mathbb{C}}_v^{algo} &= \textstyle\sum_{k=1:p_{fs}} 2\bar{\Psi}_{f,4k}^{v''}\boldsymbol{r}_k \otimes \boldsymbol{r}_k \otimes \boldsymbol{r}_k \otimes \boldsymbol{r}_k w_k \\ &+ \textstyle\sum_{k=p_{fs}+1:2p_{fs}} 2\bar{\Psi}_{s,4k}^{v''}\boldsymbol{r}_k \otimes \boldsymbol{r}_k \otimes \boldsymbol{r}_k \otimes \boldsymbol{r}_k w_k \\ &+ \textstyle\sum_{k=1:p_n} 2\bar{\Psi}_{n,4k}^{v''}\boldsymbol{r}_k \otimes \boldsymbol{r}_k \otimes \boldsymbol{r}_k \otimes \boldsymbol{r}_k w_k\end{aligned} \tag{6.66}$$

6.4.2 Proposed formulations for global-based dispersion-type anisotropic viscoelasticity

In the second approach, we define the density distribution $\rho(\boldsymbol{r})$ in global manner that acts as an multiplier to the micro-viscous free energies. In other words, the density distribution is placed outside of the micro-viscous free energy and enters the formulation during the integral averaging of stress and tangent moduli expressions. Then, the non-equilibrium part of the macroscopic free energy is defined as the angular-integration of micro-viscous free energies over the unit micro-sphere that contributes in discrete orientation sets based on von Mises probability function $\rho(\boldsymbol{r})$

$$\bar{\Psi}^v(\bar{\boldsymbol{C}}, \boldsymbol{F}; \boldsymbol{\mathcal{I}}) = \bar{\Psi}^v(\boldsymbol{\varepsilon}; \boldsymbol{\mathcal{I}}) = \frac{1}{|\mathcal{S}|}\int_{\mathcal{S}} \rho(\boldsymbol{r})\bar{\Psi}^{micv}(\boldsymbol{F}, \boldsymbol{r})\, dA, \tag{6.67}$$

where $|\mathcal{S}| = 4\pi$ is the total area of the unit sphere. By contribution of each orientation set to the macroscopic level can be defined as a continuous average over micro-sphere as follows

$$\langle \bullet \rangle = \frac{1}{|\mathcal{S}|}\int_{\mathcal{S}} (\bullet)\, dA \approx \sum_{k=1}^{p} w^k\, (\bullet)^k \quad \text{and} \quad \bar{\Psi}^v(\bar{\boldsymbol{C}}, \boldsymbol{F}; \boldsymbol{\mathcal{I}}) = \langle \rho\psi^{micv}(\varepsilon, \varepsilon^v)\rangle, \tag{6.68}$$

where ${w^k}_{k=1:p}$ are the weight factors of the set integration points related with discrete orientation directions ${\boldsymbol{r}^k}_{k=1:p}$ and p is the total number of integration points. Then, the logarithmic stresses and the thermodynamical forces conjugate to the internal variables can described identical in the form of equation 6.45. Accordingly the viscous free energy is defined in the quadratic form as follows

$$\bar{\Psi}_k^{micv}(\varepsilon_k, \varepsilon_v) = \frac{1}{2}\mu^v(\varepsilon_k - \varepsilon_k^v)^2, \tag{6.69}$$

Then, by using the relation between equations 6.45 and 6.69, the logarithmic stress and thermodynamical stress-like thermodynamical force are obtained as following in

the orientation directions

$$\sigma_k^v := \mu^v(\varepsilon_k - \varepsilon_k^v) \quad \text{and} \quad \beta_k := \sigma_k^v \tag{6.70}$$

The dissipated energy in the dashpot of the Maxwell element shown in Figure 6.3_1 is identical to equation 6.48. Both linear and nonlinear solution of the evolution equation will be provided below which will exclude the density distribution $\rho(\boldsymbol{r})$ compared to the local-based formulations.

Linear Evolution Equation

The linear evolution equations for the interval variables and corresponding backward Euler integration scheme is identical to equations 6.50 and 6.51. By using these equations, the internal variable can be determined as a closed form expression as follows

$$\varepsilon_{k,\,n+1}^v = \frac{(\Delta t/\eta)\mu\varepsilon_{k,\,n+1} + \varepsilon_{k,\,n}^v}{(1 + \Delta t\mu/\eta)}\,, \tag{6.71}$$

Then, the unimodular part of the second Piola-Kirchoff stress of the viscous response reads as a continuous average though orientations directions

$$\bar{\boldsymbol{S}}^v = \sum_{k=1:p} 4\rho(\boldsymbol{r})\bar{\Psi}_{4k}^{v'}\boldsymbol{r}_k \otimes \boldsymbol{r}_k w_k\,, \tag{6.72}$$

where $\bar{\Psi}_{4k}^{v'}$ is the derivative resultant of the micro-viscous free-energy with respect to the orientation invariants and already given in equation 6.54. Then, the unimodular part of the algoritmic viscous tangent moduli can be written as

$$\bar{\mathbb{C}}_v^{algo} = \sum_{k=1:p} 2\rho(\boldsymbol{r})\bar{\Psi}_{4k}^{v''}\boldsymbol{r}_k \otimes \boldsymbol{r}_k \otimes \boldsymbol{r}_k \otimes \boldsymbol{r}_k w_k\,. \tag{6.73}$$

where $\bar{\Psi}_{4k}^{v''}$ is the second derivative of the micro-viscous free-energy with respect to the orientation invariants and written as

$$\bar{\Psi}_{4_k}^{v'} := \frac{(c_k - 2\sigma_k)}{I_{4k}^2} \quad \text{where} \quad c_k = \frac{\partial\sigma_k}{\partial\varepsilon_k} = \frac{\partial\sigma_k}{\partial\varepsilon_k^e}\left(1 - \frac{\partial\varepsilon_k^v}{\partial\varepsilon_k}\right) = \frac{\mu\eta}{\eta + \Delta t\mu}\,. \tag{6.74}$$

Non-linear Evolution Equation

In the previous sub-section, the non-linear evolution equations 6.57-6.61 are given in the general form that includes the specific derivatives of stress and overstress with respect to strain and strain-like internal variables, respectively. Therefore, we do

not repeat the same steps here. The important point in the global-based dispersion formulations is, logarithmic stress and overstress measures do not include density distribution in local manner, see equation 6.70. Then, by using equation 6.69 and 6.70, the last derivative term in equation 6.60 and the derivative term in equation 6.61 yield the same result, such as μ due to the specific form of the micro-viscous free-energy form.

6.4.2.1 Proposed model-III - global-based bivariate von Mises dispersion formulation

The proposed model III is formulated similar to model I by using a single bivariate von Mises density distribution $\rho(\boldsymbol{r})$ for the sheet and fiber orientations. The only difference is that the density distributions are imposed in a global manner rather than embedded in the micro-viscous free energies. The fiber and sheet directions formulated based on separate shear modulus such as $\mu_{v,f}$ and $\mu_{v,s}$ respectively. Since there are defined different shear moduli for the fiber and sheet directions, it requires the integral averaging over unit micro-sphere for each of the direction. Then the micro-viscous free energy functions along fiber and sheet directions are defined as follows

$$\begin{aligned} \bar{\Psi}^{\mathrm{micv,f}}_{k=1:p}(\varepsilon_k, \varepsilon^{v,f}_k) &= \tfrac{1}{2}\mu^{\mathrm{v,f}}(\varepsilon_k - \varepsilon^{v,f}_k)^2 \\ \bar{\Psi}^{\mathrm{micv,s}}_{k=p1:2p}(\varepsilon_k, \varepsilon^{v,s}_k) &= \tfrac{1}{2}\mu^{\mathrm{v,s}}(\varepsilon_k - \varepsilon^{v,s}_k)^2 \end{aligned} \tag{6.75}$$

where p is the total number of integration points over micro-sphere. Since there is defined two separate free-energy function, it requires double of internal variables than the used integration points. In the similar manner, the local tangent terms $\mathcal{K}^i_k$ reads

$$\begin{aligned} \mathcal{K}^f_{k=1:p} &:= 1 - \Delta t \tfrac{(m+1)}{\eta^f} \left| \tfrac{\beta^f_{k,\,n+1}}{\hat{\beta}} \right|^m \mu^{\mathrm{v,f}} \\ \mathcal{K}^s_{k=p+1:2p} &:= 1 - \Delta t \tfrac{(m+1)}{\eta^s} \left| \tfrac{\beta^s_{k,\,n+1}}{\hat{\beta}} \right|^m \mu^{\mathrm{v,s}} \end{aligned} \tag{6.76}$$

Then the unimodular part of the second Piola-Kirchhoff stress of the viscous response yields to continuous averaging though orientation directions as follows

$$\bar{\boldsymbol{S}}^v = \sum_{k=1:p} 4\rho_f(\boldsymbol{r})\bar{\Psi}^{v'}_{f,4k}\boldsymbol{r}_k \otimes \boldsymbol{r}_k w_k \; + \sum_{k=p+1:2p} 4\rho_s(\boldsymbol{r})\bar{\Psi}^{v'}_{s,4k}\boldsymbol{r}_k \otimes \boldsymbol{r}_k w_k \,, \tag{6.77}$$

where $\rho_f(\boldsymbol{r})$ and $\rho_s(\boldsymbol{r})$ are the density distributions along different orthogonal directions. They can either be taken the same or different. Then, similarly the unimodular part of the algorithmic viscous tangent moduli can be written as

$$\bar{\mathbb{C}}_v^{algo} = \sum_{k=1:p} 2\rho_f(\boldsymbol{r})\bar{\Psi}_{f,4k}^{v''}\boldsymbol{r}_k\otimes\boldsymbol{r}_k\otimes\boldsymbol{r}_k\otimes\boldsymbol{r}_k w_k + \sum_{k=p+1:2p} 2\rho_s(\boldsymbol{r})\bar{\Psi}_{s,4k}^{v''}\boldsymbol{r}_k\otimes\boldsymbol{r}_k\otimes\boldsymbol{r}_k\otimes\boldsymbol{r}_k w_k \tag{6.78}$$

6.4.2.2 Proposed model-IV - global-based planar and bivariate combined dispersion formulation

The proposed model IV is formulated in a similar manner to model II by using an angular-integration type anisotropic viscoelastic constitutive model at finite strains that uses planar and bivariate von Mises distribution functions for different orthogonal directions such as fiber, sheet, and normal. In model IV, we utilize a quadratic free-energy function in logarithmic space and a power-type non-linear evolution equation in each orientation direction. The general frame work is the same as model II except the definition of the density distribution $\rho(\boldsymbol{r})$ acts on the micro-viscous free-energies in globally. On the contrary to model II, in model IV since we adopt the density distribution function in global stress and moduli expressions, it is not only satisfy the normalization condition on linear evolution-law but also meet the normalization for non-linear evolution. The micro-viscous free energy functions are defined as below

$$\begin{aligned}
\bar{\Psi}_{k=1:p_{fs}}^{\mathrm{micv,f}}(\varepsilon_k, \varepsilon_k^{v,f}) &= \tfrac{1}{2}\mu^{\mathrm{v,f}}(\varepsilon_k - \varepsilon_k^{v,f})^2 \\
\bar{\Psi}_{k=p_{fs}+1:2p_{fs}}^{\mathrm{micv,s}}(\varepsilon_k, \varepsilon_k^{v,s}) &= \tfrac{1}{2}\mu^{\mathrm{v,s}}(\varepsilon_k - \varepsilon_k^{v,s})^2 \\
\bar{\Psi}_{k=1:p_n}^{\mathrm{micv,n}}(\varepsilon_k, \varepsilon_k^{v,n}) &= \tfrac{1}{2}\mu^{\mathrm{v,n}}(\varepsilon_k - \varepsilon_k^{v,n})^2
\end{aligned} \tag{6.79}$$

Then, the unimodular part of the second Piola-Kirchhoff stress of the viscous response reads to continuous averaging though orientation directions as follows

$$\begin{aligned}
\bar{\boldsymbol{S}}^v &= \textstyle\sum_{k=1:p_{fs}} 4\rho_f(\boldsymbol{r})\bar{\Psi}_{f,4k}^{v'}\boldsymbol{r}_k\otimes\boldsymbol{r}_k w_k \\
&+ \textstyle\sum_{k=p_{fs}+1:2p_{fs}} 4\rho_s(\boldsymbol{r})\bar{\Psi}_{s,4k}^{v'}\boldsymbol{r}_k\otimes\boldsymbol{r}_k w_k \\
&+ \textstyle\sum_{k=1:p_n} 4\rho_n(\boldsymbol{r})\bar{\Psi}_{n,4k}^{v'}\boldsymbol{r}_k\otimes\boldsymbol{r}_k w_k
\end{aligned} \tag{6.80}$$

Then, similarly the unimodular part of the algorithmic viscous tangent moduli can be written as

$$\begin{aligned}\bar{\mathbb{C}}_v^{algo} &= \textstyle\sum_{k=1:p_{fs}} 2\rho_f(\boldsymbol{r})\bar{\Psi}_{f,4k}^{v''}\boldsymbol{r}_k \otimes \boldsymbol{r}_k \otimes \boldsymbol{r}_k \otimes \boldsymbol{r}_k w_k \\ &+ \textstyle\sum_{k=p_{fs}+1:2p_{fs}} 2\rho_s(\boldsymbol{r})\bar{\Psi}_{s,4k}^{v''}\boldsymbol{r}_k \otimes \boldsymbol{r}_k \otimes \boldsymbol{r}_k \otimes \boldsymbol{r}_k w_k \\ &+ \textstyle\sum_{k=1:p_n} 2\rho_n(\boldsymbol{r})\bar{\Psi}_{n,4k}^{v''}\boldsymbol{r}_k \otimes \boldsymbol{r}_k \otimes \boldsymbol{r}_k \otimes \boldsymbol{r}_k w_k\end{aligned} \tag{6.81}$$

6.4.2.3 Proposed model-V - global-based planar von Mises dispersion formulation

Proposed model-V uses planar von Mises density distribution function $\rho(\boldsymbol{r})$ for the sheet and fiber orientations and threat the normal direction by using isotropic behaviour through the unit-micro sphere. Additionally, as another alternative approach, we also add dispersion in the normal direction. This formulation is similar to model I however, it also contains the shear modulus regarding to the normal direction $\mu_{v,s}$ in addition to shear modulus of fiber and sheet directions such as $\mu_{v,f}$ and $\mu_{v,s}$ respectively. Since there are defined different viscous properties for orthogonal directions (fiber, sheet and normal), it requires the integral averaging over unit micro-sphere for each of the direction. Then the micro-viscous free energy functions along orthogonal directions are defined as follows

$$\begin{aligned}\bar{\Psi}_{k=1:p}^{\mathrm{micv,f}}(\varepsilon_k, \varepsilon_k^{v,f}) &= \tfrac{1}{2})\mu^{\mathrm{v,f}}(\varepsilon_k - \varepsilon_k^{v,f})^2 \\ \bar{\Psi}_{k=p+1:2p}^{\mathrm{micv,s}}(\varepsilon_k, \varepsilon_k^{v,s}) &= \tfrac{1}{2}\mu^{\mathrm{v,s}}(\varepsilon_k - \varepsilon_k^{v,s})^2 \\ \bar{\Psi}_{k=2p+1:3p}^{\mathrm{micv,n}}(\varepsilon_k, \varepsilon_k^{v,n}) &= \tfrac{1}{2}\mu^{\mathrm{v,n}}(\varepsilon_k - \varepsilon_k^{v,n})^2\end{aligned} \tag{6.82}$$

Then, the unimodular part of the second Piola-Kirchhoff stress of the viscous response reads to continuous averaging though orientation directions as follows

$$\begin{aligned}\bar{\boldsymbol{S}}^v &= \textstyle\sum_{k=1:p} 4\rho_f(\boldsymbol{r})\bar{\Psi}_{f,4k}^{v'}\boldsymbol{r}_k \otimes \boldsymbol{r}_k w_k \\ &+ \textstyle\sum_{k=p+1:2p} 4\rho_s(\boldsymbol{r})\bar{\Psi}_{s,4k}^{v'}\boldsymbol{r}_k \otimes \boldsymbol{r}_k w_k \\ &+ \textstyle\sum_{k=2p+1:3p} 4\bar{\Psi}_{n,4k}^{v'}\boldsymbol{r}_k \otimes \boldsymbol{r}_k w_k\end{aligned} \tag{6.83}$$

Then, similarly the unimodular part of the algorithmic viscous tangent moduli can be written as

$$\begin{aligned}\bar{\mathbb{C}}_v^{algo} &= \textstyle\sum_{k=1:p} 2\rho_f(\boldsymbol{r})\bar{\Psi}_{f,4k}^{v''}\boldsymbol{r}_k \otimes \boldsymbol{r}_k \otimes \boldsymbol{r}_k \otimes \boldsymbol{r}_k w_k \\ &+ \textstyle\sum_{k=p+1:2p} 2\rho_s(\boldsymbol{r})\bar{\Psi}_{s,4k}^{v''}\boldsymbol{r}_k \otimes \boldsymbol{r}_k \otimes \boldsymbol{r}_k \otimes \boldsymbol{r}_k w_k \\ &+ \textstyle\sum_{k=2p+1:3p} 2\bar{\Psi}_{n,4k}^{v''}\boldsymbol{r}_k \otimes \boldsymbol{r}_k \otimes \boldsymbol{r}_k \otimes \boldsymbol{r}_k w_k\end{aligned} \tag{6.84}$$

6.4.3 Numerical sensitivity of the AI-based anisotropic dispersion

It is essential to check the numerical sensitivity of the AI-based density distribution function ρ, while using different numbers of integration points on the unit micro-sphere or on the unit planar circle. The numerical integration points over the unit micro-sphere varies from 42 to 600, which is also the number of orientations for micro-fibers. The visual representation of 42 integration points over the unit micro-sphere is given in Figure 6.6$_3$. Due to the symmetry in the sphere, in numerical applications half of the total integration points are sufficient to reflect overall behaviour. Alastrué et al. [156] stated that 368 directions are sufficient to catch the accurate results where the concentration parameter $b \leq 20$. For the higher degree of anisotropy there should be used much more integration points over the unit micro-sphere. The resultant density functions, calculated for planar von Mises and bivariate von Mises distributions, are given in Figure 6.7 by the numerical integration over micro-sphere. Figure 6.7$_1$ represents the planar von Mises density distribution results by changing the concentration parameter b. 21, 39 and 55 are the numerical integration results of density functions those are calculated by 21, 39 and 55 integration points over the unit micro-sphere. The "$quad$" is the result of quadrature integral calculated on Python that provides very close result to exact one. The planar density distribution in 5.4 satisfies the normalization naturally due to the form of the density function. Therefore the quadrature gives the exact results of 1 every points of the concentration factor b. However, 21 point integration is highly accurate up to $b \leq 2.1$, 39 point integration is highly accurate up to $b \leq 4.3$ and 55 point integration is highly accurate up to $b \leq 6.4$. These limits are considered of the error is less than %1. It is also shown that by increasing the concentration parameter b, while 21 and 39 points of nu-

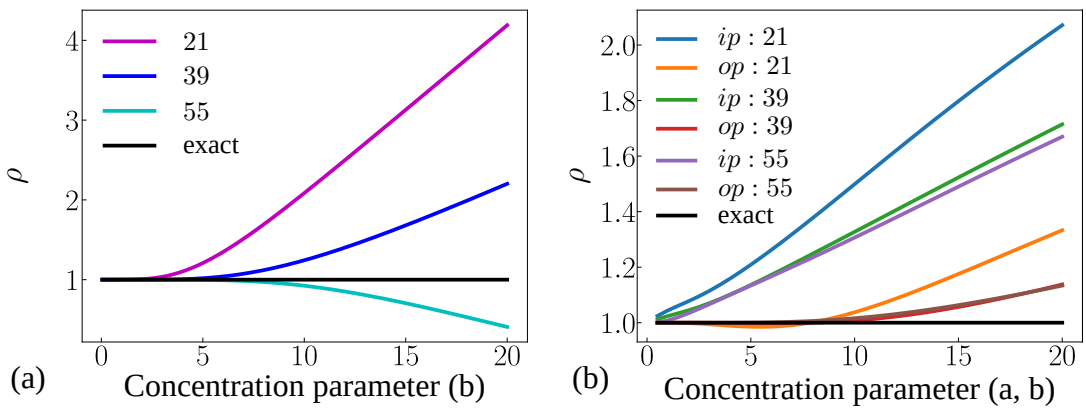

Figure 6.7: (a) Graphical representation of the relationship between the normalized planar density distribution ρ and the concentration parameter b by numerical integration over micro-sphere for different number of integration points, (b) Graphical representation of the relationship between the normalized bivariate density distribution ρ^{ip} and ρ^{op} and the concentration parameters a and b respectively by the numerical integration over micro-sphere for different number of integration points

merical integrals over unit sphere overestimates the density distribution ρ, 55 points of integration underestimates. It is also concluded that, there should be used much higher integration points over the unit micro-sphere for highly anisotropic dispersion histology.

Figure 6.7$_2$ represents the numerical results of bivariate von Mises density distribution over the unit micro-sphere by changing the concentration parameter a and b for in-plane and out-of-plane distributions, respectively. Similarly, 21, 39 and 55 are the numerical integration results of density functions those are calculated by 21, 39 and 55 integration points over the unit micro-sphere and "ip" and "op" denotes the in-plane and out-of-plane distributions separately. The in-plane numerical results for 21, 39 and 55 integration points are in divergence trend from the beginning. The out-of-plane integral results does not suffers from the accuracy in the lower values of concentration factors b. Since the overall density is multiplicatively decomposed into in-plane and out-of-plane components, their multiplicative product is the determinant of the overall behaviour and it is identical to the numerical integration results of planar density distribution which is given in Figure 6.7$_1$. The out-of-plane accuracy can be

maintained for $b \leq 4.0$ with %1 error. The deviation trend of the out-of-plane results are in nonlinear behaviour and gives more accurate result for 55 integration points over the unit micro-sphere. To reflect the more accurate results for high anisotropy for bivariate von Mises density distribution, there should be used more integration points.

Due to the three-dimensional orientation sets of the unit micro-sphere, integration points should be spread around the spherical surface in 3-D space. Therefore, it is necessary to use high number of integration points to get more accurate results for highly anisotropic dispersion histology; otherwise, low numbers of integration points cause erroneous numerical integration for highly anisotropic fiber distributions, which is determined by the concentration parameter b. Therefore, we proposed to use the unit planar circle integration for planar type of dispersion characteristics. Since planar circle integration reduces the working space from 3-D to 2-D, it is possible to get higher accuracy with small number of integration points compared to unit micro-sphere. The visual representation of 60 integration points over the unit planar circle is given in Figure 6.6$_1$. The numerical sensitivity of the unit planar circular integration approach is shown in Figure 6.8 against concentration factor b.

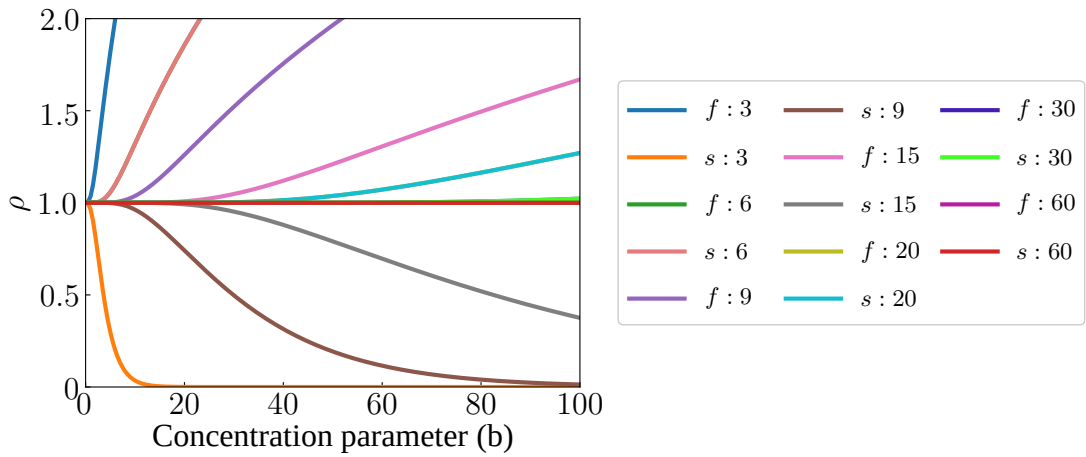

Figure 6.8: The relationship between the normalized planar density distribution ρ and the concentration parameter b by numerical integration over the unit planar circle for different number of integration points.

In the Figure 6.8, f and s refer for the direction vectors for fiber and sheet, respec-

tively. Numbers in the legend, represent the half of the integration points over the planar circle, such as $\{3, 6, 9, 15, 20, 30, 60\}$. In the sensitivity analysis, the fiber and sheet is examined in a single numerical integration calculation which takes the orthogonality of fiber and sheet into the account. Therefore, while for the even numbers of half integration points result with the overlap of fiber and sheet density distribution, the odd numbers of half integration points results with separation of density distributions for fiber and sheet directions by overestimating and underestimating behaviour in Figure 6.8. It is obvious that even for a low number of integration points over the unit planar circle (i.e. 9) it is sufficient to the get accurate results up to $b \leq 10$. By increasing the integration points up to 30, it provides sufficient accuracy even for $b = 100$ which is nearly distinct anisotropic case. It should be noted that for the orthogonal fiber families, it is important to use an even number of integration points to keep the symmetry of fiber directions.

6.5 Representative Numerical Examples

In this section, mechanical parameters of the proposed models are fitted numerically for cyclic triaxial shear and shear relaxation tests performed by [11] for human myocardium tissues. The agreement between the numerical analysis based on proposed models and the experiment has been examined for different shear modes. In order to validate the proposed models, FEAP was used as a finite element analysis program [178]. It was revealed from the experiments [101] that, human left LV myocardium presents a highly nonlinear, anisotropic, and viscoelastic response under large deformations. Biaxial test is not sufficient alone to fit a constitutive model parameters that may subject to different type of loadings. Therefore, it is essential to develop a constitutive model that also reflects the direction dependent material response to shear loadings. Accordingly, Sommer et al. [11] performed pioneering experiments to examine the shear mechanical properties of human myocardium tissue by slicing small cubic specimens from the middle wall of the left ventricle. Then, they identified the fiber, sheet, and normal directions of samples to be tested for triaxial simple tests and shear relaxations, as shown schematically in Figure 6.9. Triaxial shear loading scenario represents the six modes of simple shear loading for orthogonal shear planes

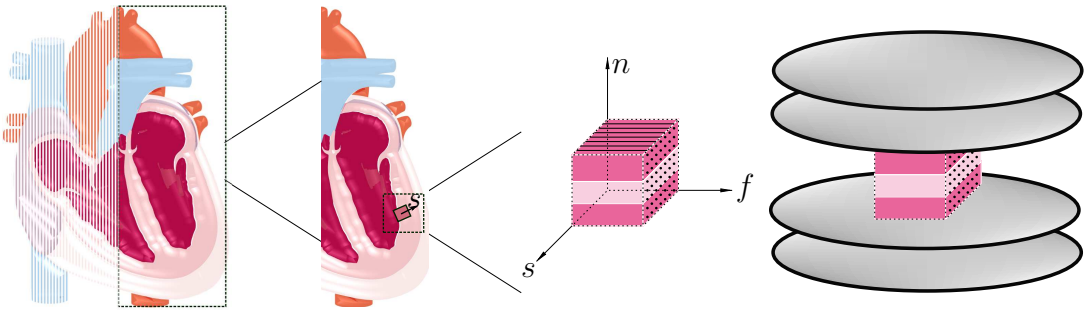

Figure 6.9: Schmetic demonstration of the experimental steps performed by Sommer et al. [11].(The sliced heart Figure was partly generated using Servier Medical Art, provided by Servier, licensed under a Creative Commons Attribution 3.0 unported license)

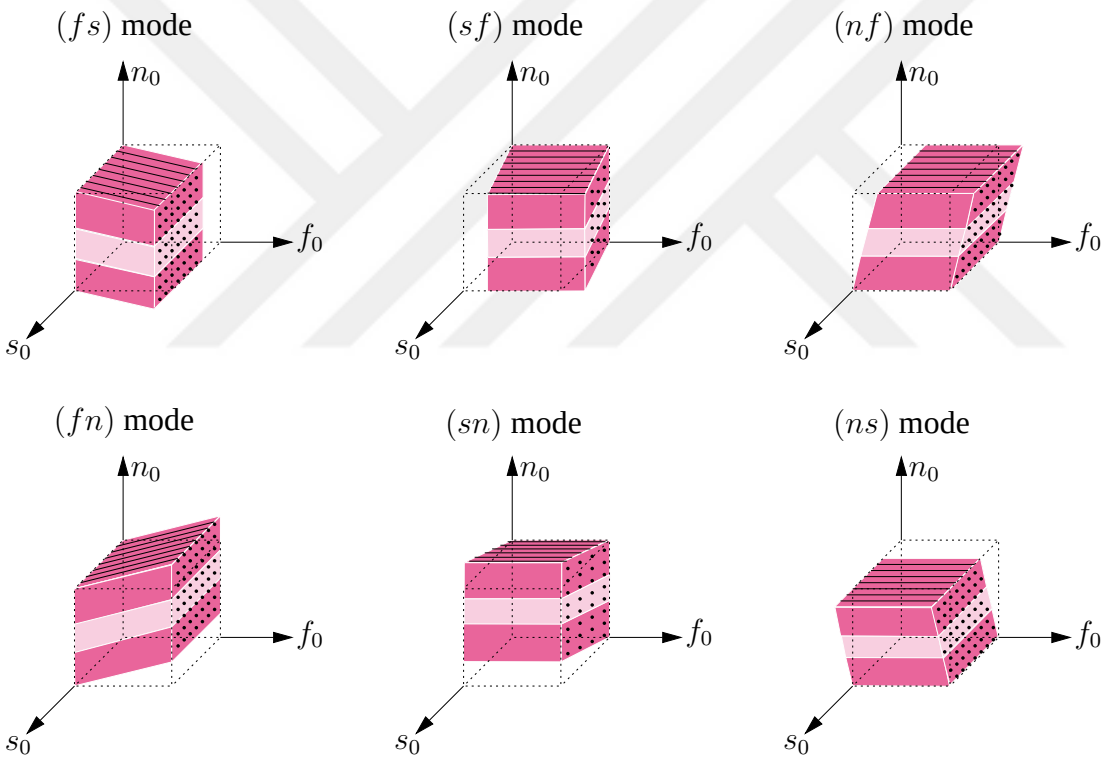

Figure 6.10: Schematic representation of six triaxial shear modes namely (fs), (sf), (nf), (fn), (sn), (ns), reproduced from [1]

those are (fs), (fn), (sf), (sn), (nf) and (ns). In the notation of shear modes, the first letter refers for the normal direction of the plane and the second letter represents the loading direction, see Figure 6.10. The corresponding deformation gradient $\boldsymbol{F}^{\alpha\beta}$

for the shear modes $\alpha\beta(\alpha, \beta = f, s, n)$ is defined as below

$$\boldsymbol{F}^{\alpha\beta} = 1 + \gamma \boldsymbol{e}_\beta \otimes \boldsymbol{e}_\alpha \tag{6.85}$$

where $\alpha \neq \beta$. Based on the period defined for the cyclic triaxial shear experiment in [1], a sinusoidal displacement have been defined in the numerical analysis in the following form

$$\gamma(t) = \gamma_{\max} \sin(2\pi t \,/\, \tau)\,, \quad \text{where} \quad \gamma_{\max} = 0.5 \quad \text{and} \quad \tau = 474\ s \tag{6.86}$$

Since elastic mechanical properties of the human myocardium tissue that is corresponding to quasi-static triaxial shear tests have already been obtained by [1] based on the baseline hyperelastic incompressible constitutive model, here we re-produce the elastic triaxial shear fits in the same manner and shown in Figure 6.11. The elastic

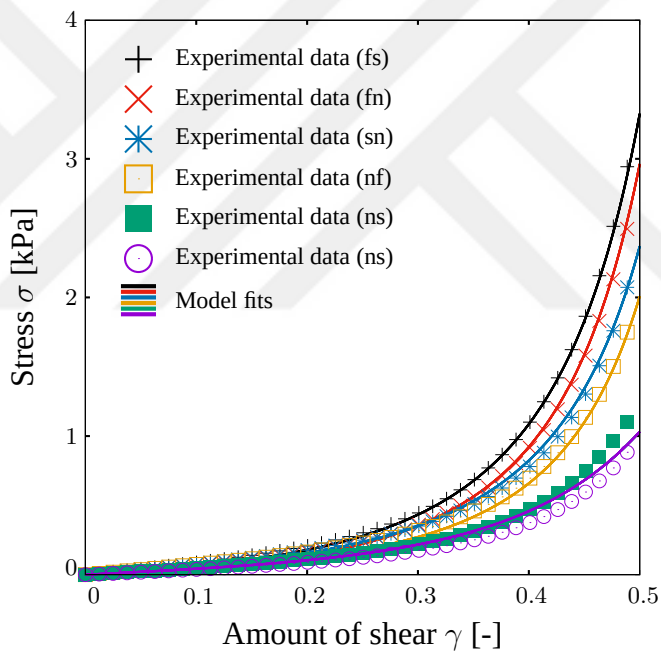

Figure 6.11: Elastic triaxial shear test and numerical fits for (fs), (sf), (nf), (fn), (sn), (ns).

parameters are given in Table 6.1 . Dispersion parameters for the fiber and for the sheet have also been identified experimentally by Sommer et al. [11] as $\kappa_f = 0.08$ and $\kappa_s = 0.09$. These parameters are corresponds for the $a_f = 3.48$ and $a_s = 3.15$ as a concentration parameters for the two orthogonal directions stated in the equation 5.11. The polar plot of the density distribution (DD) for $\boldsymbol{f}$ and $\boldsymbol{s}$ directions for the

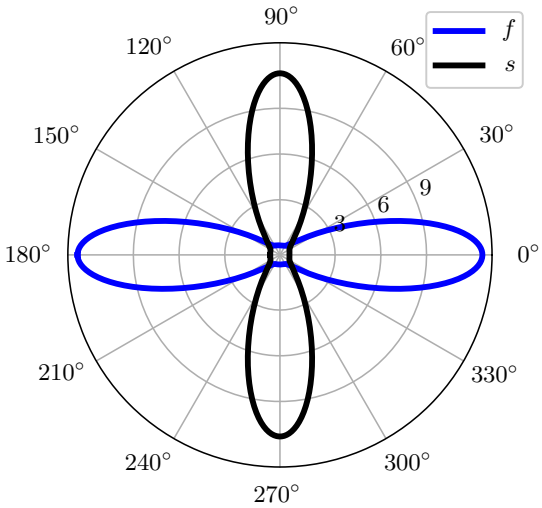

Figure 6.12: The polar plot of the two families of fibers (f and s) distribution based on density distribution (DD) for the myocardium tissue.

Table 6.1: Elastic material parameters for the baseline hyperelastic constitutive model [1] where a, a_{f}, a_{s}, a_{fs} are in [kPa], and b, b_{f}, b_{s}, b_{fs} are dimensionless.

a	b	a_{f}	b_{f}	a_{s}	b_{s}	a_{fs}	b_{fs}
0.4	6.55	3.05	29.05	1.25	36.65	0.15	6.28

human myocardium is given by Figure 6.12. Once completion of cyclic triaxial shear experiments, relaxation triaxial shear tests have been also performed by Sommer et al. [11]. They performed shear relaxation tests at 0.5 amount of shear for six shear modes in order to tract the direction dependent viscoelastic relaxation response of the tissue. Therefore an instant shear step applied to 0.5 amount of shear and it was maintained for 300 seconds. While fitting the viscous material mechanical properties, Latin Hypercube Sampling Design has been used as a design of experiment method. Randomly, 1000 design points were generated in a parameter range, and optimum data sets have been obtained. The viscoelastic material parameters are obtained by considering both triaxial cyclic and relaxation shear loadings. In the following part, the fitting performance of the proposed models in sub-section 6.4 will be presented one by one.

6.5.1 Numerical results of model-I

In this sub-section, triaxial cyclic shear and relaxation shear results of Model-I, which is introduced in sub-section 6.4.1.1, will be presented. The parameter set which provide the best fit for the both cyclic and relaxation shear tests are given in Table 6.2.

Table 6.2: Viscous material parameters for the Model-I where μ_f, μ_s are directional shear moduli in [kPa], and η_f, η_s are directional viscosities in [kPa s], $\hat{\beta}$ is the activation parameter, m_f, m_s, a and b are dimensionless.

μ_f	μ_s	η_f	η_s	β	m_f	m_s	a	b
100	90	400000	300000	1.0	2.0	2.0	5.0	5.0

Then, corresponding polar plots of the density distribution functions for the viscous response of sheet s and the fiber f directions at in-plane and for the normal n direction at out-of-plane are given in Figure 6.13.

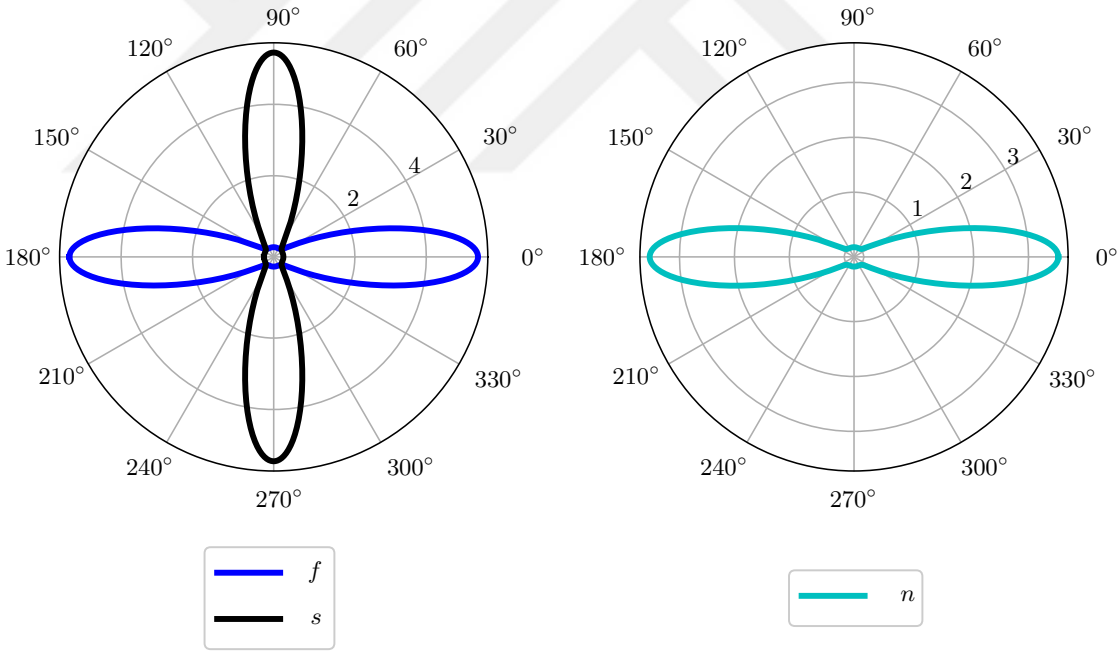

Figure 6.13: Model I - The polar plots of the two families of fiber (f) and sheet(s) directions along in-plane distribution and out-of-plane distribution through normal direction (n) for the viscous response of the myocardium.

Figure 6.14 presents the numerical results of Cauchy stress versus the cyclic amount

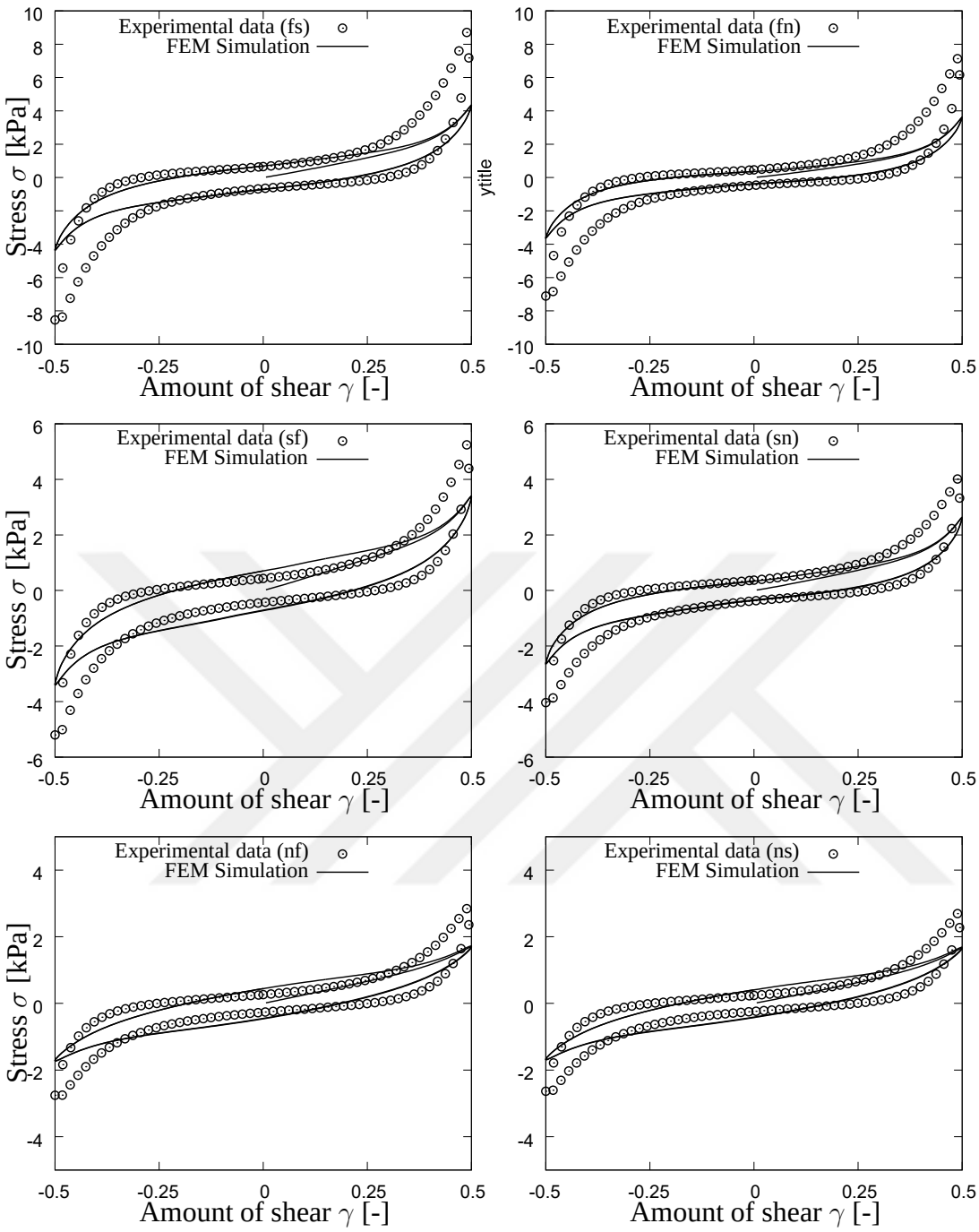

Figure 6.14: Cauchy stress σ vs amount of shear γ of Model-I response with respect to the cyclic triaxial shear test data for six of the shear modes namely (fs), (fn), (sf), (sn), (nf) and (ns).

of shear under triaxial cyclic shear loading. It is seen that, although none of the triaxial cyclic shear responses are able to catch the peak corners, Model-I averagely captures the low-level strain responses. There are deviations for all of the shear direc-

tions. Due to the decreasing effect of the local-based density distribution on nonlinear evolution law, the continiuous integral averaging cannot satisfy the normalization of the numerical integral over the micro-sphere.

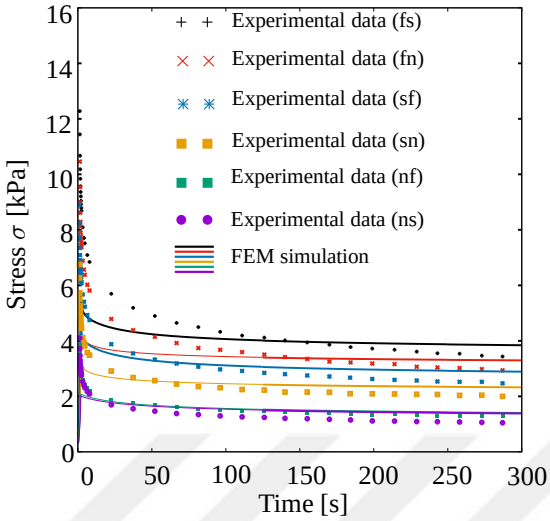

Figure 6.15: Cauchy stress σ vs relaxation time of Model-I response with respect to the triaxial relaxation shear test data for six of the shear modes namely (fs), (fn), (sf), (sn), (nf) and (ns).

Figure 6.15 presents the relaxation response of Model-I under a 300-second relaxation condition. In the experimental data, it is seen that after the instant loading of the tissue, there is a rapid decrease around the initial moments ≈0-5 seconds for all the shear modes. Then, continuation of the relaxation leads to steady-state values of stress. In the numerical Model-I, the instant decrease at the initial moments is obtained for all of the shear modes. All of the responses had nearly converged to the experimental values at the end of the test duration and were about to reach the steady-state response. Due to the local-based density distribution over the corresponding shear moduli in each direction, it causes underestimation and non-accurate observations.

The main problem in Model-I confronts itself in the integral averaging stage through stress and moduli calculations. Since, we use local-based von Mises dispersion in the formulation, density distribution $\rho(\boldsymbol{r})$ reveals in free-energy definition, see equation 6.62. Therefore, it has to be part of the stress and overstress definitions. Then, it enters the non-linear evolution equation and is used as a multiplier in the local tangent term

as defined in equation 6.63. In the local tangent term, the density distribution is not only used as a multiplier of shear moduli μ but it also ingredient of the overstress. Due to the nonlinear exponent m, the density distribution directly decrease the activation of the stress and affects the result of the evolution equation. It causes a violation of the numerical integral averaging during the stress and moduli calculations. Therefore, it is concluded that the nonlinear evolution equation is not suitable for local-based formulations.

6.5.2 Numerical results of model-II

In order to decouple the dispersion characteristics of the normal direction and fiber-sheet plane, we used a novel planar dispersion integration for the fiber-sheet plane and isotropic contribution of normal direction get involved through integral averaging over the unit-micro sphere. Since we have reported the problem of Model-I as a numerical issue that cause violation of the normalization of the density distribution $\rho(\boldsymbol{r})$ in non-linear evolution equations, in Model-II we preferred to use linear-evolution law. The best fit parameter sets for both the cyclic and relaxation shear tests are given in Table 6.3.

Table 6.3: Viscous material parameters for the Model-II where μ_f, μ_s and μ_n are directional shear moduli in [kPa], and η_f, η_s and η_n are directional viscosities in [kPa s], b is the dimensionless concentration parameter.

μ_f	μ_s	μ_n	η_f	η_s	η_n	b
90	50	40	100000	50000	3500	20.0

Accordingly, the polar plot of the density distribution (DD) function for $\boldsymbol{f}$ and $\boldsymbol{s}$ directions in human myocardium is given in Figure 6.16 for the viscous response. For the non-equilibrium response, it is shown that the fiber and sheet responses are more anisotropic. The corresponding concentration parameter for the fiber and the sheet is $b = 20$. Figure 6.17 presents the numerical results of Cauchy stress versus the cyclic amount of shear under triaxial cyclic shear loading. As revealed by the experimental studies, hysteresis increases as $f > s > n$. For (fs) and (fn), it is

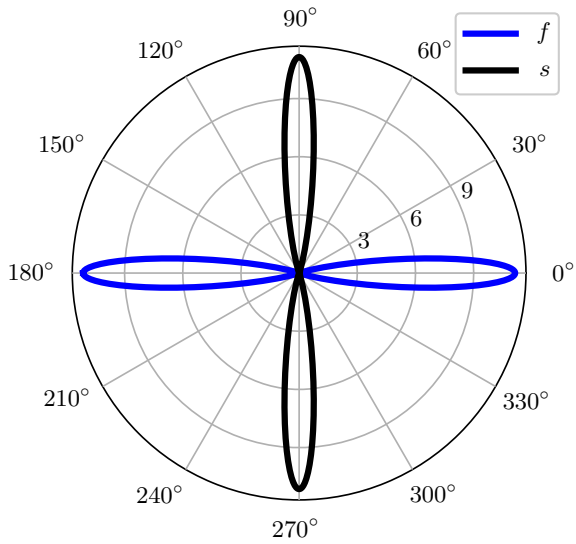

Figure 6.16: The polar plot of the two families of fibers (f and s) ased on density distributions (DD) for the viscous response of Model II.

possible to catch the upper and lower peak values by increasing the fiber and sheet shear modulus (μ) however there is a trade-off between the response of the tissue between cyclic shear and shear relaxation. Therefore, these parameters are kept as an optimum parameter set. Both (sf) and (sn) are very closely to be identical with the experimental results and reflect an accurate response. (nf) and (ns) capture the average response of the tissue except for the nonlinear behaviour at the corner peaks. Due to use of a relatively small shear modulus (μ_n) in the normal direction and low viscosity in the normal direction (η_n), corner peaks could not captured totally. Additionally, if relatively higher dispersion had been used for the viscous response of the model such as $b < 10$, then (fs) and (sf) coupling effects increases which causes rotation of the curves of coupling modes with respect to the origin and result of a larger slope of response and deviates from the experimental results.

Figure 6.18 presents the relaxation response of the proposed model under 300 seconds relaxation condition. In the Model-II, the instant decrease is captured in average manner. All of the responses nearly converges to the experimental values at the end of the test duration and about to reach the steady-state response. It is possible to obtain more consistent relaxation response by decreasing the viscosity of the isotropic behaviour based on n direction (η_n), however it will cause the decrease of peak responses of the cyclic triaxial results.

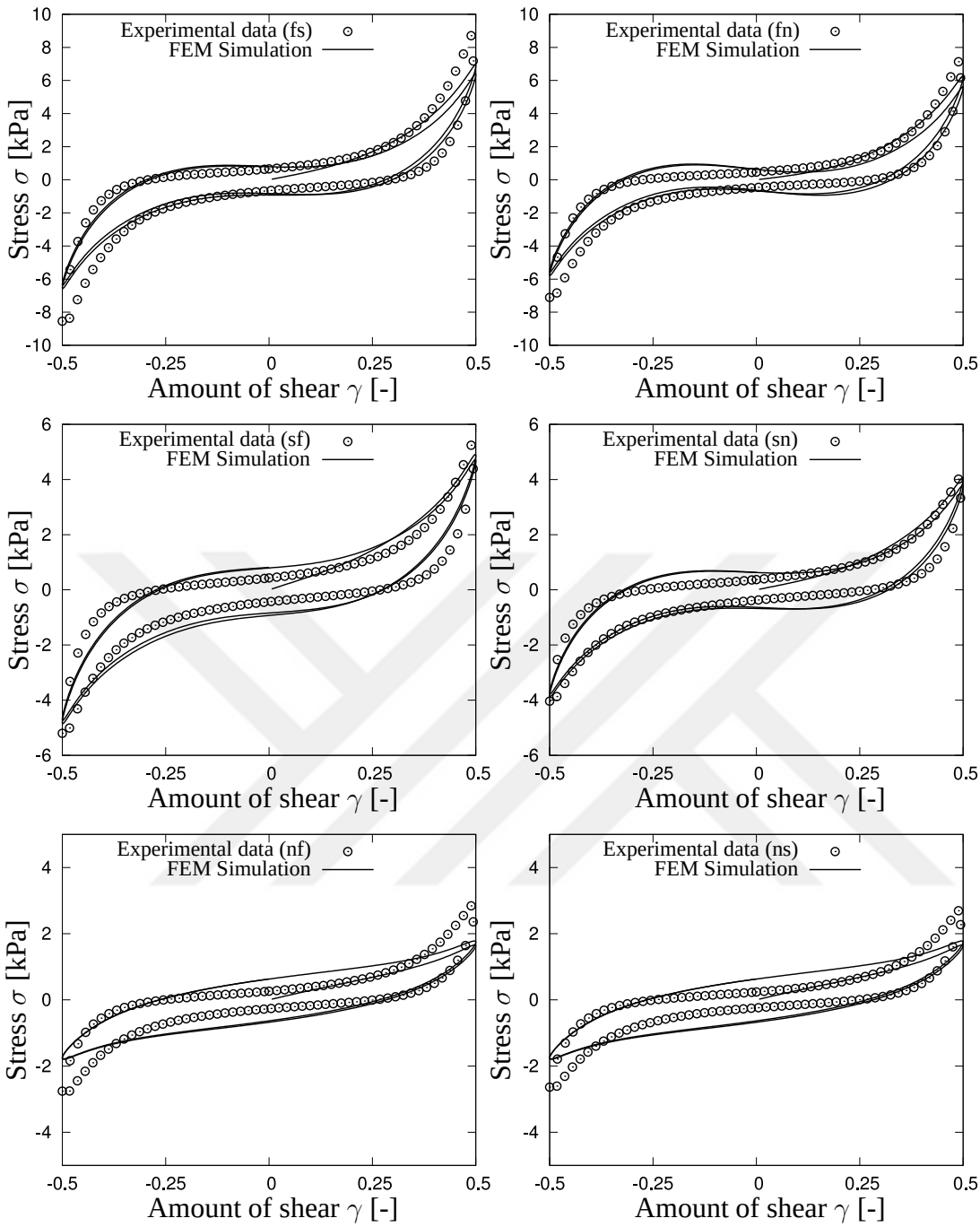

Figure 6.17: Cauchy stress σ vs amount of shear γ of Model-II response with respect to the cyclic triaxial shear test data for six of the shear modes namely (fs), (fn), (sf), (sn), (nf) and (ns).

Model II exhibit good agreement with anisotropic nature of the myocardium tissue in all shear directions. It is not only take into the account for dispersion characteristics of viscoelasticity but also it presents an accurate numerical integration over unit circle.

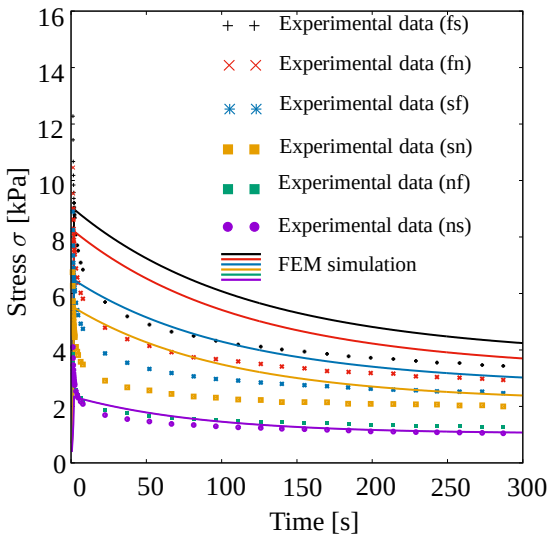

Figure 6.18: Cauchy stress σ vs relaxation time of Model-II response with respect to the triaxial relaxation shear test data for six of the shear modes namely (fs), (fn), (sf), (sn), (nf) and (ns).

6.5.3 Numerical results of model-III

The Model-III is formulated based on a global-based bivariate von Mises distribution and is presented in sub-section 6.4.2.1. The model reflects the three-dimensional dispersion characteristics through multiplication of two uncoupled density distributions namely in-plane ρ_{ip} and out-of-plane ρ_{op}. Therefore, there are not any mechanical viscous properties defined for the normal direction because it is already taken into account by the bivariate formulation automatically. The main difference of Model-III from Model-I is comes up with the constitutive modelling approach through the density distribution. Model-III uses global-based approach and use density distribution during the integral averaging of stress and moduli calculations which satisfy the normality of the numerical integral. The parameter set which gives the best fit for the both cyclic and relaxation shear tests at the same time are given in Table 6.4.

Then, corresponding polar plots of the density distribution functions for the viscous response of sheet s and fiber f directions at in-plane and for the normal n direction at out-of-plane are given in Figure 6.19. Figure 6.20 presents the numerical results of Cauchy stress versus the cyclic amount of shear under triaxial cyclic shear loading. (fs), (fn), (sf) and (sn) shear modes exhibit good agreement with experimental results.

Table 6.4: Viscous material parameters for the Model-III where μ_f, μ_s are directional shear moduli in [kPa], and η_f, η_s are directional viscosities in [kPa s], $\hat{\beta}$ is the activation parameter, m_f, m_s, a and b are dimensionless.

μ_f	μ_s	η_f	η_s	β	m_f	m_s	a	b
90	80	400000	300000	1.0	2.0	2.0	5	3.5

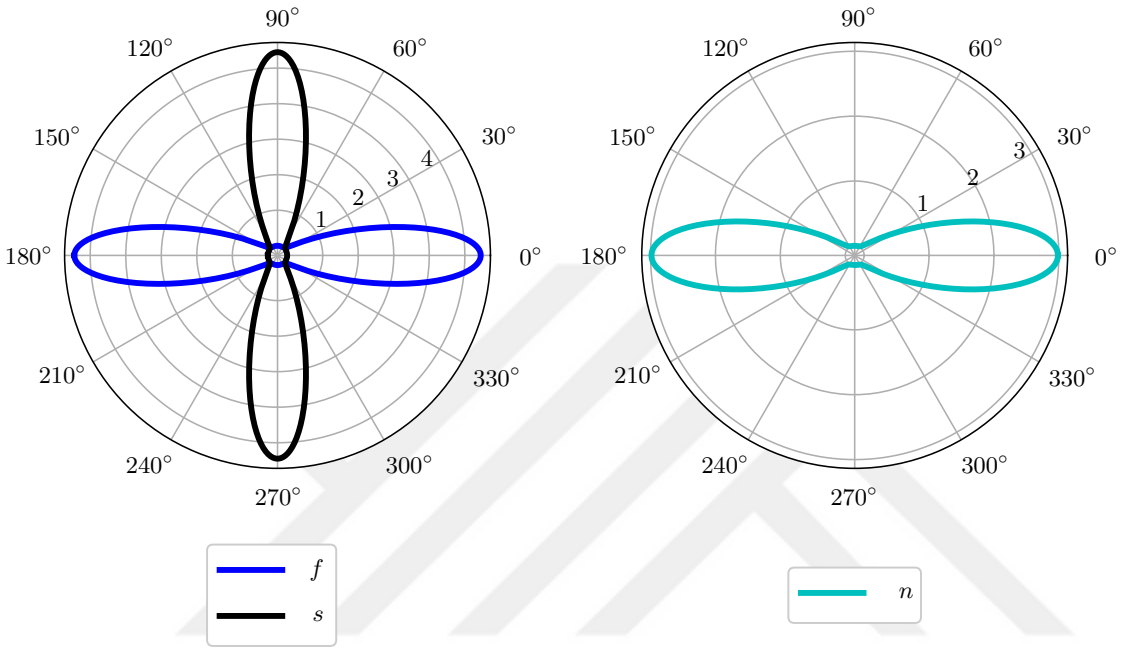

Figure 6.19: Model III - The polar plots of the two families of fiber (f) and sheet(s) directions along in-plane distribution and out-of-plane distribution through normal direction (n) for the viscous response of the myocardium.

The curved-shape behaviour can be avoided by decreasing shear moduli along orthogonal directions, but it also causes a decrease in peak stresses at corner edges. Another parameter is viscosity η that has major effect on overstress peak results. On the other hand, it causes a delay in the relaxation test, which is a trade-off for the choice of the best parameter set. (nf) and (ns) are not able to catch peak responses, but they exhibit average manner behaviour. In bivariate formulation, the viscous response of the normal direction has been imposed by the contribution of fiber and sheet direction through density distribution function ρ. In order to narrow the hysteresis regarding to the normal related shear modes, the out-of-plane concentration parameter b should be increased. However, there is a coupling effect due to the dispersion formulation,

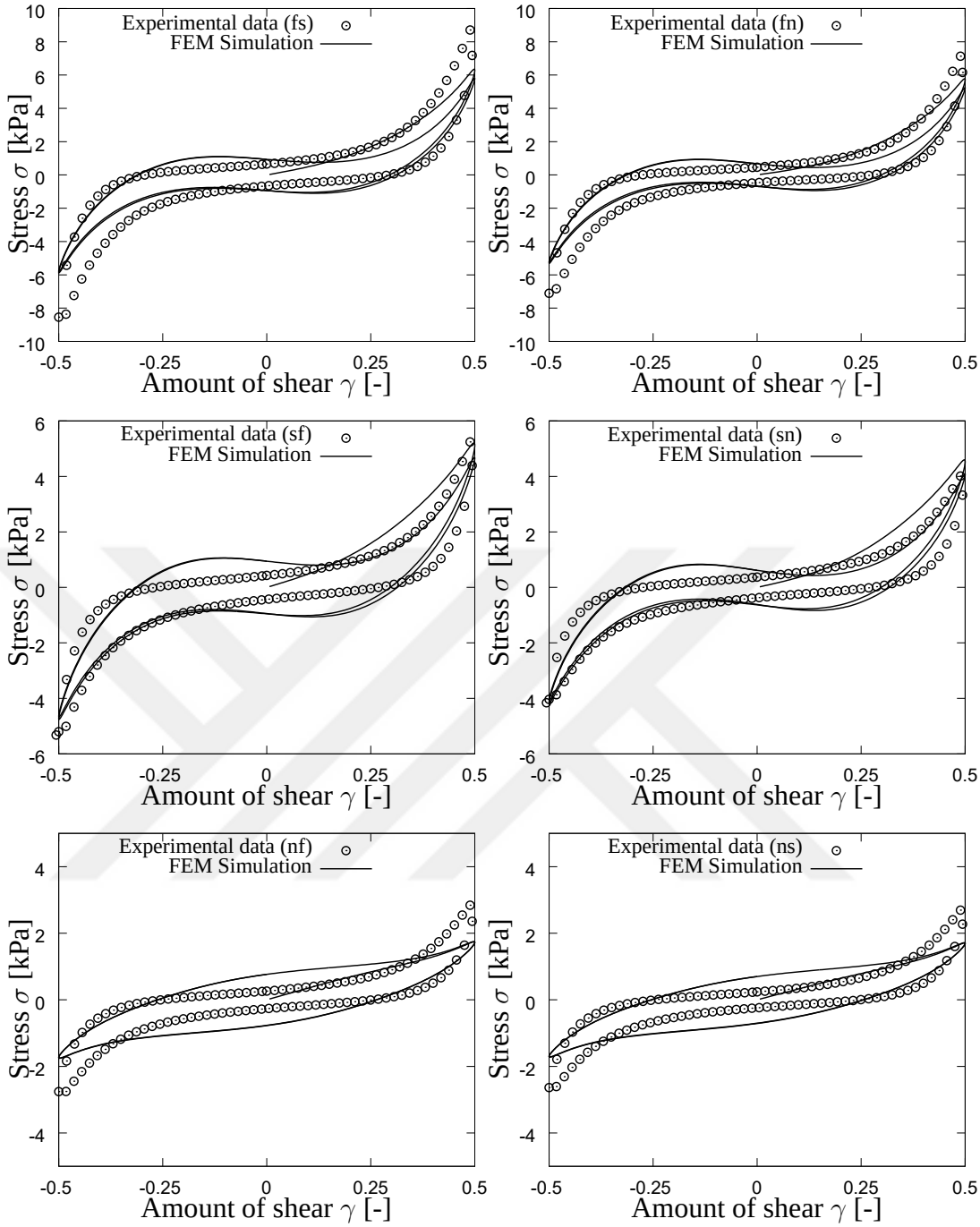

Figure 6.20: Cauchy stress σ vs amount of shear γ of Model-III response with respect to the cyclic triaxial shear test data for six of the shear modes namely (fs), (fn), (sf), (sn), (nf) and (ns).

and the decreasing contribution of the normal direction also narrows the hysteresis of the fiber and sheet directions. Therefore, the parameter set is selected to represent the optimal manner for each response.

Figure 6.21 presents the relaxation response of the Model-III under a 300-second relaxation state. The rapid decrease in Model-III much smoother than Model-I and II and more closely to experimental result. It is mostly related with the shear modulus of the fiber and sheet directions. All of the responses had nearly converged to the experimental values at the end of the test duration and were about to reach the steady-state response. The global-based bivariate model mostly exhibits anisotropy

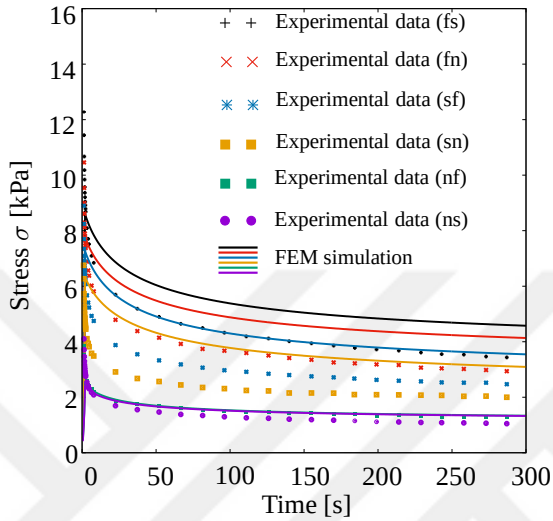

Figure 6.21: Cauchy stress σ vs relaxation time of Model-III response with respect to the triaxial relaxation shear test data for six of the shear modes namely (fs), (fn), (sf), (sn), (nf) and (ns).

in the preferred fiber and sheet directions and a minor effect of isotropic contribution of the normal direction. The model is close to the transversely isotropic nature of a tissue. Therefore, the trixial cyclic shear response that is related to the normal direction covers the experiment in an average sense.

6.5.4 Numerical results of model-IV

Due to the normalization restrictions of global-based models during the continuous integral averaging of stress and moduli, in Model-II, there has been used linear evolution law. Since, the global-based formulations directly meet the normalization condition of the numerical integral, we use a nonlinear evolution law in Model-IV. It has the same constitutive relations as the Model-II and the only change is the nonlinear-

ity of the evolution. In a similar manner, we use circular integral for the dispersion characteristics of fiber and sheet directions, and the isotropic contribution of the normal direction is maintained by using numerical integral over the unit micro-sphere. Accordingly, the optimum parameter set for the both cyclic and relaxation shear tests are given in Table 6.5. Accordingly, the polar plot of the density distribution (DD)

Table 6.5: Viscous material parameters for the Model-IV where μ_f, μ_s and μ_n are directional shear moduli in [kPa], η_f, η_s and η_n are directional viscosities in [kPa s], $\hat{\beta}$ is the activation parameter, m_f, m_s, m_n are exponents and b is the dimensionless concentration parameter.

μ_f	μ_s	μ_n	η_f	η_s	η_n	$\hat{\beta}$	m_f	m_s	m_n	b
90.7	77.0	32.3	1237500	278300	27235	1.0	2.0	2.0	2.0	20

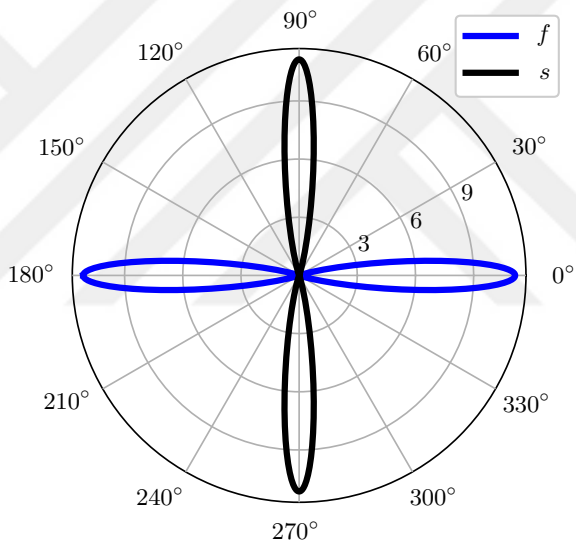

Figure 6.22: The polar plot of the two families of fibers (f and s) ased on density distributions (DD) for the viscous response of Model IV.

function for $\boldsymbol{f}$ and $\boldsymbol{s}$ directions in human myocardium is given in Figure 6.22 for the viscous response. For the non-equilibrium response, by taking advantage of the numerical accuracy advantage of the circular integration, it is possible to use a higher value of the concentration factor, which also makes the distribution more anisotropic in the fiber and sheet directions. The corresponding concentration parameter for the fiber and the sheet is $b = 20$. Figure 6.23 presents the numerical results of Cauchy stress versus the cyclic amount of shear under triaxial cyclic shear loading. Cyclic

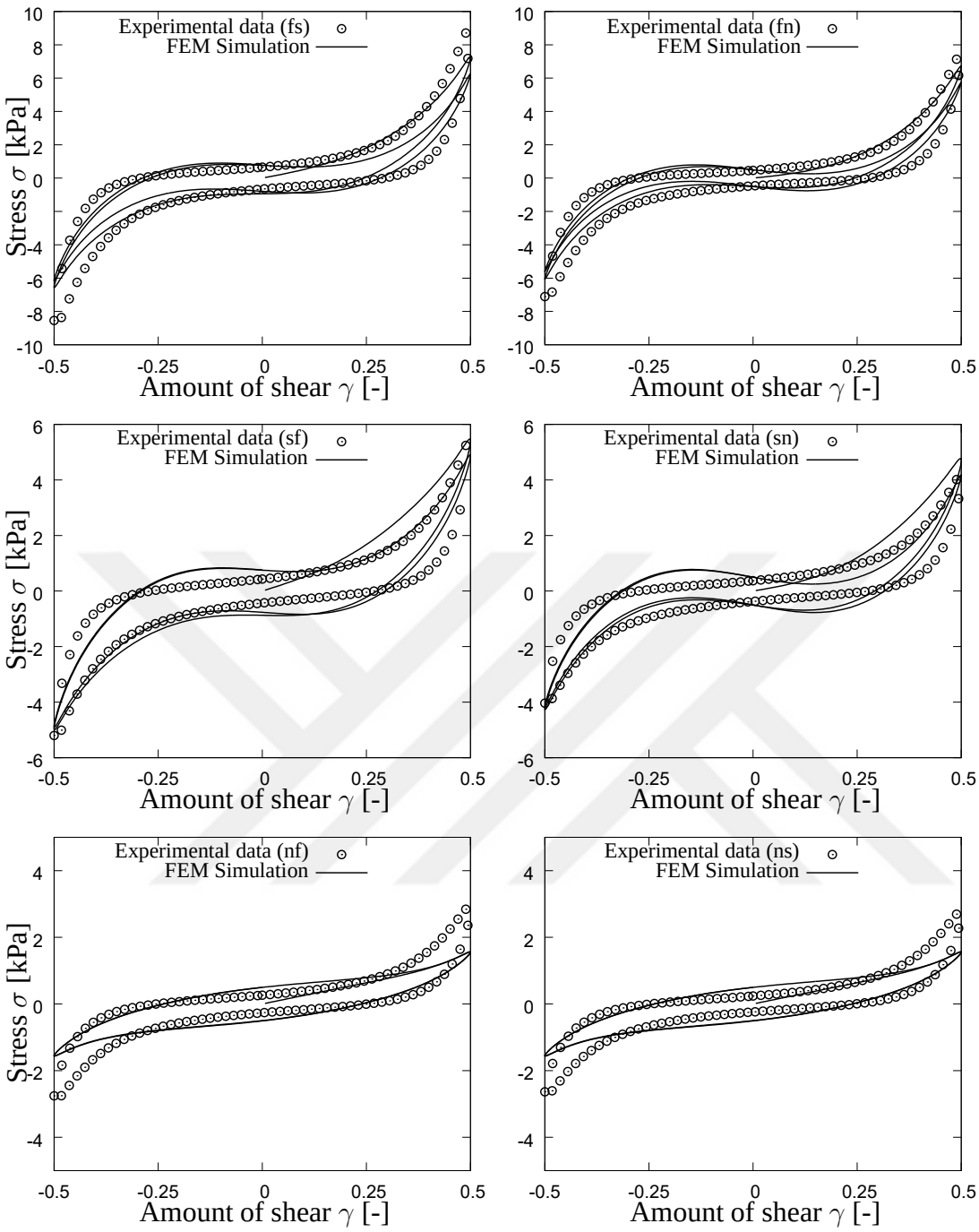

Figure 6.23: Cauchy stress σ vs amount of shear γ of Model-IV response with respect to the cyclic triaxial shear test data for six of the shear modes namely (fs), (fn), (sf), (sn), (nf) and (ns).

responses of shear modes (fs), (fn), (sf) and (sn) exhibit perfect agreement with the experimental data. (nf) and (ns) capture the average response of the tissue except for the nonlinear behaviour at the corner peaks. It is mainly because of the isotropic type

of contribution in the normal direction.

Figure 6.24 presents the relaxation response of the proposed model under 300 seconds relaxation condition. There is an offset between the experimental data and the finite element analysis results, especially for (fs) and (fn) due to the high shear moduli and viscosity along the fiber direction. (nf) and (ns) results track the experimental data, and they converge to a steady-state response at the end of the analysis. The rest of the shear modes are still in a decreasing trend, and they are about to reach steady-state response as well.

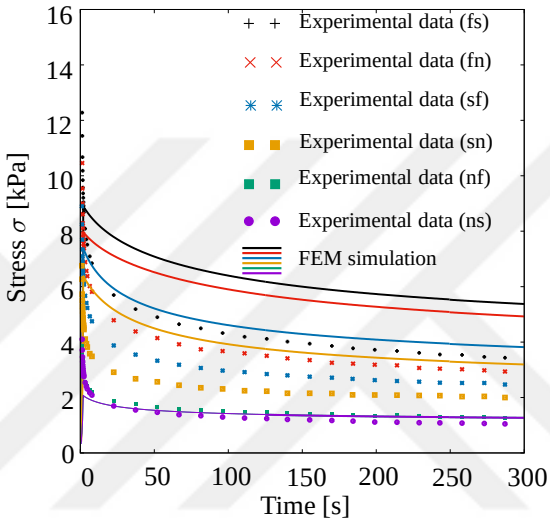

Figure 6.24: Cauchy stress σ vs relaxation time of Model-IV response with respect to the triaxial relaxation shear test data for six of the shear modes namely (fs), (fn), (sf), (sn), (nf) and (ns).

Model IV exhibits good agreement with the anisotropic nature of the myocardium tissue in all shear directions for the cyclic triaxial shear tests. The planar circular integration allows us to define highly anisotropic dispersion modeling due to its high accuracy, and it provides flexibility for fitting the numerical model.

6.5.5 Numerical results of model-V

The Model-V is formulated based on π-periodic rotationally symmetric planar von Mises distribution in fiber and sheet directions. In the first numerical solution, the

viscous response in the normal direction is assumed to be caused by the isotropic surrounding tissue and enters the formulation by integral averaging over unit microsphere with a concentration factor $b = 0$. At the second numerical solution, there is assumed to be an additional dispersion along the normal direction, and a planar von Mises distribution is also defined through the normal orientation. Although these formulations are decoupled to each other, there are also minor contribution of planar distribution over distinct orthogonal direction f, s and n. The optimum viscous parameter set for both the cyclic and relaxation shear tests are given in Table 6.6. The

Table 6.6: Viscous material parameters for the Model-V$_1$ where μ_f, μ_s, μ_n are directional shear moduli in [kPa], and η_f, η_s, η_n are directional viscosities in [kPa s], $\hat{\beta}$ is the activation parameter, m_f, m_s, a and b are dimensionless.

μ_f	μ_s	μ_n	η_f	η_s	η_n	β	m_f	m_s	m_n	$b_{f,s}$
100	70	10	400000	300000	100000	1.0	2.0	2.0	2.0	5.0

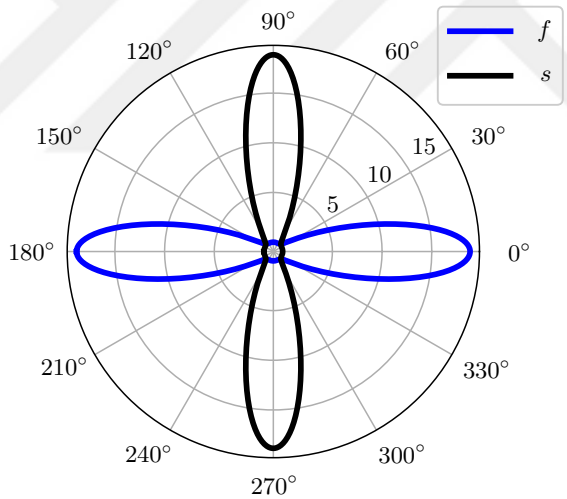

Figure 6.25: Model V$_1$ - The polar plot of the two families of fiber (f) and sheet(s) directions for a planar density distribution

polar plot that reflects the density distribution characteristics along fiber f and sheet s directions are given in Figure 6.25. Since the viscous behaviour is assumed to be isotropic with a zero concentration parameter, its polar plot would be an exact circle in the polar plot. The numerical results of Cauchy stress versus the cyclic amount of shear under triaxial cyclic shear loading are shown in Figure 6.26. The model

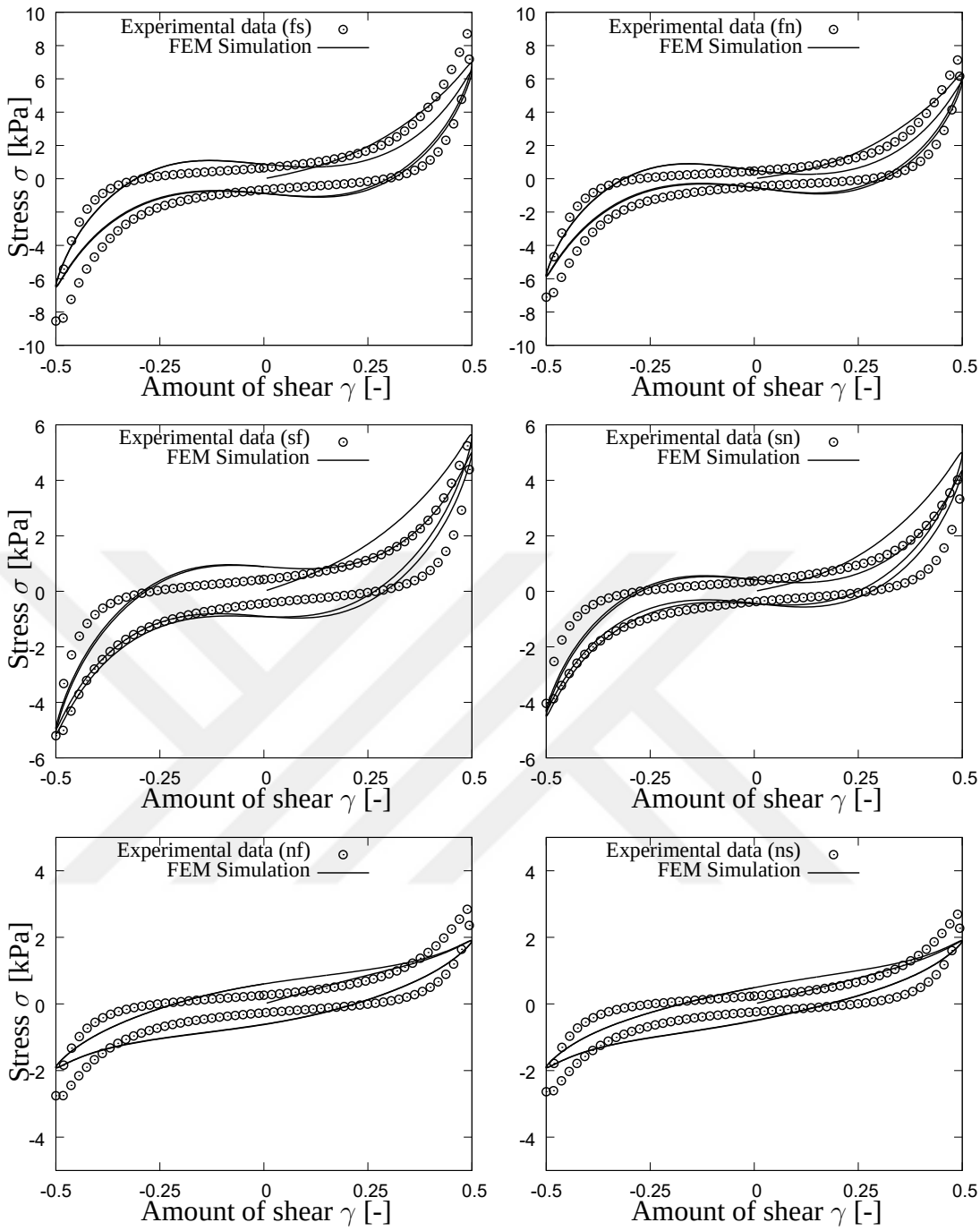

Figure 6.26: Cauchy stress σ vs amount of shear γ of Model-V_1 response with respect to the cyclic triaxial shear test data for six of the shear modes namely (fs), (fn), (sf), (sn), (nf) and (ns).

presents good agreement with the experimental test data, especially for (fs), (fn), (sf) and (sn) and it is even able to catch the highly nonlinear behaviour at peak corners. By definition of the planar von Mises distribution, dispersion effects for all orthogo-

nal directions have a minor effect to each other. Therefore, by changing one of the parameters in the viscous parameter set, directly change all of the graphs shown in Figure 6.26. (ns) and (nf) exhibit average manner agreement with the experimental data at mid-levels of shear strains. Peak responses are not well-reflected due to the isotropic formulation of normal orientation.

Figure 6.27 presents the relaxation response of Model-V_1 under 300 seconds for six of the shear modes. Shear relaxations exhibit a perfect decreasing slope with an offset. After the instant loading, the rapid relaxation drop is less than what is expected from the experimental data. All of the numerical curves are still in a decreasing trend toward a steady-state amount of stress.

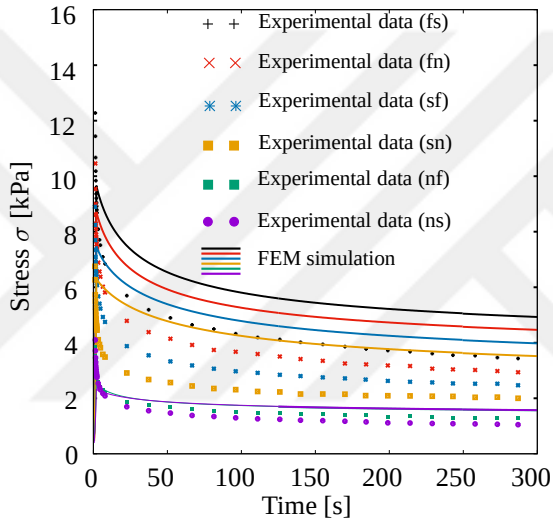

Figure 6.27: Cauchy stress σ vs relaxation time of Model-V_1 response with respect to the triaxial relaxation shear test data for six of the shear modes namely (fs), (fn), (sf), (sn), (nf) and (ns).

In the previous numerical results for the different formulations, there is provided a good agreement with cyclic triaxial experiments, especially for (fs), (fn), (sf) and (sn) and average agreement with (ns) and (nf) in the mid-range strains. It is observed that a purely isotropic formulation ($b = 0$) though the normal direction is not able to reflect the nonlinear behaviour in the cyclic triaxial tests. In order to handle this issue, we change the isotropic contribution of the normal direction to planar von Mises distribution which will exhibit the orthotropic behaviour of the myocardium. The optimum viscous parameter set for the both cyclic and relaxation shear tests are given

in Table 6.7. The corresponding polar plots of the density distribution functions for

Table 6.7: Viscous material parameters for the Model-V_2 where μ_f, μ_s, μ_n are directional shear moduli in [kPa], and η_f, η_s, η_n are directional viscosities in [kPa s], $\hat{\beta}$ is the activation parameter, m_f, m_s, a and b are dimensionless.

μ_f	μ_s	μ_n	η_f	η_s	η_n	β	m_f	m_s	m_n	$b_{f,s,n}$
100	60	30	400000	300000	100000	1.0	2.0	2.0	2.0	5.0

the viscous response of sheet s and fiber f directions at in-plane and for the normal n direction at out-of-plane are given in Figure 6.28. Figure 6.29 presents the numerical

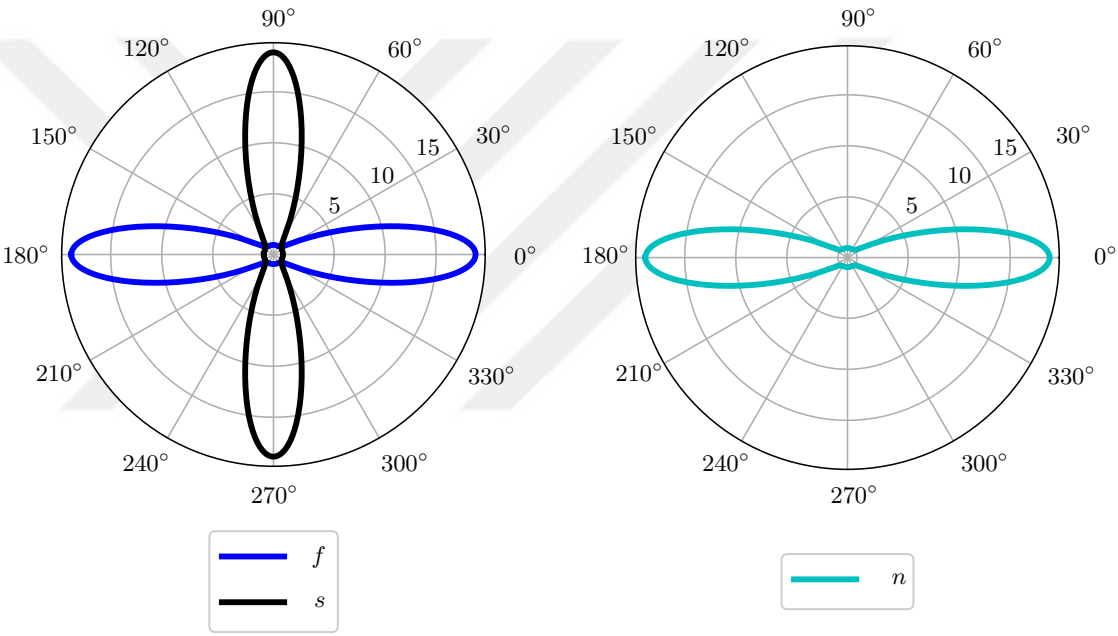

Figure 6.28: Model V_2 - The polar plots of the two families of fiber (f) and sheet(s) directions along in-plane distribution and out-of-plane distribution through normal direction (n) for the viscous response of the myocardium.

results of Cauchy stress versus the cyclic amount of shear under triaxial cyclic shear loading. By adding the anisotropic dispersion through the normal direction, the fully orthotropic viscous response is maintained. All of the shear modes exhibits perfect agreement with the experimental data. Figure 6.30 presents the relaxation response of the Model-V_2. There is still appears a little offset through upward direction however the relaxation slopes of the numerical results are well-captured. All of the stresses are

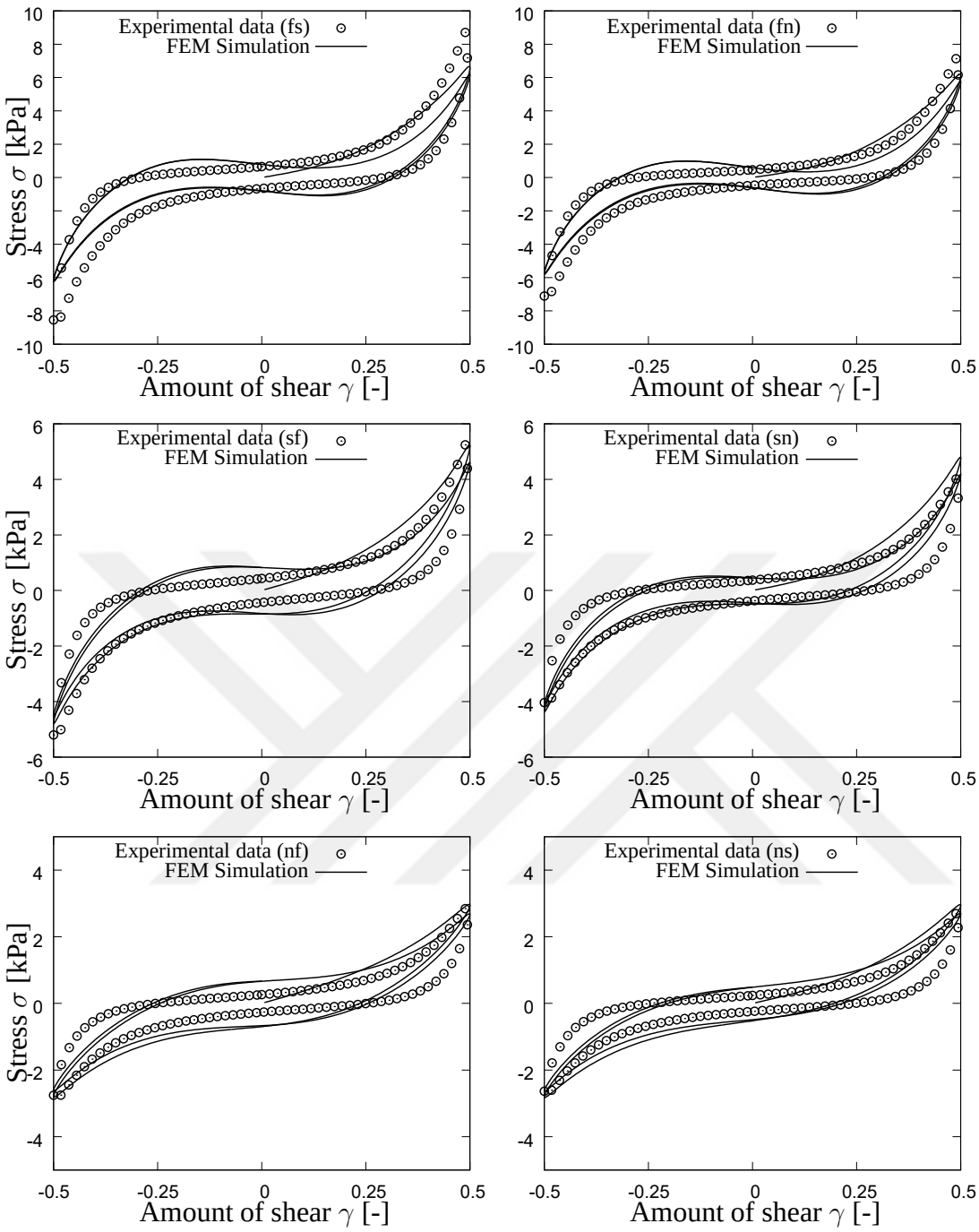

Figure 6.29: Cauchy stress σ vs amount of shear γ of Model-V_2 response with respect to the cyclic triaxial shear test data for six of the shear modes namely (fs), (fn), (sf), (sn), (nf) and (ns).

about to converge to the steady-state state and the model perform a good agreement also under the relaxation response.

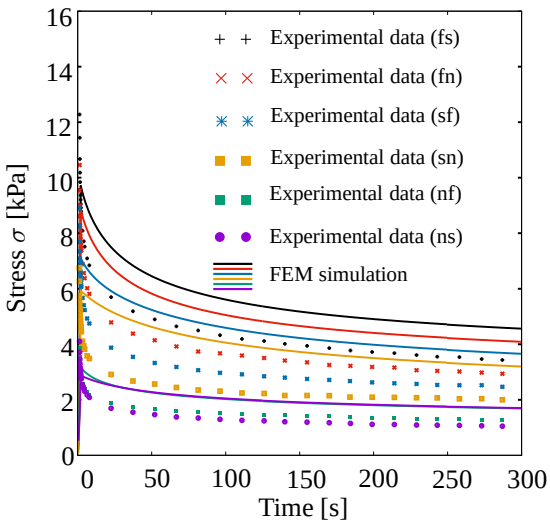

Figure 6.30: Cauchy stress σ vs relaxation time of Model-V_2 response with respect to the triaxial relaxation shear test data for six of the shear modes namely (fs), (fn), (sf), (sn), (nf) and (ns).

CHAPTER 7

CONCLUSIONS

This thesis covers two main parts under biomechanics, namely, growth-induced instabilities for soft biological tissue and dispersion-type anisotropic viscoelasticity for the human myocardium. To begin, we formulated a five-field Hu-Washizu type mixed variational formulation in FEniCS via the $T2P0F0$ element to investigate primary and secondary instabilities on bilayer-typed three-dimensional confined tissue. To the best of our knowledge, this is the first observation of three-dimensional space in the literature. Since the instability patterns lead to different wavelengths based on the fiber stiffness, we suggested using two-dimensional models to determine the exact wavelengths in three-dimensional analysis. We showed that wavelength decreases by increasing the fiber stiffness. While higher fiber stiffness on the film layer causes the first instability in the direction of fibers with a lower growth parameter, g, the effect of fiber stiffness on the secondary buckling mode is at a minor level, where it is observed perpendicular to the fiber direction. Another outcome is that the energy release mechanism at the initiation of buckling is mainly composed of isotropic and anisotropic contributions from the stiff film layer. For a higher fiber stiffness, the effect of the anisotropic energy on the first buckling becomes more dominant than other types of energy components. However, in the secondary instability, isotropic energy of the film layer plays a key role for the energy release mechanism. This study will aid in understanding the role of fiber stiffness in the buckling and post-buckling behavior of anisotropic multi-layer tissues in incompressibility and inextensibility limits.

In the second part of the study in this thesis, we have proposed five novel global-based and local-based von Mises dispersion based angular-integration type anisotropic viscoelasticity formulations that are able to reflect the distinct viscous response of the

tissue based on its fiber distribution architecture. We start with the decomposition of the free-energy function into equilibrium and non-equilibrium contributions. The baseline hyperelasticity is defined by the generalized structure tensor model. The non-equilibrium response is described by the rheological Maxwell branch with an integrated elastic spring element. It utilizes a quadratic free-energy function in logarithmic space and a power-type evolution equation in each orientation direction. The overstress response is obtained through distinct orientation directions by numerical evaluation of averaging integrals over either the unit micro-sphere or the unit planar circle. The validation of proposed constitutive models has been carried out for the human myocardium tissue, which is inhomogeneous, incompressible, anisotropic, and viscoelastic. The parameters of the proposed models were obtained from cyclic triaxial shear and triaxial shear relaxation experiments of human passive myocardium conducted by Sommer et al. [101]. Then, we demonstrate the fitting capability of the proposed dispersion-type anisotropic viscoelasticity formulations on triaxial cyclic shear and shear relaxation response of the human heart by performing numerical simulations in the finite element analysis program FEAP.

For the five proposed models, we have used different types of density distributions and integration schemes. For anisotropic dispersion densities, we used bivariate von Mises and planar von Mises density distributions with continuous average integrals over the unit-sphere and unit planar circle for different integration schemes. Since all of the proposed formulations are based on the angular integration method, the sensitivity of the numerical integration becomes paramount. The analytical integral of the density distributions is generally formalized to maintain the normalization condition. When the concentration parameter a or b is increased, the anisotropy of the distribution increases as well, and numerical integration produces a deviation based on the number of integration points used. Therefore, for more anisotropic dispersion characteristics, the integral averaging over the unit micro-sphere will require a high number of integration points, which is not feasible in terms of the computational time of the analysis. Numerical integration of the bivariate von Mises and planar von Mises density distributions is presented with different numbers of integration points, which guide the proper selection of total integration points. In order to overcome the erroneous numerical integration at high concentration parameters in planar dispersion

models, we proposed a planar circular integration scheme that provides high accuracy even for $b = 100$ where the dispersion is very close to the perfectly anisotropic case.

The fitting performance of the proposed models has been tested at the constitutive level using numerical examples for the cyclic triaxial shear test and the triaxial relaxation test from the literature. The normalization of the numerical integration is violated in the local-based dispersion models by the nonlinear evolution rule. This problem is mainly integrated by the density distribution function directly into the micro-viscous free energies. Due to the nonlinear exponent in the evolution equation, the density distribution is exposed to a decreasing trend, and activation stress cannot be reached. In order to overcome the violation of the normalization state, we suggest using a linear evolution law that results in an explicitly defined update regime. Therefore, the density distribution can be placed directly as a multiplier of the free-energy function. Although the local-based formulations provide flexibility to get into the constitutive level equations and make it possible to describe different density distributions for separate mechanical properties of the tissue, in order to keep the accuracy of the numerical integral averaging, they should only be used with linear evolution equations. To avoid violating the normalization condition, we used global-based formulations at Models III, IV, and V, where the density distribution function does not enter the micro-viscous free-energy but reveals itself in the continuous average integral over the unit-sphere or planar circle during the stress and tangent moduli calculations. This method accurately solves both linear and nonlinear evolution equations using the dispersion-type angular integration scheme.

We have formulated both bivariate von Mises and planar von Mises distributions for fiber and sheet directions. The bivariate von Mises density distribution contributes not only to in-plane dispersion but also to out-of-plane directions through the normal direction in the myocardium. Planar von Mises density distribution provides rotationally symmetric behaviour in three-dimensional space, which results in a minor effect on the out-of-plane direction. Both models work well and capture the experimental data with a good agreement, especially for cyclic triaxial shear tests. However, due to the isotropic definition in the normal direction in the first four models, the normal direction-related shear modes exhibited an average sense of agreement with the experiments. In order to reflect the true behaviour of the orthotropic nature of the

myocardium tissue, we add dispersion characteristics to the normal orientation in addition to the dispersion formulation of fiber and sheet. That formulation well-agreed with the cyclic triaxial experiment data of the human myocardium. In the trixaial relaxation numerical fittings, the same data set that is obtained from the cyclic triaxial tests are used. The relaxation slope has been well captured with some upward offset. There is a trade-off between the optimum fitting parameters of the triaxial cyclic shear and triaxial shear relaxation tests. Therefore, we kept the optimum parameter sets, which are suitable for both tests.

Dispersion-type anisotropic viscoelasticity is promosing framework for the modeling of rate-dependent response of soft biological tissues. These constitutive models provide histological-based modeling which is flexible to be used for any type of anisotropic tissue. Angular integration-based dispersion-type anisotropic viscoelasticity is able to use any type of distribution function i.e. bivariate or planar von Mises distributions based on different type of numerical integral averaging schemes such as over the unit micro-sphere and unit planar circle. The general framework has the capability to be used for not only highly dispersed behaviours but also highly anisotropic dispersion characteristics by choosing the proper number of integration points and integration scheme.

Although, we have tested the proposed models in the unique experiments provided in the literature for the human myocardium, as a future work, further numerical tests can be performed for any other type of soft anisotropic viscoelastic tissue. More experimental work is need for the understanding of the roots of viscoelastic response and its relations to tissue histology. It is also required to develop more efficient integration scheme by providing bias of integration points on the localized region of the density distribution function to increase the computational efficiency and accuracy. Additionally, in order to get a more flexible model in terms of fitting purposes, the concentration factors in the orthogonal directions can be defined independently within an optimization algorithm, which will increase the computational time and total number of independent parameters in the analysis but it will provide a larger space of parameter sets. Then, the passive mechanical response of the entire heart model can be constructed and examined numerically under pressure loads during the cardiac cycle.

REFERENCES

[1] O. Gültekin, G. Sommer, and G. A. Holzapfel, "An orthotropic viscoelastic model for the passive myocardium: continuum basis and numerical treatment," *Computer methods in biomechanics and biomedical engineering*, vol. 19, no. 15, pp. 1647–1664, 2016.

[2] K. Vinay, A. Jon C., and A. Abul K., *Robbins and Cotran's pathologic basis of disease*. Elsevier Saunders, 2015.

[3] D. H. Kim, J. H. Ahn, M. C. Won, H. S. Kim, T. H. Kim, J. Song, Y. Y. Huang, Z. Liu, C. Lu, and J. A. Rogers, "Stretchable and foldable silicon integrated circuits," *Science*, vol. 320, no. 5875, pp. 507–511, 2008.

[4] B. Li, Y. P. Cao, X. Q. Feng, and H. Gao, "Mechanics of morphological instabilities and surface wrinkling in soft materials: A review," *Soft Matter*, vol. 8, no. 21, pp. 5728–5745, 2012.

[5] H. Dal, K. Açıkgöz, and Y. Badienia, "On the Performance of Isotropic Hyperelastic Constitutive Models for Rubber-Like Materials: A State of the Art Review," *Applied Mechanics Reviews*, vol. 73, no. 2, 020802, 2021.

[6] S. Göktepe, O. J. Abilez, and E. Kuhl, "A generic approach towards finite growth with examples of athlete's heart, cardiac dilation, and cardiac wall thickening," *Journal of the Mechanics and Physics of Solids*, vol. 58, no. 10, pp. 1661–1680, 2010.

[7] K. Li and G. A. Holzapfel, "Multiscale modeling of fiber recruitment and damage with a discrete fiber dispersion method," *Journal of the Mechanics and Physics of Solids*, vol. 126, pp. 226–244, 2019.

[8] N. Horvat, L. Virag, G. A. Holzapfel, and I. Karšaj, "Implementation of collagen fiber dispersion in a growth and remodeling model of arterial walls," *Journal of the Mechanics and Physics of Solids*, vol. 153, 104498, 2021.

[9] D. Liu and G. Yan, “A multi-layer finite element model based on anisotropic hyperelastic fiber reinforcements within intestinal walls,” *Nano Biomedicine and Engineering*, vol. 9, no. 4, pp. 291–297, 2017.

[10] T. S. Eriksson, A. J. Prassl, G. Plank, and G. A. Holzapfel, “Modeling the dispersion in electromechanically coupled myocardium,” *International Journal for Numerical Methods in Biomedical Engineering*, vol. 21, no. 11, pp. 1267–1284, 2013.

[11] G. Sommer, A. J. Schriefl, M. Andrä, M. Sacherer, C. Viertler, H. Wolinski, and G. A. Holzapfel, “Biomechanical properties and microstructure of human ventricular myocardium,” *Acta Biomaterialia*, vol. 24, pp. 172–192, 2015.

[12] A. Logg, K. A. Mardal, and G. N. Wells, *Automated solution of differential equations by the finite element method*, vol. 84. Springer, 2012.

[13] Y. C. Fung, *Biomechanics: Mechanical Properties of Living Tissues.*, vol. 2. Springer, 1994.

[14] R. K. Kesharwani, R. K. Keservani, and A. K. Sharma, *Tissue Engineering Applications and Advancements*, vol. 1. Apple Academic Press, 2022.

[15] C. F. Guimarães, L. Gasperini, A. P. Marques, and R. L. Reis, “The stiffness of living tissues and its implications for tissue engineering,” *Nature Reviews Materials*, vol. 5, no. 5, pp. 351–370, 2020.

[16] E. M. Green, J. C. Mansfield, J. S. Bell, and C. P. Winlove, “The structure and micromechanics of elastic tissue,” *Interface Focus*, vol. 4, no. 2, 2014.

[17] H. Dal, A. Kağan, A. Ciara, and D. Mokarram, “An in silico-based review on anisotropic hyperelastic constitutive models for soft biological tissues,” *Archives of Computational Methods in Engineering*, submitted, 2023, arXiv preprint arXiv:2207.13985.

[18] B. Cansiz, H. Dal, and M. Kaliske, “An orthotropic viscoelastic material model for passive myocardium: theory and algorithmic treatment,” *Computer Methods in Biomechanics and Biomedical Engineering*, vol. 18, no. 11, pp. 1160–1172, 2015.

[19] H. Dal, S. Göktepe, M. Kaliske, and E. Kuhl, "A fully implicit finite element method for bidomain models of cardiac electromechanics," *Computer Methods in Applied Mechanics and Engineering*, vol. 253, pp. 323–336, 2013.

[20] B. Cansiz, H. Dal, and M. Kaliske, "Computational cardiology: A modified Hill model to describe the electro-visco-elasticity of the myocardium," *Computer Methods in Applied Mechanics and Engineering*, vol. 315, pp. 434–466, 2017.

[21] B. Cansiz, H. Dal, and M. Kaliske, "Computational cardiology: the bidomain based modified Hill model incorporating viscous effects for cardiac defibrillation," *Computational Mechanics*, vol. 62, no. 3, pp. 253–271, 2018.

[22] P. Steinmann, M. Hossain, and G. Possart, "Hyperelastic models for rubber-like materials: Consistent tangent operators and suitability for Treloar's data," *Archive of Applied Mechanics*, vol. 82, no. 9, pp. 1183–1217, 2012.

[23] G. Chagnon, M. Rebouah, and D. Favier, "Hyperelastic Energy Densities for Soft Biological Tissues: A Review," *Journal of Elasticity*, vol. 120, no. 2, pp. 129–160, 2015.

[24] C. Wex, S. Arndt, A. Stoll, C. Bruns, and Y. Kupriyanova, "Isotropic incompressible hyperelastic models for modelling the mechanical behaviour of biological tissues: A review," *Biomedizinische Technik*, vol. 60, no. 6, pp. 577–592, 2015.

[25] L. A. Mihai, L. K. Chin, P. A. Janmey, and A. Goriely, "A comparison of hyperelastic constitutive models applicable to brain and fat tissues," *Journal of the Royal Society Interface*, vol. 12, no. 110, 2015.

[26] J. Cheng and L. T. Zhang, "A General Approach to Derive Stress and Elasticity Tensors for Hyperelastic Isotropic and Anisotropic Biomaterials," *International Journal of Computational Methods*, vol. 15, no. 1, 1850028, 2017.

[27] G. A. Holzapfel, R. W. Ogden, and S. Sherifova, "On fibre dispersion modelling of soft biological tissues: A review," *Proceedings of the Royal Society A: Mathematical, Physical and Engineering Sciences*, vol. 475, no. 2224, 2019.

[28] L. A. Taber, “Biomechanics of growth, remodeling, and morphogenesis,” *Applied Mechanics Reviews*, vol. 48, no. 8, pp. 487–545, 1995.

[29] E. Kuhl, “Growing matter: A review of growth in living systems,” *Journal of the Mechanical Behavior of Biomedical Materials*, vol. 29, pp. 529–543, 2014.

[30] T. Mora, A. Boudaoud, T. Mora, A. Boudaoud, E. Physical, and J. E. Soft, “Buckling of swelling gels,” *European Physical Journal E: Soft matter and biological physics*, vol. 20, pp. 119–124, 2006.

[31] D. Y. Khang, J. A. Rogers, and H. H. Lee, “Mechanical buckling: Mechanics, metrology, and stretchable electronics,” *Advanced Functional Materials*, vol. 19, no. 10, pp. 1526–1536, 2009.

[32] M. Eskandari, M. R. Pfaller, and E. Kuhl, “On the role of mechanics in chronic lung disease,” *Materials*, vol. 6, no. 12, pp. 5639–5658, 2013.

[33] S. Budday, P. Steinmann, and E. Kuhl, “The role of mechanics during brain development,” *Journal of the Mechanics and Physics of Solids*, vol. 72, pp. 75–92, 2014.

[34] J. Ulerich, S. Göktepe, and E. Kuhl, “Dilation and hypertrophy: A cell-based continuum mechanics approach towards ventricular growth and remodeling,” *IUTAM Bookseries*, vol. 16, pp. 237–244, 2010.

[35] S. Göktepe, O. J. Abilez, K. K. Parker, and E. Kuhl, “A multiscale model for eccentric and concentric cardiac growth through sarcomerogenesis,” *Journal of Theoretical Biology*, vol. 265, no. 3, pp. 433–442, 2011.

[36] M. K. Rausch, A. Dam, S. Göktepe, O. J. Abilez, and E. Kuhl, “Computational modeling of growth: Systemic and pulmonary hypertension in the heart,” *Biomechanics and Modeling in Mechanobiology*, vol. 10, no. 6, pp. 799–811, 2010.

[37] B. Li, F. Jia, Y. P. Cao, X. Q. Feng, and H. Gao, “Surface wrinkling patterns on a core-shell soft sphere,” *Physical Review Letters*, vol. 106, no. 23, pp. 2–5, 2011.

[38] A. Javili, P. Steinmann, and E. Kuhl, “A novel strategy to identify the critical conditions for growth-induced instabilities,” *Journal of the Mechanical Behavior of Biomedical Materials*, vol. 29, pp. 20–32, 2014.

[39] J. Genzer and J. Groenewold, “Soft matter with hard skin: From skin wrinkles to templating and material characterization,” *Soft Matter*, vol. 2, no. 4, pp. 310–323, 2006.

[40] A. Buganza Tepole, C. Joseph Ploch, J. Wong, A. K. Gosain, and E. Kuhl, “Growing skin: A computational model for skin expansion in reconstructive surgery,” *Journal of the Mechanics and Physics of Solids*, vol. 59, no. 10, pp. 2177–2190, 2011.

[41] I. Hariton, G. DeBotton, T. C. Gasser, and G. A. Holzapfel, “Stress-driven collagen fiber remodeling in arterial walls,” *Biomechanics and Modeling in Mechanobiology*, vol. 6, no. 3, pp. 163–175, 2007.

[42] H. Demirkoparan and T. J. Pence, “The effect of fiber recruitment on the swelling of a pressurized anisotropic non-linearly elastic tube,” *International Journal of Non-Linear Mechanics*, vol. 42, no. 2, pp. 258–270, 2007.

[43] K. Y. Volokh, “Prediction of arterial failure based on a microstructural bi-layer fiber-matrix model with softening,” *Journal of Biomechanics*, vol. 41, no. 2, pp. 447–453, 2008.

[44] P. Sáez, E. Peña, M. A. Martínez, and E. Kuhl, “Computational modeling of hypertensive growth in the human carotid artery,” *Computational Mechanics*, vol. 53, no. 6, pp. 1183–1196, 2014.

[45] V. A. Lubarda and A. Hoger, “On the mechanics of solids with a growing mass,” *International Journal of Solids and Structures*, vol. 39, pp. 4627–4664, 2002.

[46] Z. Y. Huang, W. Hong, and Z. Suo, “Nonlinear analyses of wrinkles in a film bonded to a compliant substrate,” *Journal of the Mechanics and Physics of Solids*, vol. 53, no. 9, pp. 2101–2118, 2005.

[47] F. Brau, H. Vandeparre, A. Sabbah, C. Poulard, A. Boudaoud, and P. Damman, “Multiple-length-scale elastic instability mimics parametric resonance of nonlinear oscillators,” *Nature Physics*, vol. 7, no. 1, pp. 56–60, 2011.

[48] S. Cai, D. Breid, A. J. Crosby, Z. Suo, and J. W. Hutchinson, “Periodic patterns and energy states of buckled films on compliant substrates,” *Journal of the Mechanics and Physics of Solids*, vol. 59, no. 5, pp. 1094–1114, 2011.

[49] F. Jia and M. Ben Amar, “Theoretical analysis of growth or swelling wrinkles on constrained soft slabs,” *Soft Matter*, vol. 9, no. 34, pp. 8216–8226, 2013.

[50] J. Dervaux, P. Ciarletta, and M. Ben Amar, “Morphogenesis of thin hyperelastic plates: A constitutive theory of biological growth in the Föppl-von Kármán limit,” *Journal of the Mechanics and Physics of Solids*, vol. 57, no. 3, pp. 458–471, 2009.

[51] Z. Li, Q. Wang, P. Du, C. Kadapa, M. Hossain, and J. Wang, “Analytical study on growth-induced axisymmetric deformations and shape-control of circular hyperelastic plates,” *International Journal of Engineering Science*, vol. 170, 103594, 2022.

[52] L. Ionov, “Biomimetic hydrogel-based actuating systems,” *Advanced Functional Materials*, vol. 23, no. 36, pp. 4555–4570, 2013.

[53] Y. Liu, H. Zhang, and Y. Zheng, “A multiplicative finite element algorithm for the inhomogeneous swelling of polymeric gels,” *Computer Methods in Applied Mechanics and Engineering*, vol. 283, pp. 517–550, 2015.

[54] Y. Liu, H. Zhang, J. Zhang, and Y. Zheng, “Constitutive modeling for polymer hydrogels: A new perspective and applications to anisotropic hydrogels in free swelling,” *European Journal of Mechanics, A/Solids*, vol. 54, pp. 171–186, 2015.

[55] P. Nardinocchi, M. Pezzulla, and L. Teresi, “Anisotropic swelling of thin gel sheets,” *Soft Matter*, vol. 11, no. 8, pp. 1492–1499, 2015.

[56] P. Nardinocchi, M. Pezzulla, and L. Teresi, “Steady and transient analysis of anisotropic swelling in fibered gels,” *Journal of Applied Physics*, vol. 118, no. 24, 244904, 2015.

[57] Y. Liu, H. Zhang, J. Wang, and Y. Zheng, "Anisotropic Swelling in Fiber-Reinforced Hydrogels: An Incremental Finite Element Method and Its Applications in Design of Bilayer Structures," *International Journal of Applied Mechanics*, vol. 8, no. 7, 1640003, 2016.

[58] J. Wang, Y. Qiu, H. Zhang, Y. Zheng, and H. Ye, "A solid-shell finite element method for the anisotropic swelling of hydrogels with reinforced fibers," *European Journal of Mechanics, A/Solids*, vol. 86, 104197, 2021.

[59] W. Liu and C. R. Rahn, "Fiber-Reinforced Membrane Models of McKibben Actuators," *Journal of Applied Mechanics, Transactions ASME*, vol. 70, no. 6, pp. 853–859, 2003.

[60] Y. Fang, T. J. Pence, and X. Tan, "Fiber-directed conjugated-polymer torsional actuator: Nonlinear elasticity modeling and experimental validation," *IEEE/ASME Transactions on Mechatronics*, vol. 16, no. 4, pp. 656–664, 2011.

[61] E. Kuhl, A. Menzel, and P. Steinmann, "Computational modeling of growth. A critical review, a classification of concepts and two new consistent approaches," *Computational Mechanics*, vol. 32, no. 1-2, pp. 71–88, 2003.

[62] D. Ambrosi, G. A. Ateshian, E. M. Arruda, S. C. Cowin, J. Dumais, A. Goriely, G. A. Holzapfel, J. D. Humphrey, R. Kemkemer, E. Kuhl, J. E. Olberding, L. A. Taber, and K. Garikipati, "Perspectives on biological growth and remodeling," *Journal of the Mechanics and Physics of Solids*, vol. 59, no. 4, pp. 863–883, 2011.

[63] A. Menzel and E. Kuhl, "Frontiers in growth and remodeling," *Mechanics Research Communications*, vol. 42, pp. 1–14, 2012.

[64] A. Goriely, "Five ways to model active processes in elastic solids: Active forces, active stresses, active strains, active fibers, and active metrics," *Mechanics Research Communications*, vol. 93, pp. 75–79, 2018.

[65] S. Yang, K. Khare, and P. C. Lin, "Harnessing surface wrinkle patterns in soft matter," *Advanced Functional Materials*, vol. 20, no. 16, pp. 2550–2564, 2010.

[66] B. Audoly and A. Boudaoud, “Buckling of a stiff film bound to a compliant substrate-Part III:. Herringbone solutions at large buckling parameter,” *Journal of the Mechanics and Physics of Solids*, vol. 56, no. 7, pp. 2444–2458, 2008.

[67] A. Javili, B. Dortdivanlioglu, E. Kuhl, and C. Linder, “Computational aspects of growth-induced instabilities through eigenvalue analysis,” *Computational Mechanics*, vol. 56, no. 3, pp. 405–420, 2015.

[68] B. Dortdivanlioglu, A. Javili, and C. Linder, “Computational aspects of morphological instabilities using isogeometric analysis,” *Computer Methods in Applied Mechanics and Engineering*, vol. 316, pp. 261–279, 2017.

[69] B. Audoly and A. Boudaoud, “Buckling of a stiff film bound to a compliant substrate-Part I:. Formulation, linear stability of cylindrical patterns, secondary bifurcations,” *Journal of the Mechanics and Physics of Solids*, vol. 56, no. 7, pp. 2401–2421, 2008.

[70] B. Audoly and A. Boudaoud, “Buckling of a stiff film bound to a compliant substrate-Part II:. A global scenario for the formation of herringbone pattern,” *Journal of the Mechanics and Physics of Solids*, vol. 56, no. 7, pp. 2422–2443, 2008.

[71] H. Alawiye, E. Kuhl, and A. Goriely, “Revisiting the wrinkling of elastic bilayers I: Linear analysis,” *Philosophical Transactions of the Royal Society A: Mathematical, Physical and Engineering Sciences*, vol. 377, no. 2144, 2019.

[72] A. Ilseng, V. Prot, B. H. Skallerud, and B. T. Stokke, “Buckling initiation in layered hydrogels during transient swelling,” *Journal of the Mechanics and Physics of Solids*, vol. 128, pp. 219–238, 2019.

[73] B. Dortdivanlioglu and C. Linder, “Diffusion-driven swelling-induced instabilities of hydrogels,” *Journal of the Mechanics and Physics of Solids*, vol. 125, pp. 38–52, 2019.

[74] C. Kadapa, M. Hossain, and J. Wang, “On the advantages of mixed formulation and higher-order elements for computational morphoelasticity,” *Journal of the Mechanics and Physics of Solids*, vol. 148, 104289, 2020.

[75] A. Rachev, N. Stergiopulos, and J. J. Meister, “Theoretical study of dynamics of arterial wall remodeling in response to changes in blood pressure,” *Journal of Biomechanics*, vol. 29, no. 5, pp. 635–642, 1996.

[76] L. A. Taber, “A model for aortic growth based on fluid shear and fiber stresses,” *Journal of Biomechanical Engineering*, vol. 120, no. 3, pp. 348–354, 1998.

[77] P. Ciarletta and M. Ben Amar, “Pattern formation in fiber-reinforced tubular tissues: Folding and segmentation during epithelial growth,” *Journal of the Mechanics and Physics of Solids*, vol. 60, no. 3, pp. 525–537, 2012.

[78] P. S. Stewart, S. L. Waters, T. El Sayed, D. Vella, and A. Goriely, “Wrinkling, creasing, and folding in fiber-reinforced soft tissues,” *Extreme Mechanics Letters*, vol. 8, pp. 22–29, 2016.

[79] M. Agoras, O. Lopez-Pamies, and P. Ponte Castañeda, “Onset of macroscopic instabilities in fiber-reinforced elastomers at finite strain,” *Journal of the Mechanics and Physics of Solids*, vol. 57, no. 11, pp. 1828–1850, 2009.

[80] J. C. Michel, O. Lopez-Pamies, P. Ponte Castaeda, and N. Triantafyllidis, “Microscopic and macroscopic instabilities in finitely strained fiber-reinforced elastomers,” *Journal of the Mechanics and Physics of Solids*, vol. 58, no. 11, pp. 1776–1803, 2010.

[81] V. Slesarenko and S. Rudykh, “Microscopic and macroscopic instabilities in hyperelastic fiber composites,” *Journal of the Mechanics and Physics of Solids*, vol. 99, pp. 471–482, 2017.

[82] H. Topol, H. Demirkoparan, T. J. Pence, and A. Wineman, “Uniaxial load analysis under stretch-dependent fiber remodeling applicable to collagenous tissue,” *Journal of Engineering Mathematics*, vol. 95, no. 1, pp. 325–345, 2015.

[83] Y. Lanir, “Mechanistic micro-structural theory of soft tissues growth and remodeling: tissues with unidirectional fibers,” *Biomechanics and Modeling in Mechanobiology*, vol. 14, no. 2, pp. 245–266, 2015.

[84] K. Gou and T. J. Pence, “Hyperelastic modeling of swelling in fibrous soft tissue with application to tracheal angioedema,” *Journal of Mathematical Biology*, vol. 72, no. 1-2, pp. 499–526, 2016.

[85] K. Gou and T. J. Pence, “Computational modeling of tracheal angioedema due to swelling of the submucous tissue layer,” *International Journal for Numerical Methods in Biomedical Engineering*, vol. 33, no. 10, 2017.

[86] K. Gou, P. W. Fok, and Y. Fu, “Nonlinear tubular organ modeling and analysis for tracheal angioedema by swelling-morphoelasticity,” *Journal of Engineering Mathematics*, vol. 112, no. 1, pp. 95–117, 2018.

[87] M. Genet, M. K. Rausch, L. C. Lee, S. Choy, X. Zhao, G. S. Kassab, S. Kozerke, J. M. Guccione, and E. Kuhl, “Heterogeneous growth-induced prestrain in the heart,” *Journal of Biomechanics*, vol. 48, no. 10, pp. 2080–2089, 2015.

[88] J. D. Humphrey, *Cardiovascular solid mechanics. Cells, tissues, and organs*. Springer New York, 2002.

[89] F. B. Sachse, *Computational Cardiology Modeling of Anatomy, Electrophysiology, and Mechanics*. Springer Berlin, 2004.

[90] J. Vossoughi, R. N. Vaishnav, and D. J. Patel, “Compressibility of the myocardial tissue,” *Advances in bioengineering (ed. Van C. Mow), Bioengineering Division, American Society of Mechanical Engineers*, no. 1-2, pp. 45–48, 1980.

[91] D. Rohmer, A. Sitek, and G. T. Gullberg, “Reconstruction and visualization of fiber and laminar structure in the normal human heart from ex vivo diffusion tensor magnetic resonance imaging (DTMRI) data,” *Investigative Radiology*, vol. 42, no. 11, pp. 777–789, 2007.

[92] G. B. Sands, B. H. Smaill, and I. J. LeGrice, “Virtual sectioning of cardiac tissue relative to fiber orientation,” *Proceedings of the 30th Annual International Conference of the IEEE Engineering in Medicine and Biology Society, EMBS’08 - "Personalized Healthcare through Technology"*, pp. 226–229, 2008.

[93] G. J. Strijkers, A. Bouts, W. M. Blankesteijn, T. H. Peeters, A. Vilanova, M. C. van Prooijen, H. M. Sanders, E. Heijman, and K. Nicolay, “Diffusion tensor imaging of left ventricular remodeling in response to myocardial infarction in the mouse,” *NMR in Biomedicine*, vol. 22, no. 2, pp. 182–190, 2009.

[94] J. G. Pinto and Y. C. Fung, “Mechanical properties of the heart muscle in the passive state,” *Journal of Biomechanics*, vol. 6, no. 6, pp. 597–606, 1973.

[95] L. Demer and F. Yin, “Passive Biaxial Mechanical Properties of Isolated Canine Myocardium,” *Journal of Phys*, vol. 339, pp. 615–630, 1983.

[96] A. K. Tsaturyan, V. J. Izacov, S. V. Zhelamsky, and B. L. Bykov, “Extracellular fluid filtration as the reason for the viscoelastic behaviour of the passive myocardium,” *Journal of Biomechanics*, vol. 17, no. 10, pp. 749–755, 1984.

[97] F. C. Yin, R. K. Strumpf, P. H. Chew, and S. L. Zeger, “Quantification of the mechanical properties of noncontracting canine myocardium under simultaneous biaxial loading,” *Journal of Biomechanics*, vol. 20, no. 6, pp. 577–589, 1987.

[98] S. Dokos, I. J. LeGrice, B. H. Smaill, J. Kar, and A. A. Young, “A triaxial-measurement shear-test device for soft biological tissues,” *Journal of Biomechanical Engineering*, vol. 122, no. 5, pp. 471–478, 2000.

[99] S. Dokos, B. H. Smaill, A. A. Young, and I. J. LeGrice, “Shear properties of passive ventricular myocardium,” *American Journal of Physiology - Heart and Circulatory Physiology*, vol. 283, no. 6, pp. 2650–2659, 2002.

[100] H. Ghaemi, K. Behdinan, and A. D. Spence, “In vitro technique in estimation of passive mechanical properties of bovine heart. Part I. Experimental techniques and data,” *Medical Engineering and Physics*, vol. 31, no. 1, pp. 76–82, 2009.

[101] G. Sommer, D. C. Haspinger, M. Andrä, M. Sacherer, C. Viertler, P. Regitnig, and G. A. Holzapfel, “Quantification of Shear Deformations and Corresponding Stresses in the Biaxially Tested Human Myocardium,” *Annals of Biomedical Engineering*, vol. 43, no. 10, pp. 2334–2348, 2015.

[102] R. Avazmohammadi, D. S. Li, T. Leahy, E. Shih, J. S. Soares, J. H. Gorman, R. C. Gorman, and M. S. Sacks, “An integrated inverse model-experimental approach to determine soft tissue three-dimensional constitutive parameters: Application to post-infarcted myocardium,” *Biomechanics and Modeling in Mechanobiology*, vol. 17, no. 1, pp. 31–53, 2018.

[103] D. Martonova, M. Alkassar, J. Seufert, D. Holz, M. T. Duong, B. Reischl, O. Friedrich, and S. Leyendecker, "Passive mechanical properties in healthy and infarcted rat left ventricle characterised via a mixture model," *Journal of the Mechanical Behavior of Biomedical Materials*, vol. 119, 104430, 2021.

[104] H. Dal, "A quasi-incompressible and quasi-inextensible element formulation for transversely isotropic materials," *International Journal for Numerical Methods in Engineering*, vol. 117, no. 1, pp. 118–140, 2019.

[105] J. E. Marsden and T. J. Hughes, *Mathematical Foundations of Elasticity*. Dover Publications, Inc, 1983.

[106] G. A. Holzapfel and R. W. Ogden, "Constitutive modelling of passive myocardium: A structurally based framework for material characterization," *Philosophical Transactions of the Royal Society A: Mathematical, Physical and Engineering Sciences*, vol. 367, no. 1902, pp. 3445–3475, 2009.

[107] G. A. Holzapfel, *Nonlinear Solid Mechanics A Continuum Approach for Engineering*. John Wiley & Sons, 2000.

[108] M. C. Boyce and E. M. Arruda, "Constitutive models of rubber elasticity: A review," *Rubber Chemistry and Technology*, vol. 73, no. 3, pp. 504–523, 2000.

[109] T. Beda, "Modeling Hyperelastic Behavior of Rubber: A Novel Invariant-Based and a Review of Constitutive Models," *Journal of Polymer Science: Part B: Polymer Physics*, vol. 45, no. 13, pp. 1713–1732, 2007.

[110] M. Hossain and P. Steinmann, "More hyperelastic models for rubber-like materials: consistent tangent operators and comparative study," *Journal of the Mechanical Behavior of Materials*, vol. 22, no. 1-2, pp. 27–50, 2013.

[111] T. Beda, "An approach for hyperelastic model-building and parameters estimation a review of constitutive models," *European Polymer Journal*, vol. 50, no. 1, pp. 97–108, 2014.

[112] A. Zdunek, W. Rachowicz, and T. Eriksson, "A novel computational formulation for nearly incompressible and nearly inextensible finite hyperelasticity," *Computer Methods in Applied Mechanics and Engineering*, vol. 281, pp. 220–249, 2014.

[113] A. Zdunek, W. Rachowicz, and T. Eriksson, "A five-field finite element formulation for nearly inextensible and nearly incompressible finite hyperelasticity," *Computers and Mathematics with Applications*, vol. 72, no. 1, pp. 25–47, 2016.

[114] T. H. Pian and C. DP, "Alternative ways for formulation of hybrid stress elements," *International Journal for Numerical Methods in Engineering*, vol. 18, no. 11, pp. 1679–1684, 1982.

[115] T. H. Pian and K. Sumihara, "Rational approach for assumed stress finite elements," *International Journal for Numerical Methods in Engineering*, vol. 20, no. 9, pp. 1685–1695, 1984.

[116] J. C. Nagtegaal, D. M. Parks, and J. R. Rice, "On numerically accurate finite element solutions in the fully plastic range," *Computer Methods in Applied Mechanics and Engineering*, vol. 4, no. 2, pp. 153–177, 1974.

[117] R. T. J.C. SIMO and K. PISTER, "Variational and projection methods for the volume constraint in finite deformation elasto-plasticity," *Computer Methods in Applied Mechanics and Engineering*, vol. 51, pp. 177–208, 1985.

[118] J. C. Simo and R. L. Taylor, "Quasi-incompressible finite elasticity in principal stretches. continuum basis and numerical algorithms," *Computer Methods in Applied Mechanics and Engineering*, vol. 85, no. 3, pp. 273–310, 1991.

[119] C. Miehe, "Aspects of the formulation and finite element implementation of large strain isotropic elasticity," *International Journal for Numerical Methods in Engineering*, vol. 37, no. 12, pp. 1981–2004, 1994.

[120] H. Dal and M. Kaliske, "Bergström-Boyce model for nonlinear finite rubber viscoelasticity: Theoretical aspects and algorithmic treatment for the FE method," *Computational Mechanics*, vol. 44, no. 6, pp. 809–823, 2009.

[121] C. Kadapa and M. Hossain, "A linearized consistent mixed displacement- pressure formulation for hyperelasticity," *Mechanics of Advanced Materials and Structures*, vol. 29, no. 2, pp. 267–284, 2020.

[122] J. A. Weiss, B. N. Maker, and G. S., "Finite element implementation of transversely isotropic hyperelasticity," *Computer Methods in Applied Mechanics and Engineering*, vol. 135, no. 1–2, pp. 107–128, 1996.

[123] P. J. Flory, “Thermodynamic relations for high elastic materials,” *Transactions of the Faraday Society*, vol. 57, pp. 829–838, 1961.

[124] G. A. Holzapfel, T. C. Gasser, and R. A. Y. W. Ogden, “A New Constitutive Framework for Arterial Wall Mechanics and a Comparative Study of Material Models,” *Journal of Elasticity*, vol. 61, pp. 1–48, 2000.

[125] G. A. Holzapfel, G. Sommer, C. T. Gasser, and P. Regitnig, “Determination of layer-specific mechanical properties of human coronary arteries with nonatherosclerotic intimal thickening and related constitutive modeling,” *American Journal of Physiology - Heart and Circulatory Physiology*, vol. 289, no. 5 58-5, pp. 2048–2058, 2005.

[126] R. D. W. Javier Bonet, *Nonlinear Continuum Mechanics for Finite Element Analysis*, vol. 2. Cambridge University Press, 2008.

[127] B. P. Lamichhane, A. T. McBride, and B. D. Reddy, “A finite element method for a three-field formulation of linear elasticity based on biorthogonal systems,” *Computer Methods in Applied Mechanics and Engineering*, vol. 258, pp. 109–117, 2013.

[128] A. Chama and B. D. Reddy, “New stable mixed finite element approximations for problems in linear elasticity,” *Computer Methods in Applied Mechanics and Engineering*, vol. 256, pp. 211–223, 2013.

[129] M. Chiumenti, M. Cervera, and R. Codina, “A mixed three-field FE formulation for stress accurate analysis including the incompressible limit,” *Computer Methods in Applied Mechanics and Engineering*, vol. 283, pp. 1095–1116, 2015.

[130] S. Wulfinghoff, H. R. Bayat, A. Alipour, and S. Reese, “A low-order locking-free hybrid discontinuous Galerkin element formulation for large deformations,” *Computer Methods in Applied Mechanics and Engineering*, vol. 323, pp. 353–372, 2017.

[131] N. Viebahn, K. Steeger, and J. Schröder, “A simple and efficient Hellinger–Reissner type mixed finite element for nearly incompressible elas-

ticity," *Computer Methods in Applied Mechanics and Engineering*, vol. 340, pp. 278–295, 2018.

[132] J. Schröder, N. Viebahn, D. Balzani, and P. Wriggers, "A novel mixed finite element for finite anisotropic elasticity; the SKA-element Simplified Kinematics for Anisotropy," *Computer Methods in Applied Mechanics and Engineering*, vol. 310, pp. 475–494, 2016.

[133] P. Wriggers, J. Schröder, and F. Auricchio, "Finite element formulations for large strain anisotropic material with inextensible fibers," *Advanced Modeling and Simulation in Engineering Sciences*, vol. 3, no. 1, pp. 1–18, 2016.

[134] O. Gültekin, H. Dal, and G. A. Holzapfel, "On the quasi-incompressible finite element analysis of anisotropic hyperelastic materials," *Computational Mechanics*, vol. 63, no. 3, pp. 443–453, 2019.

[135] E. K. Rodriguez, A. Hoger, and A. D. McCulloch, "Stress-dependent finite growth in soft elastic tissues," *Journal of Biomechanics*, vol. 27, no. 4, pp. 455–467, 1994.

[136] M. K. Rausch and E. Kuhl, "On the mechanics of growing thin biological membranes," *Journal of the Mechanics and Physics of Solids*, vol. 63, no. 1, pp. 128–140, 2014.

[137] J. Wang, Q. Wang, and H. H. Dai, "Stress-free bending of a neo-Hookean plate induced by growth: Exact solution and experiments," *International Journal of Non-Linear Mechanics*, vol. 106, pp. 280–287, 2018.

[138] J. Wang, H. Zhang, Y. Zheng, and H. Ye, "High-order NURBS elements based isogeometric formulation for swellable soft materials," *Computer Methods in Applied Mechanics and Engineering*, vol. 363, 112901, 2020.

[139] S. Budday, C. Raybaud, and E. Kuhl, "A mechanical model predicts morphological abnormalities in the developing human brain," *Scientific Reports*, vol. 4, pp. 1–7, 2014.

[140] S. Budday, P. Steinmann, and E. Kuhl, "Secondary instabilities modulate cortical complexity in the mammalian brain," *Philosophical Magazine*, vol. 95, no. 28-30, pp. 3244–3256, 2015.

[141] X. Ning, Q. Zhu, Y. Lanir, and S. S. Margulies, “A Transversely Isotropic Viscoelastic Constitutive Equation for Brainstem Undergoing Finite Deformation,” *Journal of Biomechanical Engineering*, vol. 128, no. 6, pp. 925–933, 2006.

[142] G. Xu, A. K. Kunutsen, K. Dikranian, C. D. Kroenke, P. V. Bayly, and L. A. Taber, “Axons pull on the brain , but tension does not drive cortical folding,” *Journal of Biomechanical Engineering*, vol. 132, no. 7, 071013, 2010.

[143] M. Hrapko, J. A. W. V. Dommelen, and J. S. H. M. Wismans, “The influence of test conditions on characterization of the mechanical properties of brain tissue,” *Journal of Biomechanical Engineering*, vol. 130, no. 3, pp. 1–10, 2008.

[144] R. De Rooij and E. Kuhl, “Constitutive Modeling of Brain Tissue: Current Perspectives,” *Applied Mechanics Reviews*, vol. 68, no. 1, pp. 1–16, 2016.

[145] J. Zhou, J. P. Stockmann, N. Arango, T. Witzel, K. Scheffler, L. L. Wald, and F. H. Lin, “An orthogonal shim coil for 3T brain imaging,” *Magnetic Resonance in Medicine*, vol. 83, no. 4, pp. 1499–1511, 2020.

[146] H. Huang, R. Xue, J. Zhang, T. Ren, L. J. Richards, P. Yarowsky, M. I. Miller, and S. Mori, “Anatomical characterization of human fetal brain development with diffusion tensor magnetic resonance imaging,” *Journal of Neuroscience*, vol. 29, no. 13, pp. 4263–4273, 2009.

[147] B. Fischl and A. M. Dale, “Measuring the thickness of the human cerebral cortex from magnetic resonance images,” *The Proceedings of the National Academy of Sciences (PNAS)*, vol. 97, no. 20, pp. 11050–11055, 2000.

[148] K. L. Narr, R. M. Bilder, A. W. Toga, R. P. Woods, D. E. Rex, P. R. Szeszko, D. Robinson, S. Sevy, H. Gunduz-Bruce, Y. P. Wang, H. DeLuca, and P. M. Thompson, “Mapping cortical thickness and gray matter concentration in first episode schizophrenia,” *Cerebral Cortex*, vol. 15, no. 6, pp. 708–719, 2005.

[149] P. R. Amestoy, I. S. Duff, and J. Y. L’Excellent, “Multifrontal parallel distributed symmetric and unsymmetric solvers,” *Computer Methods in Applied Mechanics and Engineering*, vol. 184, no. 2–4, pp. 501–520, 2000.

[150] R. Wang, Y. Shen, D. Qian, J. Sun, X. Zhou, W. Wang, and Z. Liu, "Tensile and torsional elastomer fiber artificial muscle by entropic elasticity with thermo-piezoresistive sensing of strain and rotation by a single electric signal," *Materials Horizons*, vol. 7, no. 12, pp. 3305–3315, 2020.

[151] S. Aziz and G. M. Spinks, "Torsional artificial muscles," *Materials Horizons*, vol. 7, no. 3, pp. 667–693, 2020.

[152] T. Helps, M. Taghavi, S. Wang, and J. Rossiter, "Twisted Rubber Variable-Stiffness Artificial Muscles," *Soft Robotics*, vol. 7, no. 3, pp. 386–395, 2020.

[153] Y. Lanir, "A structural theory for the homogeneous biaxial stress-strain relationships in flat collagenous tissues," *Journal of Biomechanics*, vol. 12, no. 6, pp. 423–436, 1979.

[154] M. S. Sacks, "Incorporation of experimentally-derived fiber orientation into a structural constitutive model for planar collagenous tissues," *Journal of Biomechanical Engineering*, vol. 125, no. 2, pp. 280–287, 2003.

[155] T. C. Gasser, R. W. Ogden, and G. A. Holzapfel, "Hyperelastic modelling of arterial layers with distributed collagen fibre orientations," *Journal of the Royal Society Interface*, vol. 3, no. 6, pp. 15–35, 2006.

[156] V. Alastrué, M. A. Martínez, M. Doblaré, and A. Menzel, "Anisotropic microsphere-based finite elasticity applied to blood vessel modelling," *Journal of the Mechanics and Physics of Solids*, vol. 57, no. 1, pp. 178–203, 2009.

[157] A. J. Schriefl, H. Wolinkski, S. D. Kohlwein, and G. A. Holzapfel, "Structural Differences in Collagen Morphologies between Healthy and AAA Tissues," *The 4th Canadian Conference on Nonlinear Solid Mechanics (CanCNSM 2013)*, pp. 2–3, Montreal, Canada July 23–26 2013.

[158] G. A. Holzapfel, J. A. Niestrawska, R. W. Ogden, A. J. Reinisch, and A. J. Schriefl, "Modelling non-symmetric collagen fibre dispersion in arterial walls," *Journal of the Royal Society Interface*, vol. 12, no. 106, 2015.

[159] A. V. Melnik, H. Borja Da Rocha, and A. Goriely, "On the modeling of fiber dispersion in fiber-reinforced elastic materials," *International Journal of Non-Linear Mechanics*, vol. 75, pp. 92–106, 2015.

[160] G. A. Holzapfel and R. W. Ogden, “Comparison of two model frameworks for fiber dispersion in the elasticity of soft biological tissues,” *European Journal of Mechanics, A/Solids*, vol. 66, pp. 193–200, 2017.

[161] K. Y. Volokh, “On arterial fiber dispersion and auxetic effect,” *Journal of Biomechanics*, vol. 61, pp. 123–130, 2017.

[162] G. A. Holzapfel and R. W. Ogden, “On Fiber Dispersion Models: Exclusion of Compressed Fibers and Spurious Model Comparisons,” *Journal of Elasticity*, vol. 129, no. 1-2, pp. 49–68, 2017.

[163] A. Anssari-Benam, Y. T. Tseng, and A. Bucchi, “A transverse isotropic constitutive model for the aortic valve tissue incorporating rate-dependency and fibre dispersion: Application to biaxial deformation,” *Journal of the Mechanical Behavior of Biomedical Materials*, vol. 85, pp. 80–93, 2018.

[164] K. Li, R. W. Ogden, and G. A. Holzapfel, “An exponential constitutive model excluding fibres under compression: Application to extension–inflation of a residually stressed carotid artery,” *Mathematics and Mechanics of Solids*, vol. 23, no. 8, pp. 1206–1224, 2018.

[165] C. J. Stender, E. Rust, P. T. Martin, E. E. Neumann, R. J. Brown, and T. J. Lujan, “Modeling the effect of collagen fibril alignment on ligament mechanical behavior,” *Biomechanics and Modeling in Mechanobiology*, vol. 17, no. 2, pp. 543–557, 2018.

[166] S. Heo and Y. Xu, “Constructing Fully Symmetric Cubature Formulae for the Sphere,” *American Mathematical Society*, vol. 70, no. 233, pp. 269–279, 2001.

[167] M. Mottahedi and H. C. Han, “Artery buckling analysis using a two-layered wall model with collagen dispersion,” *Journal of the Mechanical Behavior of Biomedical Materials*, vol. 60, pp. 515–524, 2016.

[168] G. A. Holzapfel, *Computational Biomechanics of Soft Biological Tissues: Arterial Walls, Hearts Walls, and Ligaments*. Encyclopedia of Computational Mechanics Second Edition, 2017.

[169] I. Breslavsky, G. Franchini, and M. Amabili, “Effect of fiber exclusion in uniaxial tensile tests of soft biological tissues,” *Journal of the Mechanical Behavior of Biomedical Materials*, vol. 112, 104079, 2020.

[170] H. Dong and W. Sun, “A novel hyperelastic model for biological tissues with planar distributed fibers and a second kind of Poisson effect,” *Journal of the Mechanics and Physics of Solids*, vol. 151, 104377, 2021.

[171] R. C. Thompson, A. H. Allam, G. P. Lombardi, L. S. Wann, M. L. Sutherland, J. D. Sutherland, M. A.-T. Soliman, B. Frohlich, D. T. Mininberg, J. M. Monge, *et al.*, “Atherosclerosis across 4000 years of human history: the horus study of four ancient populations,” *The lancet*, vol. 381, no. 9873, pp. 1211–1222, 2013.

[172] H. Demiray, “A note on the elasticity of soft biological tissues,” *Journal of biomechanics*, vol. 5, no. 3, pp. 309–311, 1972.

[173] J. Humphrey, R. Strumpf, and F. Yin, “Determination of a constitutive relation for passive myocardium: I. a new functional form,” *Journal of Biomechanical Engineering*, vol. 112, no. 3, pp. 333–339, 1990.

[174] J. M. Guccione, A. D. McCulloch, and L. Waldman, “Passive material properties of intact ventricular myocardium determined from a cylindrical model,” *Journal of Biomechanical Engineering*, vol. 113, no. 1, pp. 42–55, 1991.

[175] M. P. Nash and P. J. Hunter, “Computational mechanics of the heart,” *Journal of elasticity and the physical science of solids*, vol. 61, no. 1, pp. 113–141, 2000.

[176] H. Schmid, M. Nash, A. Young, and P. Hunter, “Myocardial material parameter estimation–a comparative study for simple shear,” *Journal of Biomechanical Engineering*, vol. 128, pp. 742–750, 2006.

[177] S. Göktepe, S. Acharya, J. Wong, and E. Kuhl, “Computational modeling of passive myocardium,” *International Journal for Numerical Methods in Biomedical Engineering*, vol. 27, no. 1, pp. 1–12, 2011.

[178] L. Taylor and S. Govindjee, “A finite element analysis program (feap),” *Department of Civil and Environmental Engineering, University of California at Berkeley, Berkeley CA*, 2008.

[179] N. J. Driessen, C. V. Bouten, and F. P. Baaijens, “A structural constitutive model for collagenous cardiovascular tissues incorporating the angular fiber distribution,” *Journal of Biomechanical Engineering*, vol. 127, pp. 494–503, 2005.

[180] V. Alastrué, P. Sáez, M. Martínez, and M. Doblaré, “On the use of the bingham statistical distribution in microsphere-based constitutive models for arterial tissue,” *Mechanics Research Communications*, vol. 37, no. 8, pp. 700–706, 2010.

[181] L. Loeffler 3rd and K. Sagawa, “A one-dimensional viscoelastic model of cat heart muscle studied by small length perturbations during isometric contraction.,” *Circulation research*, vol. 36, no. 4, pp. 498–512, 1975.

[182] M. Yang and L. A. Taber, “The possible role of poroelasticity in the apparent viscoelastic behavior of passive cardiac muscle,” *Journal of biomechanics*, vol. 24, no. 7, pp. 587–597, 1991.

[183] J. M. Huyghe, D. H. van Campen, T. Arts, and R. M. Heethaar, “The constitutive behaviour of passive heart muscle tissue: a quasi-linear viscoelastic formulation,” *Journal of biomechanics*, vol. 24, no. 9, pp. 841–849, 1991.

[184] M. Kaliske, “A formulation of elasticity and viscoelasticity for fibre reinforced material at small and finite strains,” *Computer methods in applied mechanics and engineering*, vol. 185, no. 2-4, pp. 225–243, 2000.

[185] G. A. Holzapfel and T. C. Gasser, “A viscoelastic model for fiber-reinforced composites at finite strains: Continuum basis, computational aspects and applications,” *Computer methods in applied mechanics and engineering*, vol. 190, no. 34, pp. 4379–4403, 2001.

[186] O. Gültekin and H. Dal, “Computational finite strain orthotropic viscoelasticity of human passive myocardium,” in *Solid (Bio) mechanics: Challenges of the Next Decade*, pp. 257–278, Springer, 2022.

[187] D. Nordsletten, A. Capilnasiu, W. Zhang, A. Wittgenstein, M. Hadjicharalambous, G. Sommer, R. Sinkus, and G. A. Holzapfel, “A viscoelastic model for human myocardium,” *Acta Biomaterialia*, vol. 135, pp. 441–457, 2021.

[188] O. Z. Tikenoğulları, F. S. Costabal, J. Yao, A. Marsden, and E. Kuhl, "How viscous is the beating heart? insights from a computational study," *Computational Mechanics*, vol. 70, pp. 565–579, 2022.

[189] S. Göktepe, A. Menzel, and E. Kuhl, "The generalized hill model: A kinematic approach towards active muscle contraction," *Journal of the Mechanics and Physics of Solids*, vol. 72, pp. 20–39, 2014.

[190] C. Miehe and S. Göktepe, "A micro-macro approach to rubber-like materials. Part II: The micro-sphere model of finite rubber viscoelasticity," *Journal of the Mechanics and Physics of Solids*, vol. 53, no. 10, pp. 2231–2258, 2005.

[191] M. A. Biot, *Mechanics of incremental deformations*. John Wiley & Sons, 1965.

[192] W. J. Karlon, J. W. Covell, A. D. Mcculloch, J. J. Hunter, and J. H. Omens, "Automated measurement of myofiber disarray in transgenic mice with ventricular expression of ras," *Anatomical Record*, vol. 252, no. 4, pp. 612–625, 1998.

[193] T. P. Usyk, J. H. Omens, and A. D. McCulloch, "Regional septal dysfunction in a three-dimensional computational model of focal myofiber disarray," *American Journal of Physiology - Heart and Circulatory Physiology*, vol. 281, no. 2 50-2, pp. 506–514, 2001.

[194] S. Göktepe, *Micro-macro approaches to rubbery and glassy polymers: Predictive micromechanically-based models and simulations*. PhD thesis, University of Stuttgart, 2007.

[195] P. Bažant and B. Oh, "Efficient numerical integration on the surface of a sphere," *ZAMM-Journal of Applied Mathematics and Mechanics/Zeitschrift für Angewandte Mathematik und Mechanik*, vol. 66, no. 1, pp. 37–49, 1986.

[196] S. Heo and Y. Xu, "Constructing symmetric cubature formulae on a triangle," *Advances in Computational Mathematics*, vol. 202, p. 203, 1998.

CURRICULUM VITAE

PERSONAL INFORMATION

Name and Surname: Cem ALTUN

EDUCATION

Degree	Institution	Year of Graduation
M.Sc.	Middle East Technical University	2014
B.Sc.	Middle East Technical University Northern Cyprus Campus	2012
High School	Bursa Milli Piyango Anatolian High School	2006

PROFESSIONAL EXPERIENCE

Year	Place	Enrollment
2018-present	FIGES Engineering	R&D Manager - Structural Analysis Unit Manager
2016-2018	FIGES Engineering	Senior Structural Analysis Engineer
2012-2016	FIGES Engineering	Structural Analysis Engineer

KEY PAPERS AND PRESENTATIONS

- **Altun, C.**, Açan, A.K., Dal H. *Dispersion-type anisotropic viscoelastic constitutive model for soft biological tissues: Model validation for human myocardium*, Computational Mechanics, submitted for publication, 2023.
- **Altun, C.**, Gürses E., Dal H. *Growth-induced instabilities for transversely isotropic hyperleastic materials*, International Journal for Numerical Methods

in Biomedical Engineering, submitted for publication, 2022, arXiv preprint arXiv:2207.14573.

- Açan, A. K., **Altun, C.**, Dal H. *Dispersion-type anisotropic viscoelasticity: Model validation for myocardium*, Proceedings in Applied Mathematics and Mechanics (PAMM), Aachen, Germany, August 15-19, 2022